Exploration of Hot Switching Damage and Damage Mechanisms in MEMS Switch Contacts

A Dissertation Presented
by

Ryan Patrick Hennessy

to

The Department of Mechanical and Industrial Engineering

in partial fulfillment of the requirements
for the degree of

Doctor of Philosophy

in the field of

Mechanical Engineering

Northeastern University
Boston, Massachusetts

August, Two Thousand and Thirteen

Exploration of Hot Switching Damage and Damage Mechanisms in MEMS Switch Contacts

Ryan P. Hennessy

ABSTRACT

Ohmic contact, or contact-type, Microelectromechanical Systems (MEMS) switches employ two separable metal electrodes as a contact. In the switch environment, the switch contact may experience either of two switching modes. Cold switching refers to the application of an electrical signal across the switch only when the contact is fully closed. On the other hand, hot switching refers to the application of a signal while the switch is being opened and closed. Compared to cold switching, hot switching leads to shorter contact lifetimes.

This work explores the effect of multi-domain coupling on the behavior of an electrical contact, what makes hot switching damaging, the making of contact under bias as it compares to the breaking of contact under bias (leading versus trailing edge hot switching), and the specific mechanisms that could be responsible for hot switching damage.

Theoretically, it was found that for a contact operating under displacement control, such as an asperity on the surface of a contact bump, thermal-electrical-mechanical coupling has a significant effect. Generalized (non-dimensional) equations are presented to describe the behavior of the contact in this situation.

Experimentally, a specially built micro-contact testing system and microfabricated contact pairs were used to conduct hot switching tests to characterize hot switching damage. It was found that hot switching damage mechanisms are active on both the leading (closing) and trailing (opening) edges, resulting in directional material transfer damage of roughly the same volume at 4400 μm/s approach/separation rate. Furthermore, the direction of the material transfer damage is shown to be polarity-dependent, from the anode to the cathode. Polarity dependent damage mechanisms were found to be active at separations of less than 10 nm and in time periods on the order of hundreds of nanoseconds. Additionally, thermo-mechanical contact damage mechanism comprised of joule heating and thermal geometry was identified that transfers material away from the contact bump with strong separation rate dependence.

This work makes significant progress toward defining the specific mechanisms responsible for the additional damage associated with hot switching, thereby helping to solve a problem that has plagued the microswitch and inhibited it from significant commercial market penetration.

Exploration of Hot Switching Damage and Damage Mechanisms in MEMS Switch Contacts

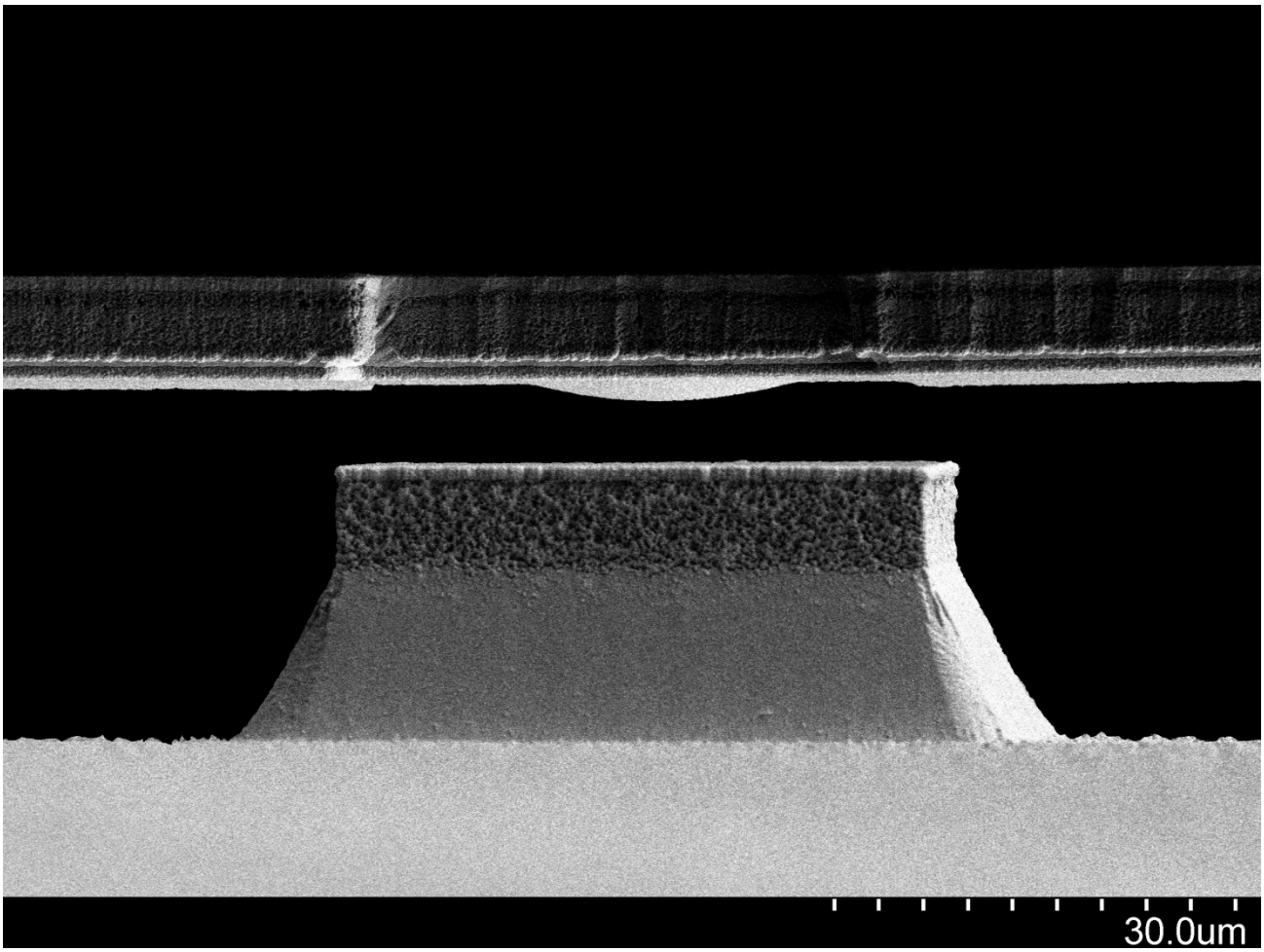

Ryan P. Hennessy

To those that came before me

Table of Contents

Chapter 5: Hot-Switching Damage Mechanisms in MEMS Switch Contacts

Chapter 6: Conclusion

Appendix: Experimental Background and Associated Material

List of Figures

Chapter 2: Literature Review

Chapter 3: Modeling of a Thermal-Electrical-Mechanical Coupled Field Contact

generated by curve-fitting. Results for V^* = 0.044 were omitted to reduce clutter because they are relatively close to V^* = 0.000.

Figure 3.8 Dimensionless contact force (P^*) vs dimensionless interference (δ^*) for varying dimensionless currents (I^*). The data points represent FEM results, while trend lines are generated by curve-fitting.

Chapter 4: Hot-Switched Lifetime and Damage Characteristics of MEMS Switch Contacts

Figure 4.1 (a) SEM of typical force sensor (b) SEM of typical pillar (c) Schematic of test setup (d) Schematic of test circuit with reversible applied voltage source.

Figure 4.2 Schematics of the four different switching modes presented in this chapter. Each test type employs a ramp-hold-ramp actuation waveform as represented by the dashed lines. The applied voltage waveforms are represented by the solid grey lines.

Figure 4.3 Contact damage for various types of switching cycled at 500 Hz for $5x10^5$ cycles.

Figure 4.4 Leading edge vs trailing edge hot switching progression tests cycled at 500 Hz, $3.54V_{Hot}$, and $77.5mA_{Cold}$ with contact bump as anode.

Figure 4.5 Leading edge vs trailing edge hot switching progression tests cycled at 500 Hz, $3.54V_{Hot}$, and $77.5mA_{Cold}$ with contact bump as cathode.

Figure 4.6 Volume analysis for leading edge vs trailing edge hot switching progression tests; each point represents the average of at least three separate tests. The error bars represent the maximum and minimum volume measurement for each condition. Error bars with long rounded caps correspond to trailing edge tests and error bars with square caps correspond to leading edge tests.

Figure 4.7 Contacts cycled at 500 Hz for $5x10^5$ cycles at $0.71V_{Hot}$ with varying I_{Cold} for both polarities.

Figure 4.8 Contacts cycled at 500 Hz for $5x10^5$ cycles at $3.54V_{Hot}$ with varying I_{Cold} for both polarities.

Figure 4.9 (a) Schematic of test circuit with external resister (b) Current spikes measured via the external resister before closing and after opening in a contact cycled at 500 Hz with $3.00V_{Hot}$ and 55 Ω of total series resistance.

Chapter 5: Hot-Switching Damage Mechanisms in MEMS Switch Contacts

Figure 5.10 Schematic of two rough surfaces coming together where contact is initially made at the peaks of the highest asperities as highlighted by the grey dashed circles.

Figure 5.11 Schematic of molten bridge formation.

Appendix: Experimental Background and Associated Material

Figure A.15 Volume calculation program rendering of AFM image.

Figure A.16 Generated surface fit with non-damaged area points (red) and damaged area points (blue).

List of Tables

Chapter 2: Literature Review

Chapter 3: Modeling of a Thermal-Electrical-Mechanical Coupled Field Contact

Chapter 4: Hot-Switched Lifetime and Damage Characteristics of MEMS Switch Contacts

Chapter 5: Hot-Switching Damage Mechanisms in MEMS Switch Contacts

Appendix: Experimental Background and Associated Material

Table A.1 General information about each of the sample types. The colors are consistent with the figure above.

Table A.2 Test structure dimensions.

Chapter 1

Introduction

1.1 Background: An Overview of MEMS Switch Contacts

Microelectromechanical Systems (MEMS) switches can be classified into two contact types: capacitive and ohmic. In a capacitive switch, two transmission lines are separated by a dielectric material, effectively forming a capacitor. The capacitance of the switch is controlled by mechanically changing the separation between the transmission lines. Because a capacitive switch is essentially a capacitor with variable capacitance, it will not function in a direct current (DC) environment and can only be used in high frequency applications. Ohmic contact, or contact-type, switches employ two separable conductive surfaces (generally metals) as the electrodes of a contact. The switch is open if the electrodes are not touching. When the electrodes are touching the switch is closed, allowing current to flow through the contact; the amount of current flowing through the contact is governed by Ohm's law, hence the name of this type of switch. Unlike capacitive switches, ohmic switches can be used for either DC or AC applications.

With applications in the aerospace, military, and commercial sectors, MEMS switches have a large potential market. Ohmic MEMS switches can switch signals from DC to at least 100 GHz and can be used in automated test equipment (ATE) as well as in industrial and medical instrumentation applications [1]. Compared to electromechanical technologies such as reed relays, contact-type MEMS switches are smaller and have faster switching times [2]. Both contact-type and capacitive MEMS switches have applications in radio frequency (RF) systems such as phased arrays and reconfigurable apertures for telecommunication systems, switching systems for satellite communications, single-pole N-throw switches for wireless portable or base-station applications, as well as in commercial cell phone antennae [3]-[8]. Compared to current solid state RF technologies such as Field Effect Transistor (FET) switches and PIN diodes, RF MEMS switches generally have lower insertion loss (0.1 dB up to 100 GHz), higher isolation (because of lower off-state capacitances of 2-4 fF at 0.1-60 GHz), lower power consumption (10-100 nJ per switching cycle), and higher linearity [1]. However there are also some disadvantages to MEMS switches such as high actuation voltages, slow switching speeds (compared to solid state technologies), and moderate power handling capabilities. Perhaps the greatest flaw of this maturing technology is reliability, especially at high power or when hot switching. Applications for RF MEMS switches require from about 100 million cycles to several hundred billion cycles [2]. Although there are several high performance and high power MEMS switches currently on the market and under development, such as the Radant switch [9], the UCSD switch [10], the Omron switch [11], and the CEA-LETI switch [12] all have reported significantly less reliability when hot switched.

In the switch environment, the switch contact may experience either of two switching modes. Cold switching refers to the application of an electrical signal across the switch only when the contact is fully closed. On the other hand, hot switching refers to the application of a signal while the switch is being opened and closed. For testing purposes, a few variations of hot and cold switching also exist. Leading edge hot switching refers to the application of a signal across the switch as it closes while trailing edge hot switching refers specifically to the application of a signal across the switch as it opens. In general leading edge and trailing edge hot switching may include the application of a different electrical signal while the contact is

fully closed. Finally, pure mechanical switching refers to cycling without an applied electrical signal.

Contact damage due to cold switching and purely mechanical switching have been studied in several papers. Cold switching damage mechanisms can result in two different types of contact failure. Stuck-open failure, generally caused by contamination [13][14] or wear [15][16], occurs when the contact resistance becomes too high for the switch to function properly. Conversely, stuck-closed failure occurs when the switch remains perpetually in the on-state, even after the actuation voltage is removed. This type of failure is generally caused by welding [17], stiction [18], or bridge transfer [19]. The dominant damage mechanism for cold-switched contacts tends to depend on the power transmitted, the contact material, and the ambient and surface preparation. Generally, at lower powers, contamination and wear tend to be the dominant damage mechanisms, whereas welding and melting tend to be the dominant damage mechanisms at higher powers.

Compared to cold switching, hot switching leads to shorter contact lifetimes [19][20]. Thus there are additional damage mechanisms that occur during hot switching as compared to cold switching. However, the specific hot switching damage mechanisms are not completely agreed upon.

The following literature review will cover in detail the experimental and theoretical work associated with contact damage mechanisms.

1.2 Thesis Statement

The focus of this work is hot switching damage in MEMS switch contacts. Specifically this work will explore the effect of multi-domain coupling on the behavior of an electrical contact, characterization of hot switching contact damage, the making of contact under bias as it compares to the breaking of contact under bias (leading versus trailing edge hot switching), and the specific mechanisms that could be responsible for hot switching damage. To advance the state of understanding of hot switching and the resulting damage, both experimental testing and theoretical modeling will by employed.

1.3 Contents of Thesis

Chapter 2 surveys the literature. The theoretical literature includes pertinent models and research in the thermal, electrical, and mechanical domains. Chapter 3 presents a multi-physics finite element model used to explore the effect of multi-domain coupling in a micro-scale electrical contact. Chapter 4 characterizes hot switching damage and specifically compares leading edge hot switching with trailing edge hot switching. The effect of mild hot switching is also explored. Chapter 5 presents possible mechanisms responsible for hot switching damage and analyzes the plausibility of each. Experimental results to support these analyses are also presented.

1.4 Division of Labor

It is very important to note that this project was a group effort. Anirban Basu deserves recognition for his large contribution to this project. Anirban ran all of the tests and performed

the majority of the SEM imaging. He contributed to the results analysis and the general understanding of hot switching damage behavior. In addition, he was also in charge of configuring and maintaining the testing circuitry.

1.5 Chapter 1 References

[1] Rebeiz G M 2003 *RF MEMS: Theory, design, and technology* (Hoboken, New Jersey: J. Wiley & Sons)

[2] Rebeiz G M and Muldavin J B 2001 RF MEMS switches and switch circuits *microwave magazine, IEEE* **2** 59-71

[3] Ehwald K, Drews J, Scholz R, Korndorfer F, Knoll D, Tillack B, Barth R, Birkholz M, Schulz K and Sun Y 2009 BEOL embedded RF-MEMS switch for mm-wave applications. In: *Electron Devices Meeting (IEDM), 2009 IEEE International*: IEEE) pp 797-800

[4] Brown E R 1998 RF-MEMS switches for reconfigurable integrated circuits *Microwave Theory and Techniques, IEEE Transactions on* **46** 1868-80

[5] Park S J, Reines I and Rebeiz G 2009 High-Q RF-MEMS tunable evanescent-mode cavity filter. In: *Microwave Symposium Digest, 2009. MTT'09. IEEE MTT-S International*: IEEE) pp 1145-8

[6] Ho K M J and Rebeiz G M 2012 Microstrip antennas with full polarization diversity using packaged RF MEMS switches. In: *Antennas and Propagation Society International Symposium (APSURSI), 2012 IEEE*: IEEE) pp 1-2

[7] Lee K Y and Rebeiz G M 2009 A miniature 8–16 GHz packaged tunable frequency and bandwidth RF MEMS filter. In: *Radio-Frequency Integration Technology, 2009. RFIT 2009. IEEE International Symposium on*: IEEE) pp 249-52

[8] Chan K Y, Daneshmand M, Mansour R R and Ramer R 2009 Scalable RF MEMS switch matrices: Methodology and design *Microwave Theory and Techniques, IEEE Transactions on* **57** 1612-21

[9] Newman H S, Ebel J L, Judy D and Maciel J 2008 Lifetime measurements on a high-reliability RF-MEMS contact switch *Microwave and Wireless Components Letters, IEEE* **18** 100-2

[10] Patel C D and Rebeiz G M 2011 RF MEMS Metal-Contact Switches With mN-Contact and Restoring Forces and Low Process Sensitivity *Microwave Theory and Techniques, IEEE Transactions on* **59** 1230-7

[11] Uno Y, Narise K, Masuda T, Inoue K, Adachi Y, Hosoya K, Seki T and Sato F 2009 Development of SPDT-structured RF MEMS switch. IEEE) pp 541-4

[12] Mercier D, Charvet P L, Berruyer P, Zanchi C, Lapierre L, Vendier O, Cazaux J L and Blondy P 2004 A DC to 100 GHz high performance ohmic shunt switch. IEEE) pp 1931-4

[13] Chen L, Lee H, Guo Z, McGruer N E, Gilbert K, Mall S, Leedy K and Adams G 2007 Contact resistance study of noble metals and alloy films using a scanning probe microscope test station *Journal of Applied Physics* **102** 074910--7

[14] Broue A, Dhennin J, Charvet P, Pons P, Jemaa N B, Heeb P, Coccetti F and Plana R 2010 Multi-Physical Characterization of Micro-Contact Materials for MEMS Switches. In: *IEEE Holm Conference on Electrical Contacts (HOLM),* (Charleston, South Carolina, USA: IEEE) pp 1-10

[15] Majumder S, Lampen J, Morrison R and Maciel J 2003 A packaged, high-lifetime ohmic MEMS RF switch. In: *MTT-S International Microwave Symposium Digest,* (Philadelphia, Pennsylvania, USA: IEEE) pp 1935-8

[16] Yang Z, Lichtenwalner D J, Morris A S, Krim J and Kingon A I 2009 Comparison of Au and Au–Ni Alloys as Contact Materials for MEMS Switches *Microelectromechanical Systems, Journal of* **18** 287-95

[17] Kwon H, Choi D J, Park J H, Lee H C, Park Y H, Kim Y D, Nam H J, Joo Y C and Bu J U 2007 Contact materials and reliability for high power RF-MEMS switches. IEEE) pp 231-4

[18] Patton S and Zabinski J 2005 Fundamental studies of Au contacts in MEMS RF switches *Tribology Letters* **18** 215-30

[19] Becher D, Chan R, Hattendorf M and Feng M 2002 Reliability study of low-voltage RF MEMS switches. pp 54-7

[20] Yang Z, Lichtenwalner D, Morris A, Krim J and Kingon A 2010 Contact degradation in hot/cold operation of direct contact micro-switches *Journal of Micromechanics and Microengineering* **20** 105028

Chapter 2

Literature Review

2.1 Analysis Literature

This section covers models and theoretical work pertinent to micro-scale electrical contacts. An electrical contact, as defined by Holm [30], is a releasable junction between two conductors, called electrodes. In an ohmic contact microswitch, the two electrodes, usually metal, are pressed together by an actuator (thermal, magnetic, electrostatic, etc) such that current can flow. The electrical current through the contact causes joule heating. If the joule heating is significant, thermo-mechanical effects such as thermal expansion, thermal softening, and changes to electrical and thermal conductivity can occur which can all affect the contact resistance. Thus, the contact of a microswitch is a highly-coupled multi-physics environment with mechanical, electrical, and thermal interactions. Therefore, it is necessary to understand the basic theory of all three domains. The following is a brief introduction to the contact environment.

When two surfaces are pressed together with load P, the area through-which electrical current and thermal energy can be conducted is generally much less than the apparent contact area A_a. Due to micro and non-scale roughness, only the tallest surface features, called asperities, make contact with each other. Thus the load bearing contact area A_b is the sum of the asperity contact areas. The relationship between load and the load-bearing area can be expressed simply

$$P = \bar{p}\, A_b \tag{2.1}$$

where $\bar{p}$ is the average pressure exerted on each asperity contact area. For a nominally flat contact surface, the average pressure can be defined as

$$\bar{p} = \xi H \tag{2.2}$$

where $0.2 < \zeta < 1.0$ and H is the Meyer's Hardness of the contact material. For typical electrical contacts, $\zeta = 0.6$ [30].

Furthermore, each of these asperity contact areas can generally be broken down into three types of regions:

1) Metal-on-metal contact – so-called 'a-spots' through which electrical current and thermal energy can travel with no discernible change in resistance at the interface of the two bodies.
2) Quasi-metallic contact – these regions can conduct electrical current and thermal energy, but have an increased resistance to conduction at the interface because the energy is conducted through impurities such as thin oxides, films, or other contaminants.
3) Insulated contact – these regions do not conduct electrical and/or thermal energy.

When applying these concepts to micro-scale contacts, it becomes apparent that the total area through which electrical and thermal energy is conducted is exceedingly small. Thus, the sections below present asperity and constriction-based theoretical models for each of the three domains: mechanical, thermal, and electrical. The theory explored herein is meant to form a solid basis of information for the work presented in this thesis, but by no-means is this collection meant to be exhaustive; there are a plethora of important and notable sources that are not touched upon here.

2.1.1 Mechanical Contact

Hertz Contact: Single Asperity Purely Mechanical Contact

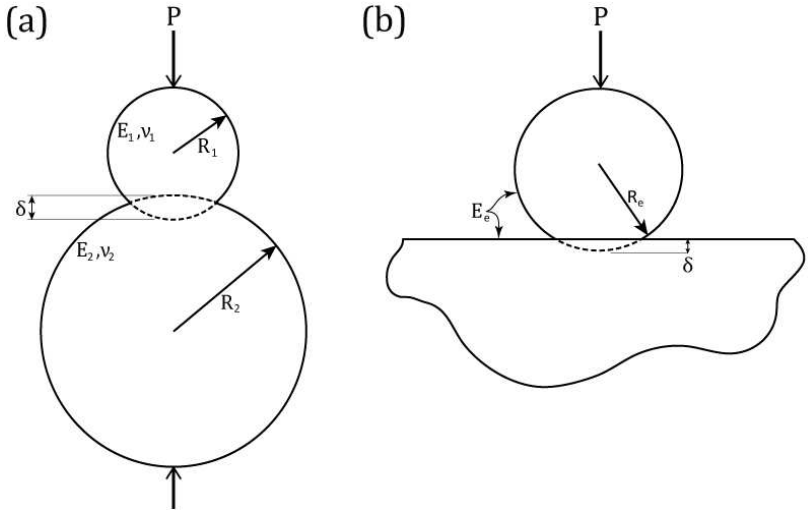

Figure 2.1 (a) Two spheres of different composition being pressed together (b) The equivalent sphere-flat system.

Heinrich Hertz developed a model to understand the effects on optical properties of holding force on stacked lenses [21]. Consider a system composed of two spheres being pressed against each other with a force, P, or a prescribed interference, δ, as depicted in Figure 2.1(a). The contact spot between the two spheres will be a circle of radius a. By the use of effective modulus E_e and radius R_e, the equivalent sphere-flat system can be formulated as depicted in Figure 2.1(b). The normal traction force profile (IE, the normal stress profile on the surfaces of the sphere) inside the circular contact area is assumed to be ellipsoidal

$$p(r) = p_0\left(1 - \left(\frac{r}{a}\right)^2\right)^{1/2} \tag{2.3}$$

$$p_0 = \left(\frac{3P}{2\pi a^2}\right) \tag{2.4}$$

as depicted in Figure 2.2.

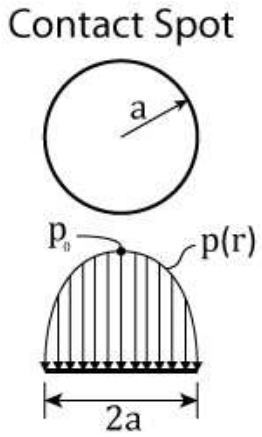

Figure 2.2 The normal stress profile of the circular contact spot between the spheres.

Using this formulation, the contact radius, a, for a prescribed interference, δ,

$$a = (R_e\delta)^{1/2} \tag{2.5}$$

Alternately, if a downward contact force, *P*, is applied to the hemisphere

$$a = \left(\frac{3PR_e}{4E_e}\right)^{1/3} = \left(\frac{PR_e}{K}\right)^{1/3} \tag{2.6}$$

where the effective radius (R_e), and effective modulus (E_e) are defined respectively as

$$R_e = \left(\frac{1}{R_1} + \frac{1}{R_2}\right)^{-1} \tag{2.7}$$

$$E_e = \left(\frac{1-\nu_1^2}{E_1} + \frac{1-\nu_2^2}{E_2}\right)^{-1} \tag{2.8}$$

$$K = \frac{4}{3}E_e \tag{2.9}$$

In Equation (2.6)-(2.9) above, E is the modulus of elasticity and ν is Poisson's ratio. The numerical subscripts correspond to the component of the contact. Note that the effective radius and effective modulus make the schematics of Figure 2.1(a) and Figure 2.1(b) exactly equivalent.

Additionally, the amount of holding force necessary to generate a prescribed interference is defined as

$$P = \left(\frac{4E_e R_e^{1/2}}{3}\right)\delta^{3/2} \tag{2.10}$$

In this form, if the interference is interpreted as a displacement, the contact can be interpreted as a non-linear spring with a non-linear spring constant being ($4E_eR_e^{1/2}/3$).

Note that this model is purely elastic and does not include surface forces such as adhesion. At the micro and nano scales, adhesion forces become extremely important because of scaling effects. Essentially there are two types of adhesion to consider: dry adhesion, which results from van der Waals forces (attraction and repulsion forces due to molecular interactions), and wet adhesion, which result from meniscus forces. As it will be explained, the characteristics of the contact determine which model to apply.

Greenwood & Williamson Model: Multi-Asperity Purely Mechanical Contact

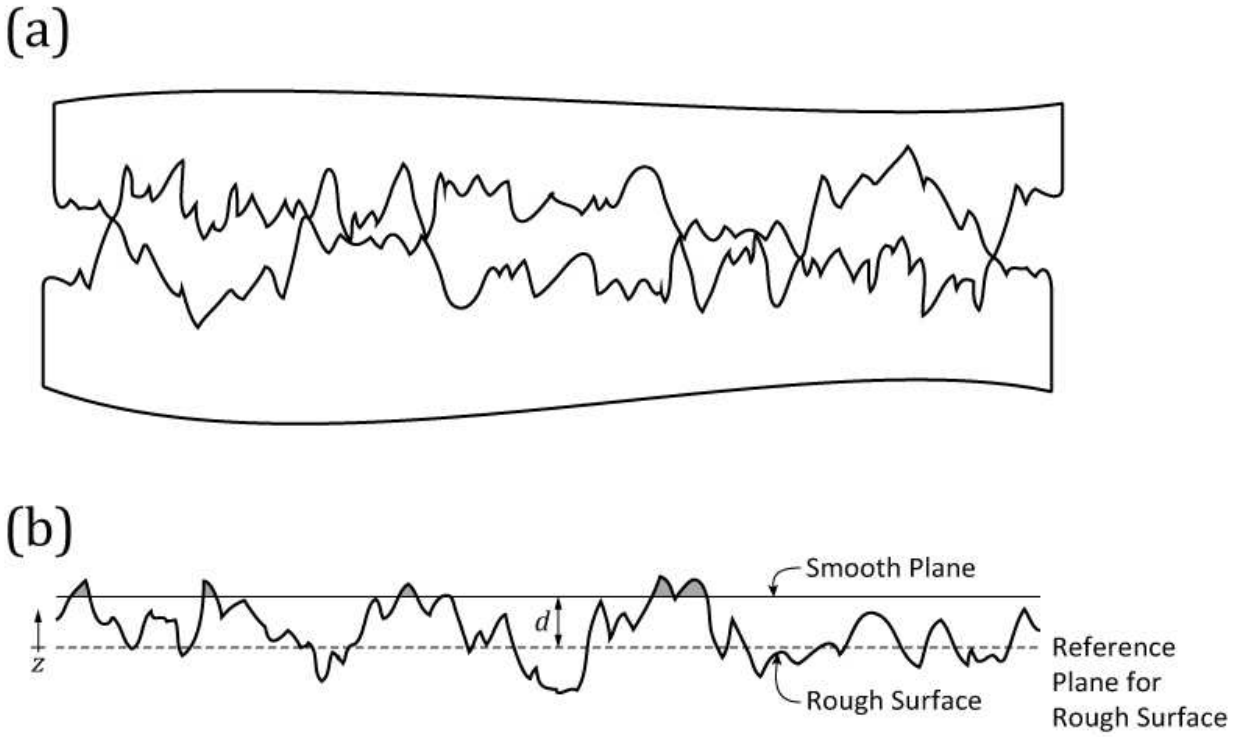

Figure 2.3 (a) Two rough surfaces in contact (b) Contact of an equivalent rough surface with a smooth plane, only the tallest asperities make contact and thus support the entire load – those asperity peaks are shaded in gray.

The Greenwood and Williamson [22] model attempts to describe the behavior when two nominally flat rough surfaces come into contact, as depicted in Figure 2.3(a). This model makes the following assumptions:

- When the rough surfaces come into contact, only the tops of the asperities contact each other.
- All of the asperities are locally spherical
- All asperity contacts are considered Hertz contacts and therefore can be represented as an equivalent sphere-flat contact. This makes Figure 2.3(a) and Figure 2.3(b) equivalent systems.
- All asperity summits have the same radius (R_e)
- Contact is between a plane and a nominally flat surface with a large number (N) asperities
- The asperity height varies randomly, thus the probability of making contact at any given asperity of height z is

$$\text{prob}(z > d) = \int_d^\infty \phi(z)dz \tag{2.11}$$

where ϕ(z) is the probability that a particular asperity has a height between z and dz above some reference plane and d is the separation between the reference planes of the two contacting surfaces, as depicted in Figure 2.3(b). This means that the expected number of contacts n is

$$n = N\int_d^\infty \phi(z)dz \tag{2.12}$$

- All asperities are sufficiently separated to be mechanically independent (the deformation of one asperity does not influence the deformation of another asperity)

Next, a normalized separation is defined as

$$h = {}^{d}/_{\sigma} \tag{2.13}$$

where σ is the standard deviation of the peak height probability density function ϕ(z). If the 'apparent' or nominal contact area is A_a, the asperity density can be defined as

$$\eta = {}^{N}/_{A_a} \tag{2.14}$$

With these definitions and the aforementioned assumptions, the following relations for total load, P, number of contacts, n, real (or 'True') contact area, A_r, can be written as

$$n = \eta A_a F_0(h) \tag{2.15}$$

$$A_r = \pi\eta A_a R_e \sigma F_1(h) \tag{2.16}$$

$$P = \frac{4}{3}\eta A_a E_e R_e^{1/2}\sigma^{3/2}F_{3/2}(h) \tag{2.17}$$

where

$$F_n(h) = N\int_h^\infty (z^* - h)^n \phi^*(z^*)dz^* \tag{2.18}$$

In this equation ϕ*(z*) represents the normalized asperity height distribution, and

$$z^* = \frac{z - m}{\sigma} \tag{2.19}$$

Again, z is a variable asperity height with respect to a reference plane, m is the mean of the height distribution, and σ is the standard deviation of the height distribution.

When the asperity heights follow an exponential distribution (which is a loose approximation of the uppermost 25% of asperity heights in a Gaussian distribution)

$$\phi^*(z^*) = e^{-z^*} \tag{2.20}$$

the equations for total load, P, number of contacts, n, real contact area, A_r, reduce to

$$n = \eta A_a e^{-h} \tag{2.21}$$

$$A_r = \pi \eta R_e \sigma A_a e^{-h} \tag{2.22}$$

$$P = \pi^{1/2} \eta R_e \sigma A_a E_e \left(\sigma/R_e\right)^{1/2} e^{-h} \tag{2.23}$$

This result is significant because it shows a linear relationship between contact force and real contact area as well as contact force and the number of contact spots. Thus the average size of the contact spots and the contact pressure are independent of the load. It is important to note that this result does not depend on the particular surface model or deformation mode. Rather, this result holds for an exponential distribution of asperity heights as long as all of the asperity contacts obey the same area / compliance and load / compliance laws. Moreover, these results suggest that the laws of Coulomb friction are indeed accurate.

This paper goes on to discuss the results from a Gaussian distribution of asperity heights. It turns out that these results come out close to those results for an exponential distribution.

Johnson-Kendall-Roberts (JKR): Single Asperity Adhesion Model

The JKR model includes elastic deformation and treats the effect of adhesion as surface energy only [23]. In this model, adhesive force (attractive tensile forces) are only considered in the contact region, and not considered at all in the separation region (the region just outside of the contact region). Using this formulation, the total energy equilibrium equation can be solved. Figure 2.4 represents a schematic of the resulting contact spot.

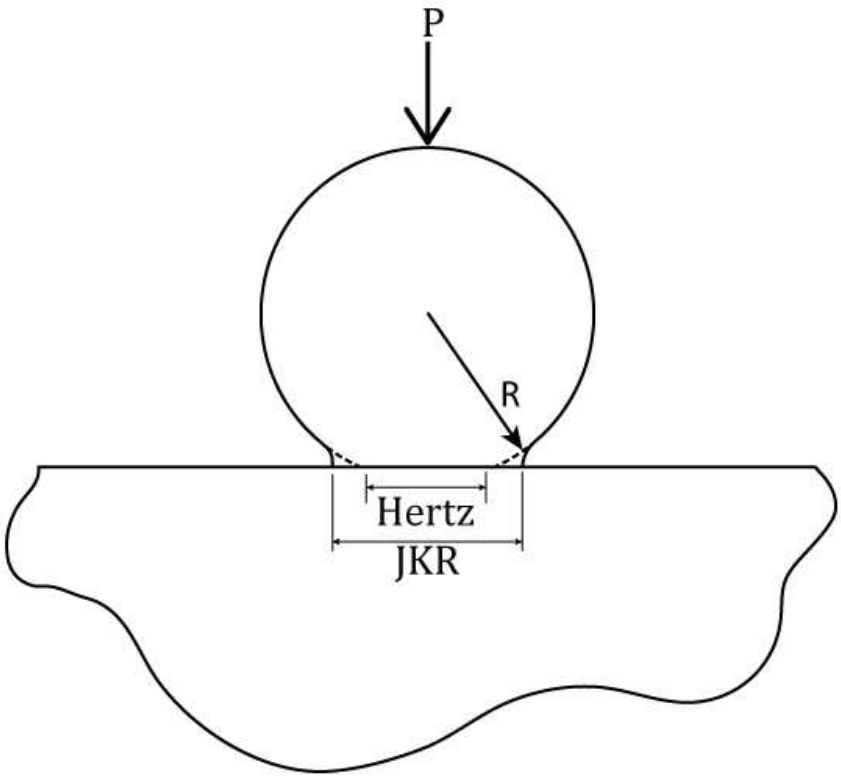

Figure 2.4 JKR adhesion model contact spot compared to Hertz purely mechanical contact spot.

For a prescribed contact force

$$a = \left(\frac{R_e}{K}\left(P + 3\pi\Delta\gamma R_e + (6\pi\Delta\gamma R_e P + (3\pi\Delta\gamma R_e)^2)^{1/2}\right)\right)^{1/3} \tag{2.24}$$

Alternately, for a prescribed interference

$$a = \left(\delta R_e + \left(\frac{8\pi a\Delta\gamma R_e^2}{3K}\right)^{1/2}\right)^{1/2} \tag{2.25}$$

$$\delta = \frac{a^2}{R_e} - \left(\frac{8\pi a\Delta\gamma}{3K}\right)^{1/2} \tag{2.26}$$

Comparing these equations to Equations (2.6) and (2.5), respectively, the additional adhesion terms become apparent. Additionally, the pull-off force is

$$F_{\text{Pull-Off, JKR}} = 1.5\pi\Delta\gamma R_e \tag{2.27}$$

It is important to note that while other adhesion models discussed in this review allow for the existence of a pull-in force, the JKR model does not.

Derjaguin-Muller-Toporov (DMT): Single Asperity Adhesion Model

The DMT model assumes that adhesive tensile stresses exist outside of the contact region (IE, tensile forces in the separation region), while the stresses inside the contact region remain identical to Hertz (IE, ellipsoidal normal force distribution) [24], as shown in Figure 2.5.

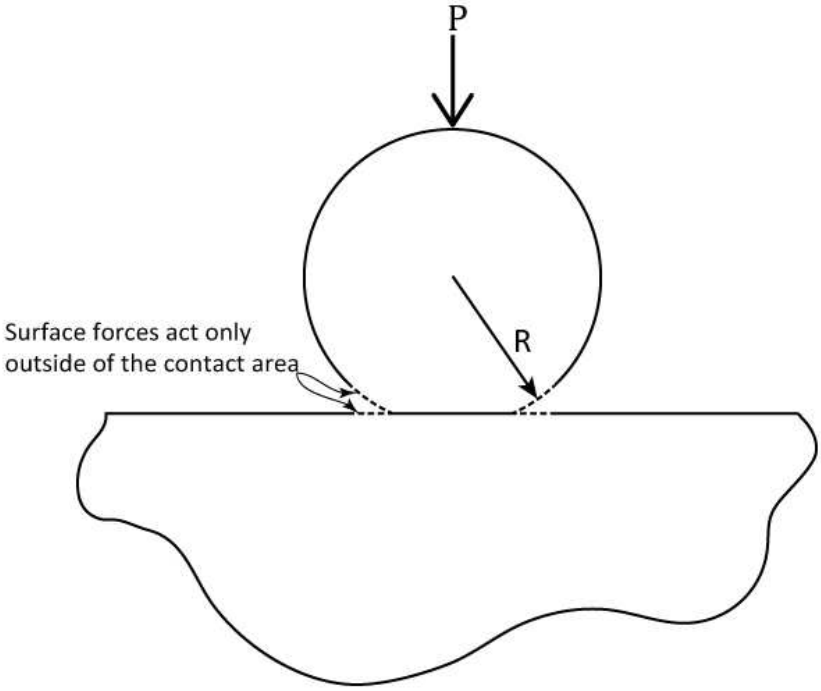

Figure 2.5 A schematic depicting the DMT model assumption as to where surface forces act.

Assuming this stress profile, the contact radius for a prescribe contact force is

$$a = \left(\frac{R_e}{K}(P + 2\pi\Delta\gamma R_e)\right)^{1/3} \tag{2.28}$$

$$P = \frac{Ka^3}{R_e} - 2\pi\Delta\gamma R_e \tag{2.29}$$

while the contact radius for a prescribed interference is

$$a = (R_e \delta)^{1/2} \tag{2.30}$$

Note that Equation (2.30) is identical to Equation (2.3); again, this is because the stress profile inside the contact is assumed to be identical to that of Hertz contact. Additionally, the pull-off force is

$$F_{\text{Pull-Off, DMT}} = 2\pi\Delta\gamma R_e \tag{2.31}$$

Tabor Parameter: Adhesion Model Application

The DMT and JKR adhesions theories were the cause of a lot of heated debate because they are seemingly in direct contrast with each other [25]. However, it was discovered that these theories are actually the limit cases of opposing ends of the same behavior spectrum. To distinguish the appropriate applications for the JKR and DMT theories, the Tabor parameter, μ, was created

$$\mu = \left(\frac{\Delta\gamma^2 R_e}{E_e^2 z_0^3}\right)^{1/3} \tag{2.32}$$

The Tabor parameter is the physical equivalent to the ratio of normal elastic deformation caused by adhesion to the spatial range of the adhesion forces [26].

Tabor parameter theory states that for μ values much less than one (stiff solids, small effective radius of curvature, weak energy of adhesion), the DMT model is appropriate. Alternately, for μ values much greater than one (compliant solids, large effective radius of curvature, large energy of adhesion), the JKR model is appropriate.

Maugis-Dugdale Model (MD): Single Asperity Adhesion Model

For intermediate values of the Tabor parameter, μ, Maugis [27] approximated the behavior of surface interaction using a Dugdale cohesive zone approximation. In this model, Maugis defines an elasticity parameter

$$\lambda = 2\sigma_0 \left(\frac{R_e}{\Delta\gamma K^2}\right)^{1/3} \tag{2.33}$$

where σ_0 is a constant adhesion stress that acts over a range of δ_t, resulting in the work of adhesion $\Delta\gamma = \sigma_0\delta_t$,. By choosing σ_0 to equal the minimum adhesion stress for a Lennard-Jones potential (with equilibrium spacing of z_0), it follows that $\delta_t = 0.97z_0$, making $\lambda = 1.1570\mu$. This leads to a the following system of three equations

(2.34)

(2.35)

(2.36)

where m = a/c, or the ratio of the contact radius to the cohesive zone radius. In this system of equations, if the elasticity parameter, λ, is not known before solving the problem, it must be found numerically. This makes finding a solution to a given problem cumbersome. However, it is generally agreed that this model is generally the best because this model encompasses the entire range of adhesion behavior. More specifically, for $\lambda > 5$, the JKR model applies, and for $\lambda < 0.1$, the DMT model applies. Figure 2.6 is a convenient adhesion map depicting the appropriate property sets in which to use the different adhesion models.

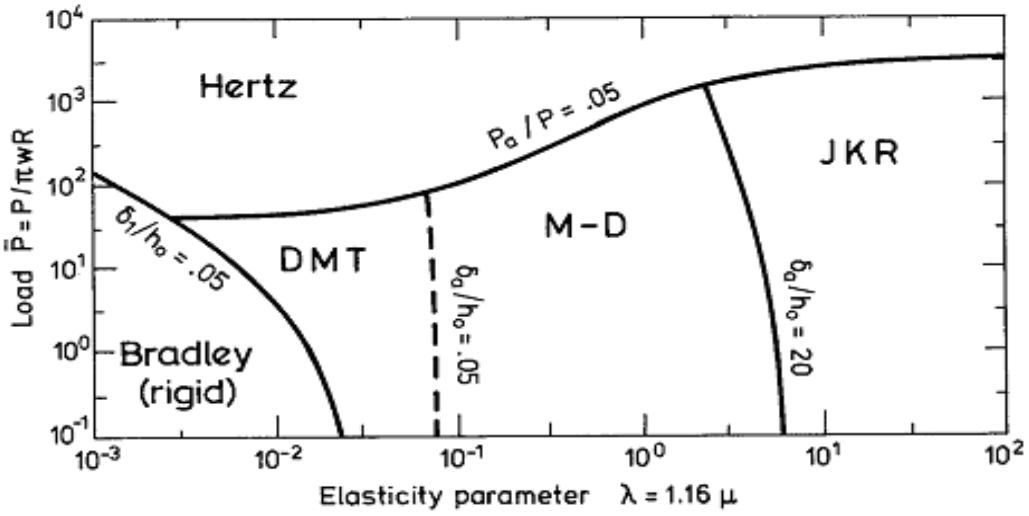

Figure 2.6 An adhesion map used to distinguish which adhesion model to apply (taken from [28]).

Additionally, Figure 2.7 provides a representative plot of force versus displacement for the different adhesion models.

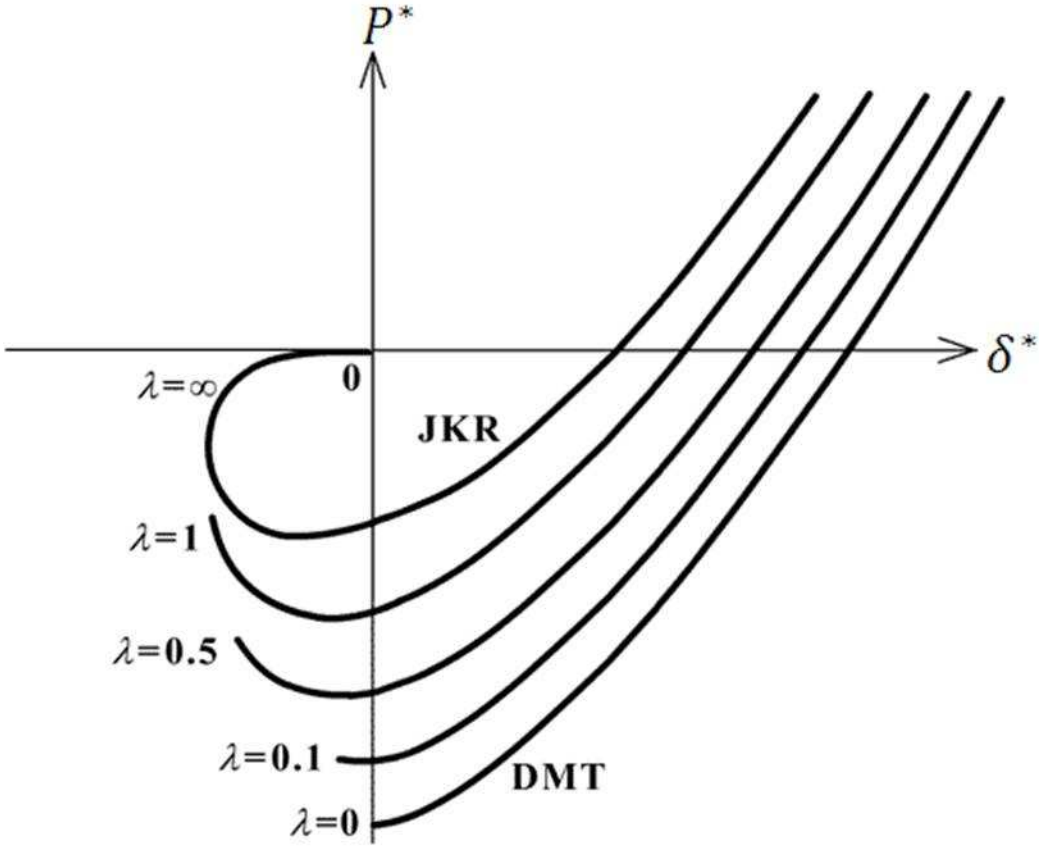

Figure 2.7 JKR, DMT, and MD Adhesion models for a given surface energy.

where the normalized values are defined as

$$P^* = \frac{P}{\pi R_e \Delta\gamma} \tag{2.37}$$

$$\delta^* = \frac{\delta}{\left(\frac{\pi^2 R_e \Delta\gamma^2}{K^2}\right)^{1/3}} \tag{2.38}$$

Carpick-Ogletree-Salmeron (COS): Simplified Single Asperity Adhesion Model

Because of the cumbersome nature of solving the Maugis system, Carpick, Ogletree, and Salmeron (COS) [29] used numerical software and curve fitting to develop a general

approximation equation to determine the contact area. They showed that the Maugis formulation could be approximated using the generalized transition equation

$$a = a_{0(\alpha)}\left(\frac{\alpha + \left(1 - P/P_{c(\alpha)}\right)^{1/2}}{1+\alpha}\right)^{2/3} \tag{2.39}$$

where α is another transition parameter and a_0 is the contact area at zero load. The α = 0 case corresponds exactly to the DMT formulation, while the α = 1 case corresponds exactly to the JKR formulation. The relationship between Maugis' elasticity parameter, and the COS transition parameter is given by

$$\lambda = -0.924\ln(1 - 1.02\alpha) \tag{2.40}$$

Using this model, computation time is greatly reduced while accuracy is retained. The step-by-step application process is outlined in the paper.

2.1.2 Electrical Contact

Maxwell Spreading Resistance

In the electrical domain, the current conducted through a single contact spot is important. The contact resistance governs the amount of electric current that flows through a contact area. Consider two semi-infinite bodies with electrical contact through only a single circular contact spot of radius a. This resistance of this contact spot is comprised of two components: effects due to imperfect electrical contact (such as resistive contaminant films), and effects due to the converging and diverging of current paths through the constriction, as illustrated in Figure 2.8. Assuming perfect electrical contact, the contact area can be modeled as a current constriction. If the contact radius is known and is much larger than the electron mean-free-path of the contact material, the contact resistance can be calculated by the Maxwell spreading resistance

$$R_{Maxwell} = \frac{\rho_1 + \rho_2}{4a} \tag{2.41}$$

for the constriction resistance between two identical half-spaces [30]. Where ρ_1 and ρ_2 are the electrical resistivities corresponding to the contact components and a is the circular constriction radius. This result was obtained by Maxwell from the solution of Poisson equation and ohms law.

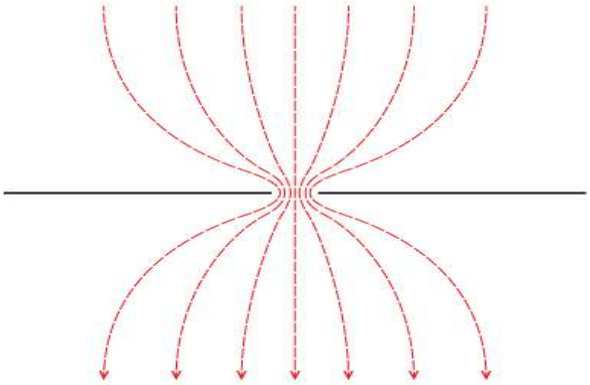

Figure 2.8 Current lines converging and diverging through a constriction.

If the contact material is the same for both components of the contact, the Maxwell spreading resistance simplifies to

$$R_{Maxwell} = \frac{\rho}{2a} \tag{2.42}$$

Constriction Resistance: Sharvin Regime

If the contact radius is small compared to the electron mean-free-path of the contact material, L, current is conducted via electrons projected ballistically through the contact without scattering [31]. The effective mean free path of the contact can be calculated as

$$\mathrm{L}_e = \frac{L_1 + L_2}{2} \tag{2.43}$$

In this case, the contact resistance is calculated using the Sharvin model.

$$R_{Sharvin} = \frac{2L_e\rho_e}{3\pi a^2} \tag{2.44}$$

Note that if the contact material is the same for both the top and bottom of the contact, the effect mean-free-path and resistivity become equal to the mean-free-path and resistivity of the material, respectively.

Constriction Resistance: Wexler Regime

If the contact radius is comparable to the electron mean-free path of the contact material, a transition equation is used to calculate the resistance. Wexler [32] developed the following equation

$$R_{Wexler} = \Gamma(K)\left(\frac{\rho}{2a}\right) + \frac{4K\rho}{3\pi a} \tag{2.45}$$

where K = l/a is known as the Knudsen ratio and is used to characterize the constriction and is plotted in Figure 2.9.

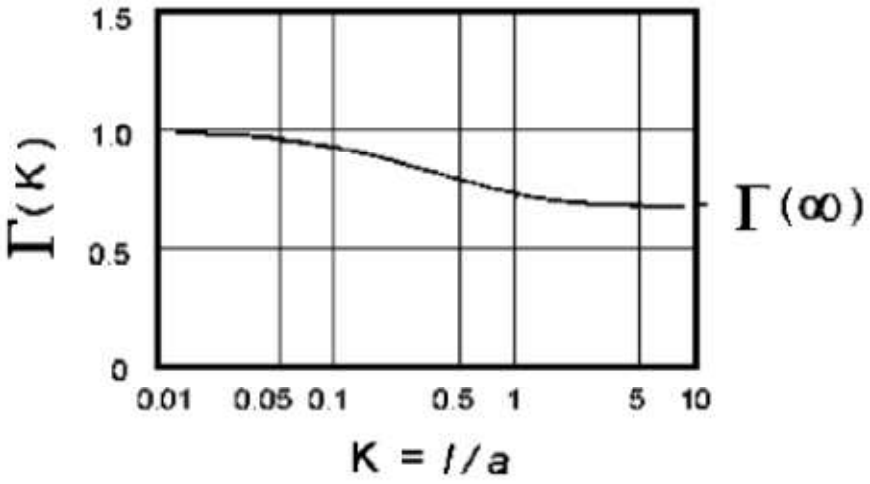

Figure 2.9 *Γ* as a function of the Knudsen ratio (taken from [32]).

2.1.3 Thermal Contact

There are three general mechanisms of heat transfer: conduction, convection, and radiation. This section will focus on heat conduction, particularly as it applies to contacting bodies. Heat conduction through a continuum is very analogous to electric current flow through a conductor. Just as electric current is driven by electric potential (voltage) gradients, heat flow is driven by temperature gradients. However, the physical mechanism of heat conduction is atomic or molecular vibration. Thermal conductivity k (W/mK) is a material property that governs how 'easily' heat flows through a given material. Just like electrical resistivity, this material property does have temperature dependence.

Thermal Constriction Resistance

Just as with electrical current lines, heat flow lines are forced to converge through contact spots (just like Figure 2.8), leading to addition resistance to heat flow through the constriction. This resistance manifests itself as a temperature drop at the interface of the two bodies. The thermal heat transfer coefficient h can be defined as

$$h = \frac{Q}{A\Delta T} \tag{2.46}$$

where (Q/A) is the heat flux into the body and ΔT is the additional temperature drop over the interface. As the equation dictates, the units of heat transfer coefficient are [W/m^{2}K]. Thermal contact resistance R can be defined as the reciprocal of the heat transfer coefficient.

Consider two semi-infinite bodies making thermal contact at one contact spot. The total thermal resistance associated with this single contact spot is defined as

$$R_{Total} = \frac{A}{4ak_1} + \frac{A}{4ak_2} = \frac{A}{2ak} \tag{2.47}$$

where

$$k = \frac{2k_1k_2}{k_1 + k_2} \tag{2.48}$$

is the effective thermal conductivity and A is the contact area. If the contact spot is assumed to be circular, the heat transfer coefficient for the contact spot can be written as

$$h = \frac{2k}{\pi a} \tag{2.49}$$

Thus, just as in the electrical domain, thermal conduction also experiences additional resistance through a constriction [44].

Electro-Thermal Interaction in a Contact Spot (The φ-ϑ Relation)

When electric current flows through a constriction, Joule heating results from the additional constriction resistance in the electrical domain. By virtue of the similarity between electric current flow and heat conduction (as described above), a simple relationship between electric potential (voltage) and the theoretical maximum local temperature near a contact spot has been developed; this is referred to as the ϕ-θ relation [30]. Under the following assumptions, it can be shown that only small deviations appear in the common (shared) paths of electric and thermal current:

1) There is almost perfect symmetry around the contact spot
2) Both members of the contact are the same material and are isotropic in conduction of both thermal and electric current
3) The electrical resistivity ρ and thermal conductivity k are dependent only on temperature
4) The contact surface is equipotential and isothermal
5) The highest local temperature is at the contact surface

6) The contact spot is the only place through which electrical and thermal current are conducted (meaning that the gaps between the members where contact is not made are assumed to be insulted in the electric and thermal domains)

Using the concept that electrical and thermal currents flow in the same paths

$$\int_0^{\Theta} \varrho k d\theta = \frac{U^2}{8} \tag{2.50}$$

where ρ is the electrical resistivity, k is the thermal conductivity of the contact material, θ is referred to at the supertemperature and is defined as ($T - T_0$) with T_0 as bulk temperature of the body (the limit in temperature far away from the contact spot). The electric potential difference between the bodies is denoted by U and Θ the maximum supertemperature or ($T_{max} - T_0$). Recall that the maximum supertemperature occurs at the isothermal contact area. Often, suitable mean values of electrical resistivity and thermal conductivity can be found and Equation (2.50) can be simplified to

$$\overline{\varrho k}\Theta = \frac{U^2}{8} \tag{2.51}$$

For metallic contact materials, the relationship between electrical resistivity and thermal conductivity can generally be expressed using the Wiedemann-Franz law

$$\varrho k = LT \tag{2.52}$$

where L is Lorenz constant. Generally, L = 2.47x10^{-8} (V/K)^2 is considered to be a good approximation for most metals [30]. However, it should be noted that this value varies slightly from metal to metal.

2.2 Experimental Literature

Two distinct contact failure modes have been identified experimentally for metal contact MEMS switches. A 'stuck-open' failure is characterized by an increase in contact resistance such that the switch no longer performs adequately. A 'stuck-closed' failure, also known as stiction, occurs when the adhesion force at the switch contact exceeds the restoration force of the actuator resulting in perpetual contact even when the switch is no longer being actuated. This section covers experimental work pertinent to micro-scale contacts with an emphasis on the mechanisms that lead to stuck-open and stuck-closed failure. Other pertinent work done in the field of MEMS contacts will be also touched on as well.

2.2.1 Switch and Contact Testing (Cold Switching)

As stated in the introduction, the contact of the microswitch is one of the most prominent limiting features of the switch. As such, a lot of research has been conducted to find the most suitable contact materials. Choosing a contact material is an optimization between the

mechanical and electrical material properties. Lee *et al* [45] explore the mechanical and electrical properties of several potential contact materials and alloys. Table 2.1 presents some potential contact materials along with their measured hardnesses and moduli. This data was taken using a nano-indenter indenting thin films of sputtered metal on a silicon substrate. It should be noted that both hardness and modulus varied with indention depth.

Table 2.1 Elastic Modulus and Hardness of Potential Contact Materials (taken from [45]).

	300 nm film thickness		1500 nm film thickness	
	Modulus (GPa)	Hardness (GPa)	Modulus (GPa)	Hardness (GPa)
Au	86.31	1.04	99.64	0.81
Pt	183.77	5.39	190.52	4.75
Rh	256.86	9.75	298.52	8.96
Ru	292.25	15.28	347.47	15.09
Au-30%Rh	153.30	4.87	155.86	3.58
Au-70%Rh	217.57	9.57	234.95	7.99
Au-30%Ru	154.83	6.18	168.92	6.69
Au-70%Ru	231.93	11.46	263.86	12.29
Au-10%Pt	124.87	2.79	119.97	1.47
Au-50%Pt	155.11	5.1	161.58	4.58

Note: The values were measured at 24 nm for 300 nm thickness and 120 nm for 1500 nm thickness films, respectively.

Another very nice result presented in this paper is a measured resistivity versus measured hardness plot of these contact materials - Figure 2.10.

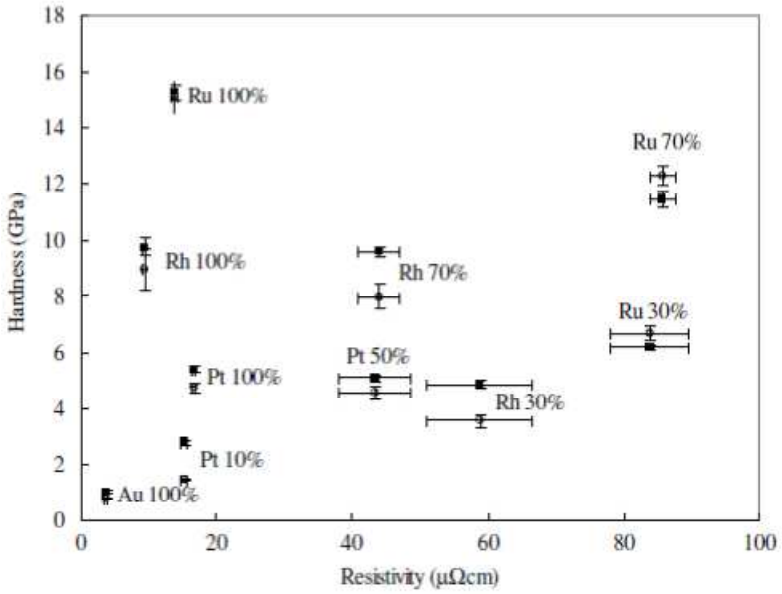

Figure 2.10 Electrical resistivity versus hardness where solid squares indicate 300 nm thickness and hallow circles indicate 1500 nm thickness films (taken from [45]).

From the Maxwell spreading resistance (presented above), the contact resistance depends largely on the contact area and the resistivity of the contact material. From Figure 2.10, of the material presented, gold has the lowest resistivity and hardness. Furthermore, gold

has a naturally high resistance to corrosion and oxidation and is easy to work with in the micro-machining processes. For these reasons, gold is a very attractive contact material selection. However, softer materials can be more susceptible to wear and plastic deformation, leading to shorter contact lifetimes.

In [46], an AFM based micro-contact tester is used to explore the cold-switching lifetime of gold and gold-nickel alloy contacts. From the lifetime cycling tests, it is determined that the primary failure mechanism for gold-gold contacts is wear as shown in Figure 2.11, which results in a stuck-open (high resistance) failure.

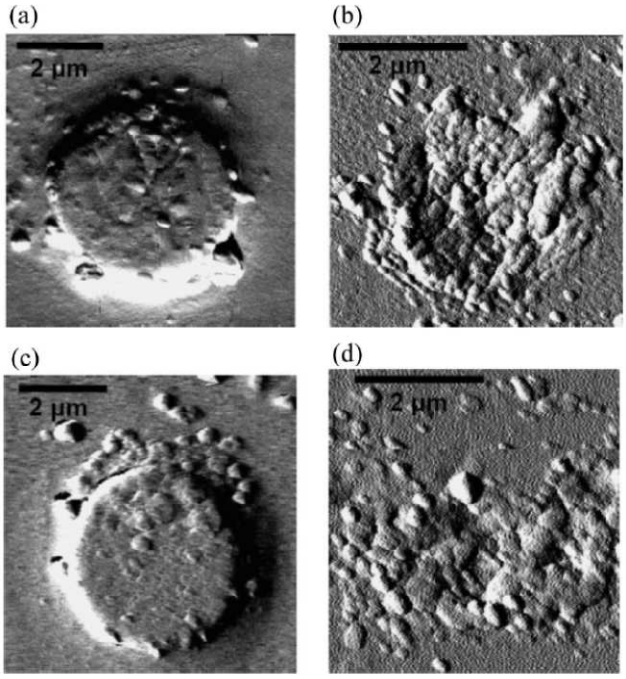

Figure 2.11 Wear failure in gold-gold contacts (taken from [46]).

To improve contact lifetimes, this group experimented with alloying the gold with nickel. It was found that a two-phase AuNi alloy (20 at % Ni) significantly increased lifetime while keeping the contact resistance low (for the same contact force). In the interest of reducing wear and extending contact lifetime, many harder contact materials, as well as their alloys with gold have been tested. Harder materials generally tend to have different failure mechanisms when cold switched.

Contamination failure, another type of 'stuck-open' contact failure, was studied by Chen et al [47]. In this experimental work, thin films of platinum, rhodium, and ruthenium and their alloys with gold were explored as electrical contact materials for MEMS switches using an AFM-based micro-contact tester. It was found that because of the formation of friction polymers (a type of contaminant film) during cycling, the contact resistance increases rapidly after a characteristic number of cycles have occurred with stable resistance. This characteristic number of cycles depends on the contact material. Of the materials tested, gold-on-gold contacts held a stable resistance for the most number of cycles (10^8 cycles) and ruthenium-on-ruthenium held a stable resistance for the least number of cycles (10^4 cycles), as shown in Figure 2.12.

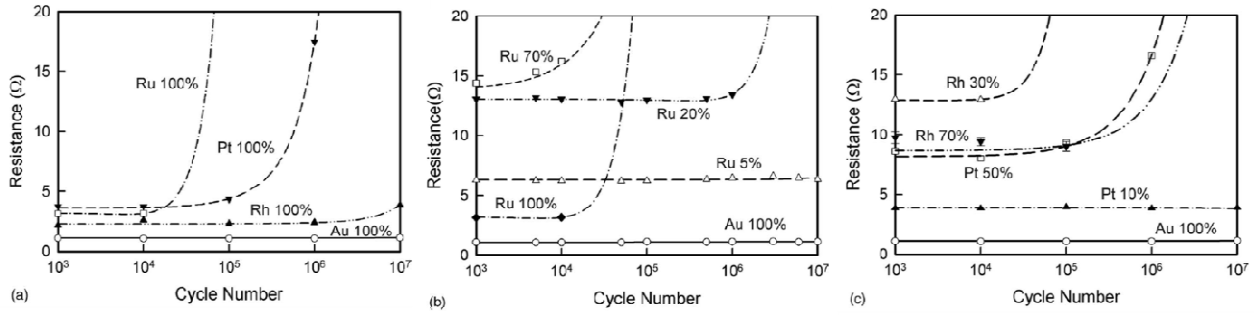

Figure 2.12 Resistance versus cycle for different contact materials (taken from [47]).

It was found that the noble metals ruthenium, rhodium, and platinum were more susceptible to the growth of a contamination film as compared to pure gold. Furthermore, when alloyed with gold, the contaminant film growth rate for these metals decreased with increasing composition of gold.

For unpackaged contact testing, the ambient and surface preparation plays a significant role in the lifetime of the contact. In [53], Chen *et al* studied the effects of different surface treatments on ruthenium-ruthenium contacts by taking resistance measurement before and after cleaning the contact surface, as presented in Figure 2.13.

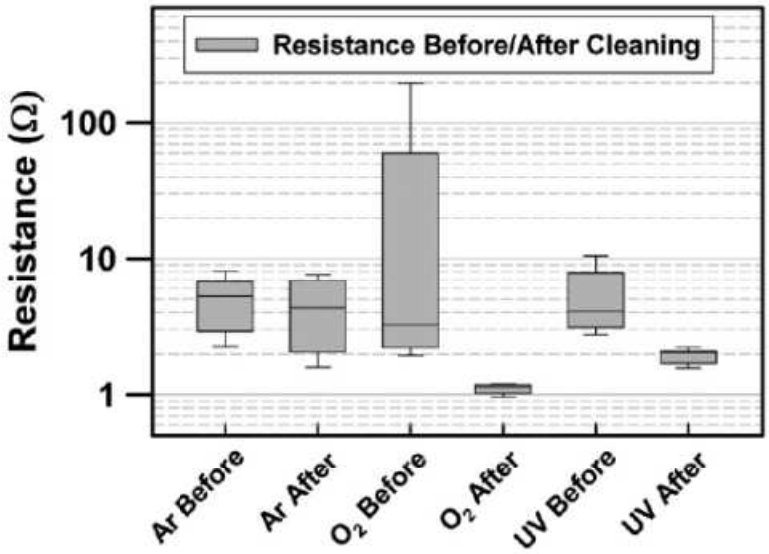

Figure 2.13 Contact resistance before and after cleaning for three different surface cleaning techniques for ruthenium-ruthenium contacts at 100 uN force (taken from [53]).

As indicated in the figure, both 0_2 plasma and UV-ozone resulted in lower contact resistance, while argon plasma did not. It is deduced from these results that the oxygen radicals are effective at cleaning ruthenium surfaces, while argon is ineffective at cleaning ruthenium surfaces. Next, the result of in-situ oxygen plasma cleaning was conducted. To do this, a gold-gold contact was cycled in the chamber of a plasma system. The result of the test is shown in Figure 2.14.

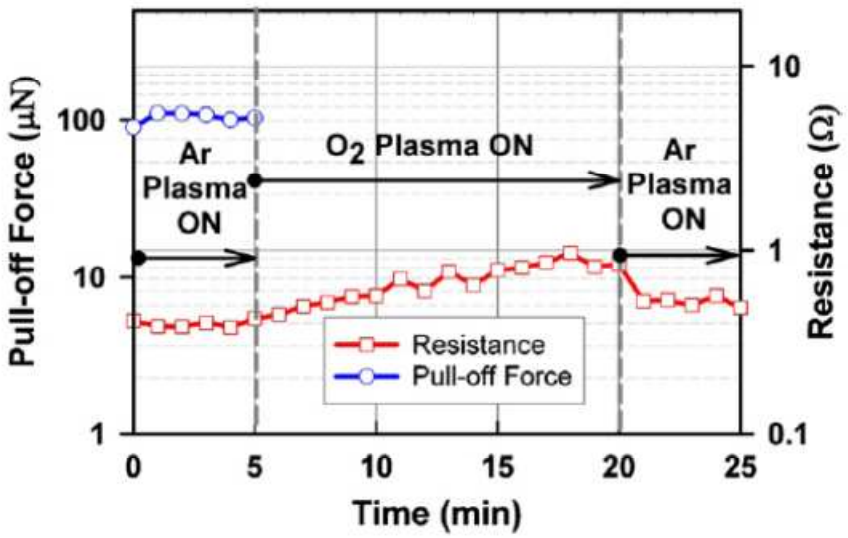

Figure 2.14 Contact resistance and pull-off force of a Au-Au contact during in-situ plasma treatment cycling at 1 Hz whith 100 uN of force (taken from [53]).

The oxygen plasma results in an increased contact resistance while almost eliminating adhesion in the contact. These results suggest that the oxygen oxidized the contact surface resulting in AuO_3. Thus oxygen has a much different effect on gold contact as compared to ruthenium contacts.

Using packaged (hermetically sealed) RF MEMS switches, Czaplewski *et al* [49] explored the failure modes of gold-gold, gold-iridium, and gold-platinum contact pairs. The lifetime testing of these switches was done with 1 mW of cold switching RF power at 200 Hz with 100 μN of contact force. Under these conditions, stuck-open was the main failure type for the dissimilar contact type (gold-platinum and gold-iridium). These failures were attributed to the accumulation of a carbon-based frictional polymer as shown in Figure 2.15. Auger electron spectroscopy was used to identify the carbon based accumulation.

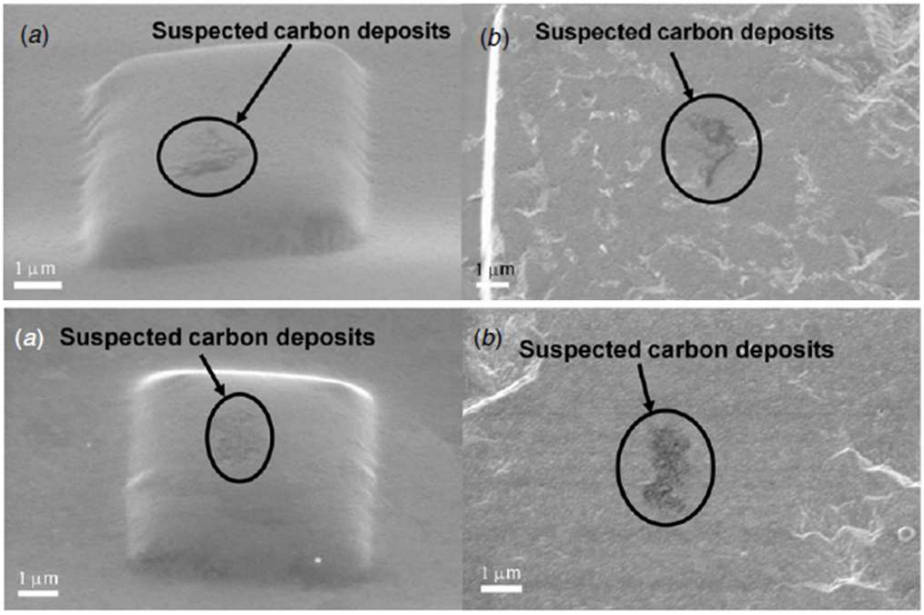

Figure 2.15 SEM micrographs of gold-iridium (top) and gold-platinum (bottom) contact pairs showing carbon based firctional polymers leading to a stuck-open failure (taken from [49]).

For the gold-gold contacts studied in this paper, both stuck-open and stuck-closed failures were reported. The stuck-open failures for gold-gold contacts were attributed to a combination of wear and carbon contamination, as shown in Figure 2.16.

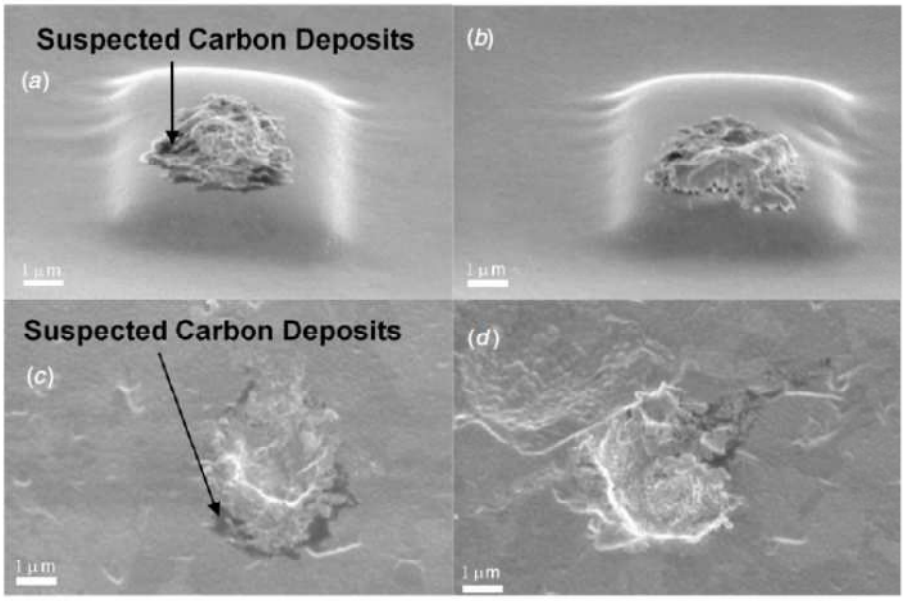

Figure 2.16 Two gold-gold contact pairs illustrating both wear and carbon deposits, both were stuck-open failures (taken from [49]).

The stuck-closed failures reported in the paper were attributed to contact welding. The authors support this theory by pointing to the material transfer illustrated in the gold-gold contacts (see above), which they took to be a symptom of 'ripping and tearing' of the soft contact material.

Using a nano-indenter-based contact tester, Broue *et al* [48] explored different MEMS contact materials in five combinations including gold-on-gold, ruthenium-on-ruthenium, rhodium-on-rhodium, gold-on-ruthenium, and gold-on-nickel. The focus of these contact tests was on low to moderate power and contact force under 'quasi-cold' switching conditions. The observed contact resistances and pull-off forces for gold-on-gold and ruthenium-on-ruthenium contacts were comparable to those results reported by Chen *et al* [47]. Using AFM imaging, this group also presents an adhesion based stuck-closed failure mechanism.

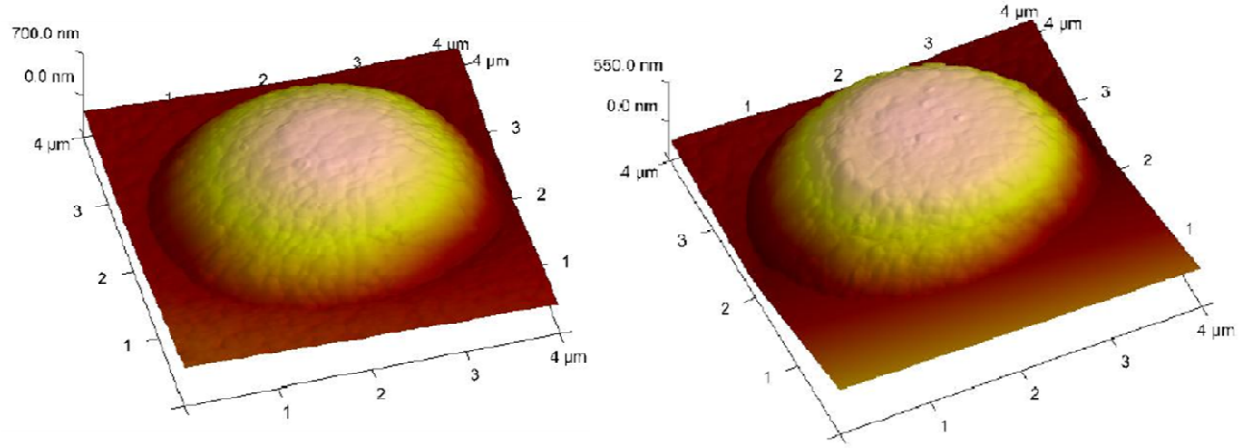

Figure 2.17 AFM images of (Left) An untested gold contact bump and (Right) Plastic deformation of a tested gold contact bump (taken from [48]).

For gold contacts, this group observed that there was a large amount of plastic deformation. The authors suggest that the increased 'flatted' area of the contact was the reason for high adhesion observed in gold-gold contacts in their testing.

Along the same lines, Majumder *et al* [50] developed a simplified analytical model for contact resistance and adhesion in a gold contact switch cycled more than once. This paper modeled a switch contact using a single asperity elastic-plastic adhesion model in a multi-asperity model via a Gaussian distribution of asperity heights. Model results predicted an increased pull-off force due to plastic deformation of individual asperities. These results matched reasonably well with measured experimental results from a cold switched RF MEMS switch.

Du *et al* [51] explored the effect of adhesion on deformation and stresses during loading and unloading in an elastic-plastic finite element model of a single hemispherical asperity pressed against a rigid flat. This model predicted two types of separation modes – ductile and brittle separation. That work predicted low adhesion and brittle separation for ruthenium-ruthenium contacts, and high adhesion and ductile separation for gold-gold contacts. Experimentally, Chen *et al* [52] explored adhesion effects by varying the rate of separation of a micro-scale contact to identify the difference between ductile and brittle separation.

It is important to note that there is a multitude of additional papers published addressing cold switching damage mechanisms and exploration of these mechanisms via testing, both in- and ex-situ. This literature review is not intended to be exhaustive.

2.2.2 Hot Switching Material Transfer and Damage Mechanisms

Bridge Transfer

Bridge, or fine, transfer as described by Holm in [30] is the formation of molten metal bridges between the electrodes of the contact due to high current during the last phase of physical contact upon opening. Material transfer is a result of asymmetrical dividing of the molten bridge; the hottest section of the bridge is where it will rupture, and this location can be offset from the center of the bridge. The Thompson effect and the Kohler effect were both used to predict the amount of material transferred from the anode to the cathode due to bridge transfer[30][42]. These models predict different amounts of resulting material transfer, but it is generally agreed upon that bridge transfer is overwhelmed by the effects of arc transfer (discussed below) [38].

In [43], Patton and Zabinski performed several hot switching tests on gold contacts. The test setup consisted of a micro/nano adhesion apparatus. This instrument uses a ball-on-flat configuration with both electrodes of the contact coated with approximately 4µm of gold. So-called 'rapid' hot switching was performed (5 Hz) at varying currents. At low currents (1-10 µA), the group observed slightly higher resistances, higher adhesion, and longer lifetime. At higher currents (1-10 mA), the group observed lower resistances, low adhesion, less contact bounce, and poor reliability / durability. High current tests often resulted in stuck-shut failure as illustrated in Figure 2.18(a) for a 1 mA hot switching test. The authors claim that the damage structures presented in (b) are the flattened remnants of bridges formed between the electrodes causing the stuck-shut failure.

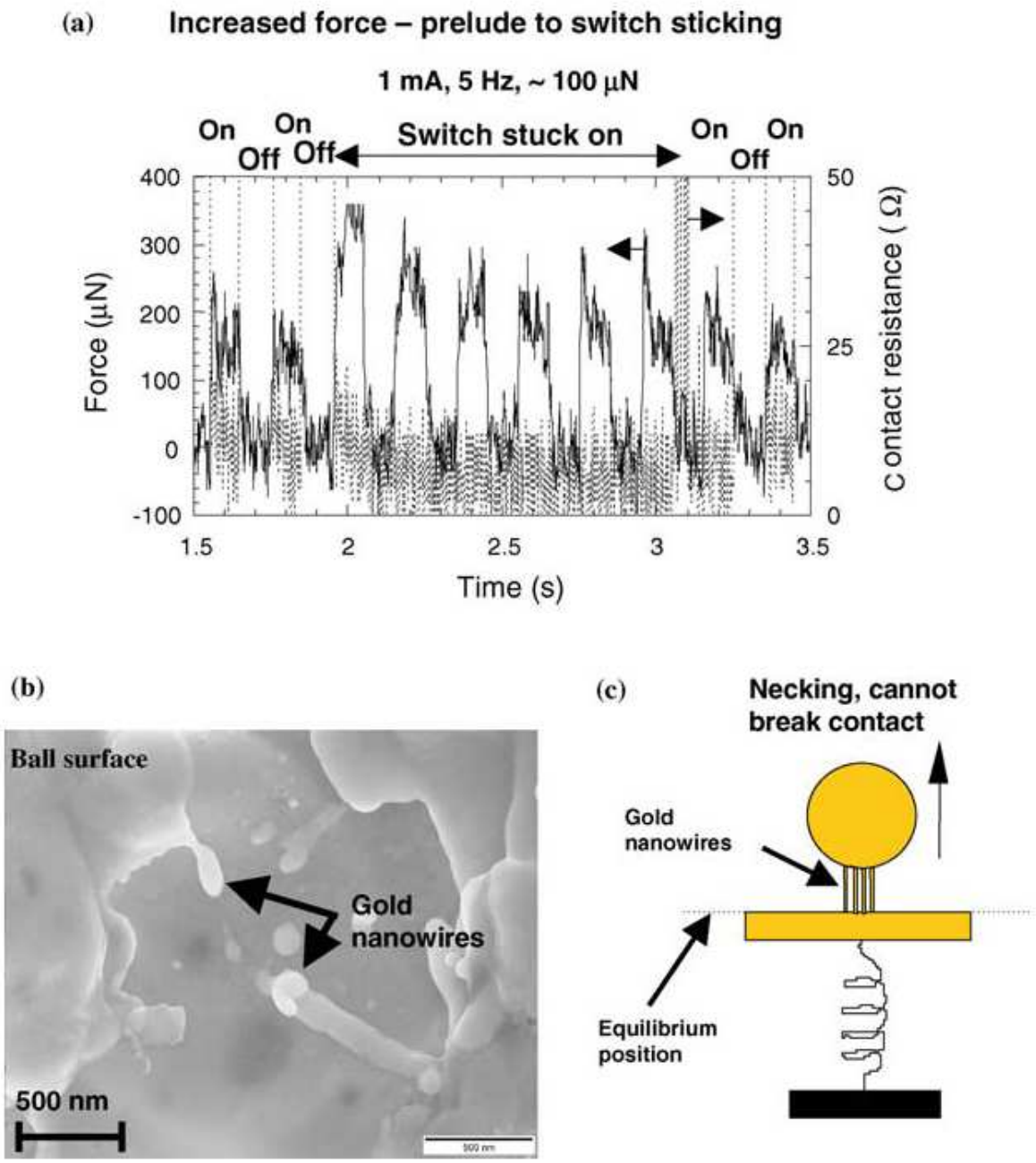

Figure 2.18 Stuck shut failure of gold contacts under 1 mA of hot switching current resulting in what the authors interpret as bridges (taken from [43]).

Field Evaporation

Field evaporation is the removal of a surface molecule, as an ion, by a very strong local electric field [33]. Though this phenomenon is generally understood in principle, the details are less agreed upon. The theoretical local electric field necessary to induce field evaporation is estimated in [34] for various metals, such as gold (52.5 V/nm for n = +2) and ruthenium (42 V/nm for n = +2), among many others. The direction of material transfer in field evaporation is

dependent on the electric field orientation as well as the material itself. Both positive and negative field evaporation have been demonstrated experimentally [35]. In positive field evaporation, electrons from the surface of the anode are drawn into the bulk while positive material ions travel from the anode to the cathode via the electric field resulting in a very small electric current. In negative field evaporation, negative material ions travel from the cathode (where there is an excess of electrons and negative ions) to the anode.

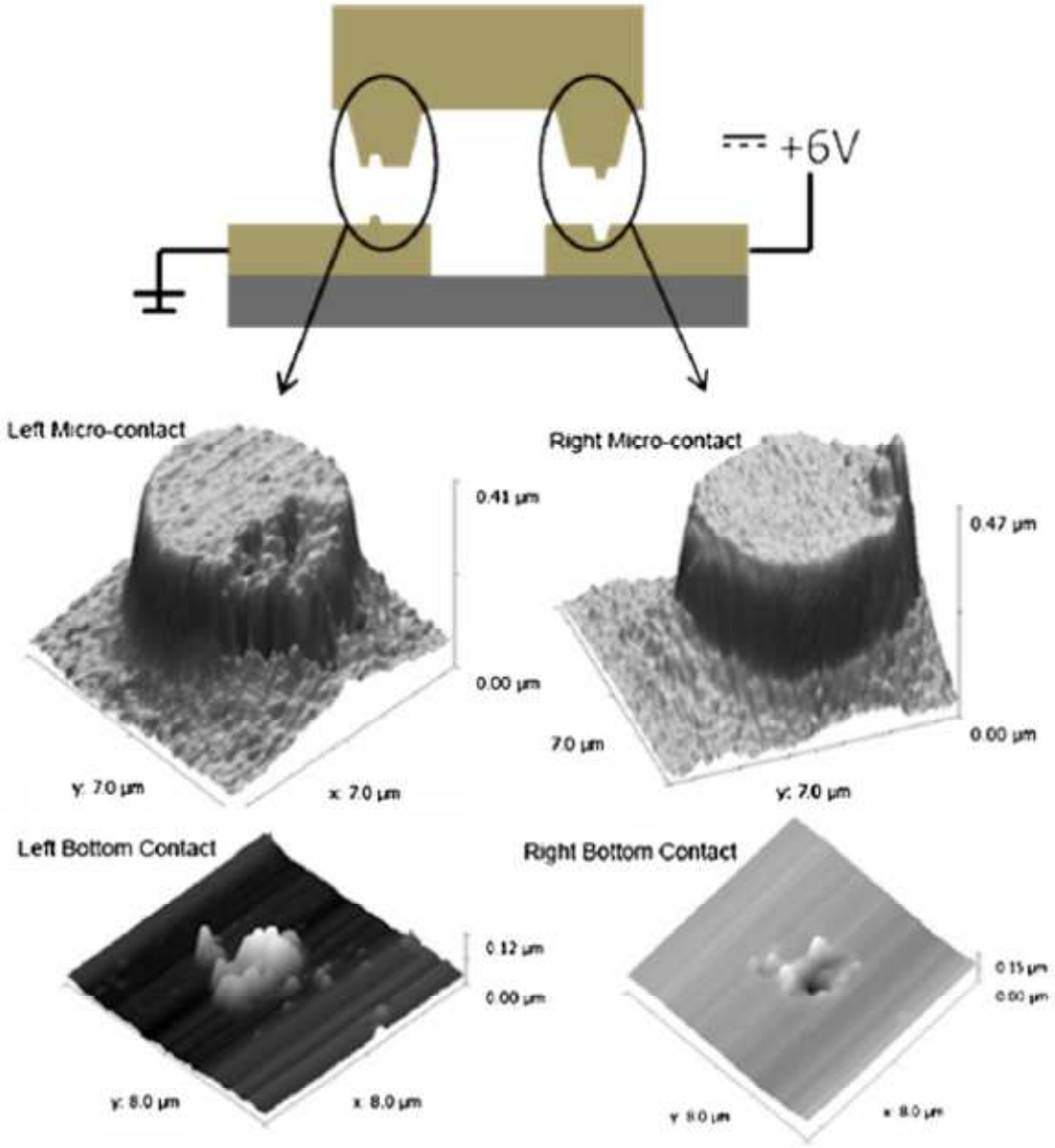

Figure 2.19 AFM images of Yang *et al* contact pads after 2000 cycles with $V_{Hot} = V_{Cold} = 6V$, I = 1mA (taken from [20]).

Yang *et al* [20] present evidence of field evaporation material transfer in switch contacts. Gold contacts were hot switched at voltages higher than the field evaporation threshold for gold (~4V), but lower than the gold ionization threshold (9.42V) so as to avoid electric arc failure. Material transfer was observed from anode to cathode as illustrated in

Figure 2.19. The authors observed no electric arcs (in the form of voltage spikes in the testing circuit) over the contact during making or breaking of contact as illustrated in Figure 2.20.

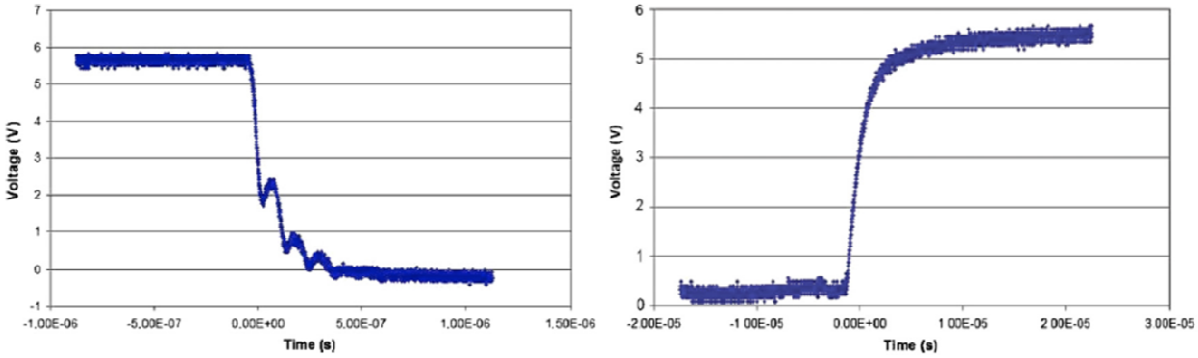

Figure 2.20 Voltage across the contact during closing (left) and opening (right) (taken from [20]).

Further testing conducted at the low potential of 1V (below the reported minimum gold field evaporation voltage) revealed behavior more closely resembling thermal wear (similar to bridge transfer). Thus, material transfer under hot switched testing was assumed to be the result of field evaporation.

Electric Arcing

Electric arc material transfer may also occur between the electrodes of a microswitch contact during hot switching. An electric arc occurs when electrical current flows through the medium that separates the electrodes of an electrical contact; this can only happen when the medium becomes locally conductive. If the medium between the electrodes is a gas, the gas must be ionized in order to conduct current and to allow arcing to occur; the breakdown voltage (at which ionization occurs) is a characteristic of the gas medium. This breakdown process, knows as Townsend discharge, is generally started by thermal emission or cold tunneling of a small number of electrons from the cathode due to a very strong local electric field. These released electrons cause an avalanche-type of ionization of the medium separating the electrodes. Strong *et al* [36] studied this type of discharge on the micro scale on stationary electrodes separated by air gaps of 2-20 µm. It was found that initial Townsend discharges between 50-400pA transitioned into a second stage of discharge between 2-20nA.

Alternatively, vapor arc breakdown occurs when a metallic vapor between the electrodes is ionized by the combination of the strong local electric field and thermal emission of electrons from the cathode. It has been shown that softened or molten bridges may form (as discussed above); heating effects from current running through a relatively small structure could result in an explosive vaporization of all or parts of the metallic bridge causing the expulsion of metal vapor into the gap between the electrodes. Once the vapor is ionized and becomes conductive, the free electrons flow toward the anode and the metallic ions flow toward the cathode. For the arc to be sustained, a characteristic potential and current must be sustained [38]. However, it has been shown that short duration micro-arcs can occur under lower voltage conditions.

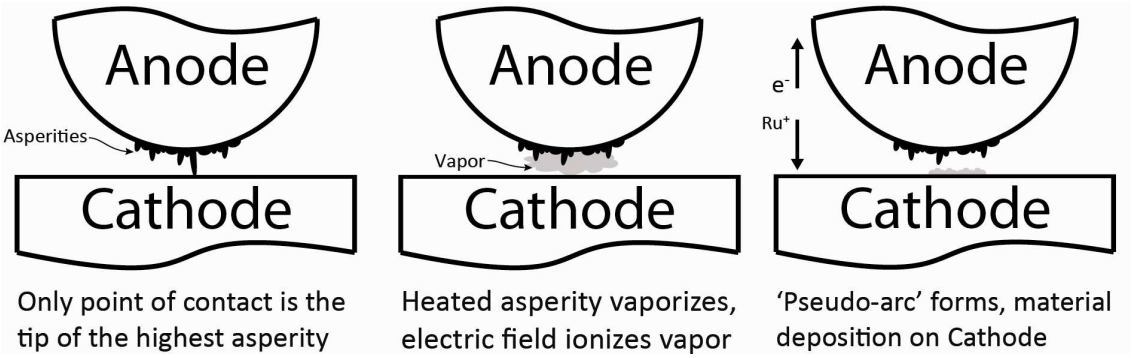

Figure 2.21 Schematic of micro-arc material transfer mechanism.

In [39], Dickrell *et al* performed several 3.3 V hot switching tests on gold-on-platinum metal MEMS switch contacts and found that these contacts failed via high resistance. The authors reported voltage transients during the making and breaking of contact while cycling without a 'capacitive-quench' circuit as illustrated in Figure 2.22; they interpreted these voltage transients as micro-arcs. It was concluded that the primary damage mechanism to their contact was micro-arc induced contamination growth (in the form of carbon) which lead to high resistance failure. The idea was that the ionization from arcing resulted in the carbonaceous ions to be deposited on the electrodes.

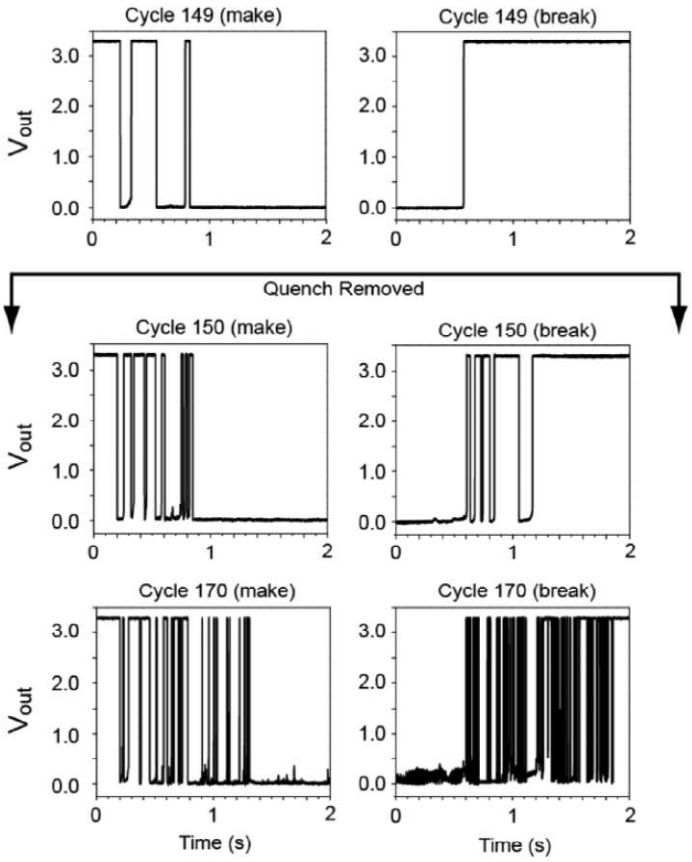

Figure 2.22 Voltage over the contact during closing (left column) and opening (right column) both with a capacitive quench circuit (top two figures) and without a capacitive quench circuit (bottom four figures) (taken from [39]).

Field Emission

In 2011, Poulain *et al* introduced a field emission theory for material transfer that they observed in relatively low voltage (10 V) DC micro-contacts [40]. According to this theory, field emission material transfer occurs when a surface asperity on the cathode side of a local electric field emits electrons via tunneling as governed by the Fowler-Norheim theory. These released electrons follow the electric field and bombard the anode causing local heating which results in material evaporation. The evaporated material is then deposited on the cathode resulting in a net material transfer from the anode to the cathode as illustrated in Figure 2.23.

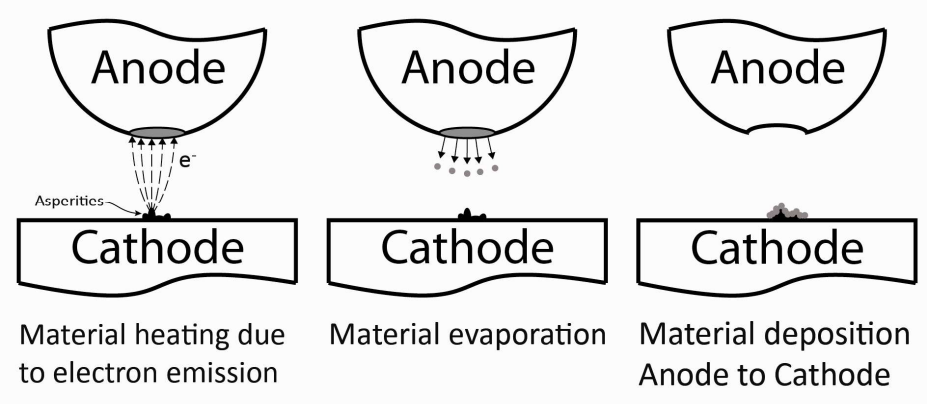

Figure 2.23 Schematic of the field emission material transfer mechanism.

Experimental work substantiated the field emission theory they developed by demonstrating an unstable current before contact during testing. This behavior presented several current 'spikes' of magnitude ~0.5µA while the electrodes were on the order of 5-10 nm apart as shown in Figure 2.24. Figure 2.25 illustrates these current spike events for different contact materials.

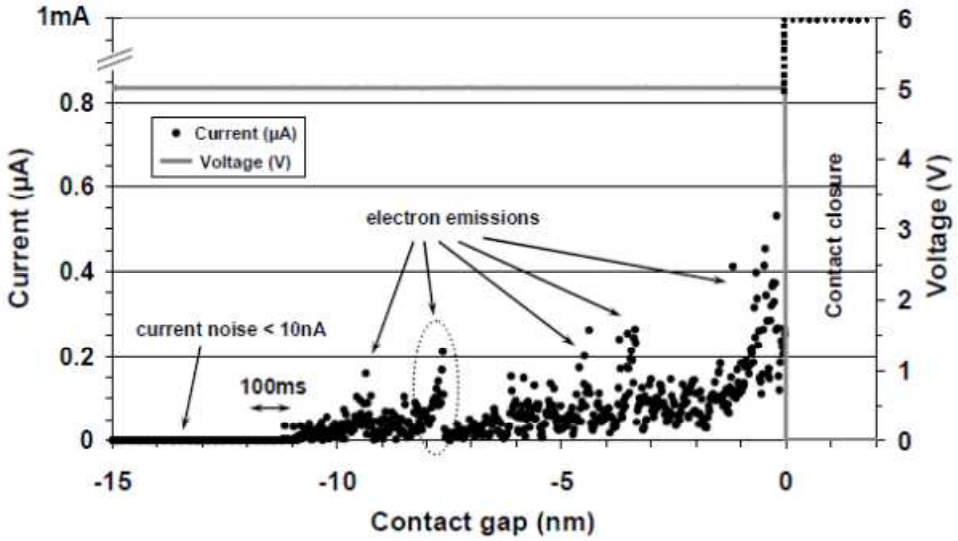

Figure 2.24 Typical evolution of the current and voltage as a function of the contact gap upon closing (taken from [40]).

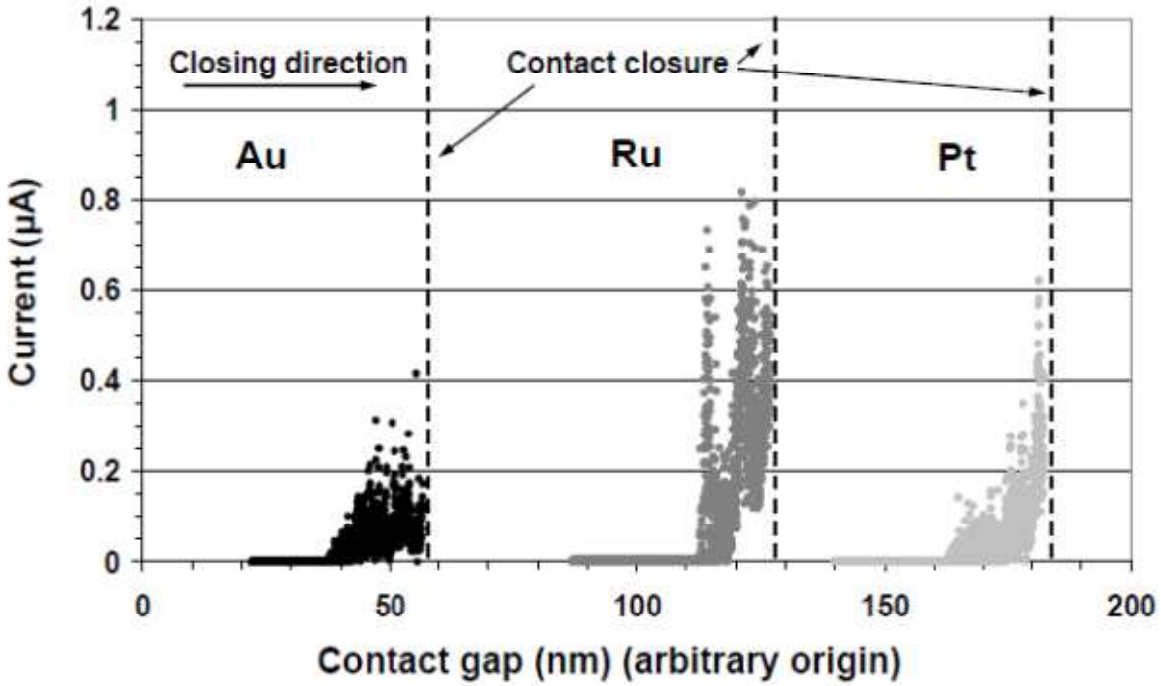

Figure 2.25 Current spike events upon closing for different contact materials (taken from [40]).

Upon inspection of the test data, the measured currents matched fairly well in magnitude and behavior with the Fowler-Nordheim theory of electron emission. Furthermore, material transfer from anode to cathode was illustrated in detail.

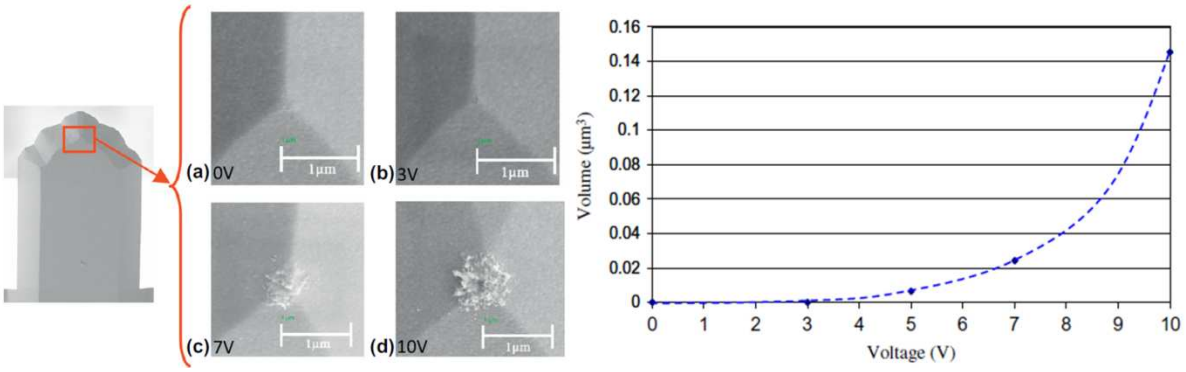

Figure 2.26 Material transfer observed from anode to cathode as a function of applied potential (taken from [41]).

In [41], this group characterized the amount of volume transferred from the anode to the cathode after 50 cycles as a function of applied voltage for their gold contacts as shown in Figure 2.26. They found that for their contacts, 5V is the threshold at which 'acceleration of the transfer rate' occurs.

2.3 Chapter 2 References

[1] Rebeiz G M 2003 *RF MEMS: Theory, design, and technology* (Hoboken, New Jersey: J. Wiley & Sons)

[2] Rebeiz G M and Muldavin J B 2001 RF MEMS switches and switch circuits *microwave magazine, IEEE* **2** 59-71

[3] Ehwald K, Drews J, Scholz R, Korndorfer F, Knoll D, Tillack B, Barth R, Birkholz M, Schulz K and Sun Y 2009 BEOL embedded RF-MEMS switch for mm-wave applications. In: *Electron Devices Meeting (IEDM), 2009 IEEE International*: IEEE) pp 797-800

[4] Brown E R 1998 RF-MEMS switches for reconfigurable integrated circuits *Microwave Theory and Techniques, IEEE Transactions on* **46** 1868-80

[5] Park S J, Reines I and Rebeiz G 2009 High-Q RF-MEMS tunable evanescent-mode cavity filter. In: *Microwave Symposium Digest, 2009. MTT'09. IEEE MTT-S International*: IEEE) pp 1145-8

[6] Ho K M J and Rebeiz G M 2012 Microstrip antennas with full polarization diversity using packaged RF MEMS switches. In: *Antennas and Propagation Society International Symposium (APSURSI), 2012 IEEE*: IEEE) pp 1-2

[7] Lee K Y and Rebeiz G M 2009 A miniature 8–16 GHz packaged tunable frequency and bandwidth RF MEMS filter. In: *Radio-Frequency Integration Technology, 2009. RFIT 2009. IEEE International Symposium on*: IEEE) pp 249-52

[8] Chan K Y, Daneshmand M, Mansour R R and Ramer R 2009 Scalable RF MEMS switch matrices: Methodology and design *Microwave Theory and Techniques, IEEE Transactions on* **57** 1612-21

[9] Newman H S, Ebel J L, Judy D and Maciel J 2008 Lifetime measurements on a high-reliability RF-MEMS contact switch *Microwave and Wireless Components Letters, IEEE* **18** 100-2

[10] Patel C D and Rebeiz G M 2011 RF MEMS Metal-Contact Switches With mN-Contact and Restoring Forces and Low Process Sensitivity *Microwave Theory and Techniques, IEEE Transactions on* **59** 1230-7

[11] Uno Y, Narise K, Masuda T, Inoue K, Adachi Y, Hosoya K, Seki T and Sato F 2009 Development of SPDT-structured RF MEMS switch. IEEE) pp 541-4

[12] Mercier D, Charvet P L, Berruyer P, Zanchi C, Lapierre L, Vendier O, Cazaux J L and Blondy P 2004 A DC to 100 GHz high performance ohmic shunt switch. IEEE) pp 1931-4

[13] Chen L, Lee H, Guo Z, McGruer N E, Gilbert K, Mall S, Leedy K and Adams G 2007 Contact resistance study of noble metals and alloy films using a scanning probe microscope test station *Journal of Applied Physics* **102** 074910--7

[14] Broue A, Dhennin J, Charvet P, Pons P, Jemaa N B, Heeb P, Coccetti F and Plana R 2010 Multi-Physical Characterization of Micro-Contact Materials for MEMS Switches. In: *IEEE Holm Conference on Electrical Contacts (HOLM),* (Charleston, South Carolina, USA: IEEE) pp 1-10

[15] Majumder S, Lampen J, Morrison R and Maciel J 2003 A packaged, high-lifetime ohmic MEMS RF switch. In: *MTT-S International Microwave Symposium Digest,* (Philadelphia, Pennsylvania, USA: IEEE) pp 1935-8

[16] Yang Z, Lichtenwalner D J, Morris A S, Krim J and Kingon A I 2009 Comparison of Au and Au–Ni Alloys as Contact Materials for MEMS Switches *Microelectromechanical Systems, Journal of* **18** 287-95
[17] Kwon H, Choi D J, Park J H, Lee H C, Park Y H, Kim Y D, Nam H J, Joo Y C and Bu J U 2007 Contact materials and reliability for high power RF-MEMS switches. IEEE) pp 231-4
[18] Patton S and Zabinski J 2005 Fundamental studies of Au contacts in MEMS RF switches *Tribology Letters* **18** 215-30
[19] Becher D, Chan R, Hattendorf M and Feng M 2002 Reliability study of low-voltage RF MEMS switches. pp 54-7
[20] Yang Z, Lichtenwalner D, Morris A, Krim J and Kingon A 2010 Contact degradation in hot/cold operation of direct contact micro-switches *Journal of Micromechanics and Microengineering* **20** 105028
[21] Hertz H 1882 {Über} die {B} erührung fester elastischer {K} örper *J. für die reine u. angew. Math.* **92**
[22] Greenwood J and Williamson J 1966 Contact of nominally flat surfaces *Proceedings of the Royal Society of London. Series A. Mathematical and Physical Sciences* **295** 300
[23] Johnson K, Kendall K and Roberts A 1971 Surface energy and the contact of elastic solids *Proceedings of the Royal Society of London. A. Mathematical and Physical Sciences* **324** 301-13
[24] Derjaguin B, Muller V and Toporov Y P 1975 Effect of contact deformations on the adhesion of particles *Journal of colloid and interface science* **53** 314-26
[25] Tabor D 1977 Surface forces and surface interactions *Journal of colloid and interface science* **58** 2-13
[26] Grierson D, Flater E and Carpick R 2005 Accounting for the JKR–DMT transition in adhesion and friction measurements with atomic force microscopy *Journal of adhesion science and technology* **19** 291-311
[27] Maugis D 1992 Adhesion of spheres: the JKR-DMT transition using a Dugdale model *Journal of colloid and interface science* **150** 243-69
[28] Johnson K and Greenwood J 1997 An adhesion map for the contact of elastic spheres *Journal of colloid and interface science* **192** 326-33
[29] Carpick R W, Ogletree D F and Salmeron M 1999 A general equation for fitting contact area and friction vs load measurements *Journal of colloid and interface science* **211** 395-400
[30] Holm R and Holm E 1967 *Electric contacts: theory and application* vol 9: Springer-Verlag New York)
[31] Jansen A G M, Gelder A P and Wyder P 1980 Point-contact spectroscopy in metals *Journal of Physics C: Solid State Physics* **13** 6073
[32] Wexler G 1966 The size effect and the non-local Boltzmann transport equation in orifice and disk geometry *Proceedings of the Physical Society* **89** 927
[33] Müller E W 1941 Abreißen adsorbierter Ionen durch hohe elektrische Feldstärken *Naturwissenschaften* **29** 533-4
[34] Zurlev D N and Forbes R G 2003 Field ion emission: the effect of electrostatic field energy on the prediction of evaporation field and charge state *Journal of Physics D: Applied Physics* **36** L74

[35] Miskovsky N, Wei C M and Tsong T T 1992 Field evaporation of silicon in the field ion microscope and scanning tunneling microscope configurations *Physical review letters* **69** 2427-30

[36] Strong F W, Skinner J L and Tien N C 2008 Electrical discharge across micrometer-scale gaps for planar MEMS structures in air at atmospheric pressure *Journal of Micromechanics and Microengineering* **18** 075025

[37] Kruglick E J J and Pister K S J 1999 Lateral MEMS microcontact considerations *Microelectromechanical Systems, Journal of* **8** 264-71

[38] Slade P G 1999 *Electrical contacts: principles and applications* vol 105: CRC)

[39] Dickrell D and Dugger M T 2007 Electrical contact resistance degradation of a hot-switched simulated metal MEMS contact *Components and Packaging Technologies, IEEE Transactions on* **30** 75-80

[40] Poulain C, Peschot A, Vincent M and Bonifaci N 2011 A Nano-Scale Investigation of Material Transfer Phenomena at Make in a MEMS Switch. IEEE) pp 1-7

[41] Peschot A, Poulain C, Souchon F, Charvet P L, Bonifaci N and Lesaint O 2012 Contact degradation due to material transfer in MEM switches *Microelectronics Reliability*

[42] Llewellyn-Jones F 1957 *The physics of electrical contacts*: Clarendon Press Oxford)

[43] Patton S and Zabinski J 2005 Fundamental studies of Au contacts in MEMS RF switches *Tribology Letters* **18** 215-30

[44] Madhusudana , C. V., 1995, Thermal contact conductance, Springer.

[45] Lee H, Coutu R A, Mall S and Leedy K D 2006 Characterization of metal and metal alloy films as contact materials in MEMS switches *Journal of Micromechanics and Microengineering* **16** 557

[46] Yang Z, Lichtenwalner D, Morris A, Krim J and Kingon A 2010 Contact degradation in hot/cold operation of direct contact micro-switches *Journal of Micromechanics and Microengineering* **20** 105028

[47] Chen L, Guo Z, Joshi N, Eid H, Adams G and McGruer N 2012 An improved SPM-based contact tester for the study of microcontacts *Journal of Micromechanics and Microengineering* **22** 045017

[48] Broue A, Dhennin J, Charvet P, Pons P, Jemaa N B, Heeb P, Coccetti F and Plana R 2010 Multi-Physical Characterization of Micro-Contact Materials for MEMS Switches. In: *IEEE Holm Conference on Electrical Contacts (HOLM),* (Charleston, South Carolina, USA: IEEE) pp 1-10

[49] Czaplewski D A, Nordquist C D, Dyck C W, Patrizi G A, Kraus G M and Cowan W D 2012 Lifetime limitations of ohmic, contacting RF MEMS switches with Au, Pt and Ir contact materials due to accumulation of 'friction polymer'on the contacts *Journal of Micromechanics and Microengineering* **22** 105005

[50] Majumder S, McGruer N and Adams G G 2005 Adhesion and contact resistance in an electrostatic MEMS microswitch. In: *STLE/ASME International Joint Tribology Conference,* (Ponte Vedra Beach, Florida, USA: IEEE) pp 215-8

[51] Du Y, Chen L, McGruer N E, Adams G G and Etsion I 2007 A finite element model of loading and unloading of an asperity contact with adhesion and plasticity *Journal of colloid and interface science* **312** 522-8

[52] Chen L, McGruer N E, Adams G G and Du Y 2008 Separation modes in microcontacts identified by the rate dependence of the pull-off force *Applied Physics Letters* **93** 053503

[53] Chen L, Guo Z, Joshi N, Eid H, Adams G and McGruer N 2012 An improved SPM-based contact tester for the study of microcontacts *Journal of Micromechanics and Microengineering* **22** 045017

Chapter 3

Modeling of a Thermal-Electrical-Mechanical Coupled Field Contact

This chapter is the final manuscript of a paper that was accepted to the Journal of Tribology in July 2012

3.1 Abstract

This paper presents a finite element approach for modeling a thermal-electrical-mechanical coupled-field contact comprised of an elastic hemisphere pressed against an elastic half-space. The goal of this investigation is to develop a fundamental understanding of the behavior of this multi-physics contact with a particular interest on the contact area through which current flows. The results from the model illustrate a distinct difference in contact behavior between force control and displacement control in the presence of an applied electrical potential / current. It is shown that, while Hertz contact theory can be used to accurately predict the behavior of the contact under force control, a new relationship is established to accurately predict the behavior of the contact under displacement control.

3.2 Introduction

In the field of Microelectromechanical Systems (MEMS), metallic contact microswitches have shown great potential in a variety of low power applications. Such applications include relay replacement in Automatic Test Equipment (ATE) for industrial and medical instrumentation, as well as in radio frequency (RF) communications such as cell phones, phased array RADAR, base-station and defense applications, and satellite applications [1]. An electrostatically actuated metal contact RF MEMS switch has a low insertion loss (0.1 dB up to 100 GHz), a high isolation (because of low off-state capacitances of 2-4 fF at 0.1-60 GHz), low power consumption (10-100 nJ per switching cycle), and high linearity as compared to solid state switches such as Field Effect Transistor (FET) switches and PIN diodes [2]. For applications such as these, a switch life time in excess of 10 billion cycles is necessary. However, the low reliability of the metal contacts has greatly limited the average life-time of these types of switches.

Two distinct contact failure modes have been identified experimentally for metal contact MEMS switches. A ‘stuck-open’ failure is characterized by an increase in contact resistance such that the switch no longer performs adequately [3]. A ‘stuck-closed’ failure, also known as stiction, occurs when the adhesion force at the switch contact exceeds the restoration force of the actuator resulting in perpetual contact even when the switch is no longer being actuated [4]. Adhesion forces that cause stiction for metal contact switches are generally due to van der Waals forces, meniscus forces, and, if the contact is very clean, metallic bonding [5].

The study of ‘stuck-open’ contact failure has primarily been addressed experimentally due to the complicated multi-faceted nature of the problem. Contamination failure, the main type of ‘stuck-open’ contact failure, was studied by Chen et al [6]. In this experimental work, thin films of platinum, rhodium, and ruthenium and their alloys with gold were explored as electrical contact materials for MEMS switches using an AFM-based micro-contact tester. It was found that because of the formation of friction polymers (a type of contaminant film) during cycling, the contact resistance increases rapidly after a characteristic number of cycles have occurred with stable resistance. This characteristic number of cycles depends on the contact material. Of the materials tested, gold-on-gold contacts held a stable resistance for the most number of cycles (108 cycles) and ruthenium-on-ruthenium held a stable resistance for the least number of cycles (104 cycles).

Using a nano-indenter-based contact tester, Broue et al [7] explored different MEMS contact materials in five combinations including gold-on-gold, ruthenium-on-ruthenium, rhodium-on-rhodium, gold-on-ruthenium, and gold-on-nickel. The focus of these contact tests was on low to moderate power and contact force under 'quasi-cold' switching conditions. The observed contact resistances and pull-off forces for gold-on-gold and ruthenium-on-ruthenium contacts were comparable to those results reported by Chen et al [6].

Most of the work done on 'stuck-closed' contact failures has focused on adhesion. Majumder et al [8] developed a simplified analytical model for contact resistance and adhesion in a metal RF MEMS switch. Model results matched reasonably well with experimental results. Du et al [9] explored the effect of adhesion on deformation and stresses during loading and unloading in an elastic-plastic finite element model of a single hemispherical asperity pressed against a rigid flat. This model predicted two types of separation modes – ductile and brittle separation. That work predicted low adhesion and brittle separation for ruthenium-ruthenium contacts, and high adhesion and ductile separation for gold-gold contacts. Experimentally, Chen et al [10] explored adhesion effects by varying the rate of separation of a micro-scale contacts to identify the difference between ductile and brittle separation. Eid et al [11] developed a multi-scale model of rough ruthenium-ruthenium micro-contacts. This model incorporated the results from molecular dynamic models of nano-scale asperities to account for roughness and included the effects of plasticity and adhesion.

The contact occurring in a MEMS microswitch presents an intricate tribological environment. When such a switch is closed, the contact bump of the switch is held firmly against the drain such that electrical current can flow. If the surfaces are rough, the real contact area is comprised of the sum of many individual asperity contact areas. Of the mechanical models described above, none have taken into account the electrical or thermal domains when modeling the behavior of a contact. Joule heating due to the flow of current causes a temperature distribution near the contact above that of the ambient. The resulting thermal-elastic expansion can change the contact area which, in turn, affects the contact resistance and Joule heating. Thus, including the electrical and thermal domains in a model can provide more insight into the behavior of a micro-scale metal contact. Furthermore thermal softening can cause reshaping of the contact region thereby affecting adhesion and contact failure.

Bottauscio in [12] explores heat generation and thermal diffusion in an electrical contact by solving the thermal, electrical, mechanical coupled-field contact problem using the finite difference method. Later, Monnier et al [13] solved a nearly identical problem using the finite element method. This study explores the thermal and electrical transient behavior during and shortly after contact is made. The ANSYS model developed considered a millimeter-scale hemisphere contacting a deformable flat. Two materials were considered: oxygen-free high thermal conductivity copper (OFHC Cu) and pure gold. The thermal and electrical results of this model agreed fairly well with experimental data of a 45 mm hemisphere made of gold contacting a planar gold substrate. However, this study fails to generalize the results of the model for use in other applications. Rather, the conclusion of this study is that a multi-physics finite element contact model can be used to accurately predict the behavior of a macro-scale contact.

This paper presents a finite element approach for modeling a thermal-mechanical-electrical coupled field contact comprised of an elastic hemisphere pressed against an elastic

half-space. The goal of this investigation is to develop a fundamental understanding of the steady-state behavior of a multi-physics contact with a particular interest in the contact area. This general solution can be applied to either a smooth contact or to individual asperities in a rough contact.

3.3 Theoretical Background

Consider either a smooth contact bump or a single asperity from a rough bump contacting the nominally flat surface of the drain. Figure 3.1 depicts an elastic hemisphere contacting an elastic half-space of the same material where E is the elastic modulus, ν is Poisson's ratio, α is the coefficient of thermal expansion, ρ is the electrical resistivity, and λ is the thermal conductivity. When a downward displacement, δ, is applied to the top of the hemisphere of radius R, a circular contact area of radius a, is formed.

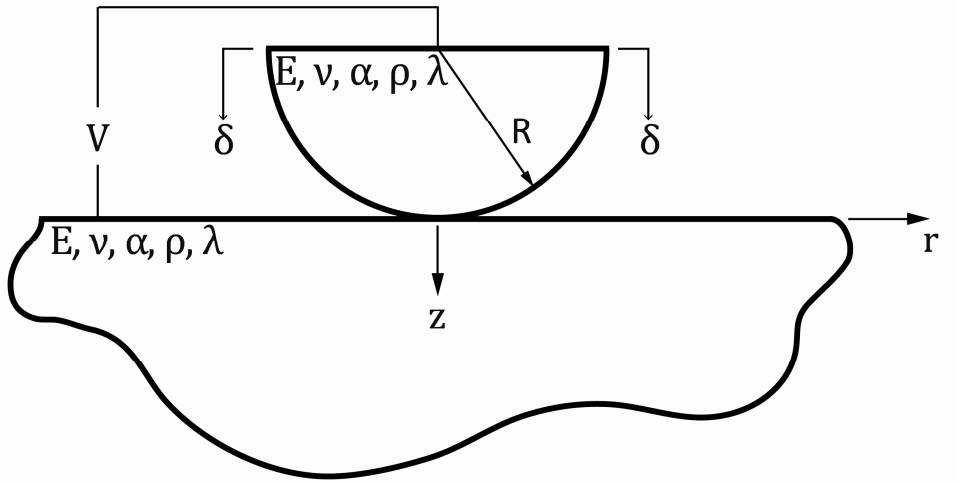

Figure 3.1 An elastic hemisphere contacting an elastic half space.

In a purely mechanical system, Hertz contact theory can be used to calculate the contact radius for a prescribed interference using

$$a = (R_e \delta)^{1/2} \tag{3.1}$$

Alternately, if a downward contact force, P, is applied to the hemisphere

$$a = \left(\frac{3PR_e}{4E_e}\right)^{1/3} \tag{3.2}$$

where the effective radius (R_e), and effective modulus (E_e) are defined respectively as

$$R_e = \left(\frac{1}{R_1} + \frac{1}{R_2}\right)^{-1} \tag{3.3}$$

$$E_e = \left(\frac{1 - \nu_1^2}{E_1} + \frac{1 - \nu_2^2}{E_2} \right)^{-1} \tag{3.4}$$

and the numerical subscripts correspond to the components of the contact. In the system illustrated in Figure 3.1, the radius of curvature of the half-space is considered infinite, making the effective radius of the system equal to the radius of the hemisphere ($R_e = R$). The Hertz equations (3.1)-(3.4) are based on a rigid paraboloid indenting a deformable half space. Application of these equations to the system depicted in Figure 3.1 assumes that the contact radius is much less than the effective radius of curvature such that a paraboloid of revolution is a good approximation to a sphere.

If the upper and lower bodies are held at different electrical potentials, electrical current will flow through the through the bodies via the contact area causing Joule heating. The magnitude of electrical current depends on the geometries of the bodies, the electrical resistivity of the materials, and the size of the contact area.

In the electrical domain, the contact resistance restricts the amount of electric current that flows through the contact area. This contact resistance is comprised of two components: effects due to imperfect electrical contact (such as resistive contaminant films), and effects due to the converging and diverging of current paths through the constriction. Assuming perfect electrical contact, the contact area can be modeled as a current constriction. If the contact radius is known and is much larger than the electron mean-free-path of the contact material, the contact resistance can be calculated by the Maxwell spreading resistance

$$\Omega_c = \frac{\rho}{2a} \tag{3.5}$$

for the constriction resistance between two identical half-spaces [14]. Note that the application of this equation to the system depicted in Figure 3.1 assumes that the contact radius is small compared to the z-dimensions of the system. In [15], Timsit illustrates that the spreading resistance decreases with decreasing film thickness. In essence, should the contact radius exceed 2% of the depth of the flat contacting body, the electrical behavior would reflect that of a thin film as opposed to a half space resulting in a spreading resistance that is significantly less than that calculated by Equation 3.5. This behavior appears to be counter-intuitive, but as pointed out in [15] the total resistance is composed of the spreading resistance and the bulk resistance; the latter component does increase as the film thickness decreases.

In another limit, if the contact radius is small compared to the electron mean-free-path of the contact material, current is conducted via electrons projected ballistically through the contact without scattering. In this case, the contact resistance is calculated using the Sharvin model [16]. Additionally, an interpolation equation was developed by Wexler [17] that bridges between the Maxwell and Sharvin regimes.

In the thermal domain, the maximum temperature in the contact can be calculated using

$$T_{max} = \frac{V^2}{8\rho\lambda} + T_0 \tag{3.6}$$

where T_0 is the bulk temperature of the body far away from the contact point [14]. Note the interesting result that the maximum contact temperature is independent of the size of the contact area and only depends on the applied potential.

When the hemisphere and half-space are pressed together, Joule heating from electrical current and the corresponding thermal expansion make the calculation of the contact radius a non-linear coupled problem in the thermal, mechanical, and electrical domains. Unfortunately, a closed-form analytical solution is not possible for this multi-domain problem. Thus, the finite element method is used to predict the behavior of this multi-physics contact. It is emphasized that the results given in subsequent sections were determined using the finite element method; Equations (3.5) and (3.6) provide benchmarks for comparison.

3.4 Modeling

A multi-physics finite element model (FEM) of the system in Figure 3.1 was built using ANSYS 11®. The model, presented in Figure 3.2, was meshed with six-node triangular coupled-field axisymmetric elements (PLANE223). Each of the six nodes in a triangular PLANE223 element has four degrees of freedom: displacement in the radial (r) and vertical (z) directions, electric potential, and temperature. The mesh was graded radially outward from the initial point of contact with the densest mesh in the contact region. Three-node coupled-field contact (CONTA172) and target (TARGE169) elements were used to mesh the contacting surfaces of the hemisphere and half-space, respectively. The contact and target element nodes have the same four degrees of freedom as the PLANE223 element nodes, ensuring that there is conduction across the contact interface. Furthermore, electric and thermal contact between the surfaces was considered to be perfect; additional thermal and electrical resistances in the contact region due to contaminant films were not considered. Sharvin effects were also not included. The top and bottom bodies of the contact were composed of the same elastic, homogeneous, and isotropic material; plasticity and temperature-dependent material properties were not considered.

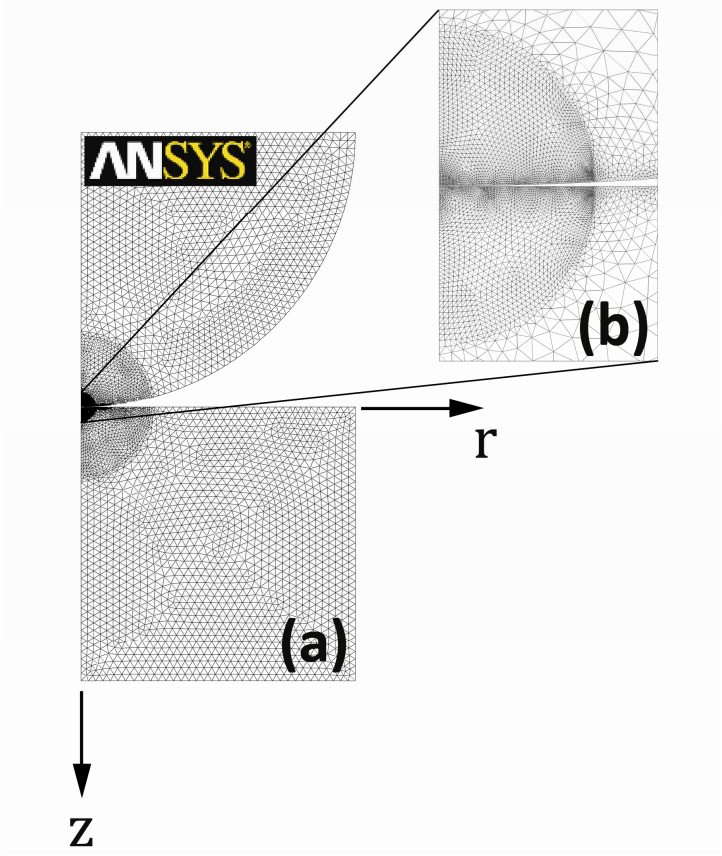

Figure 3.2 (a) Axisymmetric FEM mesh with ANSYS 11® **(b)** A zoomed in view of the mesh in the contact region.

Displacement boundary conditions of the model consisted of a prescribed uniform vertical displacement on the upper-most surface with the bottom-most surface vertically fixed; neither surface was constrained in the radial direction (i.e. zero shear stress). Axisymmetry was applied to the left-most boundary, resulting in zero horizontal displacement. All of the remaining surfaces were unconstrained in the vertical and horizontal directions. Thermally, the upper-most and bottom-most surfaces of the model were held at the same constant temperature. This temperature serves as a reference, relative to which all temperatures in the model were measured. The lateral surfaces of both bodies were considered thermally insulated. Thermal axisymmetry dictates thermal insulation of the left-most boundary. Only solid body conduction was included in this model; convective and radiative heat transfer were not considered. Electrically, a prescribed potential was applied to the upper-most surface, and the bottom-most surface was electrically grounded. Axisymmetry on the left-most boundary results in electrical insulation. The lateral surfaces of both bodies were also considered electrically insulated.

The system initially started with zero displacement, corresponding to zero interference between the hemisphere and half-space. To load the system, an electric potential and a uniform downward vertical displacement were applied to the upper-most surface of the system, resulting in a positive interference exactly equal to the downward displacement. The electric potential was held constant while the vertical displacement was incremented

downward from zero to 0.75% of the hemisphere radius. Without electrical current flow, this interference would correspond to a contact radius equal to 8.66% of the hemisphere radius, which encompasses the entire elastic range for most materials. To unload, the vertical displacement was stepped upward and past zero displacement until separation occurred. Each incremental change in vertical displacement (upward or downward) constitutes a load step. Further, each data point in Figures 3.5-3.7 represents a single load step at which static equilibrium was achieved.

Thermal expansion from Joule heating makes it possible to have contact at zero and negative interferences, but only after contact has been previously initiated, such as in the unload portion of the load/unload cycle described above. In a real switch, this situation occurs when a voltage is applied to the switch during the opening and closing of the contact; this condition is referred to as hot switching. During the loading part of the cycle a negative interference will not produce contact. Thus a negative interference can have two different results. The results presented below for negative interferences are applicable to the opening segment of the contact cycle during hot switching.

3.5 Results and Discussion

In the system described above, calculation of the contact area is paramount; the electrical and thermal conduction through the contact is directly dependent on the contact radius. For generality, results are presented in non-dimensional form with the normalization scheme outlined in Table 3.1. This normalization scheme was inspired by the closed form solution of a hot rigid sphere indenting an elastic half-space presented by Barber [20], although it is not identical. This normalization scheme was determined empirically; multiple simulations were run of the same model with varying material properties and system dimensions to verify its validity.

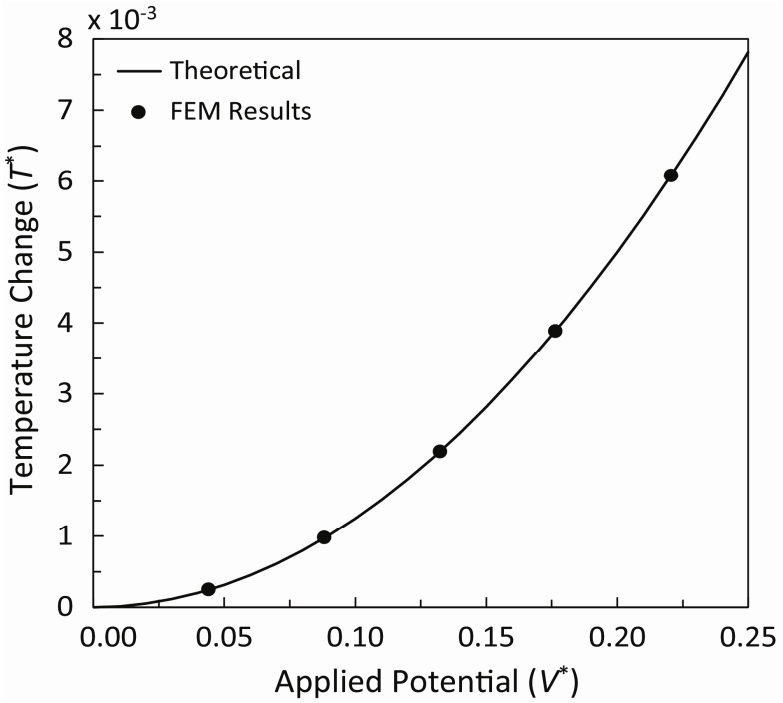

Figure 3.3 Dimensionless maximum contact temperature change (T*) vs dimensionless applied electrical potential (V*). The theoretical curve represents the relationship presented in Equation (3.6).

Figure 3.3 is a plot of the predicted dimensionless maximum contact temperature increase as a function of the applied potential. Note that the temperature increase is measured with respect to the constant temperature prescribed to the upper-most and bottom-most boundaries. Because several interferences were simulated for each applied potential (corresponding to many different radii), each point represents the average of all of the predicted maximum contact temperature increases for each applied potential. The maximum deviation from the average was 0.25%. This plot illustrates that the FEM predicts a maximum contact temperature that agrees extremely well with the theoretical maximum contact temperature change as presented in Equation (3.6).

Table 3.1 Normalization Scheme for FEM Results where an asterisk (*) superscript represents a normalized quantity.

Property	**Normalized Form**
Contact Force (P)	$P^* = \frac{P}{E_e R_e^2}$
Contact Radius (a)	$a^* = \frac{a}{R_e}$
Interference (δ)	$\delta^* = \frac{\delta}{R_e}$
Electrical Potential (V)	$V^* = \frac{V}{\left(\frac{\rho\lambda}{\alpha(1+\nu)^{1/2}}\right)^{1/2}}$
Electrical Current (I)	$I^* = \frac{I}{\left(\frac{\lambda R_e^2}{\alpha\rho(1+\nu)^{1/2}}\right)^{1/2}}$
Electrical Resistance (Ω)	$\Omega^* = \frac{\Omega}{(\rho/R_e)}$
Temperature (T)	$T^* = \alpha(1+\nu)^{1/2}(T - T_0)$

Invariably, the FEM predicted the maximum contact temperature to occur close to the contact region and slightly on the asperity side. Furthermore, the temperature in the contact region was predicted to be constant within 1%. The theoretical temperature distribution due to Joule heating for two half-spaces contacting over a circular region is a constant in the contact area which is greater that the temperature elsewhere [14]. The location of the maximum temperature for the simulation can be justified by reasoning that there is a greater thermal resistance on the asperity side of the contact as compared to the half-space side of the contact.

The magnitude of the maximum contact temperature is important when choosing a contact material. It is important to note that for some materials, large values of the

dimensionless potential (V^*) could result in dimensional temperatures (T) that are sufficiently high to induce significant changes in the material properties of the contact. For example, a dimensionless potential of V^* = 0.221 applied to a gold contact (α=1.4x10^{-5} K^{-1}, ν=0.44 at 300 K) causes a 362 K rise in contact temperature. Therefore, the resulting maximum contact temperature would be 662 K, well above the softening temperature of gold (373 K) [14]. Thermal softening can reshape the contact and lead to greater adhesion. Furthermore, the thermal conductivity would decrease from 320 W/mK to 295 W/mK and the electrical resistivity would increase from 2.44x10^{-8} Ωm to 5.87x10^{-8} Ωm. Thus the results for a dimensionless potential of V^* = 0.221 applied to gold are beyond the intended range of this model. Conversely, a dimensionless potential of V^* = 0.221 applied to a titanium contact (α = 8.6x10^{-6} K^{-1}, ν=0.36 at 300 K) would result in a maximum contact temperature of 907 K. In this case, the resulting maximum temperature is approximately equal to the softening temperature of ~900 K [14].

Table 3.2 Material properties for several common contact materials. All values were obtained from [18], except for OFHC Cu [19].

	E (GPa)	**ν**	**$\rho_{Electric}$ (10^{-8} Ω m)**	**$\lambda_{Thermal}$ (W/mK)**	**$\alpha_{Thermal}$ (10^{-6} 1/K)**
Au	80	0.44	2.44	318	14.0
Pt	170	0.39	10.60	71.1	8.8
Rh	379	0.26	4.51	150	8.2
Ru	432	0.25	7.60	117	6.4
Ti	120	0.36	42.00	11.4	8.6
OFHC Cu	117	0.34	1.71	391.1	17.6

When applying the results presented in this paper to a specific contact material, it is important to know the voltage limit which may lead to significant changes in material properties. Because the maximum temperature varies as the square of the voltage, an applied dimensionless voltage of V^* = 0.1 would yield a maximum temperature approximately equal to the softening temperature of gold. For titanium an applied dimensionless voltage of V^* = 0.220 would yield a maximum temperature approximately equal to its softening temperature. Hence the uppermost simulated dimensionless voltage V^* = 0.221 was chosen purposely to encompass the vast majority of contact metals. Refer to Table 3.2 for the material properties of several common contact materials. Note that the material properties in Table 3.2 are bulk material properties taken at ~300 K and may vary depending on processing and thickness. Table 3.3 contains all simulated dimensionless voltages and the corresponding actual voltages for each of these contact materials; this table may be useful for interpreting the following plots.

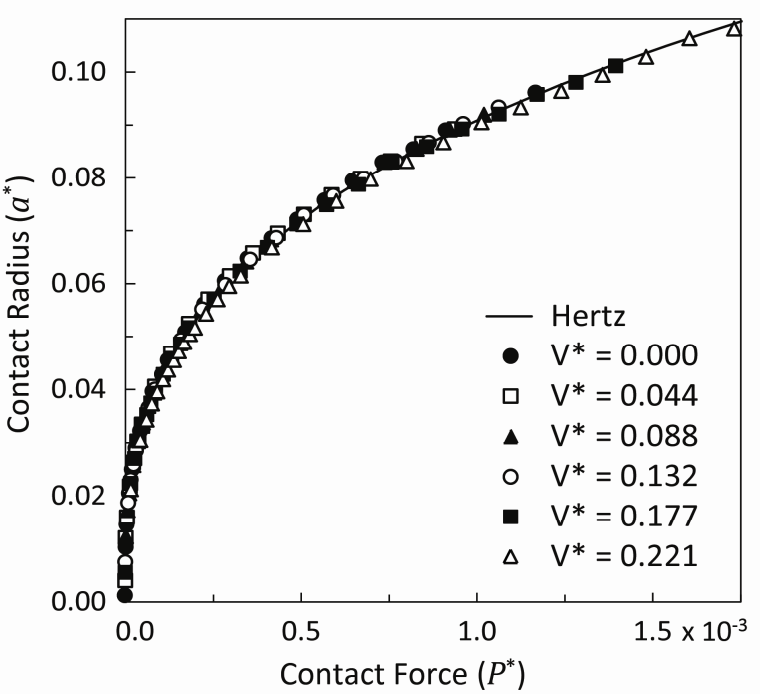

Figure 3.4 Dimensionless contact radius (a*) vs dimensionless contact force (P*).

Figure 3.4 is a plot of the predicted dimensionless contact radius as a function of contact force for different applied potentials, i.e. a force controlled problem. Essentially this plot illustrates that for a given contact force the contact radius is almost independent of the applied voltage. Furthermore, all of the voltages produced contact radii that agree with Hertz contact theory within a maximum 3.15% error for P^* > 1.32x10^{-6}; because of the vertical slope at the origin in Figure 3.4, the percent error of the FEM results can be large for very small values of the contact radius.

Table 3.3 All simulated dimensionless applied electrical potentials (*V**) and the corresponding voltages for several common contact materials.

	Voltage (V)					
V*	**Au**	**Pt**	**Rh**	**Ru**	**Ti**	**OFHC Cu**
0.000	0.000	0.000	0.000	0.000	0.000	0.000
0.044	0.030	0.038	0.038	0.049	0.031	0.025
0.088	0.060	0.075	0.076	0.098	0.061	0.051
0.132	0.090	0.113	0.114	0.148	0.092	0.076
0.177	0.120	0.150	0.151	0.197	0.122	0.101
0.221	0.150	0.188	0.189	0.246	0.153	0.126

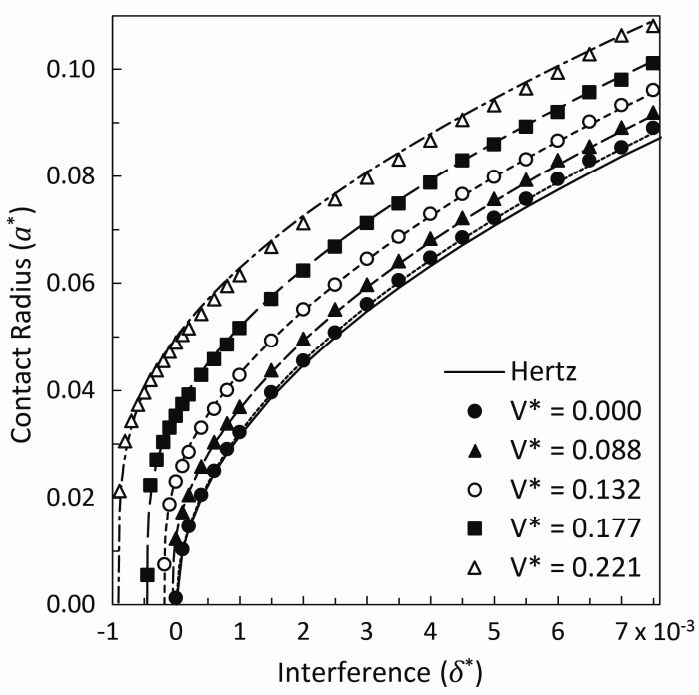

Figure 3.5 Dimensionless contact radius (a^*) vs dimensionless interference (δ^*). The data points represent FEM results, while trend lines are generated by curve-fitting. Results for V^* = 0.044 were omitted to reduce clutter because they are relatively close to V^* = 0.000.

Figure 3.5 is a plot of the dimensionless contact radius as a function of interference for different applied electric potentials, i.e. a displacement controlled problem. It is noted that there is a fundamental issue with such problems because the temperature fields vary as $(r^2 + z^2)^{-1/2}$. The thermal strains then also vary as $(r^2 + z^2)^{-1/2}$ and consequently the displacements are logarithmic in $(r^2 + z^2)^{-1/2}$ [20]. Thus for calculating global displacements, a rigid body term which depends on the finite dimensions of the contacting bodies becomes necessary. In essence, the displacement of any specific point on the surface varies with the finite dimensions of the body. However, for a system containing more than one asperity, such as a multi-asperity

system (like the Greenwood and Williamson model for contact of rough surfaces [21]), the rigid body term does not affect the *relative* displacement between two asperities on the same surface. Therefore when using this model as a building block in such a system, the rigid body term can be chosen arbitrarily.

With zero applied potential (V^* = 0.000), the FEM predicted radii agree closely with Hertz contact theory. The small discrepancy at higher interferences can be explained by the subtle difference between the Hertz problem, which is derived from a rigid paraboloid indenting an elastic half-space, and the FEM, which is an elastic hemisphere indenting a finite size model of an elastic half-space. For small interferences, the radius of curvature of a paraboloid is almost identical to that of a spherical object. However, as the interference increases, the radius of curvature of the paraboloid increases, while the radius of curvature of a spherical object remains constant. This effect tends to make the simulated contact radius smaller as compared to Hertz contact for the same value of interference. Another effect is the finite dimensions in the FEM which, according to the simulations, tends to increase the simulated contact radius under displacement control. This effect becomes more important as the contact radius increases relative to the dimensions of the model. These two opposing effects do not quite cancel resulting in the FEM simulating slightly greater contact radii than Hertz contact theory.

Figure 3.5 also shows that for a given interference, the contact radius increases with applied potential. This result is an expected consequence of thermal expansion due to Joule heating. As stated above, the FEM predicts the maximum temperatures to occur in the region close to the contact. Local thermal expansion in the contact region results in an effective interference between the two heated bodies that is greater than the interference as defined between the two unheated bodies. Thus, under displacement control an applied electric potential has a significant effect on increasing the contact radius.

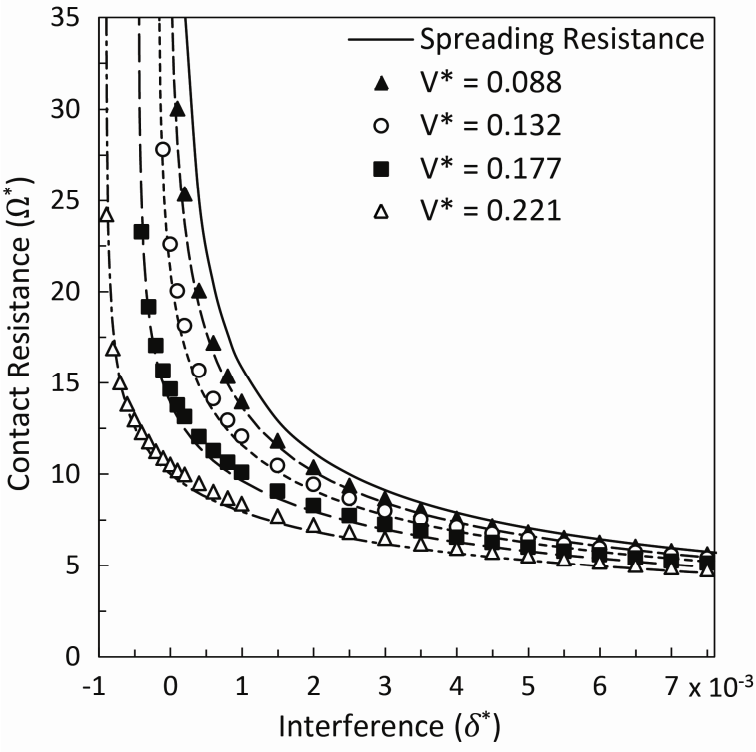

Figure 3.6 Dimensionless contact resistance (Ω*) vs dimensionless interference (δ*). The data points represent FEM results, while trend lines are generated by curve-fitting. Results for V* = 0.044 were omitted to reduce clutter because they are relatively close to V* = 0.000.

Figure 3.6 shows that under displacement control, the FEM predicted electrical constriction resistance decreases with the applied potential. Larger contact areas, due to greater Joule heating resulting from larger applied potentials, leads to smaller constriction resistances. For validation, a theoretical value for the constriction resistance can be calculated using Equation (3.5) in conjunction with the contact radii from the FEM presented in Figure 3.5. The predicted constriction resistances of Figure 3.6 match these theoretical values to within a maximum 4% error. It is important to note that the FEM did not take into account Sharvin effects, thus the lower limit of validity of this model depends on the mean-free-path of electrons for the contact material prescribed. For example, the mean-free-path of electrons for Au is about 41 nm [22]. Therefore, it should be expected that the results presented become less accurate as the contact radius approaches this value.

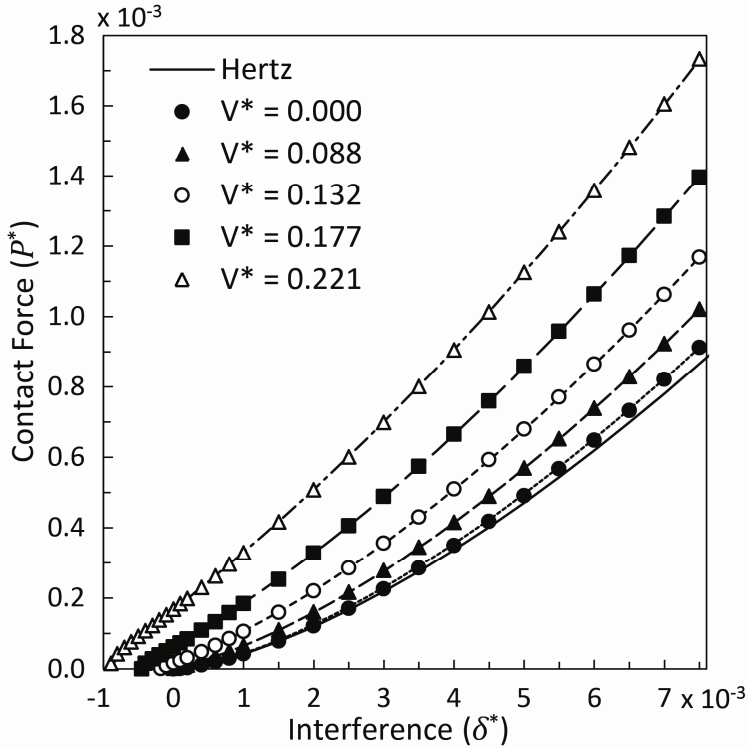

Figure 3.7 Dimensionless contact force (P*) vs dimensionless interference (δ*) for varying dimensionless potentials (V*). The data points represent FEM results, while trend lines are generated by curve-fitting. Results for V* = 0.044 were omitted to reduce clutter because they are relatively close to V* = 0.000.

The relationship between contact force and interference is plotted in Figure 3.7. Curve-fitting to these plots leads to

$$P^*(V^*, \delta^*) = \left[A(V^*)\left(\delta^* - C(V^*)\right)^2 + B(V^*)\left(\delta^* - C(V^*)\right)\right]^{3/4} \tag{3.7}$$

$$A(V^*) = A_4 V^{*4} + A_3 V^{*3} + A_2 V^{*2} + A_1 V^* + A_0 \tag{3.8}$$

$$B(V^*) = B_4 V^{*4} + B_3 V^{*3} + B_2 V^{*2} + B_1 V^* + B_0 \tag{3.9}$$

$$C(V^*) = C_4 V^{*4} + C_3 V^{*3} + C_2 V^{*2} + C_1 V^* + C_0 \tag{3.10}$$

where *A(V*)*, *B(V*)*, and *C(V*)* are functions of V* generated from curve-fitting the data from Figure 3.7. The coefficients are provided in Table 3.4. These curve-fits are represented by the dashed curves plotted in Figure 3.7. When V* = 0.000, Equation (3.7) collapses into the same form as the normalized form of Hertz contact theory. Note that the approximately 5% maximum difference between the Hertz curve and the curve fit for V* = 0.000 reflects the aforementioned discrepancy between the Hertz problem and the FEM simulation.

Table 3.4 Curve-fit Coefficients for the relationship between dimensionless contact force (P^*) and dimensionless interference (δ^*) for a dimensionless applied electrical potential (V^*). The column numbers correspond to the subscripts of the coefficients in Equations 3.8-3.10.

	4	3	2	1	0
A_i	-273.8	79.68	-2.073	1.222	1.574
B_i	-8.161×10^{-1}	9.523×10^{-1}	-1.303×10^{-2}	3.008×10^{-3}	0.000
C_i	1.844×10^{-2}	-9.770×10^{-2}	2.158×10^{-3}	-1.499×10^{-5}	0.000

Of course these curve-fits are valid only within a restricted range. The lower bound of validity of the contact force curve-fits is either zero interference (during closing) or the minimum negative interference shown in Figure 3.5 (during opening). The upper bound of validity is governed by the onset of plastic yielding. Because yielding is dependent on material properties, it is very important to be aware of the limitations of the contact material when applying these results. For example, for gold (E = 86 GPa, ν = 0.44, H = 1.04 GPa, from [23] for a 300 nm film) the von Mises failure criterion indicates that yielding occurs at $P^* = 7.14\times10^{-6}$ (corresponding to $\delta^* = 0.306\times10^{-3}$ for a Hertz contact); the onset of yielding occurs at a very small contact force because gold is a relatively soft metal. At the other end of the spectrum of materials, yielding for ruthenium (E = 292 GPa, ν = 0.25, H = 15.3 GPa from [23] a 300 nm film) occurs at $P^* = 0.917\times10^{-3}$ (corresponding to $\delta^* = 7.79\times10^{-3}$ for a Hertz contact); the onset of yielding occurs at a much greater contact force because ruthenium is a relatively hard metal. Note that these two examples represent the range of typical contact material hardness; the limits of this model as presented were mindfully chosen to encompass a majority of possible contact materials.

As shown in Figure 3.4, the relationship between contact radius and contact force is very well approximated by Hertz contact theory. Thus, Equations (3.7)-(3.10) were used in conjunction with Hertz contact theory to generate the contact radius curves represented by the dashed lines plotted in Figure 3.5. These contact radius curves were in turn used to generate the constriction resistance curves represented by the dashed lines plotted in Figure 3.6. For $P^* > 2.26\times10^{-5}$, the contact force curve fits match the FEM results to within a maximum 9.75% error, the contact radius curve fits match the FEM results to within a maximum 8.34% error, and the contact resistance curves match the FEM results to within a maximum 7.13% error. Thus, the curve-fits agree well with the FEM results.

In some applications, the simulated electrical contact may be exposed to a current controlled environment, where an electrical current is applied over the contact instead of an electrical potential. For example, while a MEMS switch is closing, the contact experiences an environment that resembles a voltage control state, so the behavior may be accurately modeled using the applied potential curve-fits. However, when the MEMS switch is in the steady-state closed position, the contact experiences an environment that resembles a current control state. Hence, a relationship between contact force and interference for an applied electrical current was found using the contact force curve-fit in Equation (3.7) in conjunction with Hertz contact theory of Equation (3.2) and the Maxwell spreading resistance of Equation (3.5). These constant current curves are shown in Figure 3.8.

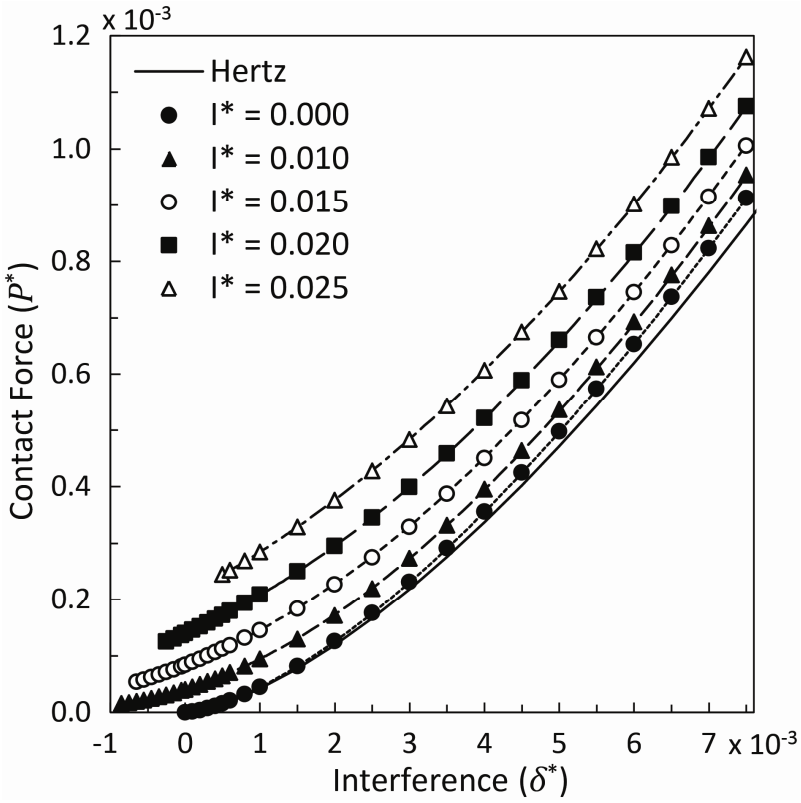

Figure 3.8 Dimensionless contact force (P*) vs dimensionless interference (δ*) for varying dimensionless currents (I*). The data points represent FEM results, while trend lines are generated by curve-fitting.

This plot shows that for a given interference, the contact force required increases with current, much like the behavior displayed in Figure 3.7. However, unlike the behavior in Figure 3.7, the contact force curves approach a zero slope as the interference decreases into the negative region. Curve fitting the constant current plots leads to

$$P^*(I^*,\delta^*) = \left[\left(D(I^*)I^{*\delta^*/E(I^*)} + F(I^*)\right)\delta^{*2} + G(I^*)\delta^* + H(I^*)\right]^{3/4} \tag{3.11}$$

$$D(I^*) = D_4I^{*4} + D_3I^{*3} + D_2I^{*2} + D_1I^* + D_0 \tag{3.12}$$

$$E(I^*) = E_4I^{*4} + E_3I^{*3} + E_2I^{*2} + E_1I^* + E_0 \tag{3.13}$$

$$F(I^*) = F_4I^{*4} + F_3I^{*3} + F_2I^{*2} + F_1I^* + F_0 \tag{3.14}$$

$$G(I^*) = G_4I^{*4} + G_3I^{*3} + G_2I^{*2} + G_1I^* + G_0 \tag{3.15}$$

$$H(I^*) = H_4I^{*4} + H_3I^{*3} + H_2I^{*2} + H_1I^* + H_0 \tag{3.16}$$

where *D(I*)*, *E(I*)*, *F(I*)*, *G(I*)*, and *H(I*)* are functions of I^* generated from curve fitting of the data from Figure 3.8, and the coefficients are provided in Table 3.5. These curve-fits are represented by the dashed curves plotted in Figure 3.8. When I^* = 0.000, Equation (3.11) collapses into the same form as the normalized form of Hertz contact theory. Note that the I^* = 0.000 produces an identical curve to the V^* = 0.000.

Table 3.5 Curve-fit coefficients for the relationship between dimensionless contact force (P^*) and dimensionless interference (δ^*) for a dimensionless applied electrical current (I^*). The column numbers correspond to the subscripts of the coefficients in Equations 3.12-3.16.

	4	**3**	**2**	**1**	**0**
$\boldsymbol{D_i}$	-7.457x10^6	4.648x10^5	-9.671x10^3	63.22	-0.7017
$\boldsymbol{E_i}$	-338.7	-819.3	17.02	0.8636	6.499x10^{-3}
$\boldsymbol{F_i}$	3.801x10^5	-3.916x10^4	1.201x10^3	-16.29	1.574
$\boldsymbol{G_i}$	-2.463x10^3	90.73	2.385	0.1535	0.000
$\boldsymbol{H_i}$	8.613	0.0000	1.440x10^{-2}	0.0000	0.000

It is important to note that the constant-current curve-fits are only valid for applied potentials less than V^* = 0.221, because they are based on the applied potential curve-fits. This is the upper limit of validity of the applied potential curve fits because this was the greatest applied potential simulated with the FEM. Thus the applied current curves presented in Figure 3.8 have been truncated appropriately using

$$\delta_0^*(I^*) = 2958I^{*4} + 0.413I^{*2} - 0.0009201 \tag{3.17}$$

where δ_0^* is the lower limit of validity of interference for the current control curve-fits, and I^* > 0.000. For a given current, any interference less than this limit would demand an applied

potential greater than V^* = 0.221. The upper limit of validity is again determined by the onset of yielding, as described above.

In displacement controlled situations, as an alternative to Figure 3.5 and 3.6, the curve-fits to the results in Figures 3.7 and 3.8 allow contact force to be determined for a given interference. The contact radius can then be found from Equation (3.2) and the contact resistance from Equation (3.5).

These results can be useful when applied to a MEMS switch. For instance, a smooth contact bump would experience a force-controlled environment because the stiffness of the actuator is typically orders of magnitude less than that of the contact. However in a rough contact the stiffness of any one asperity is much less than the combined stiffness of the other asperities. Thus each asperity experiences a displacement-controlled environment in which the curve-fit Equations (3.7)-(3.10) can be used to calculate the corresponding asperity contact radius.

Because these results were developed from a DC model, they are directly applicable to DC contacts of appropriate geometry. A real MEMS switch contact is often fabricated by coating an electrically non-conducting substrate with an electrically conductive material, such as gold or ruthenium [3]. As stated in the theoretical background, this model assumes that the contacting bodies are thick compared to the contact radius. Otherwise the electrical behavior would reflect the contact of thin films (as presented in [15]), as opposed to the contact of half-spaces (as presented in [14]), resulting in significantly different electrical resistances and, by effect, significantly different mechanical and thermal results.

The results presented in this paper may also be applied to low frequency AC contact as well as some high frequency AC contacts, such as RF MEMS switch contacts, subject to a restriction on geometry. In an AC environment the electrical current is redistributed such that the current density decreases rapidly with increasing distance from the conducting body surface, a phenomenon known as the skin effect. The skin effect alters the current density distribution, thereby changing the Joule heating distribution [24]. Therefore, as the signal frequency increases, the heating becomes more localized to the surface resulting in higher temperatures as compared to a DC current. However, if the dimensions of the system normal to the surface are less than the skin depth, the current density of an AC system will not significantly differ that of a DC system [25]. For example, the skin depths for gold (ρ=2.44x10^{-8} Ω·m, Relative Permeability = 0.99996) [26] at 1GHz and 10GHz are 2.5 μm and 0.79 μm, respectively. In either case, the skin depth is greater than that of the contact bump height (0.3 μm) and the drain height (0.3 μm) of the RF MEMS switch developed at Northeastern University [28]. Thus, the results from the presented contact model should be applicable to at least some RF MEMS contacts.

3.6 Conclusions

A finite element model was used to establish a fundamental understanding of the multi-physics behavior of a thermal-electrical-mechanical contact. In the thermal domain, it was shown that the maximum temperature predicted by the FEM agreed well with theory. In the mechanical domain, the results from the FEM establish the distinct difference between force control (applicable to a smooth contact) and displacement control (applicable to individual asperities in

a rough contact) in the presence of an applied electric potential / current. Under force control, the contact radius was relatively unchanged by the presence of electrical loading; Hertz contact theory was found to predict the contact radius well. However, under displacement control, the contact radius increased as the applied electric potential/current was increased.

Furthermore, the FEM data was used to establish curve-fit relations between contact force and interference for varying applied electrical potentials and applied electrical currents. The purpose of these curve-fits is to define the fundamental behavior of a multi-physics contact under displacement control. These curve-fit relations can be used with Equation (3.2) and Equation (3.5) to accurately predict the contact radius and contact resistance, respectively.

Figures 3.5-3.8 present contact behavior in the thermal, electrical, and mechanical domains while current is flowing through a single asperity contact. These results have implications in the behavior of a MEMS switch contact under hot or cold switching conditions. At negative interferences, such conditions represent those experienced by a MEMS switch contact during hot switching, specifically during the opening segment of the contact cycle. Future work will focus on using the results of this model to explore possible hot switching damage mechanisms in a switch contact.

This model shows that local Joule heating from even moderate electrical current can lead to thermal expansion which can produce a change in the geometry of the bodies in the contact region. These results also have implications in adhesion in MEMS switch contacts. For example, according to Figure 3.5, an applied voltage $V^* = 0.088$ results in a contact radius 8.5% larger than that of a purely mechanical asperity ($V^* = 0.000$) at a displacement of $\delta^* = 2.5\text{x}10\text{-}3$. Further, as previously mentioned, an applied voltage $V^* = 0.100$ corresponds to the thermal softening temperature for a pure gold contact. A localized change in geometry of the contact members as well as thermal softening of the contact material would affect the adhesion of the contacting surfaces because the adhesion force is related to the degree of the conformity of the contacting materials. Furthermore, the trends illustrated in Figures 3.7 and 3.8 indicate that the contact force increases with applied potential or current for a given interference; this behavior affects the onset of plasticity in the contact. These effects and their relation to contact failure have yet to be addressed, to the best of our knowledge, and will be studied in future work.

More generally, these results are not restricted to the micro-scale. Although this investigation was motivated by MEMS switch contacts, the intent of this analysis is also to aid in the design of electrical contacts in various other types of switches. The dimensionless quantities used allow these results to be used for different materials and scales.

3.7 Acknowledgements

This work was supported by the Defense Advanced Research Projects Agency (DARPA) N/MEMS S&T Fundamentals program under grant no. N66001-10-1-4006 issued by the Space and Naval Warfare Systems Center Pacific (SPAWAR).

3.8 Chapter 3 References

[1] Rebeiz G M 2003 *RF MEMS: Theory, design, and technology* (Hoboken, New Jersey: J. Wiley & Sons)
[2] Thakur S, SumithraDevi K and Rajput S 2009 Low-loss RF MEMS fixed free capacitive switch characterization. In: *Applied Electromagnetics Conference (AEMC),* (Kolkata, India: IEEE) pp 1-4
[3] Majumder S, McGruer N, Adams G G, Zavracky P, Morrison R H and Krim J 2001 Study of contacts in an electrostatically actuated microswitch *Sensors and Actuators A: Physical* **93** 19-26
[4] McGruer N, Adams G, Chen L, Guo Z and Du Y 2006 Mechanical, thermal, and material influences on ohmic-contact-type MEMS switch operation. In: *IEEE International Conference on Micro Electro Mechanical Systems* (Istanbul: IEEE) pp 230-3
[5] Adams G G and McGruer N E 2010 A Review of Adhesion in an Ohmic Microswitch *Journal of Adhesion Science and Technology, 24* **15** 2571-95
[6] Chen L, Lee H, Guo Z, McGruer N E, Gilbert K, Mall S, Leedy K and Adams G 2007 Contact resistance study of noble metals and alloy films using a scanning probe microscope test station *Journal of Applied Physics* **102** 074910--7
[7] Broue A, Dhennin J, Charvet P, Pons P, Jemaa N B, Heeb P, Coccetti F and Plana R 2010 Multi-Physical Characterization of Micro-Contact Materials for MEMS Switches. In: *IEEE Holm Conference on Electrical Contacts (HOLM),* (Charleston, South Carolina, USA: IEEE) pp 1-10
[8] Majumder S, McGruer N and Adams G G 2005 Adhesion and contact resistance in an electrostatic MEMS microswitch. In: *STLE/ASME International Joint Tribology Conference,* (Ponte Vedra Beach, Florida, USA: IEEE) pp 215-8
[9] Du Y, Chen L, McGruer N E, Adams G G and Etsion I 2007 A finite element model of loading and unloading of an asperity contact with adhesion and plasticity *Journal of colloid and interface science* **312** 522-8
[10] Chen L, McGruer N E, Adams G G and Du Y 2008 Separation modes in microcontacts identified by the rate dependence of the pull-off force *Applied Physics Letters* **93** 053503
[11] Eid H, Adams G, McGruer N, Fortini A, Buldyrev S and Srolovitz D 2011 A Combined Molecular Dynamics and Finite Element Analysis of Contact and Adhesion of a Rough Sphere and a Flat Surface *Tribology Transactions* **54** 920-8
[12] Bottauscio O, Crotti G and Farina G 1993 Numerical analysis of heating transient of electric contacts under short-circuit conditions *Transactions on Components, Hybrids, and Manufacturing Technology* **16** 563-70
[13] Monnier A, Froidurot B, Jarrige C, Teste P and Meyer R 2007 A mechanical, electrical, thermal coupled-field simulation of a sphere-plane electrical contact *IEEE Transactions on Components and Packaging Technologies* **30** 787-95
[14] Holm, R., and Holm, E., 1967, *Electric contacts: theory and application*, Springer-Verlag New York, NY, Chap. 5-13.
[15] Timsit R S 2010 Constriction resistance of thin film contacts *IEEE Transactions on Components and Packaging Technologies* **33** 636-42
[16] Jansen A G M, Gelder A P and Wyder P 1980 Point-contact spectroscopy in metals *Journal of Physics C: Solid State Physics* **13** 6073
[17] Wexler G 1966 The size effect and the non-local Boltzmann transport equation in orifice and disk geometry *Proceedings of the Physical Society* **89** 927

[18] Totemeier T C and Smithells C J 2004 *Smithells metals reference book* (Waltham, Massachusetts, USA: Butterworth-Heinemann)
[19] Bronze., A. ,2012, *OFHC Copper Material Spec Sheet*, Available: http://www.atlasbronze.com/C10100_product_sheet.html
[20] Barber J R 1973 Indentation of the semi-infinite elastic solid by a hot sphere *International Journal of Mechanical Sciences* **15** 813-9
[21] Greenwood J and Williamson J 1966 Contact of nominally flat surfaces *Proceedings of the Royal Society of London. Series A. Mathematical and Physical Sciences* **295** 300
[22] Omar M A 1975 *Elementary solid state physics: principles and applications* vol 157: Addison-Wesley)
[23] Lee H, Coutu R A, Mall S and Leedy K D 2006 Characterization of metal and metal alloy films as contact materials in MEMS switches *Journal of Micromechanics and Microengineering* **16** 557
[24] Lamb H 1883 On Electrical Motions in a Spherical Conductor *Philosophical Transactions of the Royal Society of London* **174** 519-45
[25] Kazimierczuk, M. K., 2009, *High-frequency magnetic components*, Wiley, New York, NY.
[26] Hayt, W. H., Buck, J. A., 2001, *Engineering electromagnetics*, McGraw-Hill, Boston, Massachusetts, USA.

Chapter 4

Hot-Switched Lifetime and Damage Characteristics of MEMS Switch Contacts

This chapter is a revised version of a paper published in the Journal of Micromechanics and Microengineering, March 2013

4.1 Abstract

Using a custom built contact testing system, DC micro contact damage under hot-switching conditions was explored in ruthenium-on-ruthenium contacts operated at a contact force of approximately 400 μN. For the first time, contact damage on making and breaking contact under bias (leading and trailing edge hot switching) is compared. The high-voltage tests (3.5V) lead to polarity-dependent material transfer, with material moving in the direction of the electric field. The amount of material transfer does not depend strongly on the current limit from 0.78 to 380 mA. The low voltage (0.71V) tests result in much less damage, and the material transfer does not have a clear directionality. However, the amount of damage does increase significantly as the current limit is increased from 16 to 78 mA. Also observed for the first time is a new type of high-current, short duration current spike associated with hot switching events at voltages above 1.5V. The fact that these spikes occur at the higher voltage but not at the lower voltage suggests (but does not prove) that they are associated with the polarity dependent material transfer.

4.2 Introduction

Microelectromechanical Systems (MEMS) switches can be classified into two contact types: capacitive and ohmic. In a capacitive switch, two transmission lines are separated by a dielectric material, effectively forming a capacitor. The capacitance of the switch is controlled by mechanically changing the separation between the transmission lines. Because a capacitive switch is essentially a capacitor with variable capacitance, it will not function in a direct current (DC) environment and can only be used in high frequency applications. Ohmic contact, or contact-type, switches employ two separable conductive surfaces (generally metals) as the electrodes of a contact. The switch is open if the electrodes are not touching. When the electrodes are touching the switch is closed, allowing current to flow through the contact; the amount of current flowing through the contact is governed by Ohm's law, hence the name of this type of switch. Unlike capacitive switches, ohmic switches can be used for either DC or AC applications.

With applications in the aerospace, military, and commercial sectors, MEMS switches have a large potential market. Ohmic MEMS switches can switch signals from DC to at least 100 GHz and can be used in automated test equipment (ATE) as well as in industrial and medical instrumentation applications [1]. Compared to electromechanical technologies such as reed relays, contact-type MEMS switches are smaller and have faster switching times [2]. Both contact-type and capacitive MEMS switches have applications in radio frequency (RF) systems such as phased arrays and reconfigurable apertures for telecommunication systems, switching systems for satellite communications, single-pole N-throw switches for wireless portable or base-station applications, as well as in commercial cell phone antennae [3]-[8]. Compared to current solid state RF technologies such as Field Effect Transistor (FET) switches and PIN diodes, RF MEMS switches generally have lower insertion loss (0.1 dB up to 100 GHz), higher isolation (because of lower off-state capacitances of 2-4 fF at 0.1-60 GHz), lower power consumption (10-100 nJ per switching cycle), and higher linearity [1]. However there are also some disadvantages to MEMS switches such as high actuation voltages, slow switching speeds (compared to solid state technologies), and moderate power handling capabilities. Perhaps the

greatest flaw of this maturing technology is reliability, especially at high power or when hot switching. Applications for RF MEMS switches require from about 100 million cycles to several hundred billion cycles [2]. Although there are several high performance and high power MEMS switches currently on the market and under development, such as the Radant switch [9], the UCSD switch [10], the Omron switch [11], and the CEA-LETI switch [12], all have reported significantly less reliability when hot switched.

In the switch environment, the switch contact may experience either of two switching modes. Cold switching refers to the application of an electrical signal across the switch only when the contact is fully closed. On the other hand, hot switching refers to the application of a signal while the switch is being opened and closed. For testing purposes, a few variations of hot and cold switching also exist. Leading edge hot switching refers to the application of a signal across the switch as it closes while trailing edge hot switching refers specifically to the application of a signal across the switch as it opens. In general leading edge and trailing edge hot switching may include the application of a different electrical signal while the contact is fully closed. Finally, pure mechanical switching refers to cycling without an applied electrical signal.

Contact damage due to cold switching and purely mechanical switching have been studied in several papers. Cold switching damage mechanisms can result in two different types of contact failure. Stuck-open failure, generally caused by contamination [13]-[17] or wear [18]-[20], occurs when the contact resistance becomes too high for the switch to function properly. Conversely, stuck-closed failure occurs when the switch remains perpetually in the on-state, even after the actuation voltage is removed. This type of failure is generally caused by welding [21], stiction [17], or so-called bridging [22].

Compared to cold switching, hot switching leads to shorter contact lifetimes [22],[23]. Thus there are additional damage mechanisms that occur during hot switching as compared to cold switching. However, the specific hot switching damage mechanisms are not completely agreed upon. Currently, there are four categories of material transfer mechanisms postulated to account for damage in hot switched micro contacts: field evaporation, field emission, arc or pseudo-arc transfer, and ohmic heating/bridge transfer.

Field evaporation is the removal of a surface molecule, as an ion, by a very strong local electric field [24]. The theoretical local electric field necessary to induce field evaporation is estimated in [25] for various metals, such as gold (52.5 V/nm) and ruthenium (42 V/nm), among many others. The direction of material transfer in field evaporation is dependent on the electric field orientation as well as the material itself. Both positive and negative field evaporation have been demonstrated experimentally [26].

Yang *et al* [23] present what they believe to be evidence of field evaporation material transfer in switch contacts. Gold contacts were hot switched at voltages higher than the field evaporation threshold for gold (~4V), but lower than the gold ionization threshold (9.42V) so as to avoid electric arc failure (discussed below). Material transfer was observed from anode to cathode. The authors observed no electric arcs (in the form of voltage spikes in the testing circuit) over the contact during making or breaking of contact. Further testing conducted at the low potential of 1V (below the reported minimum gold field evaporation voltage) revealed behavior more closely resembling thermal wear (similar to bridge transfer). Thus, material transfer under hot switched testing was assumed to be the result of field evaporation.

Electric arc material transfer may also occur between the electrodes of a microswitch contact during hot switching. An electric arc occurs when electrical current flows through the medium that separates the electrodes of an electrical contact; this can only happen when the medium becomes locally conductive. If the medium between the electrodes is a gas, the gas must be ionized in order to conduct current and to allow arcing to occur; the breakdown voltage (at which ionization occurs) is a characteristic of the gas medium. This breakdown process, known as Townsend discharge, is generally started by thermal emission or tunneling of a small number of electrons from the cathode due to a very strong local electric field. These released electrons cause an avalanche-type of ionization of the medium separating the electrodes. Alternatively, vapor arc breakdown occurs when a metallic vapor between the electrodes is ionized by the combination of the strong local electric field and thermal emission of electrons from the cathode. It has been shown that softened or molten bridges may form (bridge transfer) [28]; heating effects from current running through a relatively small structure could result in an explosive vaporization of all or parts of the metallic bridge causing the expulsion of metal vapor into the gap between the electrodes. Once the vapor is ionized and becomes conductive, the free electrons flow toward the anode and the metallic ions flow toward the cathode. For the arc to be sustained, a characteristic potential and current must be sustained [29]. However, it has been shown that short duration micro-arcs can occur under lower voltage conditions. In [30], Dickrell *et al* performed several 3.3 V hot switching tests on gold-on-platinum metal MEMS switch contacts and found that these contacts failed via high resistance. The authors reported voltage transients during the making and breaking of contact while cycling without a 'capacitive-quench' circuit; they interpreted these voltage transients as micro-arcs. It was concluded that the primary damage mechanism to their contact was micro-arc induced contamination growth (in the form of carbon) which lead to high resistance failure.

In 2011, Poulain *et al* introduced a field emission theory for material transfer that they observed in relatively low voltage (10 V) DC micro-contacts [31]. According to this theory, field emission material transfer occurs when a surface asperity on the cathode side of a local electric field emits electrons via tunneling as governed by the Fowler-Nordheim field emission theory. These released electrons follow the electric field and bombard the anode causing local heating which results in material evaporation. The evaporated material is then deposited on the cathode resulting in a net material transfer from the anode to the cathode. Experimental work substantiated the field emission theory they developed by demonstrating an unstable current before contact during testing. This behavior presented several current 'spikes' of magnitude ~0.5nA while the electrodes were on the order of 5-10 nm apart. Upon inspection of the test data, the measured currents matched fairly well in magnitude and behavior with the Fowler-Nordheim theory of electron field emission. Furthermore, material transfer from anode to cathode was illustrated in detail.

The purpose of this chapter is to explore, describe, and attempt to explain the contact damage in DC MEMS contacts under various hot and cold switching conditions. As a baseline, a set of hot switched contacts is compared to pure cold switched and mechanically cycled contacts. To further explore the effects of hot switching, contact damage from leading edge hot switching is compared in detail to contact damage resulting from trailing edge hot switching for both polarities. The effects of varying the hot switching voltage and the cold switching current are studied to attempt to differentiate hot switching damage from cold switching damage, also

for both polarities. Finally, an exploration of the electrical behavior immediately before making and immediately after breaking the contact is studied to provide insight into possible hot switching mechanisms.

4.3 Experimental Setup

It can be extremely time consuming and expensive to perform contact tests on MEMS switches. Thus several researchers have designed contact testing systems for microcontact studies [14],[23],[30],[32]. The benefit of using such a test system is that fabrication of an entire MEMS switch is not necessary, saving time and cost. Furthermore, a wide variety of contact tests can be evaluated relatively simply in a flexible and robust test system. The most important measurements to consider when testing contacts are contact force and contact resistance, because these properties provide an important assessment of the performance of the contact. Thus a well-designed contact testing system should be able to take both measurements simultaneously.

A JEOL 5200 scanning probe microscope (SPM) based testing system [32] was used to study micro-contacts in a variety of hot and cold switching test conditions presented in this chapter. The test system accurately and continuously measures contact resistance using a four-wire measurement. The test system also facilitates the examination of contact force and contact adhesion using custom micro-fabricated test specimens. Each test specimen pair consists of a bridge-like force structure with integrated contact bump and opposing elevated flat surface referred to as a pillar. This pair is opened and closed while a specified electric potential waveform is applied to emulate contact operation in a microswitch.

4.3.1 Contact Test Specimen

Figure 4.1(a) shows a typical force sensor. This fixed-fixed bridge structure is fabricated from silicon with the dimensions presented in Table 4.1 and then coated with a metal film. The dimensions are determined by measurement under a well calibrated optical microscope. The stiffnesses of the force sensors with these dimensions were calculated to be approximately 3380 N/m for the ‘long’ length beams and 8300 N/m for the ‘short’ beams using finite element analysis with roughly a +/- 10% uncertainty (due to variations in the dimensions from sample to sample). The optical lever paddles are used to reflect the SPM laser from the source to the photo detector, as depicted in Figure 4.1(c). The force sensor acts in the same manner as an SPM probe; as the beam is vertically deflected (upward or downward) the optical paddle is rotated thus changing the reflected position of the SPM laser on the photo detector. Upward deflection of the center of the beam represents a compressive contact force such as that occurring during actuation. Downward deflection of the center of the beam represents a tensile contact force such as that occurring during release if adhesion is present. The relationship between the angular rotation of the optical paddle and the applied force was determined using a finite element model with measured dimensions; thus the contact and adhesion forces can be measured for every cycle.

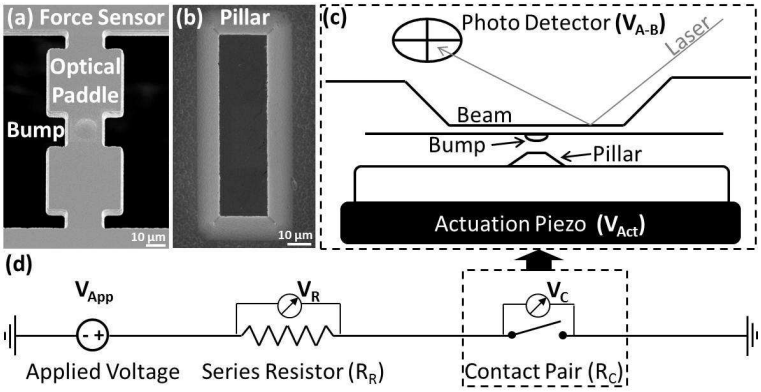

Figure 4.1 (a) SEM of typical force sensor (b) SEM of typical pillar (c) Schematic of test setup (d) Schematic of test circuit with reversible applied voltage source.

The integrated contact bump of the force sensor has a radius of 6 µm, a height of 0.3 µm, and a radius of curvature of approximately 60 µm. The dimensions of the test contact bumps are designed to be representative of contact bumps found in actual MEMS switches.

Table 4.1 Force Sensor Dimensions. These dimensions are explicitly defined in the Appendix.

	Dimension (µm)	
Feature	**Short Structure**	**Long Structure**
Length	90	120
Paddle Width	40	40
Paddle Length	35	40
Middle Spacing	10	20
End Spacing	5	10
Beam Width	20	20
Beam Thickness	4.5	4.5

Because the force sensors employ a fixed-fixed beam geometry, the opposing contact surface was created using a pillar structure, as shown in Figure 4.1(b), to ensure that contact only occurs at the contact bump while also providing a suitable range for actuation. One advantage of using a fixed-fixed geometry is that the symmetrical deflection of the beam results in very little sliding upon contact, sometimes referred to as 'contact scrubbing', thus minimizing contact damage due to sliding. Another advantage of the fixed-fixed beam geometry is very good sensitivity. For example, as compared to a cantilever beam, the amount of angular rotation at the optical paddle of the force sensor is much greater for a given displacement. Thus the contact forces and especially the relatively smaller adhesion forces can be measured with 5 µN resolution.

4.3.2 Contact Materials and Test Environment

All of the tests presented in this chapter consist of ruthenium-on-ruthenium contacts. The choice of ruthenium for a contact material is based on previous work. For example in [32] it was found that ruthenium-on-ruthenium contacts exhibited little adhesion while maintaining low contact resistance ~0.80 Ω for contact forces above 300 μN. To ensure proper bonding of ruthenium to the surfaces of the force sensor and pillar, a 2-6 nm chromium adhesion layer was sputtered immediately before ruthenium deposition. The ruthenium films on both the force sensor and pillar were sputtered to a nominal thickness of 300 nm for most of the tests. The films used for tests expected to result in the greatest amount of material transfer were sputtered to a nominal thickness of 600 nm; these tests include leading and trailing edge hot switching tests cycled at 500 Hz, 3.54V_{Hot}, and 77.5mA_{Cold} for 10^6 cycles (both polarities). On the pillar side, the sloped sides of the pillar could result in poor electrical conduction through the Ru due to the directionality of the sputtering process. Therefore, an additional 300 nm of gold was sputtered onto the pillars before Ru deposition in order to ensure good electrical conductivity (and minimal additional resistance) down the sides of the pillar. The resistivities of the sputtered gold and ruthenium were measured to be 4.94 μΩ·cm and 15.4 μΩ·cm, respectively.

Before testing, the ruthenium contact surfaces were conditionally cleaned using plasma. An argon (0.3 lpm) and oxygen (0.5 lpm) mixture plasma was generated at 4 Torr using a MKS-AX7670 remote plasma system immediately before testing. If, and for what duration, the samples were plasma cleaned depended on the time since ruthenium deposition. Samples tested within 48 hours of deposition were not plasma-cleaned. Samples tested between 2 and 5 days of deposition were plasma cleaned for 3 minutes. Samples tested 5 or more days after deposition were cleaned for 5 minutes. This plasma clean was used to remove organic surface contaminants that can develop during transportation and storage between deposition and testing as well as to oxidize the ruthenium contact surfaces (RuO_2) to improve the contact behavior [33]. Note that is has been shown that ruthenium becomes oxidized (RuO_2) when exposed to O_2 plasma for sufficient amounts of time [34] and that ruthenium oxide is stable and conductive [35]. Based on these findings and previous work [36], it is expected that the contact surfaces will be primarily oxide at the start of the test, as opposed to pure ruthenium. However, no measurements were conducted to determine the oxide thickness of the test samples after plasma cleaning. It is important to note that the ex-situ plasma cleaning presented above was found empirically to not affect the results of the hot switching tests presented in this chapter.

Testing for all of the data presented in this chapter was done in nitrogen at room temperature and atmospheric pressure with a constant 0.8 lpm flow of dry nitrogen from a liquid source onto the contact region. It was found that the nitrogen flow in the contact region discourages the buildup of contamination on the ruthenium contact surfaces during testing [32].

4.3.3 Contact Tester System

To test the contacts, the force structure is fixed while the pillar is actuated upward using a piezoelectric actuator (Physik Instrumente PL022.31), as depicted in Figure 4.1(c). The pillar is electrically isolated from the piezoelectric actuator. All of the tests presented in this chapter

employed a ramp-hold-ramp actuation waveform. The pillar is ramped from complete separation of 600 nm to a contact force of 400 μN, held for a short time, ramped back down, and held at the initial separation. The ramping period, holding period, and duty cycle of the actuation waveform are all controlled remotely by the test program. The initial alignment and initial separation of the pillar with respect to the force structure are set up manually using the SPM x-y stage and stepper motor, respectively. While the alignment of the SPM stage is very stable, it should be noted that the vertical stage does tend to drift over long time periods, thus the built-in SPM piezo is controlled by the operator via the test program to compensate and keep the 600 nm spacing constant. This process is automated for long duration tests with a force feedback control system.

While the contact is being cycled via the actuation waveform, a synchronized voltage potential waveform is applied to the contact through the series resistor; the polarity, form, duty cycle, and amplitude of which are test-specific and controlled remotely by the test program. For both polarity configurations, the cathode is held ground and positive (+) voltages are applied to the anode. Figure 4.1(d) is a schematic of the test circuit. The series resistor is also test specific, but generally its value is large compared to the contact resistance. Because the voltage source does not limit the current flowing in the system, the series resistor serves as a current-limiter for the entire circuit. Thus, for a given applied potential, larger resistance results in smaller current flowing through the circuit while the contact is closed. The contact resistance (R_C) is calculated using a four-wire measurement with

$$R_C = \frac{V_C}{V_R} R_R \tag{4.1}$$

where V_R is the voltage drop over the series resistor, V_C is the voltage drop over the contact, and R_R is the series resistance; both the resister voltage and the contact voltage are monitored by the test program.

4.3.4 Contact Testing Program

A flexible contact testing program was custom-built using LabVIEW™ 8.6. This testing program has four primary functions: two output functions and two input functions. The LabVIEW™ software interfaces with a National Instruments PCI-6259 DAQ for both output and input. For output, the PCI-6259 has a DAQ rate of 1.5 MS / Channel / second, and thus has a resolution of two-thirds of a micro-second. The two primary output functions are:

A) *Control the actuation and SPM piezos*: The program supplies an independent voltage waveform to each piezo. Thus the program is the source of the ramp-hold-ramp actuation voltage waveform supplied to the actuation piezo. Additionally, the DC voltage signal supplied to the SPM piezo from the program allows the operator to control the separation spacing between the pillar and contact bump during testing. Both signals can be changed in magnitude/amplitude, form, and/or period on-the-fly (while testing) giving the operator great control to ensure consistent and repeatable contact force during testing, regardless of piezo or stage drift.

B) *Control the applied voltage waveform*: Via the DAQ, the program is able to supply the test circuit with a voltage waveform that is fully synchronized with the actuation waveform. This

synchronization allows for precise timing of the applied voltage such that any combination of hot/cold switching with any combination of magnitudes up to 10 V is possible.

For input, the PCI-6259 has a DAQ rate of 200 kS / Channel / second and thus has a resolution of 5 micro-seconds. The two primary input functions are to:

C) *Read in the deflection of the force sensor:* The signal from the SPM photo detector (V_{A-B}) is continuously read during testing to monitor the contact force in real time using an oscilloscope-type display. The operator uses this real-time display to adjust the output signals accordingly for consistent testing. The program also analyzes the input signal to count the cycles in real-time allowing for automated data capture of individual or groups of cycles while cycling at high rates.

D) *Read in the voltage drops over the series resistor and contact:* The voltage drops are also displayed in real-time for the operator to monitor the contact resistance and the quality of the electrical contact. This process allows the operator to terminate a test immediately if a contact fails due to high resistance.

Operator monitoring of the real-time contact force and contact resistance provides valuable information such as cycles until failure, type of failure (stuck open or stuck closed), or intermittent sticking (where the contact sticks together for only a small number of cycles) as well as the contact behavior leading up to any of these events.

Using this test program, a series of experiments were designed to characterize hot switching contact damage. The four different switching modes tested in this chapter are schematically represented in Figure 4.2(a)-(d). Note that although different in the figure, the hot and cold switching voltages can be the same. Different hot and cold switching voltages were used in this figure to emphasize the hot and cold switching 'segments' of a typical cycle. At 500 Hz the fully-closed on-state period is 0.5 ms, the ramp-up and ramp-down periods have the same duration of 0.25 ms each, and a fully-separated off state period is 1 ms.

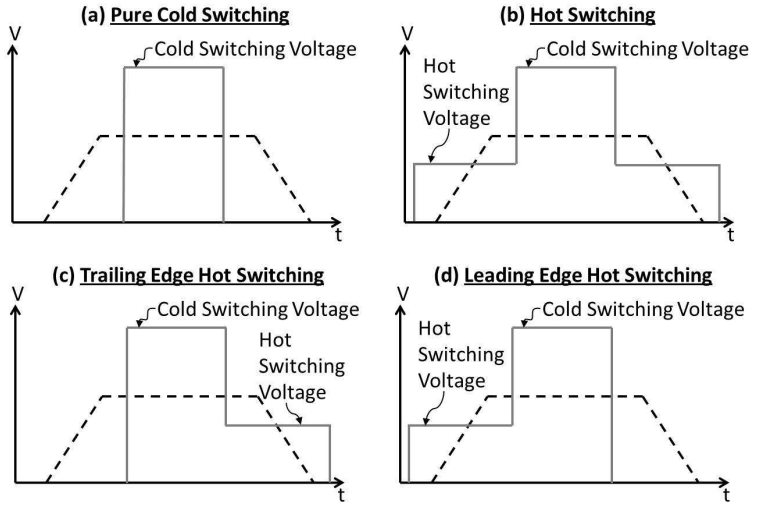

Figure 4.2 Schematics of the four different switching modes presented in this chapter. Each test type employs a ramp-hold-ramp actuation waveform as represented by the dashed lines. The applied voltage waveforms are represented by the solid grey lines.

4.4 Test Results and Discussion

The test results in this chapter are described in terms of contact damage (qualitative and quantitative), contact resistance data, contact adhesion data, and voltage/current waveforms. Contact damage is presented qualitatively using SEM micrographs and quantitatively using AFM measurements of material transfer volume.

Volume calculations were performed via a well-calibrated atomic force microscope (AFM) used to scan the topography of a region, including damaged areas as well as the surrounding undamaged region. The amount of material gained or lost was calculated to be the volume contained by the difference between a surface fit of the undamaged surface and the measured damaged surface. The details of this procedure are outlined in the Appendix. While it is noted that there are expected imperfections in this method such as the error associated with the radius of the AFM probe and curve fitting an incomplete surface, these volume calculations were found to be very repeatable, and thus provide a dependable way to compare material transfer in different individual tests.

It is noted that all of the results presented in this chapter were verified by repeating each test at least twice. Although each SEM depicts a single sample, an effort was made to choose the picture that best represents the qualitative results for a given test.

4.4.1 Mechanical Switching, Cold Switching, and Hot Switching

To explore the contact damage caused by different types of switching, tests were conducted for each type of switching. Figure 4.3 shows the contact bump and opposing pillar for each of five different switching tests: mechanical switching; pure cold switching in both polarities with a cold switching current of I_{Cold} = 77.5 mA; and hot switching in both polarities with a hot switching potential of V_{Hot} = 3.54 V and cold switching current of I_{Cold} = 77.5 mA. All tests were conducted with a 50 Ω series resistor at 500 Hz for $5x10^5$ cycles. Note that in a 50 Ω system, an applied potential of 3.87 V corresponds to 0.30 W of power and 3.54 V corresponds to 0.25 W of power while the contact is closed; the contact resistance is small (2 Ω or less at 400 μN of contact force) for a typical contact pair in the closed state. The DMT contact model [37] yields a theoretical contact radius of approximately 440 nm for 400 μN contact force (E = 410 GPa, ν = 0.3, R = 60 μm)[37], on the order of the radius of the contact spots illustrated in Figure 4.3(a) – (f). A pull-off force of 30 μN was used to calculate surface force effects – the average pull-off force for a typical test (see **Error! Reference source not found.Error! Reference source not found.** below). This model assumes fully-elastic contact behavior, smooth and clean contact surfaces, and no electrical or thermal effects. However, it should be noted that the real contact surfaces do have roughness as well as contamination and oxidation. These factors are expected to result in a smaller real contact area, through which electrical current can flow.

For pure mechanical switching, test results show very little contact damage. For pure cold switching, test results show more contact damage as compared to mechanical switching. The damage done to the contacts do not have clear polarity dependence. The hot switching tests show a much larger amount of contact damage while also exhibiting a clear polarity dependence of material transfer in the direction of the electric field, from anode to cathode. The volume calculations for each hot switching electrode are shown at the bottom of the

corresponding micrograph Figure 4.3(g)-(j). In both hot switching tests the measurements of material missing from the anode and added to the cathode are approximately equal. Furthermore, the amount of material transferred for the two polarities is approximately equal. Both of these results are typical and serve as a validation of the volume calculation method; conservation of mass is observed from one electrode to the other in a given test.

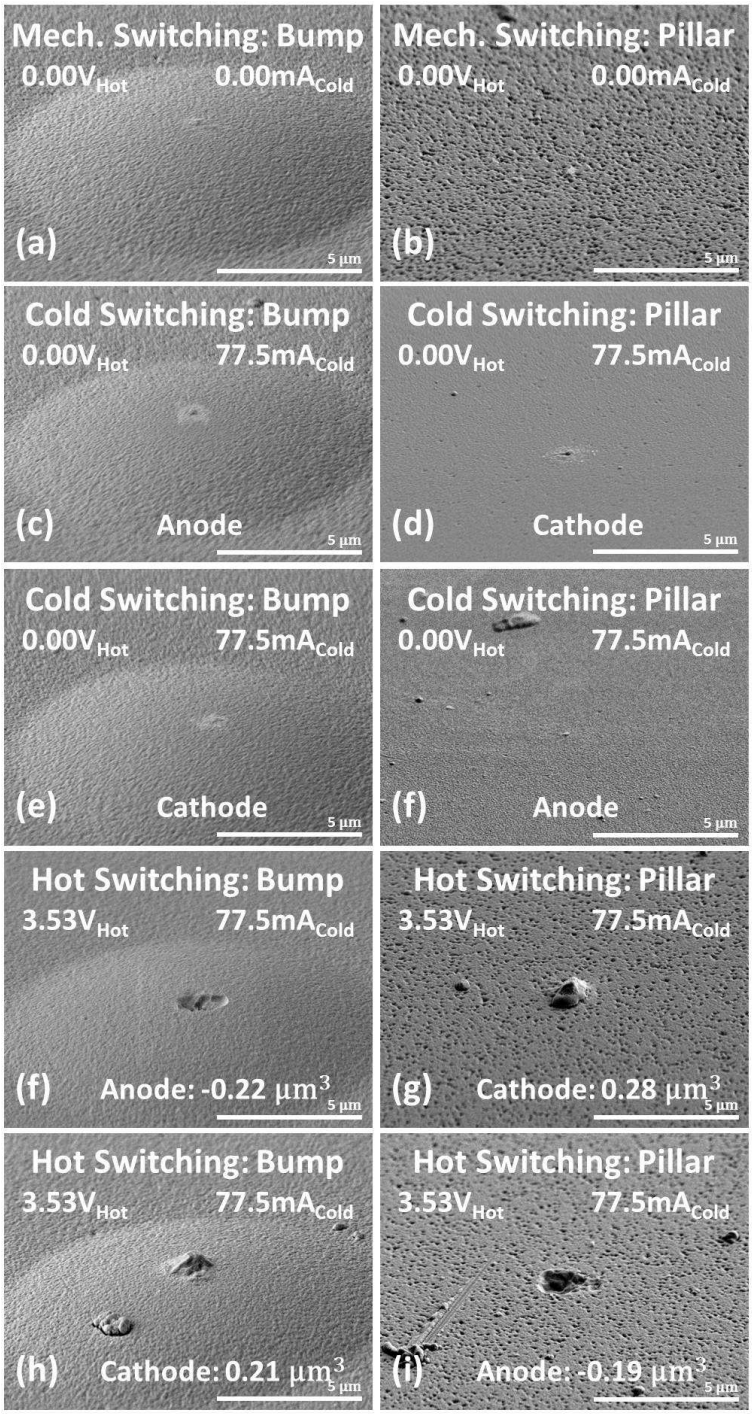

Figure 4.3 Contact damage for various types of switching cycled at 500 Hz for $5x10^5$ cycles.

Based on these tests, it is clear that there are damage mechanisms associated with mechanical switching, additional damage mechanisms associated with cold switching, and even more additional damage mechanisms associated with hot switching. While this result is by no means novel [17],[23],[31],[32] these tests serve as a baseline for comparison of contact damage for the rest of the data presented in this chapter.

4.4.2 Leading Edge Hot Switching versus Trailing Edge Hot Switching

To compare leading edge hot switching with trailing edge hot switching, two sets of tests were performed to explore the progression of contact damage with cycling: one set with the contact bump as the anode, and another set with the contact bump as the cathode. Each set of six tests is comprised of three leading edge hot switching tests terminated after 10^4, 10^5, and 10^6 cycles, respectively, and three trailing edge hot switching tests terminated at the same intervals. Figure 4.4 shows a set of six tests in which the contact bump was the anode, and Figure 4.5 shows a set of six tests in which the contact bump was the cathode. All of the tests were cycled at 500 Hz with a 50 Ω series resistor, 3.54 V_{Hot}, and I_{Cold} = 77.5 mA.

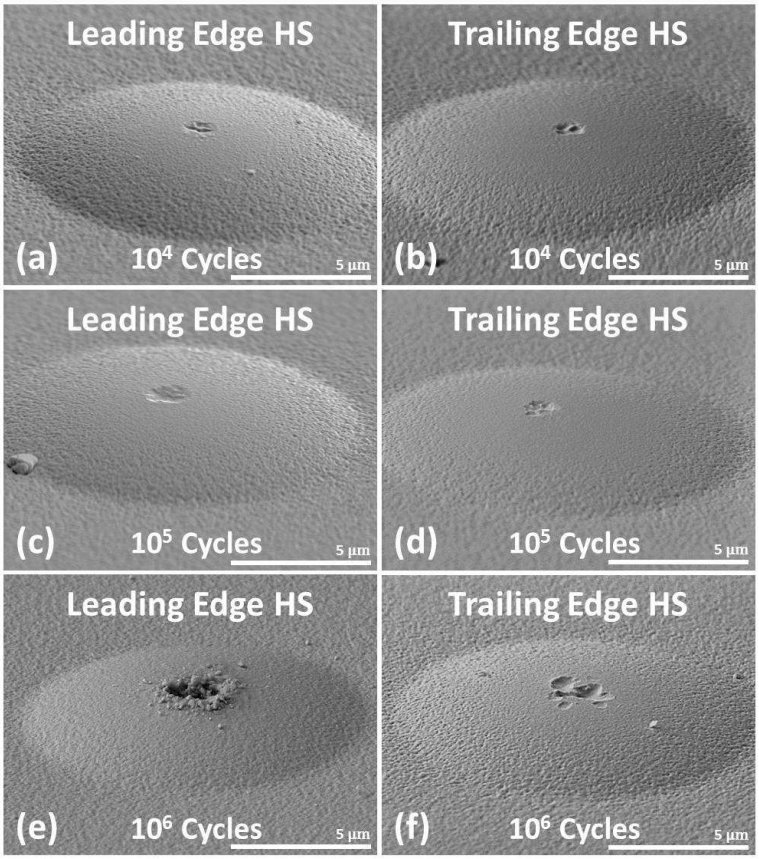

Figure 4.4 Leading edge vs trailing edge hot switching progression tests cycled at 500 Hz, 3.54V_{Hot}, and 77.5mA_{Cold} with contact bump as anode.

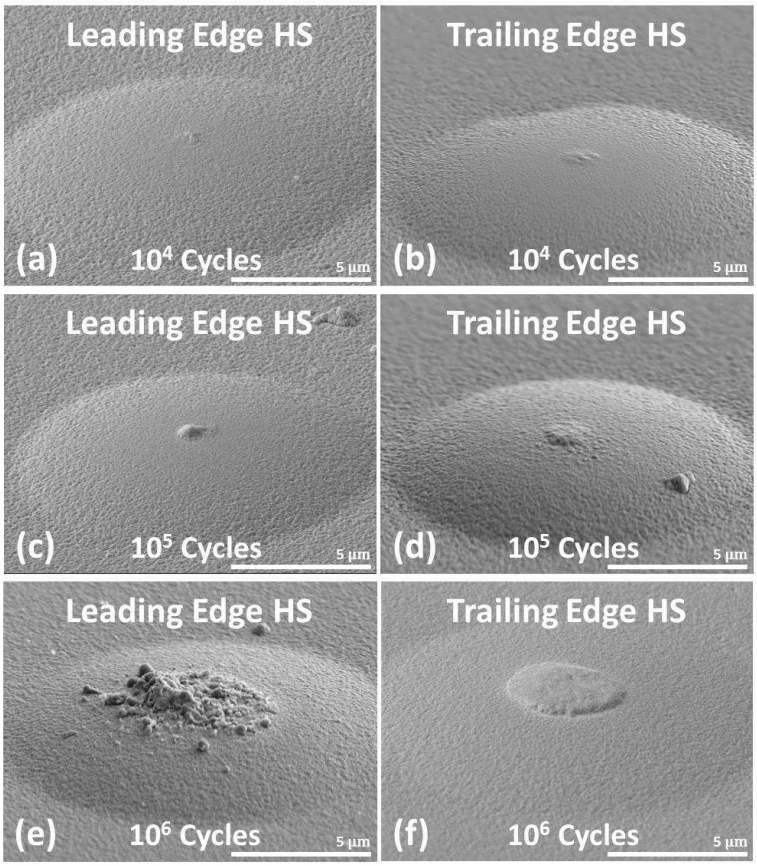

Figure 4.5 Leading edge vs trailing edge hot switching progression tests cycled at 500 Hz, 3.54V_{Hot}, and 77.5mA_{Cold} with contact bump as cathode.

Qualitatively, both leading and trailing edge hot switching tests follow the same trends: the damage area grows with cycling and material transfer is from anode to cathode. Figure 4.6 is a plot of the calculated volume transfer for each progression test length. Each point on the plot represents the average of the volume calculations from at least three separate tests. Quantitatively, this plot provides a few interesting results. First, the amount of volume transferred due to leading edge hot switching is roughly equal to that due to trailing edge hot switching. This result indicates that the material transfer mechanisms occurring on the leading and trailing edges result in about the same amount of material transfer. This interpretation assumes that the material transfer does indeed occur before closing and after opening – an assumption supported by Figure 4.3. Second, this plot also illustrates that the rate of material transfer decreases somewhat as the number of cycles increases, and averages about 500 nm^3 / cycle for the first 10^6 cycles for both leading and trailing edge hot switching. This result indicates that the material transfer mechanisms change only modestly as the contact surfaces are damaged and reshaped with cycling. And third, there is a significant amount of variation in the amount of material transferred from test to test for a given set of test conditions, as indicated by the error bars. This variation is to be expected given the complex nature of these micro-scale contacts, especially when hot switched. However, the trends shown by the

averages for each of the test conditions seem to indicate a fair degree of repeatability over an average of at least three tests.

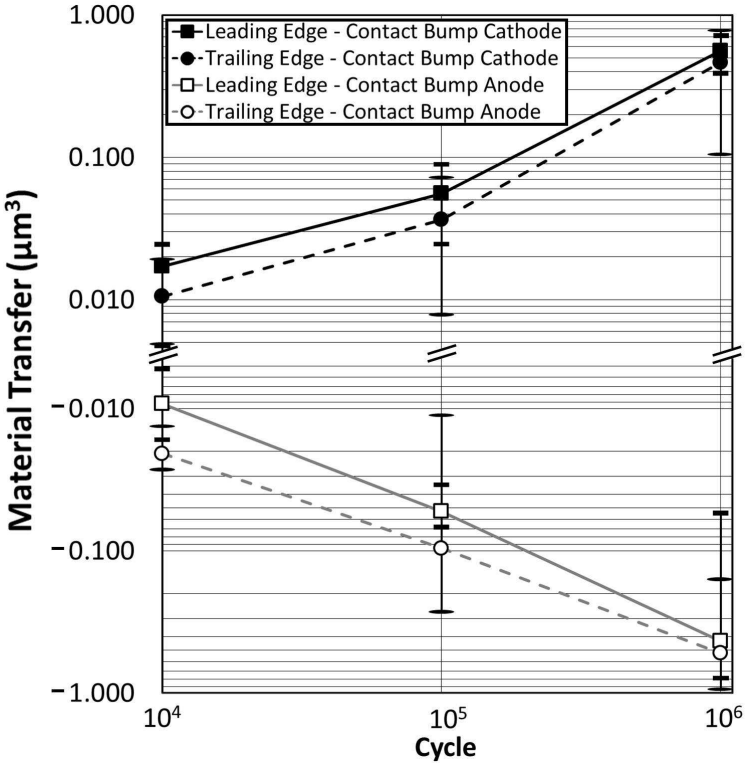

Figure 4.6 Volume analysis for leading edge vs trailing edge hot switching progression tests; each point represents the average of at least three separate tests. The error bars represent the maximum and minimum volume measurement for each condition. Error bars with long rounded caps correspond to trailing edge tests and error bars with square caps correspond to leading edge tests.

The behavior illustrated in Figure 4.4, Figure 4.5, and Figure 4.6 strongly suggest that the material transfer mechanisms on the leading edge are the same as the material transfer mechanisms on the trailing edge. However, it is noted that the damage mechanisms on the leading and trailing edges are not necessarily the same. Evidence of this can be found when comparing the qualitative damage of leading edge tests to trailing edge tests. Generally, trailing edge contact damage was smoother than leading edge contact damage. This is readily apparent when comparing Figure 4.4(e) to (f) and Figure 4.5(e) to (f).

It is noted that generally the pull-off force did not vary significantly over the course of a test. Significant increases in pull-off force were only observed in failing contacts at the end of their lifetimes, however only non-failed contacts were analyzed in this chapter.

4.4.3 Current and Potential Variation Tests

To further explore the role of cold switching current on contact damage and material transfer, a set of contacts were cycled at a low hot switching potential of 0.71 V_{Hot}. Figure 4.7(a) and (b) shows contacts cycled with a cold switching current of 15.5 mA_{Cold} using a 50 Ω series resistor

and (c) and (d) were cycled with a cold switching current of 77.5 mA_{Cold} using a 10 Ω series resistor. All these tests were done at 500 Hz for $5x10^5$ cycles. There are three clear trends illustrated by this group of tests. First, the direction of material transfer does not seem to be dependent on the electric field; these low hot switching potential test conditions do not illustrate the strict anode to cathode net material transfer direction demonstrated above. Rather, material seems to be transferred to the contact bump – independently of polarity – for all cases except for (a) in which the contact damage is extremely small. This behavior indicates that for low hot switching potential, material transfer directionality is not dictated by the direction of the electric field. The second trend illustrated in this group of tests is that the amount of damage at the low hot switching voltage is relatively small. Finally, there is a clear current dependence for damage in low-voltage hot switching; the 77.5 mA_{Cold} tests for both polarities resulted in more damage than the 15.5 mA_{Cold} tests.

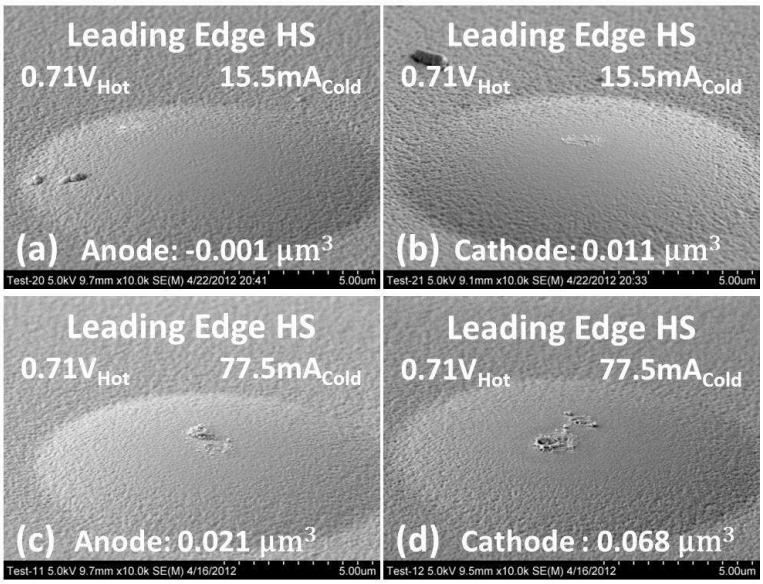

Figure 4.7 Contacts cycled at 500 Hz for $5x10^5$ cycles at 0.71V_{Hot} with varying I_{Cold} for both polarities.

To further explore the role of hot switching potential on contact damage and material transfer, a set of contacts were cycled at a high hot switching potential of 3.54 V_{Hot} while varying the cold switching current from 0.78 mA_{Cold} to 387 mA_{Cold} using series resistors of 5000 Ω, 50 Ω, and 10 Ω. Again, these contacts were cycled at 500 Hz for $5x10^5$ cycles. All of the contacts presented in Figure 4.8 show polarity dependence of material transfer from the anode to the cathode. Additionally, the contact bumps in Figure 4.8 show significantly more damage than the contact bumps in Figure 4.7, even with a very low cold switching current of 0.78 mA_{Cold}. Quantitatively, there does not seem to be a strong relationship between cold switching current and material transfer in these contacts for either polarity. This shows that the hot switching potential-controlled contact damage mechanisms are dominant at this hot switching voltage.

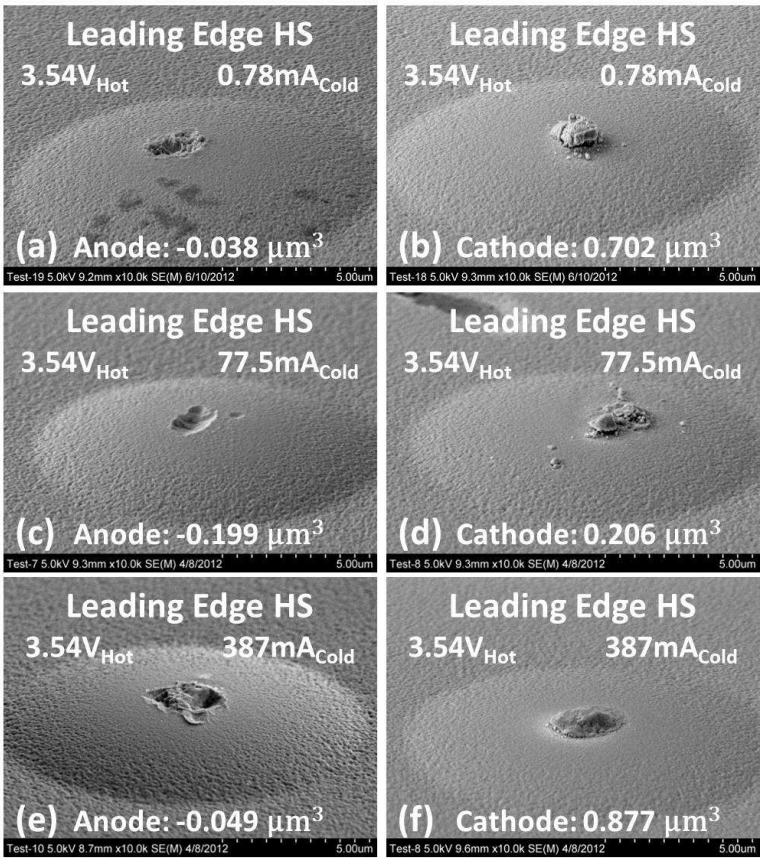

Figure 4.8 Contacts cycled at 500 Hz for $5x10^5$ cycles at $3.54V_{Hot}$ with varying I_{Cold} for both polarities.

The tests presented in Figure 4.3 - Figure 4.8 suggest the presence of multiple contact damage mechanisms. Though the damage mechanisms have both current and potential dependence, the high hot switching potential mechanisms seem to result in more contact damage and material transfer during hot switching than any of the other mechanisms.

4.4.4 Current Behavior Before Closing and After Opening

To monitor in detail the current behavior before closing and after opening of the contact, a 50 Ω external resistor was placed in series with the contact in addition to the built-in testing system 5 Ω series resistor, as shown in Figure 4.9(a). The voltage across this added resistor (V_{Ext}) was measured with an oscilloscope with an acquisition rate of (500 MS/s); current in the circuit was calculated using Ohm's law.

Several current monitoring tests were conducted at various applied voltages and frequencies for both leading edge and trailing edge hot switching. Figure 4.9(b) illustrates an example of typical current behavior observed before closing and after opening of a contact cycled at 500 Hz with 55 Ω total series resistance and hot switching potential 3.00 V_{Hot}. There are a several properties of note presented in this figure. First, the magnitude and anatomy of the spikes is remarkably similar. It is important to note that the plotted data came from two different cycles and that not all of the current spikes observed look identical to the those

presented; there was some variation in magnitude, duration, and periodicity observed. The similarities in the current spikes suggest that the same underlying mechanism is causing both. Second, the magnitude of the current spikes is about 45 mA at the peak. This equates to an effective resistance of 11.7 Ω at the peak of the spike. Finally, notice the current behavior upon opening of the contact. The relatively slow initial decline in current suggests that the contact resistance grows as the contact is pulled open. This behavior gives rise to another possible trailing edge damage mechanism. With increasing constriction resistance, comes increased joule heating. This additional heating coupled with the observed increased adhesion lends merit to the presence of a 'melt and pull' damage mechanism on the trailing edge. More experiments are currently being conducted to explore this potential damage mechanism.

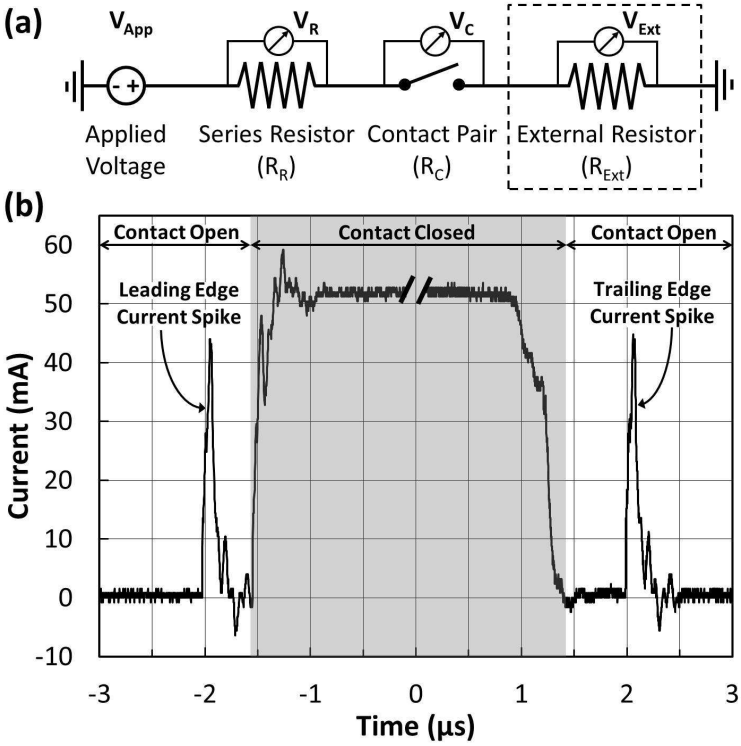

Figure 4.9 (a) Schematic of test circuit with external resister (b) Current spikes measured via the external resister before closing and after opening in a contact cycled at 500 Hz with 3.00V_{Hot} and 55 Ω of total series resistance.

For both leading and trailing edge hot switching tests, the current spike behavior was independent of cycling rate (1-500 Hz). At a hot switching voltage of 3.00 V_{Hot} roughly 20% of the cycles observed had at least one spike on the leading edge and roughly 20% of the cycles observed had at least one spike on the trailing edge. Some had as many as three either before closing or after opening. Furthermore, the fraction of cycles with current spikes decreased with hot switching voltage and became zero for hot switching voltages less than 1.50 V_{Hot}. As illustrated in Figure 4.7, asymmetric material transfer also did not occur for a hot switching voltage of 0.71 V_{Hot}. These observations support a connection between the asymmetric material transfer mechanism and the current spike behavior. These current spikes could be explained by either physical contact (such as the initiation of contact at the tops of a very small

number of asperities followed shortly by their destruction), or some sort of field effect (including but not limited to one of the phenomena discussed in the introduction). Although the time between switch opening and current spikes on the trailing edge – albeit irregular –is on the order of the inverse of the natural frequency of the test specimen, contact bounce is unlikely to be the sole cause of these current spikes due to their irregularity (~20% of the cycles observed), and dependence on applied voltage. Furthermore, on the leading edge, the time between individual current spikes as well as the time between the last current spike and switch closure was approximately inversely proportional to the closing velocity. More experiments are currently being conducted to explore this current spike behavior and its relationship to material transfer.

4.5 Conclusions

Using a custom built contact testing system, DC micro contact damage was explored in ruthenium-on-ruthenium contacts operated at a contact force of approximately 400 μN. Contact damage in all cases was evaluated qualitatively using SEM micrographs and quantitatively using AFM-based volume analysis. For the first time, contact damage on making and breaking contact under bias (leading and trailing edge hot switching) is compared. The amount of contact damage seen for the leading and trailing edge cases is very similar and this is true for the low-voltage tests (0.71V) as well as for the high-voltage tests (3.5V). However, qualitatively, leading edge hot switching looks different than trailing edge hot switching, so the results for the two types of switching are not identical. On the other hand, the amount and type of damage to the contacts is very different for the high and low-voltage cases. The high-voltage tests (3.5V) lead to polarity-dependent material transfer, with material moving in the direction of the electric field. The amount of material transfer does not depend strongly on the current limit from 0.78 to 380 mA. The low voltage (0.71V) tests result in much less damage, and the material transfer does not have a clear directionality. However, the amount of damage does increase significantly as the current limit is increased from 16 to 78 mA for the low-voltage tests.

Also observed for the first time is a new type of high-current, short duration current spike associated with hot switching events at voltages above 1.5V. The fact that these spikes occur at the higher voltage but not at the lower voltage suggests (but does not prove) that they are associated with the polarity dependent material transfer.

This work does not definitively exclude or confirm any of the previously suggested mechanisms for material transfer (field emission, field evaporation, micro-pseudo-arc, ohmic heating/bridge formation), but it shows that there is more than one mechanism active. Specifically, a polarity-dependent mechanism is active at higher voltages and a polarity-independent mechanism at lower voltages. The most likely candidate for the low-voltage mechanism may be ohmic heating, which would be expected to cause more damage as more current flows. The high-voltage mechanism is not yet identified among the three possibilities. While the current spikes seem likely to represent some kind of pseudo-arc, the current-independence of the material transfer results argues for a different mechanism, perhaps field emission or field evaporation. Future work will be devoted to identifying the hot switching damage mechanisms by a combination testing and modeling.

4.6 Acknowledgments

This work was supported by the Defense Advanced Research Projects Agency (DARPA) N/MEMS S&T Fundamentals program under grant no. N66001-10-1-4006 issued by the Space and Naval Warfare Systems Center Pacific (SPAWAR) as well as the membership of the RF MEMS Center at UCSD.

4.7 Chapter 4 References

[1] Rebeiz G M 2003 *RF MEMS: Theory, design, and technology* (Hoboken, New Jersey: J. Wiley & Sons)
[2] Rebeiz G M and Muldavin J B 2001 RF MEMS switches and switch circuits *IEEE microwave magazine* **2** 59-71
[3] Ehwald K, Drews J, Scholz R, Korndorfer F, Knoll D, Tillack B, Barth R, Birkholz M, Schulz K and Sun Y 2009 BEOL embedded RF-MEMS switch for mm-wave applications. *IEDM: IEEE International Electron Devices Meeting* pp 1-4
[4] Brown E R 1998 RF-MEMS switches for reconfigurable integrated circuits *IEEE Transactions on Microwave Theory and Techniques* **46** 1868-80
[5] Park S J, Reines I and Rebeiz G 2009 High-Q RF-MEMS tunable evanescent-mode cavity filter. *IEEE International Microwave Symposium Digest* pp 1145-8
[6] Ho K M J and Rebeiz G M 2012 Microstrip antennas with full polarization diversity using packaged RF MEMS switches. *APSURSI: IEEE Antennas and Propagation Society International Symposium* pp 1-2
[7] Lee K Y and Rebeiz G M 2009 A miniature 8–16 GHz packaged tunable frequency and bandwidth RF MEMS filter. *IEEE International Symposium on Radio-Frequency Integration Technology* pp 249-52
[8] Chan K Y, Daneshmand M, Mansour R R and Ramer R 2009 Scalable RF MEMS switch matrices: Methodology and design *IEEE Transactions on Microwave Theory and Techniques* **57** 1612-21
[9] Newman H S, Ebel J L, Judy D and Maciel J 2008 Lifetime measurements on a high-reliability RF-MEMS contact switch *IEEE Microwave and Wireless Components Letters* **18** 100-2
[10] Patel C D and Rebeiz G M 2011 RF MEMS Metal-Contact Switches With mN-Contact and Restoring Forces and Low Process Sensitivity *IEEE Transactions on Microwave Theory and Techniques* **59** 1230-7
[11] Uno Y, Narise K, Masuda T, Inoue K, Adachi Y, Hosoya K, Seki T and Sato F 2009 Development of SPDT-structured RF MEMS switch. *IEEE Solid-State Sensors, Actuators and Microsystems Conference* pp 541-4
[12] Mercier D, Charvet P L, Berruyer P, Zanchi C, Lapierre L, Vendier O, Cazaux J L and Blondy P 2004 A DC to 100 GHz high performance ohmic shunt switch. *IEEE International Microwave Symposium Digest* pp 1931-4
[13] Chen L, Lee H, Guo Z, McGruer N E, Gilbert K, Mall S, Leedy K and Adams G 2007 Contact resistance study of noble metals and alloy films using a scanning probe microscope test station *Journal of Applied Physics* **102** 074910--7

[14] Broue A, Dhennin J, Charvet P, Pons P, Jemaa N B, Heeb P, Coccetti F and Plana R 2010 Multi-Physical Characterization of Micro-Contact Materials for MEMS Switches. *IEEE Holm Conference on Electrical Contacts* pp 1-10
[15] Ke F, Miao J and Oberhammer J 2008 A ruthenium-based multimetal-contact RF MEMS switch with a corrugated diaphragm *Journal of Microelectromechanical Systems* **17** 1447-59
[16] Czaplewski D A, Nordquist C D, Dyck C W, Patrizi G A, Kraus G M and Cowan W D 2012 Lifetime limitations of ohmic, contacting RF MEMS switches with Au, Pt and Ir contact materials due to accumulation of 'friction polymer'on the contacts *Journal of Micromechanics and Microengineering* **22** 105005
[17] Patton S and Zabinski J 2005 Fundamental studies of Au contacts in MEMS RF switches *Tribology Letters* **18** 215-30
[18] Majumder S, Lampen J, Morrison R and Maciel J 2003 A packaged, high-lifetime ohmic MEMS RF switch. *IEEE International Microwave Symposium Digest* pp 1935-8
[19] Yang Z, Lichtenwalner D J, Morris A S, Krim J and Kingon A I 2009 Comparison of Au and Au–Ni Alloys as Contact Materials for MEMS Switches *Journal of Microelectromechanical Systems,* **18** 287-95
[20] Coutu Jr R A, Kladitis P E, Leedy K D and Crane R L 2004 Selecting metal alloy electric contact materials for MEMS switches *Journal of Micromechanics and Microengineering* **14** 1157
[21] Kwon H, Choi D J, Park J H, Lee H C, Park Y H, Kim Y D, Nam H J, Joo Y C and Bu J U 2007 Contact materials and reliability for high power RF-MEMS switches. *IEEE International Conference on Micro Electro Mechanical Systems* pp 231-4
[22] Becher D, Chan R, Hattendorf M and Feng M 2002Reliability study of low-voltage RF MEMS switches. *GaAs MANTECH Conference* pp 54-7
[23] Yang Z, Lichtenwalner D, Morris A, Krim J and Kingon A 2010 Contact degradation in hot/cold operation of direct contact micro-switches *Journal of Micromechanics and Microengineering* **20** 105028
[24] Müller E W 1941 Abreißen adsorbierter Ionen durch hohe elektrische Feldstärken *Naturwissenschaften* **29** 533-4
[25] Zurlev D N and Forbes R G 2003 Field ion emission: the effect of electrostatic field energy on the prediction of evaporation field and charge state *Journal of Physics D: Applied Physics* **36** L74
[26] Miskovsky N, Wei C M and Tsong T T 1992 Field evaporation of silicon in the field ion microscope and scanning tunneling microscope configurations *Physical review letters* **69** 2427-30
[27] Strong F W, Skinner J L and Tien N C 2008 Electrical discharge across micrometer-scale gaps for planar MEMS structures in air at atmospheric pressure *Journal of Micromechanics and Microengineering* **18** 075025
[28] Kruglick E J J and Pister K S J 1999 Lateral MEMS microcontact considerations *Journal of Microelectromechanical Systems* **8** 264-71
[29] Slade P G 1999 *Electrical contacts: principles and applications* (New York, New York: Marcel Dekkar)

[30] Dickrell D and Dugger M T 2007 Electrical contact resistance degradation of a hot-switched simulated metal MEMS contact *Components and Packaging Technologies, IEEE Transactions on* **30** 75-80
[31] Poulain C, Peschot A, Vincent M and Bonifaci N 2011 A Nano-Scale Investigation of Material Transfer Phenomena at Make in a MEMS Switch. *IEEE Holm Conference on Electrical Contacts* pp 1-7
[32] Chen L, Guo Z, Joshi N, Eid H, Adams G and McGruer N 2012 An improved SPM-based contact tester for the study of microcontacts *Journal of Micromechanics and Microengineering* **22** 045017
[33] Morrison Jr R H, McGruer N E and Hopwood J A 2007 Method of preparing electrical contacts used in switches. (Patent)
[34] Iwasaki Y, Izumi A, Tsurumaki H, Namiki A, Oizumi H and Nishiyama I 2007 Oxidation and reduction of thin Ru films by gas plasma *Applied surface science* **253** 8699-704
[35] Lee J, Min S and Choh S H 1994 Deposition and properties of reactively sputtered ruthenium dioxide thin films as an electrode for ferroelectric capacitors *Japanese journal of applied physics* **33** 7080-5
[36] Walker M, Nordquist C, Czaplewski D, Patrizi G, McGruer N and Krim J 2010 Impact of in situ oxygen plasma cleaning on the resistance of Ru and Au-Ru based rf microelectromechanical system contacts in vacuum *Journal of Applied Physics* **107** 084509--7
[37] Derjaguin B, Muller V and Toporov Y P 1975 Effect of contact deformations on the adhesion of particles *Journal of colloid and interface science* **53** 314-26
[38] Du Y, Chen L, McGruer N E, Adams G G and Etsion I 2007 A finite element model of loading and unloading of an asperity contact with adhesion and plasticity *Journal of colloid and interface science* **312** 522-8

Chapter 5

Hot-Switching Damage Mechanisms in MEMS Switch Contacts

This chapter is a compilation of the experimental results and modeling that has been done since last publication

5.1 Introduction

In Chapter 4 [1], a custom built micro contact testing system was used to explore the damage caused by making and breaking contact under bias (leading and trailing edge hot switching, respectively) in ruthenium-on-ruthenium contacts. Evidence of both voltage dependent and current dependent contact damage mechanisms was found. For 3.5 V_{Hot}, polarity dependent material transfer damage (net material transfer from anode to cathode) was present for both leading and trailing edge tests, and it was the dominant damage mode for these tests. For 0.71 V_{Hot}, much less contact damage was observed on the leading edge. However, a much stronger dependence on current was observed for these tests.

The main purpose of that work was to explore and document the damage done by hot switching. More specifically, that work set out to document the hot switching damage on the leading and trailing edges qualitatively and quantitatively. The aim of the work presented in this chapter is to explore and differentiate between the possible mechanisms causing hot switching damage observed on the leading and trailing edges. This work presents and defines several possible hot switching damage mechanisms in detail.

Modeling is combined with unique and explicitly designed experiments to deepen and enrich the understanding of the nature of hot switching contact damage. The models presented in this chapter are mostly based on micro and continuum scale physics. It is noted that the physics governing the actual hot switching damage mechanisms is not necessarily the same at the scales that they operate. The modeling presented is not meant to describe the exact behavior, but rather estimate and approximate.

This work shows that hot switching damage mechanisms can occur in extremely small length scales (possibly extending to the atomic regime), and in very short time scales (possibly on the order of nanoseconds). Indeed, the concept of the contact being open or closed grows exceedingly less distinct at these length scales. Additionally, the highly coupled nature in the thermal, electrical, and mechanical domains must be considered. Thus, the task of definitively determining the exact hot switching damage mechanisms at work is a very difficult problem to solve. At such scales, individual molecules and electrons interact with each other. Because of these discrete interactions, the physics that governs continuum models does not necessarily apply to such small scale behavior.

5.2 Thermo-Mechanical Hot Switching Damage Mechanisms

Thermo-mechanical hot switching damage mechanisms can occur on both the leading and trailing edges. Some of the thermo-mechanical mechanisms are polarity dependent and some are not. Discussed below are the most plausible thermo-mechanical mechanisms.

5.2.1 Leading Edge Thermo-Mechanical Damage Mechanisms

On the leading edge, melting or even vaporizing of the initially contacting asperities is possible during leading edge hot switching. The moment the electrodes make contact, as illustrated in Figure 5.1, a large amount of current will be forced through a small contact area of the initial contact asperities resulting in excessive heating. Slade provides an equation to estimate the

maximum temperature in the contact spot based on the Wiedemann-Franz law (assuming that it holds over for the given contact material over the temperature range evaluated)

$$V_c^2 = 4L(T_m^2 - T_b^2) \tag{5.1}$$

where V_c is the voltage drop over the contact, L is the Lorenz constant (2.45×10^{-8} V^2/K^2), T_m is the maximum temperature in the contact spot, and T_b is the bulk temperature far away from the contact spot. If the full 3.5 V_{Hot} is assumed to be applied over the extremely small initial contacting areas, this relationship yields a maximum contact temperature of ~11×10^3 K. It should be noted that the Wiedemann-Franz law does not apply at such high temperatures because the Lorenz number L will vary significantly at such temperature ranges. Furthermore, Equation (5.1) does not take into account heating resulting from the additional Sharvin resistance through contact spots smaller than the mean free path of electrons in ruthenium. Rather, this is an order of magnitude calculation to show that the change in temperature of the initial contacting asperities could be heated to melting or even super-heated to vaporization or annihilation.

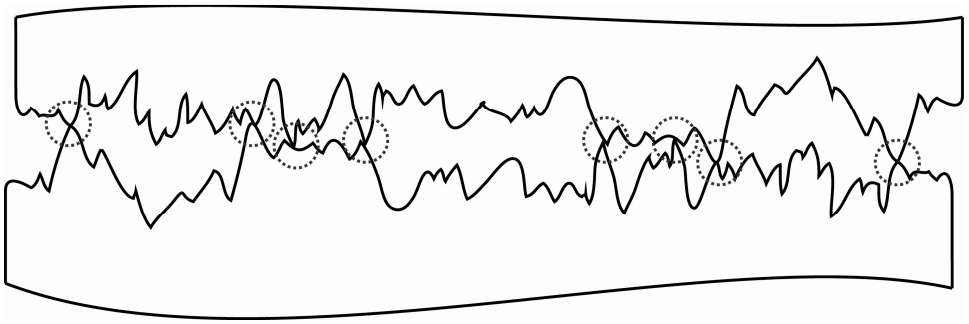

Figure 5.1 Schematic of two rough surfaces coming together where contact is initially made at the peaks of the highest asperities as highlighted by the grey dashed circles.

If there is enough heating in the contact (in essence, the high temperatures extend a significant distance into the electrodes with respect to the contact radius), then there will be a slight geometrical bias of material transfer toward the pillar, the body that is the more efficient heat sink. However, if there is not sufficient heating to cause significant temperature increases into both the electrodes, melting will stay localized to the individual asperities and the small regions around them. Melting of just the initially contacting asperities might not be directional because at the asperity scale, the geometrical bias of material transfer would be in the direction of the larger asperity; statistically, this material transfer would equal out over a significant number of cycles.

5.2.2 Trailing Edge Thermo-Mechanical Damage Mechanisms

Bridge, or fine, transfer is the formation of molten metal bridges between the electrodes of the contact due to high current during the last phase of physical contact upon opening [1], as shown in Figure 5.2. Note that the name 'bridge' transfer can be somewhat misleading. Here, the bridge of molten metal between electrodes does not necessarily denote a long drawn out structure of metal with a low thickness to length ratio. In fact, Holm defines bridges into two

categories: long bridges (low thickness to length ratio) and short bridges (high thickness to length ratio). A long bridge attains a kind of equilibrium whereby its shape is dominated by surface tension. A short bridge does not attain an equilibrium shape.

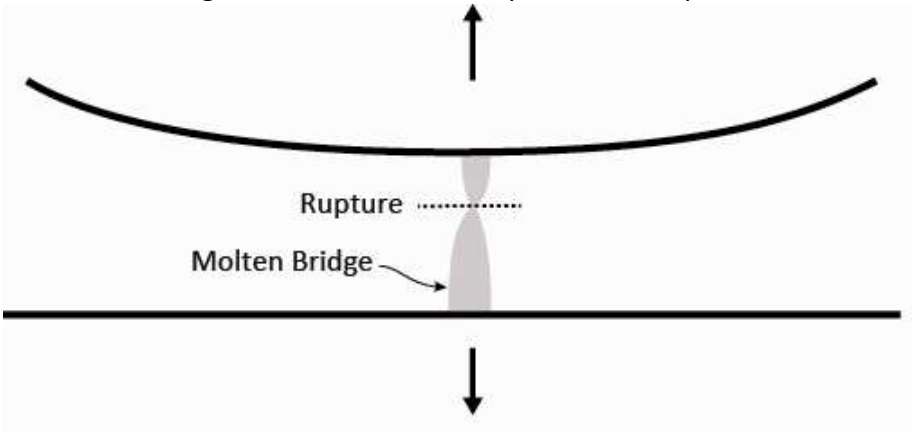

Figure 5.2 Schematic of molten bridge formation.

The progression of bridge forming starts as the electrodes are coming apart under bias (trailing edge hot switching). As the contact force goes down, the contact resistance goes up. As the contact resistance goes up, so too does the voltage drop across the electrodes of the contact. From Equation (5.1), it is easy to see that as contact voltage goes up, temperature goes up. If the contact voltage is sufficient, at some stage the maximum temperature in the contact spot will equal the melting temperature of the contact material. The separation of the electrodes draws out the molten volume, constituting a bridge.

The hottest section of the bridge is where it will rupture. Rupture in long bridges can be caused by boiling, but because the shape of the bridge is defined by surface tension, the combination of temperature and mechanical pulling is also a viable rupture mode. Rupture in short bridges has been observed to occur at a range of contact voltages between melting and boiling. Table 5.1 contains the approximate melting and boiling voltages for ruthenium using Equation (4.1) and temperature values provided by Slade [13]. For reference, the corresponding contact resistances for a 50 Ω, 3.5 V_{Hot} test are also included; these are the approximate contact resistance values that the testing system would read.

Table 5.1 Melting and boiling contact voltages and resistances based on a room temperature of 300 K.

	Temperature (K)	V_C (V)	R_C (Ω)
Melting Temperature	2624	0.82	15.3
Boiling Temperature	5174	1.62	43.1

If the system were completely symmetrical in all three domains, the location of the maximum temperature (and thus rupture) in the bridge (long or short) would be directly in the middle of the two electrodes resulting in zero net material transfer. However, the location of the hottest section of the bridge can be offset from the middle, thus leading to a net material transfer in one direction. There are three effects that could offset the rupture position of the bridge.

The thermal geometry effect will bias material transfer away from the hotter body. If two identical uniformly heated bodies of the same material are brought into contact and the temperature sufficiently far away from the interface is forced to be relatively low, the resulting steady state temperature field will be symmetrical about the interface (contact spot) of the two bodies, with the highest temperature at the interface [2]. However, if the contacting bodies are of different geometry, the body with more mass near the interface will be a better heat sink, assuming the bodies are made of the same material [5]. In this case, the highest temperature would be shifted into the body with less mass near the interface. In [6], a thermal-electrical-mechanical coupled field contact comprised of a hemisphere and a half space clearly showed a maximum temperature shift into the hemisphere side of the contact. Assuming sufficient heating in the contact, this thermal geometry factor could plausibly manifest itself in the form of a unidirectional material transfer away from the contact bump (the body with less mass in the vicinity of the contact spot). It stands to reason that the separation rate could have an effect on the thermal geometry effect. The thermal diffusivity will ultimately determine how quickly the fully developed temperature profile develops. If the separation rate is short compared to the thermal settling time, there should not be much of a bias.

The Thomson effect works as if positive current carriers coming from warmer sections of a conductor give off heat to the cooler sections; the charge carriers act as having heat capacity. The Thomson effect is defined in terms of a coefficient (aptly name the Thomson coefficient) that is either positive (heat is transferred to the cathode), or negative (heat is transferred to the anode). Some metals can have a variable coefficient dependent on temperature. Platinum for example has a negative Thomson coefficient in the solid state (anode hotter) and a positive Thomson coefficient in the liquid state (cathode hotter). It is unclear exactly what, if any, influence the Thomson effect will have on the tests presented here. After an extensive literature search, the Thomson coefficient for ruthenium could not be found. For example, the Thomson coefficient for platinum, gold, and silver at 400 K is -10, 1, and 5, respectively. Therefore, the Thomson effect cannot not be conscionably ruled out and must be considered as a possible material transfer damage mechanism.

The Kohler effect is a process the leads to material transfer toward the cathode in repeated cycling (opening and closing) of the contact. During the opening phase of the contact cycle, an oxygen mono-film deposits and chemisorbs on the electrodes. During the subsequent opening of the contact, the current density becomes high in the last contacting area or bridge and the chemisorbed oxygen leads to heating of the anode, leading to a biased rupture toward the anode, and a net material transfer to the cathode. This effect, however, should negligible, if at all present, for the experiment presented here because all tests are done under a constant flow of nitrogen over the contact region.

5.3 Field Effect Hot Switching Damage Mechanisms

Field effect hot switching damage mechanisms are so-named because they are driven by electric field or electric potential between the electrodes of the contact. As such, these mechanisms are all polarity dependent, resulting in material transfer damage with directionality based on the electric field direction.

5.3.1 Arcing and Vapor Arcing

An electric arc occurs when an electrical breakdown results in electrical current flow through the medium that separates the electrodes of a contact. This can only happen when the medium becomes locally conductive. During approach (leading edge hot switching), the medium separating the electrodes is gas, assuming that initial contact has not already been made. In this case, the breakdown process, known as Townsend (or avalanche) discharge, is generally started by thermal emission or cold tunneling of a small number of electrons from the cathode due to a strong local electric field. These released electrons will cause an avalanche-type of ionization of the medium separating the electrodes, but only if they have enough energy to do so. At a <2 µm gap at room temperature and atmospheric pressure, the breakdown voltage for nitrogen is measured to be greater than 100 V [14]. The breakdown voltage of a nitrogen medium is likely to decrease with decreasing spacing. However, as the gap approaches the mean free path of nitrogen (~130 nm), arcing becomes increasingly less likely because there are fewer molecules to ionize in the space between the electrodes, and thus conduct current. Therefore it seems unlikely that arcing will occur between the electrodes of the test setup presented in this work.

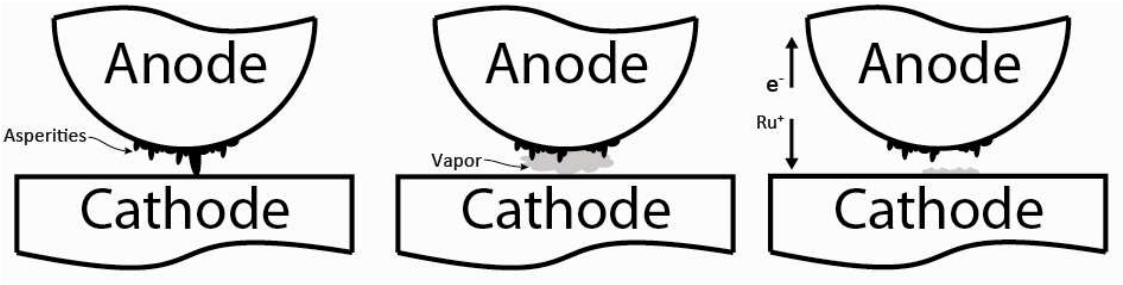

Figure 5.3 Vapor arcing causes a net material transfer from the anode to the cathode.

Alternatively, vapor arc breakdown occurs when a metallic vapor between the electrodes is ionized by the combination of the strong local electric field and thermal emission of electrons from the cathode, as depicted in Figure 5.3. Once the vapor is ionized and becomes conductive, the free electrons flow toward the anode and the metallic ions flow toward the cathode, leading in a net material transfer from the anode to the cathode. Thermo-mechanical damage hot switching damage mechanisms (as described above) were shown to potentially result in metal vapor on both the leading and trailing edges. On the leading edge, if the initial contact asperities are vaporized there will be metal vapor and an abundance of thermal energy. Three byproducts of boiling bridge rupture on the trailing edge are metal vapor, potentially sharp asperities on both sides of the contact, and an abundance of thermal energy at the surfaces and between the electrodes. These conditions are also favorable for vapor arcing.

5.3.2 Field Evaporation Material Transfer

Field evaporation is the removal of a surface molecule, as an ion, by a very strong local electric field [8], as illustrated in Figure 5.4. The theoretical local electric field necessary to induce field evaporation for ruthenium (in the form of Ru^{2+}) is estimated to be 42 V/nm [9].

Table 5.2 Select atomic properties of ruthenium.

Property	Value	Unit
Atomic Radius	0.130	nm
Covalent Radius	0.146	nm
Inter-Atomic Spacing (hcp)	0.280	nm

Table 5.2 presents some pertinent atomic properties of ruthenium. These values will be references in this section as well as in the discussion of other possible mechanisms.

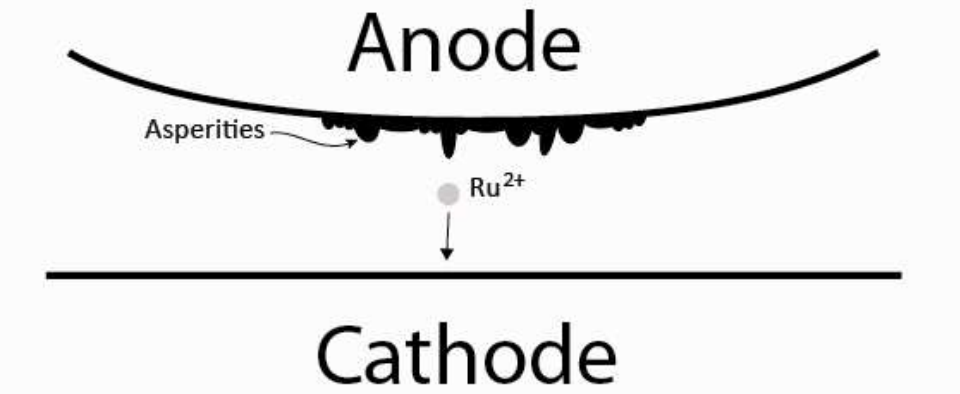

Figure 5.4 Schematic of field evaporation of a ruthenium ion as Ru^{2+}.

In the typical experimental range of hot switching voltages (1-10 V_{Hot}), it is impossible to achieve a local electric field capable of producing field evaporation if both electrodes are atomically smooth in the contact region. For example, the spacing to produce a sufficient electric field at 10 V is 0.24 nm, less than the inter-atomic spacing of ruthenium in its natural hexagonal close-packed (hcp) crystal structure (Table 5.2). However, real contact electrode surfaces have asperities. If these peaks on both electrodes are assumed to be locally spherical, the local electric field can be estimated by the maximum electric field between two charged spheres of the same radius

$$E_{Max} = 0.9\frac{V}{x}\left(\frac{a + {}^{x}/_{2}}{a}\right) \tag{5.2}$$

or if the asperity is modeled as a sphere-flat interaction, the maximum electric field is

$$E_{Max} = 0.9\frac{V}{x}\left(\frac{a + x}{a}\right) \tag{5.3}$$

where V is the potential between the electrodes, x is the separation between the spheres surfaces, and a is the radius of the spheres [11]. In a real contact, the interaction probably lies somewhere between these two models. The radius required to induce a local electric field equal to 42 V/nm are plotted in Figure 5.5.

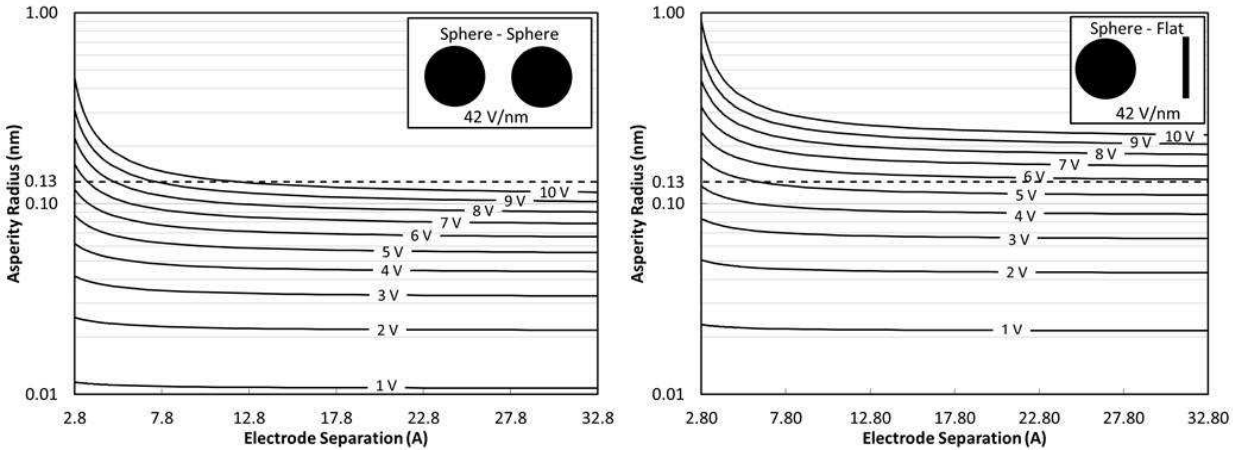

Figure 5.5 Asperity radius required to produce a 42 V/nm local electric field for two different configurations.

In these plots, the atomic radius of ruthenium (~0.130 nm) is represented as a dashed line. Because the atomic radius is the absolute minimum radius of curvature that an asperity can have, any point below this demarcation is a physical impossibility. Additionally, electrode separations of less than the inter-atomic spacing (~0.280 nm) were not considered. These plots suggest that the local electric field required for field evaporation is impossible for applied voltages below 4 V_{Hot}, regardless of which interaction model is used. This suggests that field evaporation cannot possibly be responsible for the material transfer observed experimentally at 3.5 V_{Hot}. In the more conservative model (sphere-sphere) suggests that field evaporation is only possible for electrode spacing of less than 10 angstrom, even for the highest applied voltages. The less conservative model (sphere flat) suggests that field evaporation is only possible for applied voltages greater than 6 V_{Hot}.

However, [10] presents theory to suggest that the electric field necessary for field evaporation can decrease significantly (up to 30% for some metals) for separations less than 20 angstrom. The reasoning is that the surface atoms begin to interact effectively lowering the potential barrier that a given atom must activate over. If this behavior is applied to ruthenium, the electric field necessary to cause field evaporation would be 29.4 V/nm. The adjusted values are plotted in Figure 5.6.

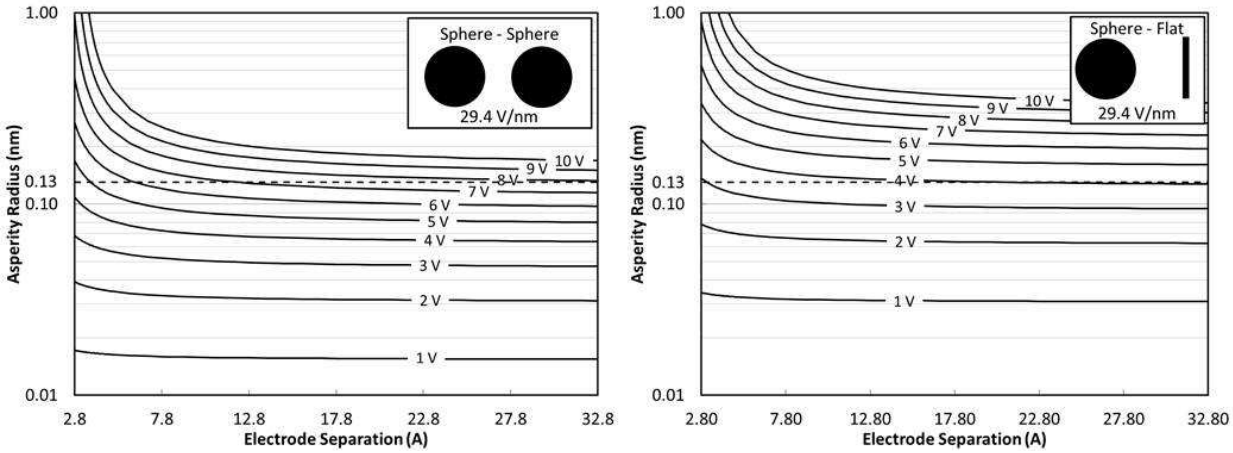

Figure 5.6 Asperity radius required to produce a 29.4 V/nm local electric field for two different configurations.

These plots illustrate that with a 30% reduced critical local electric field, even the less conservative model predicts that field evaporation is only possible at 3.5 V_{Hot} for electrode separations less than 0.6 nm, or about two times the inter-atomic spacing. At these separations, the direct interaction between atoms is more dominant than electric field, and as such, the concept of field evaporation is somewhat obscured [10]. Therefore, if field evaporation is responsible for the material transfer observed at 3.5 V_{Hot} it is most-likely occurring at extremely small separations.

If field evaporation were assumed to be the cause of the material transfer observed, the amplitude of the current associated with transferring 500 nm^3 of ruthenium would be inversely proportional to the duration of the transfer. This relationship is plotted in Figure 5.7. This simple calculation is based on the field evaporation of Ru^{2+} ions with spherical atomic volume based on the covalent bond radius. Note that the constant of proportionality is equal to the total charge transferred, approximated as 1.23×10^{-14} C.

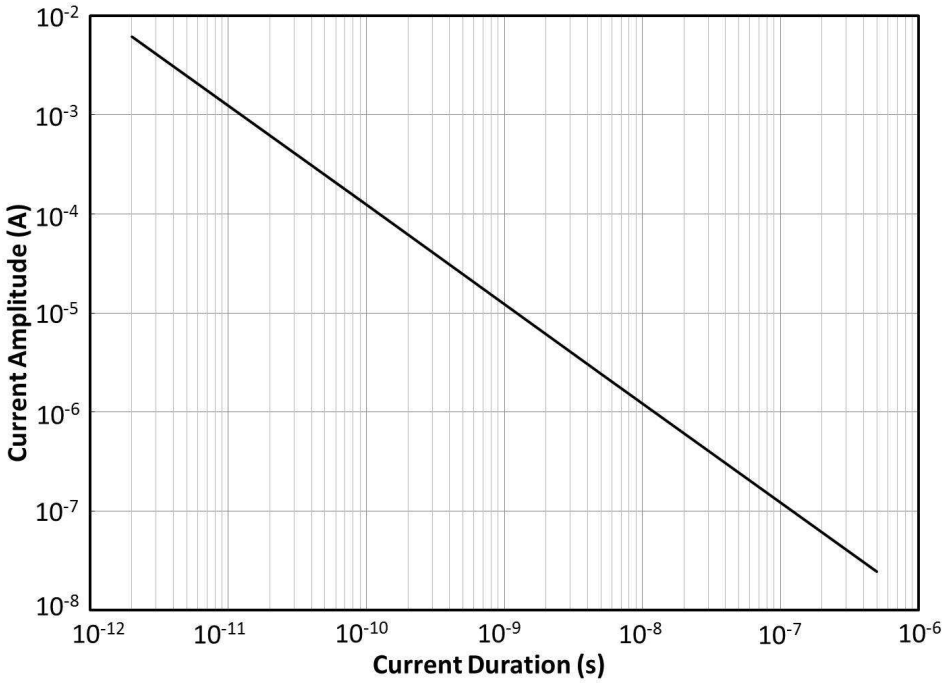

Figure 5.7 Approximated amplitude and duration of field evaporation of 500 nm^3 of ruthenium.

This relationship can be used as an approximation of the type of current behavior to look for during testing. For example, if the maximum duration of current activity is expected to be 100 ns (discussed in the pull-off behavior section below), current activity of less than 0.1 μA should be expected if field evaporation is responsible for the material transferred. Note that an upper limit to field evaporation current can also be made using Child's equation (discussed below).

5.3.3 Emission Induced Material Transfer

In emission induced material transfer, the electric field induces electron emission from the cathode to the anode resulting in enough energy transfer to cause melting or evaporation of anode surface material.

- ***Melt & Stamp*** In the case of melting, the instant that contact is initiated, the molten volume is cooled by the cooler body (the cathode). Assuming temperature dependent material properties, the thermal conduction away from the molten volume will be greater in the direction of the cooler body leading to a bias in the temperature gradient in the now contacting bodies. The result is a directional net material transfer from the anode to the cathode. However, this mechanism can only occur on the leading edge. This mechanism is illustrated in Figure 5.8(a).
- ***Evaporate & Condense*** In the case that enough energy is supplied to cause evaporation, the evaporated anode surface material condenses on the cooler cathode resulting in a net material transfer from the anode to the cathode. This mechanism can occur on both the leading and trailing edges. This mechanism is illustrated in Figure 5.8(b).

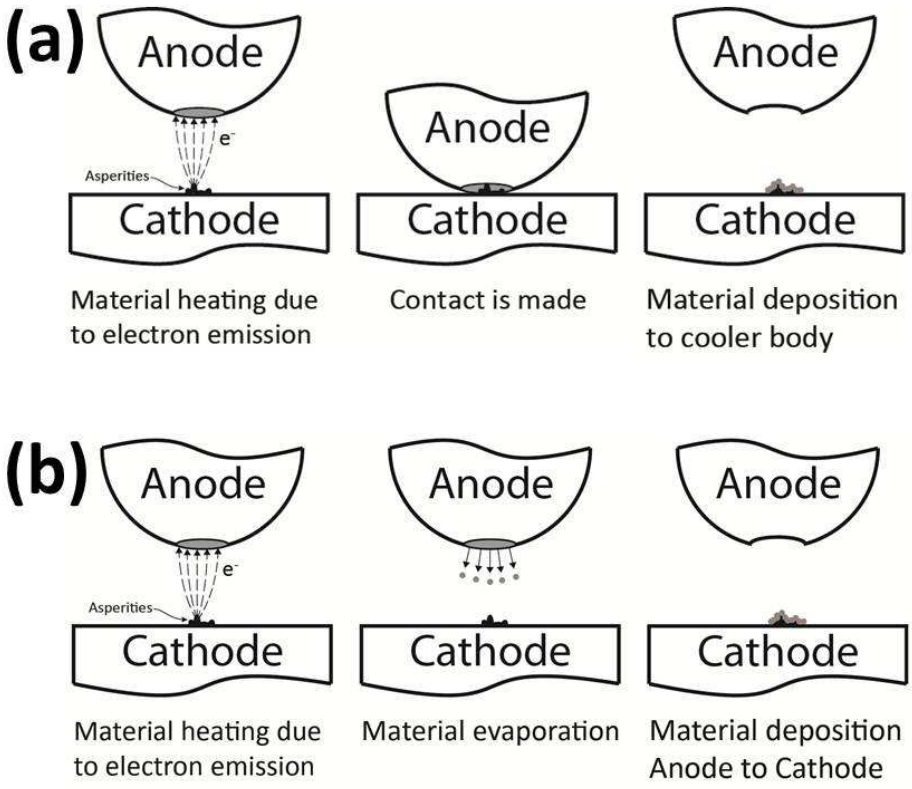

Figure 5.8 Schematic of emission induced material transfer for (a) Melt & Stamp and (b) Evaporate and Condense.

Electron emission from the cathode could plausibly result from two distinct effects: electron tunneling into the vacuum energy state (Fowler-Nordhiem tunneling or field emission) or electron tunneling from the conduction band of the cathode to conduction band of the anode (direct tunneling). Fowler-Nordhiem tunneling can only occur when the energy difference of the electrons on the respective electrode surfaces is greater than the work function of the surface material. In this case, the work function of ruthenium is ~4.7 eV [13]. Therefore, for the electrons on the cathode to surmount the work function energy barrier and tunnel into the vacuum between the electrodes, the applied potential must be greater than 4.7 V. Note that if this condition is satisfied, electron emission can occur at relatively large separations. Direct tunneling occurs at potentials lower than the work function at relatively smaller separations [12]. Figure 5.9 contains band diagrams for both types of tunneling, where E is potential (eV), x is a length scale, and E_f is the Fermi energy level of electrons in a given electrode.

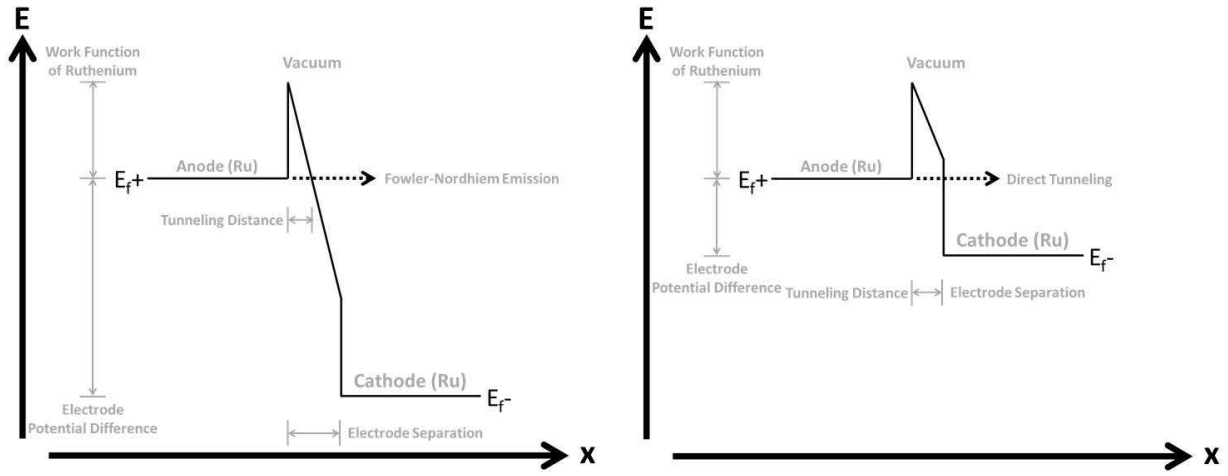

Figure 5.9 Band diagrams for Fowler-Nordhiem emission and direct tunneling.

To better understand the plausibility of this mechanism, it is necessary to determine the amount of energy required to vaporize ruthenium. In Chapter 4 [1] it was determined that roughly 500 nm^3 of material was transferred per cycle. The energy required to bring ruthenium from room temperature to vapor is approximately 8.4 MJ/kg (based on enthalpy) [3][13]. Assuming an initial (room temperature) density of 12450 kg/m^3 [3], the mass of 500 nm^3 of ruthenium is 6.225×10^{-21} kg. Using these values, 52.3 fJ is required to vaporize 500 nm^3 of ruthenium. This same exercise can also be conducted for just melting: 6.46 fJ is required to bring 500 nm^3 of ruthenium from room temperature to melting. Note that it takes about ten times more energy to vaporize ruthenium as it does to melt it. These calculations do not account for any source of inefficiency in energy transfer or any energy lost to the surrounding environment – both would be present in any real system. Thus, these numbers are lower limits of energy required to melt and vaporize 500 nm^3 of ruthenium.

The issue of energy lost to the surroundings of the system can be addressed, to a certain degree, by including the effects of heat conduction away from the heat source. Assuming that the impact area of the emission electrons is small compared to the thickness of the electrode, this system can be modeled by the classical heat conduction problem of a semi-infinite body heated by a circular heat source at its surface, represented schematically in Figure 5.10(a).

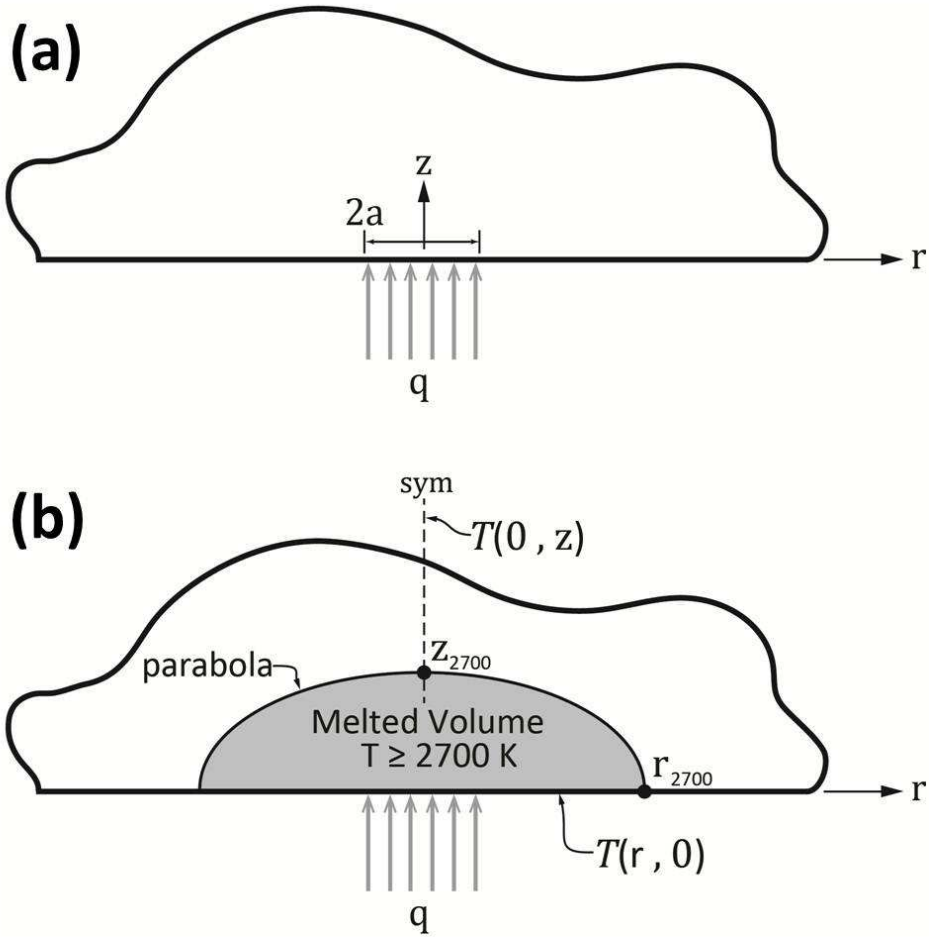

Figure 5.10 Schematic of a half space being heated by a circular heat source at its surface.

Here, q is a heat flux (W/m^2), a is the flux radius, and k is the thermal conductivity of the half space material. For ruthenium, the thermal conductivity k was taken to be 114 W/mK at room temperature and 79.6 W/mk at melting temperature (~2700 K) [16]. Using this model, it is possible to calculate the power required to melt a 500 nm^3 volume at the surface of a half-space by calculating the volume encompassed by the isotherm that corresponds to the melting temperature of the ruthenium. From this power, energy approximation can be estimated. Carslaw and Jeager [5] present the analytical solution to the steady state temperature profile

$$T(r,z) = \frac{qa}{k}\int_0^\infty e^{-\lambda z} J_0(\lambda r) J_1(\lambda a)\frac{d\lambda}{\lambda} \tag{5.4}$$

However, this semi-infinite integral with Bessel functions in the integrand makes numerically integrating difficult, if not impossible. Furthermore, there is no simple form for calculation of the isotherms defined by this function. In order to get around these problems, exact simplified equations for temperature profile along the surface and axis of symmetry will be used to calculate the melting temperature point on each axis. The temperature profile along each axis are given by

$$T(0,z) = \frac{qa}{k}\left(\sqrt{\left(\frac{z}{a}\right)^2 + 1} - \left(\frac{z}{a}\right)\right) \tag{5.5}$$

$$T(r,0) = \begin{cases} \dfrac{2qa}{\pi k}\mathbf{E}\left(\dfrac{r}{a}\right), & r \le a \\ \dfrac{2qr}{\pi k}\left[\mathbf{E}\left(\dfrac{a}{r}\right) - \left(1 - \left(\dfrac{a}{r}\right)^2\right)\mathbf{K}\left(\dfrac{a}{r}\right)\right], & r \ge a \end{cases} \tag{5.6}$$

where $\mathbf{K}$ and $\mathbf{E}$ are complete elliptic integrals of the first and second kind, respectively [15]. The isotherms are approximated by a parabola connecting the radial and depth coordinates where the temperature is equal to the melting temperature. The melted volume is taken to be the volume contained under this parabola revolved about the axis of symmetry, as shown in Figure 5.10(b). Using this approximation method, the power (Figure 5.11) and current (Figure 5.12) required to melt 500 nm^3 of ruthenium are calculated.

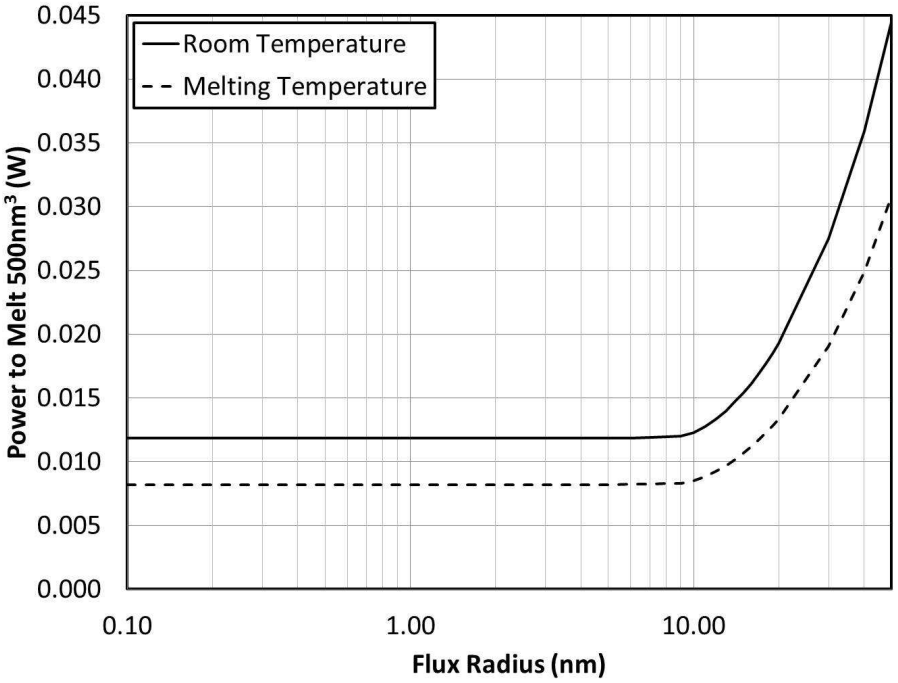

Figure 5.11 Power required to melt 500 nm^3 of ruthenium at the surface of a half space for thermal conductivities of room temperature and melting temperature.

The thermal conductivities of both melting and boiling were used because Equations (5.4) - (5.6) do not take into account temperature dependent material properties. Therefore, these two curves act as limits on the temperature dependent behavior. Notice that as the flux radius gets smaller, the power and current approach a limit. This is because the induced temperature profile far away from the heat source is spherically symmetrical. In essence, the farther away the point of interest is from the heat source (or as the flux radius decreases with respect to the

distance to that point of interest), the more the temperature profile behaves as if it is induced by a point source. Thus increasing the flux radius not only grows the ratio of flux radius to distance, but it also decreases the distance to the point of interest.

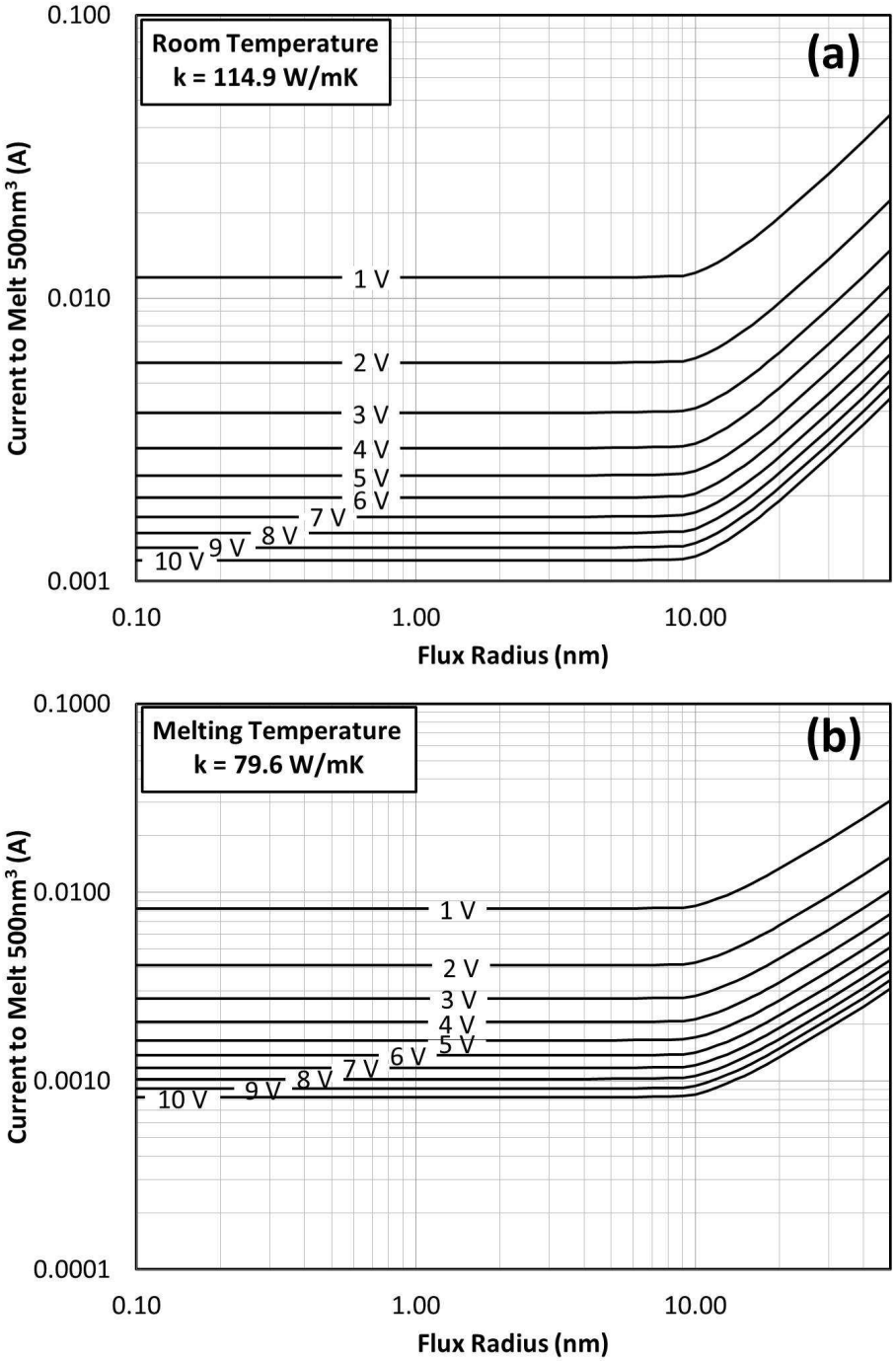

Figure 5.12 Current required to melt 500 nm3 of ruthenium at the surface of a half space with thermal conductivity for (a) room temperature and (b) melting temperature.

Later (in the pull-in and pull-out behavior sections), it will be shown that these mechanisms operate within 10 nm of separation and the maximum amount of time that they

reside in this separation window is around 100 ns. If it is assumed that the maximum electron emission spike has this duration, an estimate of the energy can be simply calculated, as presented in Figure 5.13.

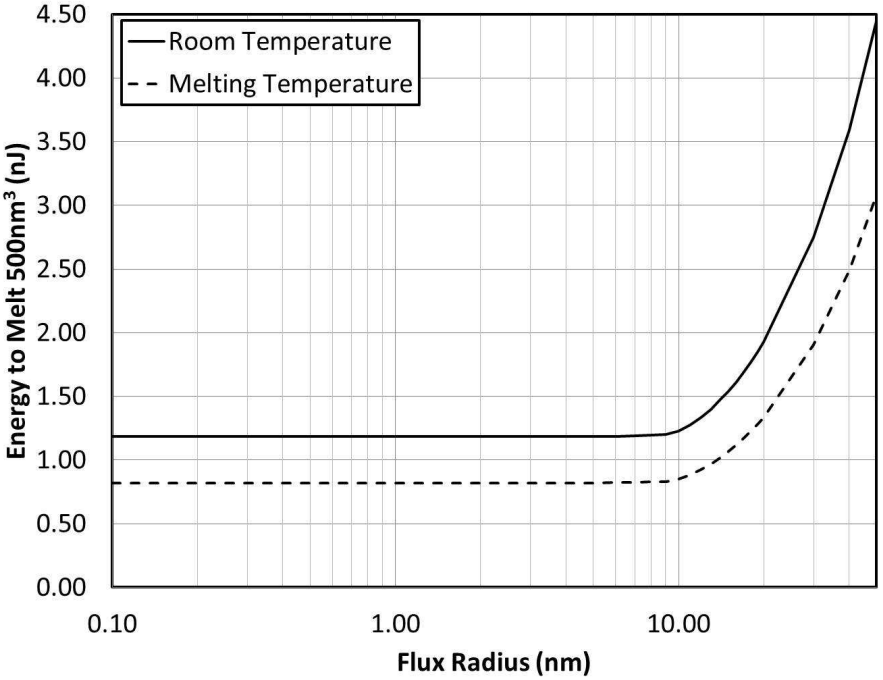

Figure 5.13 Energy required to melt 500 nm^3 of ruthenium at the surface of a half space.

If this melting is caused by Fowler-Nordhiem emission, an upper-limit estimate on the current versus separation can be made using Child's equation

$$J = K\frac{V^{3/2}}{d^2} \tag{5.7}$$

$$K = \frac{4}{9}\varepsilon_0\left(\frac{-2C}{m}\right)^{1/2} \tag{5.8}$$

where J is the maximum current density possible, ε_0 is the permittivity of free space, C is the charge of the particle being emitted, and m is the mass of the particle being emitted. This equation calculates the maximum current possible due to the space charge density. Essentially the theory states that there is a current density at which the electric field at the emitting electrode surface is too weak to support a higher flow. In this scenario, this equation can be used to calculate the maximum spacing at which the current required to melt 500 nm^3 can be sustained for a given potential. For an electron, the particle that is being emitted, the charge was taken to be 1.602x10^{-19} C and the mass was taken to be 9.109x10^{-31} kg. This calculation is plotted in Figure 5.14. Only 5-10 V_{Hot} were plotted because it is assumed that Fowler-Nordhiem emission does not occur below the work function.

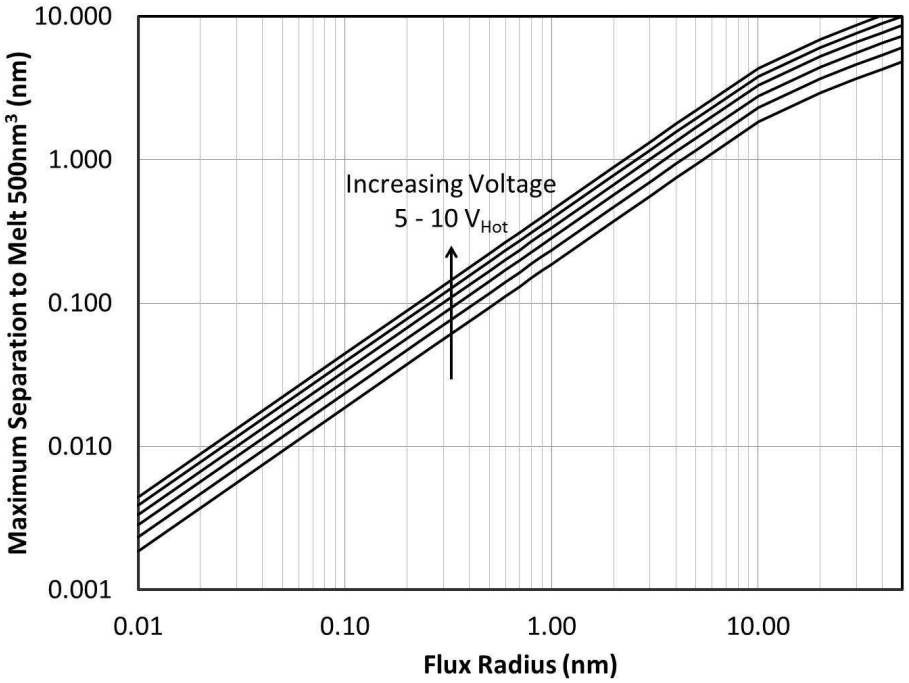

Figure 5.14 Maximum separation at which Fowler-Nordhiem emission can provide enough current (for a given voltage) to melt 500 nm^3 of material.

This plot can be interpreted in several ways. One interesting result from this data is that it suggests that the flux radius (in essence, the radius of the electron 'beam') is between 1 - 10 nm. This is based on the fact that the atomic radius of ruthenium is 0.130 nm and that these mechanisms occur at less than 10 nm of separation (discussed below).

For applied potentials below 4.7 V_{Hot}, any electron emission that occurs will be governed by direct tunneling behavior. In this case, Child's equation for space charge limited current does not apply. Theoretically, the upper limit to direct tunneling current should be the rate at which current can be supplied; this would be governed by the test circuitry.

In summary, it seems that an emission induced material transfer mechanism is reasonably plausible. The energy and time requirements make evaporation seem less likely to occur than melting. However, the fact that directional material transfer in roughly the same amount occurs on the leading and trailing edges seem to argue that evaporation is likely.

5.4 Pull-Off and Pull-In Behavior During Hot Switching

As defined above, hot switching is the application of voltage over the contact as it is closed and/or opened. Because hot switching results in significantly more damage than cold switching in otherwise identical conditions, the behavior of the electrodes upon closing and opening is exceedingly important in order to gain a better understanding of the damage mechanisms. The following sections will explore the pull-off behavior exhibited in trailing edge hot switching and the pull-in behavior exhibited in leading edge hot switching. Exploration of pull-in and pull-off behavior provides insight into the critical timing and spacing of the electrodes when the hot switching damage mechanisms are active. It is noted that some of the behavior discussed is

specific to the testing apparatus used and may or may not apply to an actual switch. However, it is important to identify effects unique to the test setup for the purpose of differentiation from actual damage mechanism effects.

5.4.1 Pull-Off Behavior

While performing experiments, it was observed that trailing edge hot switching resulted in larger pull-off forces as compared to leading edge hot switching. Figure 5.15 is a bar chart of the average pull-off force for all recorded cycles in each of the tests represented in Figure 4.6 (progression tests); each bar represents the average pull-off force of at least three tests. Increased pull-off force represents higher mechanical tensile forces upon release in trailing edge hot switching contacts. This behavior suggests that there are different damage mechanisms on the leading and trailing edges. However, upon closer inspection the trailing edge hot switching pull-off behavior was exceptionally different as compared to that of leading edge hot switching.

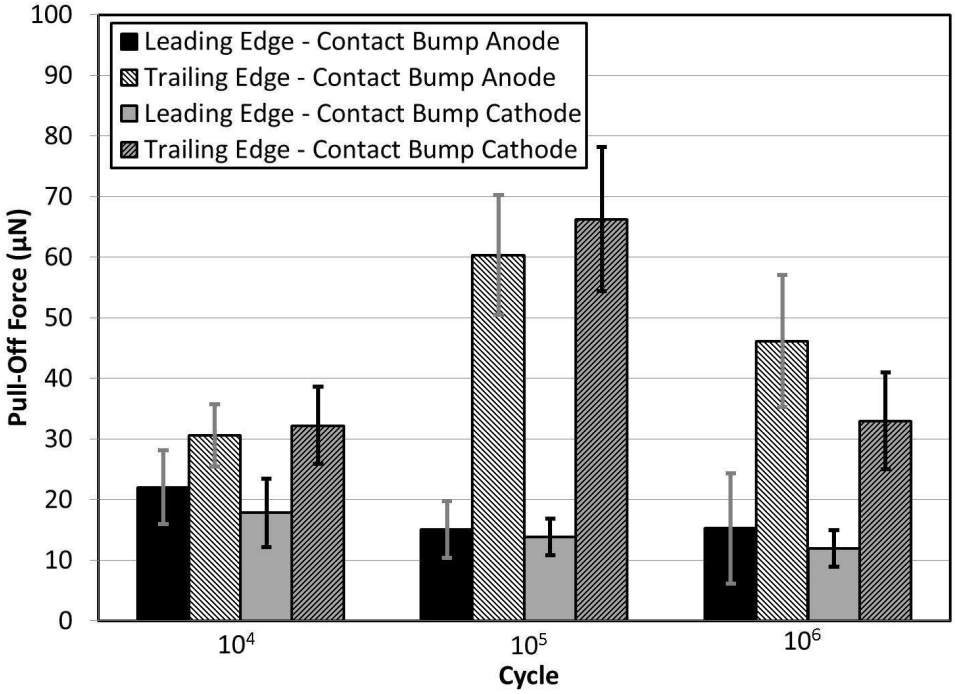

Figure 5.15 Average pull-off force for leading and trailing edge hot switching.

To explore the difference between the pull-off behavior of leading and trailing edge hot switching tests, single cycles from the recorded data were analyzed. Figure 5.16 contains two individual cycles: one from a trailing edge hot switching test and one from a leading edge hot switching test. Though the amount of pull-off force is roughly the same, the pull-off behavior is notably different. The leading edge test comes out of contact abruptly. The contact force increases from roughly -50 µN to zero in less than 5 µs (the time between individual samples). However, the trailing edge test comes out of contact more gradually, increasing the same amount force over a period of roughly 0.1 ms.

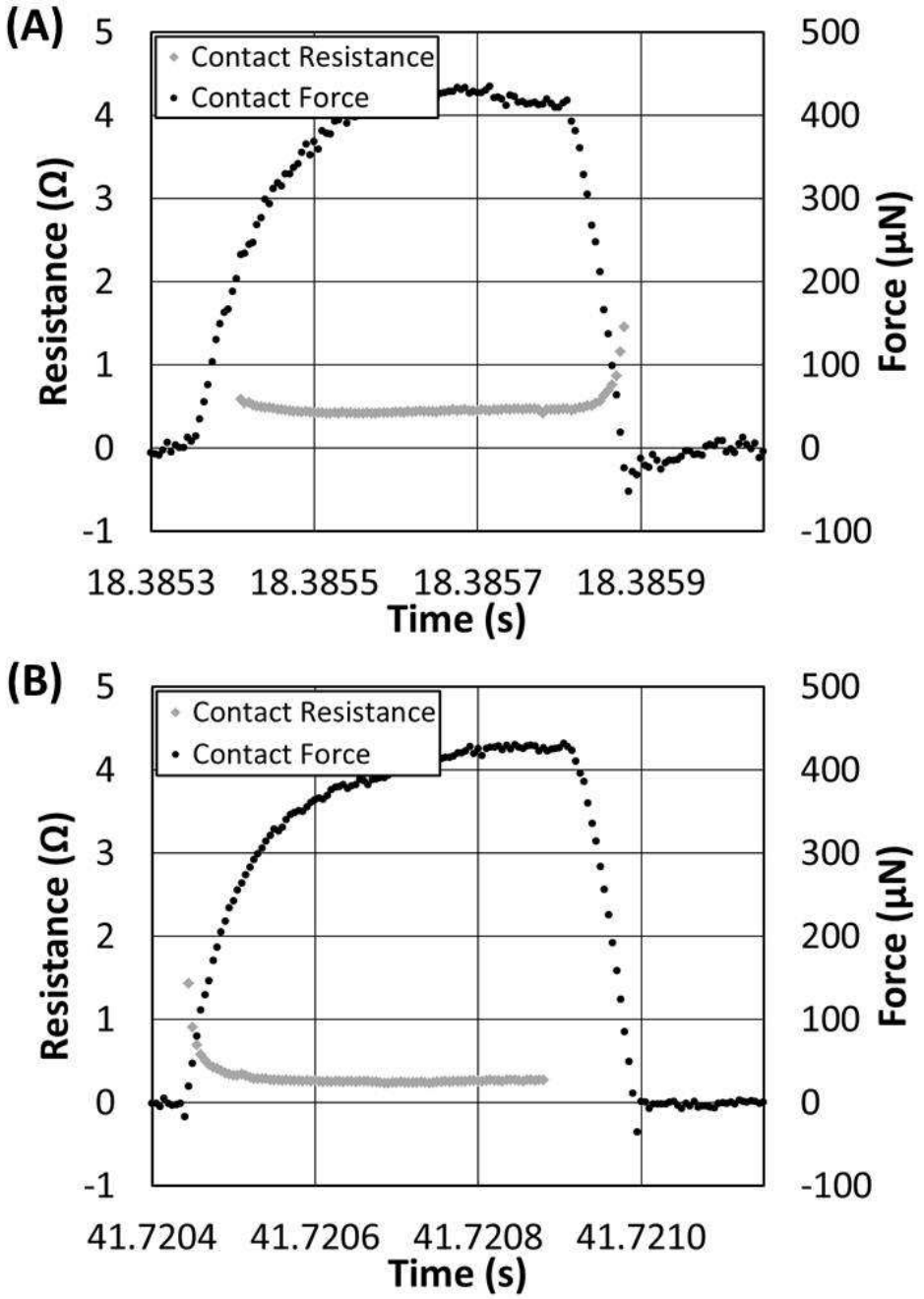

Figure 5.16 Trailing edge (A) versus leading edge (B) hot switching pull-off behavior for 3.5 V_{Hot}, 77.5 mA_{Cold} at 500 Hz.

The relaxation behavior on the trailing edge was explored further by conducting a unique trailing edge hot switching test. The hot switching voltage was ramped 1-10 V_{Hot} by one volt increments over successive cycles (cycle 1: 1 V_{Hot}, cycle 2: 2 V_{Hot}, etc), and then repeated. All cycles were conducted with a medium length structure (see Appendix for detailed

dimensions) with 77.5 mA_{Cold} at 300 Hz, 400 Hz, and 500 Hz. Several hundred cycles were captured and compiled. The analysis of the pull-off force behavior was broken down into time-dependence and magnitude.

In the time domain, the relaxation behavior was independent of cycling rate (separation speed) and had dependence only on the trailing edge hot switching voltage. Furthermore, a clear exponential decay of force (from the largest pull-off force to zero) with time was exhibited upon separation for voltages greater than 4 V_{Hot}. Point clouds generated with the pull-off force data from at least four cycles for each 5-10 V_{Hot} were curve-fit using the curve-fit toolbox feature in MATLAB© to the equation

$$F(t) = Ae^{-t/\tau} + B \tag{5.9}$$

where $F(t)$ is contact force as a function of time t, and A, B, and τ are constants solved for by the curve-fitting tool using the bisquare method with trust-region algorithm. The exponential decay time constant is plotted versus applied voltage in Figure 5.17.

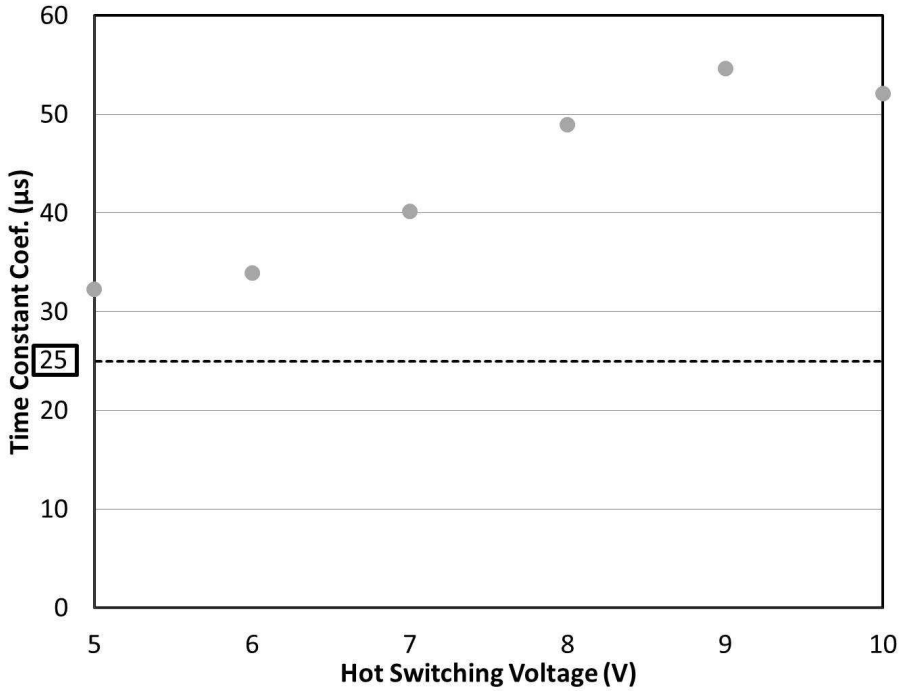

Figure 5.17 Transient response of the test structure in the form of the exponential decay time constant τ of contact force after release. The boxed value corresponds to the primary time constant of the one dimensional transient heat flow problem, as discussed below.

To analyze the pull-off force magnitude, the pull-off force from at least four cycles was averaged for each 1-10 V_{Hot} for 300 Hz, 400 Hz, and 500 Hz. These results are presented in Figure 5.18. Note that the pull-off force generally decreased with increased cycling rate. However, the general trend of pull-off force behavior with voltage is consistent for all three cycling rates.

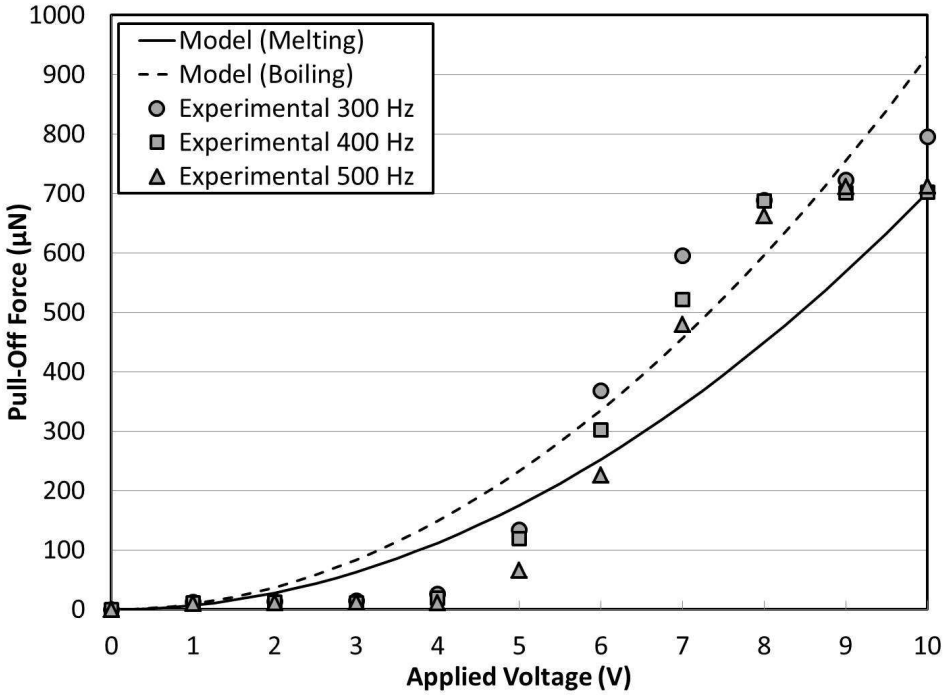

Figure 5.18 Magnitude of pull-off force versus applied voltage for 300 Hz, 400 Hz, and 500 Hz cycling rate experimental results as well as the predicted pull-off force from the model for both melting and boiling upon release.

To explain this behavior, the experimental test structure can be thought of as a bi-metallic strip: ruthenium on silicon. The current running through the contact spot and ruthenium layer causes a significant amount of heating in the test structure, leading to a temperature profile along the length of the structure. Because the thermal expansion coefficient of ruthenium is greater than that of silicon, the structure must bow in the direction of the ruthenium layer to reach a state of static stress equilibrium, essentially resulting in a thermal actuation.

To model the transient, or time-response, behavior bi-metallic action of the test structure, only the thermal domain must be considered. This is based on the assumption that the induced temperature profile (which causes the deflecting) is the only-variant process in the system. To approximate the transient thermal behavior of the test structure as it cools, it can be modeled as an unsteady-state one-dimensional plate with an initial arbitrary temperature profile and bounded with constant ambient temperature end conditions. In this case, the temperature as a function of time t and position z is given by

$$T(z,t) = \sum_{n=1}^{\infty} A_n e^{-\alpha\lambda_n^2 t} \sin \lambda_n z \tag{5.10}$$

$$\lambda_n = \frac{n\pi}{L} \tag{5.11}$$

$$\alpha = \frac{k}{\rho c} \tag{5.12}$$

where A_n are coefficients calculated via Fourier sine expansion of the arbitrary initial temperature profile, L is the length of the one-dimensional plate, α is the thermal diffusivity, k is the thermal conductivity, ρ is the mass density, and c is the specific heat. Using the room temperature material properties from Table 5.3, effective material properties of the layered beam can be calculated as

$$k_{eff} = \frac{t_{Si}k_{Si} + t_{Ru}k_{Ru}}{t_{Si} + t_{Ru}} = 145 \ {}^{W}/_{mK} \tag{5.13}$$

$$\rho_{eff} = \frac{t_{Si}\rho_{Si} + t_{Ru}\rho_{Ru}}{t_{Si} + t_{Ru}} = 3503 \ {}^{kg}/_{m^3} \tag{5.14}$$

$$c_{eff} = \frac{t_{Si}c_{Si} + t_{Ru}c_{Ru}}{t_{Si} + t_{Ru}} = 708 \ {}^{W}/_{kgK} \tag{5.15}$$

Table 5.3 Material Properties [13][2][3].

Property	Value	Units
k_{Ru}	117	W/mK
k_{Si}	149	W/mK
ρ_{Ru}	12300	kg/m^3
ρ_{Si}	2330	kg/m^3
c_{Ru}	239	J/kgK
c_{Si}	770	J/kgK
t_{Ru}	0.6	µm
t_{Si}	4.5	µm
E_{Ru}	432	GPa
E_{Si}	170	GPa

From these equations, the primary (n = 1) time constant can be defined as

$$\tau_1 = \frac{k_{eff}}{\rho_{eff}c_{eff}}\left(\frac{\pi}{L}\right)^2 = 40000 \ {}^{1}/_{s} \Rightarrow 25 \ \mu s \tag{5.16}$$

This value is boxed in Figure 5.17. This value is less than all of the experimentally measured values. However, this is to be expected because this model does not take into account temperature dependent material properties. For both ruthenium and silicon, the thermal conductivity decreases with temperature, specific heat increases with temperature, and density decreases with temperature [3]. Referring to Equation (4.16), the net result of these material property changes would tend to increase the relaxation time. Furthermore, the temperature

dependence of material properties could also explain the trend of increasing relaxation time with applied voltage exhibited by the experimental data presented in Figure 5.17.

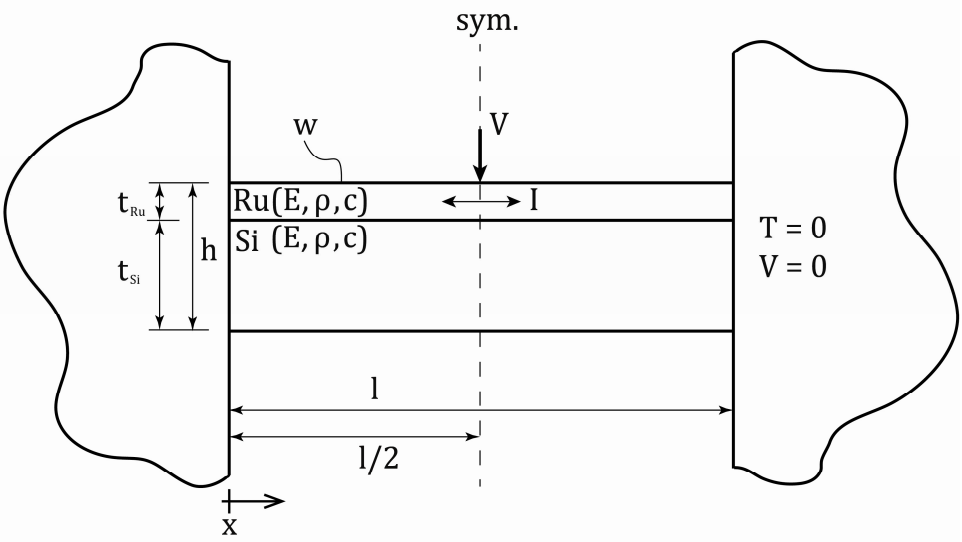

Figure 5.19 Bi-metallic strip model schematic for thermal, electrical, and mechanical domains.

To model the magnitude of the bi-metallic action (deflection) of the test structure all three domains must be considered. Figure 5.19 represents a schematic of the bi-metallic strip model of the test structure in all three domains. In the electrical domain, the structure is modeled as a simple square cross-section ruthenium wire of length l, width w, and height t_{Ru}. Current I originates at the mid-length of the wire (l/2) and flows evenly toward each end, thus the system is symmetrical. The current running through the wire results in Joule heating

$$\dot{Q} = \frac{I^2 \rho_{Ru} l}{2 t_{Ru} w} \tag{5.17}$$

where ρ_{Ru} is the electrical resistivity or ruthenium. The total height of the beam is assumed to be sufficiently small enough treat the joule heating in the ruthenium layer as a uniform volumetric heat source

$$\dot{q} = \frac{I^2 \rho_{Ru}}{t_{Ru} h w^2} \tag{5.18}$$

Additionally, the heat generated from the current constriction of the contact bump is expected to contribute a heat flux

$$q'' = \frac{I^2 R_C}{hw} \tag{5.19}$$

where R_C is the contact resistance. This flux is assumed to act evenly across the entire beam cross-section. Note that only a quarter of this heat flux is assumed to enter each half of the beam (the remaining half is assumed to go into the pillar side of the contact).

In the thermal domain, the beam is modeled as a one-dimensional steady-state beam with uniform cross-section and internal volumetric heat generation. Heat is assumed to only be conducted out of the ends of the beam. With these boundary conditions, the general steady state heat conduction equation is readily solved for induced symmetrical temperature profile

$$T(x) = -\frac{\dot{q}}{k}\left[x^2 - \left(l + \frac{I^2 R_C}{2\dot{q}hw}\right)x\right] \qquad 0 \le x \le l/2 \tag{5.20}$$

where k is the effective thermal conductivity of the beam, as solved for in Equation (4.13).

In the mechanical domain, the deflection profile of the beam is solved for using the characteristic differential for bimetallic strips [4]

$$\frac{d^2 z}{dx^2} = 6(\alpha_{Si} - \alpha_{Ru})\frac{t_{Ru} + t_{Si}}{t_{Si}^2 \mathrm{K}} T(x) \tag{5.21}$$

$$\mathrm{K} = 4 + 6\left(\frac{t_{Ru}}{t_{Si}}\right)^2 + \frac{E_{Ru}}{E_{Si}}\left(\frac{t_{Ru}}{t_{Si}}\right)^3 + \frac{E_{Si}}{E_{Ru}}\left(\frac{t_{Si}}{t_{Ru}}\right) \tag{5.22}$$

Using the temperature profile above, symmetry, and the principle of superposition, the deflection and slope as a function of position can be solved for. For brevity, these lengthy equations are omitted.

The result of this model for a medium length beam is plotted in Figure 5.15. The material properties contained in Table 5.3 were used for this calculation. A thermal conduction width equal to the end width of a medium beam (20 μm) was assumed because all of the thermal energy will be conducted out of the structure through this width. The magnitude of the numerical model match fairly well to those pull-off forces recorded experimentally. However, the model has a very poor fit to the qualitative trend exhibited by the experimental results; the model predicts comparatively higher pull-off forces for low voltages, and comparatively lower pull-off forces for high voltages. The high voltage behavior can be reasonably justified by the model's lack of temperature dependent material properties. The thermal expansion coefficients for both silicon and ruthenium approach a finite limit, respectively, as temperature is increased. In essence, the coefficient of linear thermal expansion is only constant over a confined range of temperature. Thus, although there will be more and more localized heating with higher temperature (by the reasons stated above), it should be expected that the thermal expansion in the actual structures versus temperature will effectively approach a limit. The discrepancy between the model and the experimental result for lower applied voltages is more inexplicable. A trend of lower contact resistances upon separation at lower voltages could explain such behavior, but no such trend was present in the experimental data. Regardless, this simplified model seems to predict the approximate magnitude of the pull-off force with fair accuracy, but it certainly does not capture all that is occurring in the actual test structure during pull-off. However, when considering both the transient and magnitude models together, it seems reasonable to conclude that thermal actuation via bi-metallic strip action is a significant factor in the pull-off behavior.

The heating and subsequent bowing of the test structure effectively move the equilibrium position of the contact downward with respect to the actuation direction. Therefore, the ramifications of the bi-metallic strip action should theoretically occur on both the leading and the trailing edge. Bi-metallic strip action on the leading edge is discussed in the pull-in behavior section (Section 5.4.2).

On the trailing edge, one result of the bi-metallic strip action is the pull-off force being interpreted as larger than what it actually is. This is an artifact of the contact force measurement structures. Just because the equilibrium position of the structure – or, to put it another way, the structure curvature corresponding to zero contact force – is shifted in the opposite direction of actuation does not necessarily mean that the force required to separate the contact bump from the pillar surface is increased. Furthermore, the thermally induced stresses are not sufficient to buckle the structure. Therefore, the stiffness and natural frequency of the test structure are not expected to change significantly while thermally actuated. Consequently, the pull-off behavior is also not expected to change significantly as a result of this effect. When combined, these factors suggest that the actual pull-off force should not be different for trailing edge hot switching as compared to leading edge hot switching.

If this is true, an approximation of the pull-off time can be made as roughly one quarter of the natural period. Additionally, assuming an actual pull-off force of 15-20 μN (equal to the average pull-off force range exhibited by leading edge hot switching in Figure 5.15), an approximation of the pull-off distance can be made. Here, the pull-off distance refers to the distance that the pillar and structure separate upon release, and the pull-off time refers to the amount of time that it takes for this distance to be covered. These properties are summarized in Table 5.4. These numbers should be used to provide context for the trailing edge damage mechanisms, especially the field effects that occur while the electrodes are separated. One surprising result from these simple calculations is that the pillar retracts only about one tenth of the pull-off distance in one pull-off time assuming a separation rate of 4400 μm/s. This puts into perspective just how slow the pillar is moving with respect to the dynamics of the test structure.

Table 5.4 Approximation of pull-off characteristics.

	Stiffness (μN/μm)	Natural Frequency (MHz)	Pull-Off Distance (nm)	Pull-Off Time (ns)	Pillar Movement (nm)
Short Beam	8300	4.07	1.8 - 2.4	61	0.27
Medium Beam	3380	2.36	4.4 - 5.9	106	0.47

A second result of the bi-metallic strip action is slightly more contact time per cycle for trailing edge tests as compared to leading edge tests of the same cycling rate. Because the small contact force / high contact resistance portion of the contact cycle is being elongated, there is a possibility that this effect could exacerbate the thermal-mechanical trailing edge damage mechanisms. This is discussed in relation to the variable ramping rate tests.

5.4.2 Pull-In Behavior

Figure 5.16 clearly illustrates a pull-in behavior while the contact is closing for leading edge hot switching, but not for trailing edge hot switching. This pull-in behavior is observed to increase with applied potential as well as counter-intuitively with the current. The importance of

exploring this behavior lies in determining if this is an effect that could be observed in real switches, or if this behavior is simply an artifact of the testing apparatus.

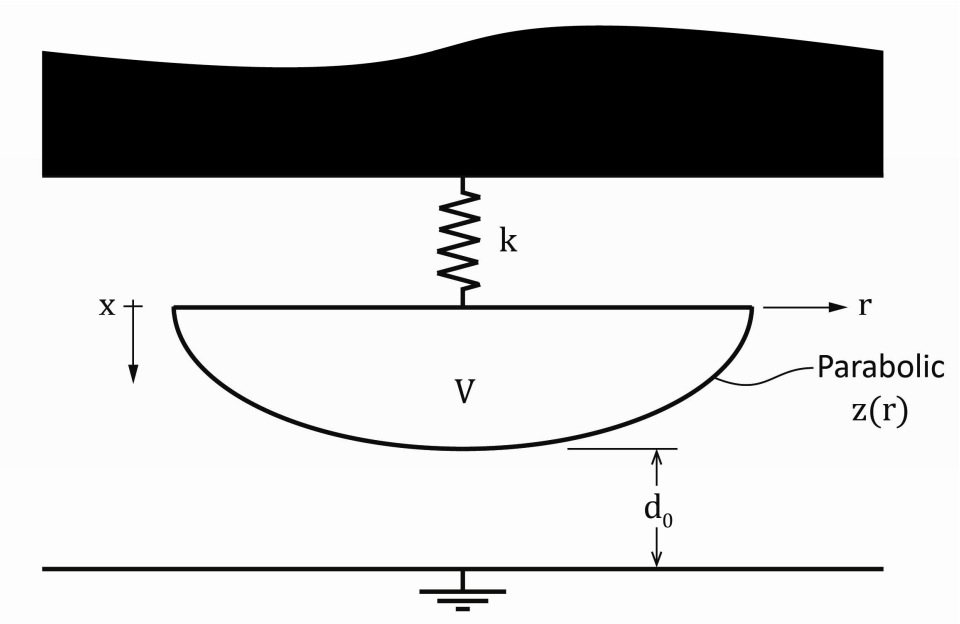

Figure 5.20 Schematic of the simplified model used to calculate the theoretical electrostatic pull-in force.

Figure 5.20 represents a simplified model of the test structure used to calculate the theoretical electrostatic pull-in force. In this model, k is the effective stiffness of the test structure, V is the potential applied over the contact, and d_0 is the un-deflected separation between the contact bump and pillar. The subtlety in the definition of this variable warrants clarification: d_0 is the electrode separation if the stiffness were infinite or if there was zero potential applied over the contact. The profile of the contact bump is approximated by a parabola

$$z(r) = \frac{r^2}{2R} \tag{5.23}$$

where R is the radius of curvature of the contact bump and r = 0 is defined as the axis of symmetry. The electrostatic force between two parallel plates is defined as

$$f = \frac{\varepsilon V^2 A}{2z^2} \tag{5.24}$$

where ε is the permittivity of free space and A is the parallel cross sectional area. From these equations, the total electrostatic force exerted on the contact bump as a function of separation

$$F(d) = \int_0^\infty \frac{\varepsilon V^2 (2\pi r dr)}{2\left(\frac{r^2}{2R} + d\right)^2} = \frac{\varepsilon \pi V^2 R}{d} \tag{5.25}$$

where $d = d_o - x$. Static equilibrium of the system dictates the spring force be equal to the electrostatic force, yielding

$$\tilde{F} = \tilde{x}(1 - \tilde{x}) = \frac{\varepsilon \pi V^2 R}{k d_0^2} \tag{5.26}$$

where the tilde represents a non-dimensional variable, with displacement x being normalized by un-deflected separation d_0. When the equilibrium force is plotted as a function of displacement, a local max is exhibited at a normalized displacement of 0.5, as shown in Figure 5.21.

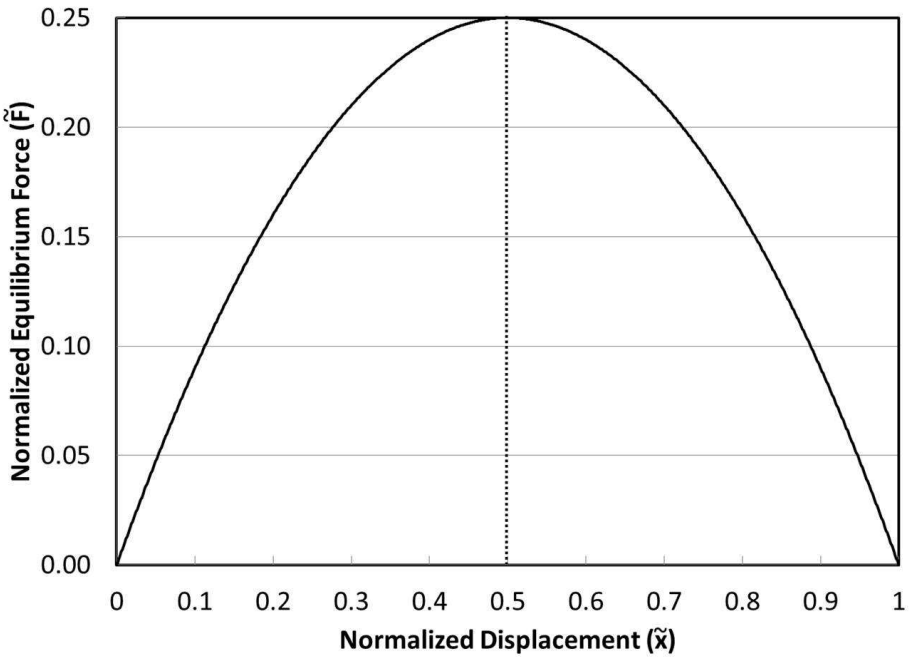

Figure 5.21 Normalized equilibrium force versus normalized displacement.

This critical displacement represents the dynamic instability point of electrostatic snap-in. Plugging in $\tilde{x} = 0.5 -$ or alternatively, plugging in $\tilde{F} = 0.25 -$ into Equation 5.26 and rearranging yields

$$d_0 = 2V^2 \sqrt{\frac{\epsilon \pi R}{k}} \tag{5.27}$$

This is the critical un-deflected separation at which the structure with snap into contact. To put it another way, this is the electrode spacing that will induce a static displacement equal to the critical snap-in displacement. Consequently, the distance the contact will snap through is

$$d_{snap} = d_0(1 - 0.5) = 0.5d_0 \tag{5.28}$$

This is the displacement that should be observed experimentally via a 'jump' in the A-B signal. The force exerted on the contact at this displacement (the so-called threshold force) is

$$F_{Th} = 0.5kd_0 \tag{5.29}$$

Using these equations and the values presented in Table 5.5, plots for the theoretical pull-in distance and threshold force are presented in Figure 5.22 and Figure 5.23, respectively.

Table 5.5 Pull-in Model Properties.

Property	Value	Unit
ε	$8.85\text{x}10^{-12}$	s^4A^2/m^3kg
R_{Large}	$60\text{x}10^{-6}$	m
R_{Small}	$15\text{x}10^{-6}$	m
k_{Medium}	8300	N/m
k_{Short}	3380	N/m

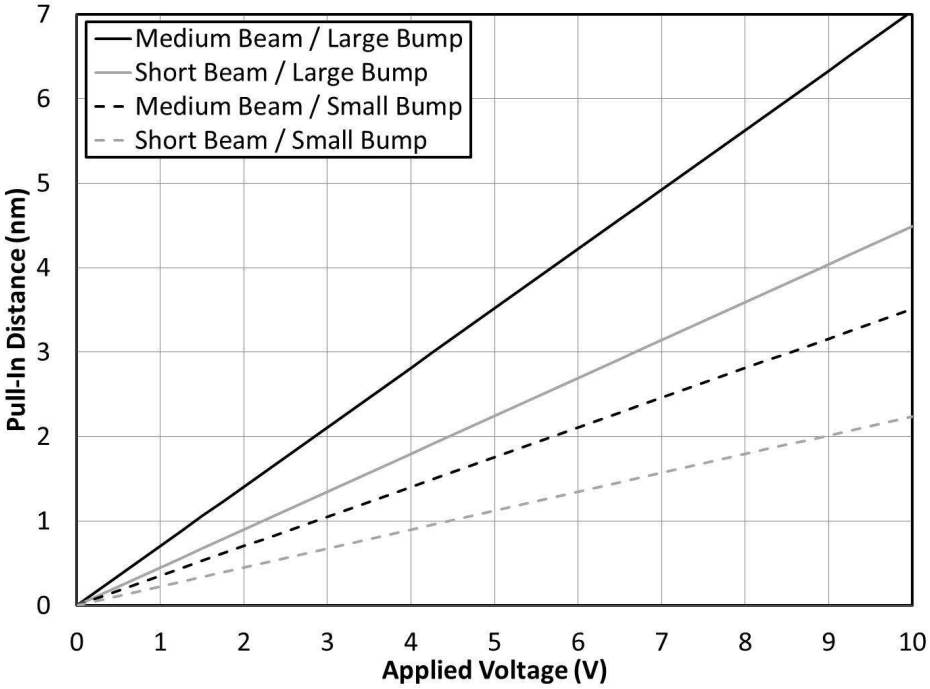

Figure 5.22 Theoretically calculated pull-in distance versus applied voltage.

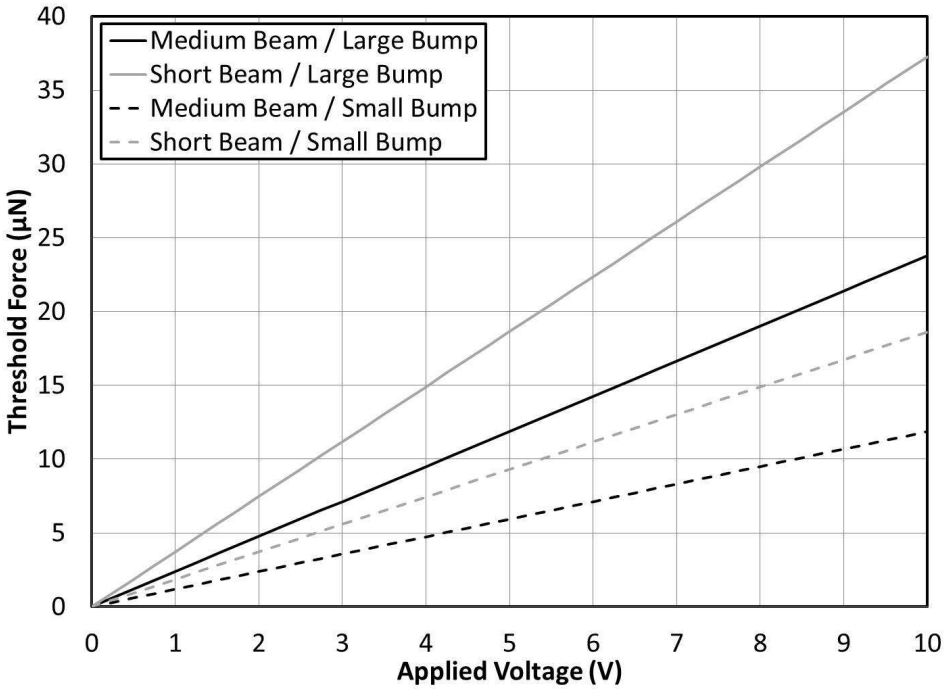

Figure 5.23 Theoretically calculated threshold force versus applied voltage.

To verify this behavior exists in the test setup, a leading edge hot switching experiment was conducted with an extremely slow approach rate of 2.2 nm/s. The mechanical behavior (in the form of the A-B signal) was recorded for 1-10 V_{Hot}. In order to negate the effects of heating (and bi-metallic action), a 5 kΩ series resistance was used to minimize current. The results are presented in Figure 5.24.

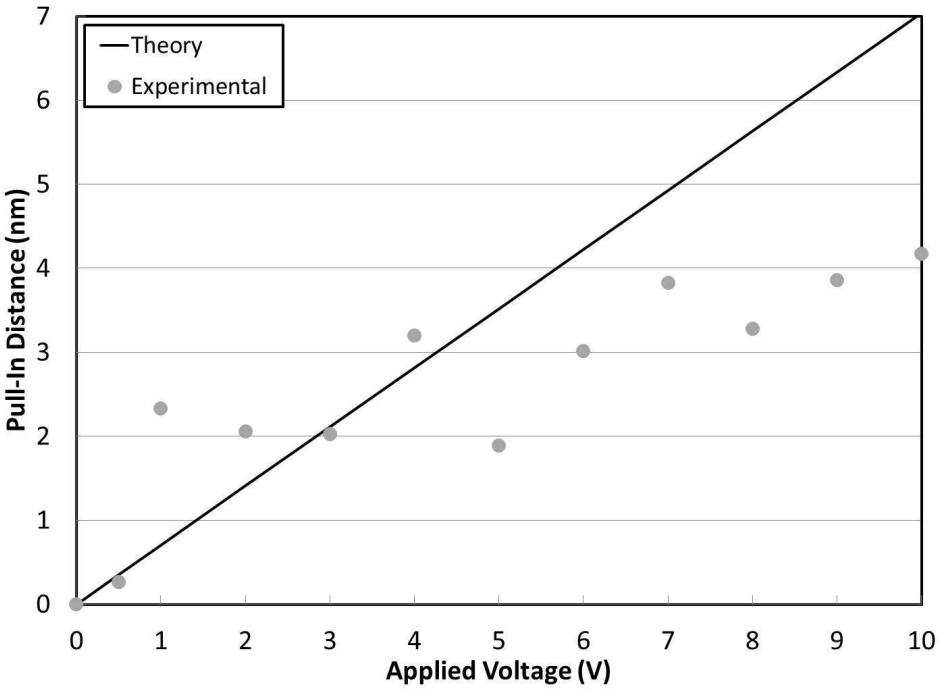

Figure 5.24 Pull-in distance as a function of applied voltage.

These results suggest that the model predicts the magnitude of the pull-in distance fairly well for lower voltages, but not as well for higher voltages. If the pull-in distances for the two lowest applied voltages are considered to be inaccurate measurements (because they are well below the level of noise in the signal), the remaining experimental behavior seems to be roughly linear with applied voltage suggesting that the pull-in behavior is more or less in agreement with the model. In addition, the experimental data seems to have a non-zero intercept. This can be explained by the presence of adhesion (van der Waals forces). The discrepancy between the model and the experimental data could be explained by slight inaccuracies in the assumed properties used, such as the contact bump radius of curvature or structure stiffness. With this considered, it seems reasonable to assume that the pull-in effect is predominantly an electrostatic pull-in effect.

It is important to note that this same experiment was performed with a 50 Ω series resistor. The results from this experiment yielded what seemed like larger snap-in distances. However, the larger observed snap-in distances are believed to be an artifact related to the bi-metallic strip action. As shown in the previous section, the heating leads to a thermally induced downward curvature (in the opposite direction of actuation). When combined with any sort of contact force loading, the thermally induced deflection profile of the structure will superpose with the contact force induced deflection profile. In this case, the snapped-in deflection profile of the initially unheated beam would superpose with the thermally induced deflection profile to produce slightly larger rotation angles at the paddles. This is interpreted as a larger perceived snap-in distances. Furthermore, assuming a fully developed thermal deflection profile develops within a 3-4 time constants of initial contact (~150 – 200 μs), it is impossible to distinguish the development of thermally induced profile from the snap-in event while sampling at 2000 samples/second (1 sample every 0.5 ms), the sampling rate used for these tests.

The ramifications of the electrostatic pull-in occur on the leading edge, as the electrodes come together. If all the assumptions above are correct, this means that as long as the closing rate is less than the snap-in rate, the contact will be pulled-in roughly the same distance every cycle for a given structure (length/bump size) and V_{Hot}, regardless of regardless of series resistance. Those approximate distances are plotted in Figure 5.22. Should the leading edge damage mechanisms be active within snap-in distances, these snap-in periods provide a timeframe.

5.5 Variable Ramping Rate Tests

The ramping rates (on approach and separation) can be very important to the relative dominance of the active damage mechanisms on both the leading and trailing edges. To study the effect of slower ramping rates, the approach and retract rates were varied. The tests presented in Figure 5.25 compare ramping rates of 4400 µm/s, 440 µm/s, and 115 µm/s for 3.5 V_{Hot} and 77.5 mA_{Cold} over 10^5 cycles for both leading edge and trailing edge hot switching. It is important to note that even though the ramping rates for these tests were varied, the cold switching time was not.

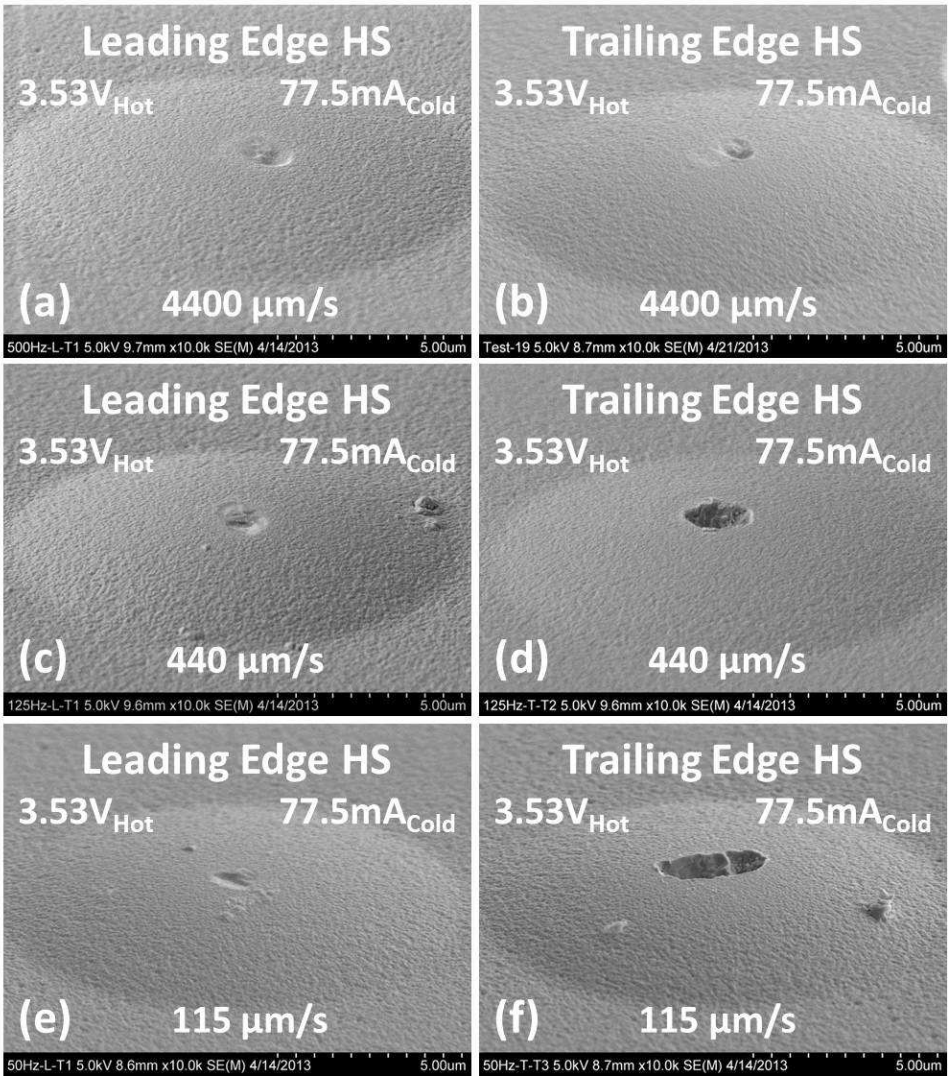

Figure 5.25 Varied ramping rate tests for the leading and trailing edges.

The first observation from this group of tests is that (a) and (b) reaffirm the previously found result that the leading edge and trailing edge hot switching cause roughly the same amount of material transfer damage at 500 Hz testing (4400 µm/s). In essence, the field mechanisms and thermo-mechanical mechanisms do the same amount of damage on the leading edge as they do on the trailing edge at this ramping rate.

Comparing leading edge tests against each other shows that the amount of damage done by leading edge hot switching is independent of approach rate. Recall the pull-in behavior explored above. One ramification of electrostatic pull-in is that the distance and time of snap-in will not be affected by approach rate, unless that rate is faster than the average pull-in speed. Thus the behavior exhibited by the leading edge tests suggests that the damage mechanisms on the leading edge occur within the snap-in. More specifically, the leading edge mechanisms occur in separations of less than 10 nm in time on the order of tens of nanoseconds. Furthermore, if it can be shown that the same amount of damage is done for both short and

medium beams alike (a study not yet done), the timing and separation window could be narrowed.

Comparing the trailing edge tests against each other shows that the amount of damage done by trailing edge hot switching is dependent on retract rate: damage increases with decreasing separation rate. Note that this figure may be slightly misleading. Some of the trailing edge tests at 115 µm/s resulted in about the same amount of material transfer. The difference in material transfer between 4400 µm/s and 440 µm/s was always comparable for all tests run, but the difference in material transfer between 440 µm/s and 115 µm/s was not always distinguishable.

This rate dependent material transfer suggests that one or both (field effect / thermo-mechanical effect) is more active on the trailing edge with slower separation rates. Therefore, it becomes important to analyze the separation rates with respect to pillar retract speed. Recall Table 5.4, for 500 Hz testing (4400 µm/s ramping rate) the pillar only moved about one tenth of the pull-off distance in the case of both short and medium beams (fractions of a nanometer). Thus, for 440 µm/s, the pillar will only move about 1% of the pull-off distance, and ~0.25% of the pull-off distance for 115 µm/s. The pull-off dynamics seem to be dominated by the pull-off time, and not the separation rate, making the result of the trailing edge tests surprising. Being as the field effects are the mechanisms working while the contact is separated, it seems unlikely that slowing the separation rate would affect the field effect mechanisms.

If the field effects are not significantly affected by ramping rate, then the thermo-mechanical effects must be. It is conceivable that the bi-metallic strip action cycle-extension behavior (discussed above) could account for the increased activity of the thermo-mechanical mechanism on the trailing edge for slower ramping rates. Using the data from Figure 5.15, the average difference in average pull-off force between leading and trailing edge tests was calculated to be roughly 25 µN; this can be interpreted as the 'additional' force added per cycle due to bi-metallic strip action of the test structure. From this force, the corresponding shift in equilibrium position and thus the additional time per cycle can be approximated for each of the separation rates. These results are summarized in Table 5.6.

Table 5.6 Additional time per cycle as a result of the bi-metallic strip action.

	Stiffness (µN/µm)	ΔF (µN)	Δd (nm)	Δt_{4400} (µs)	Δt_{440} (µs)	Δt_{115} (µs)
Short Beam	8300	25	3.01	0.68	6.85	26.19
Medium Beam	3380	25	7.40	1.68	16.81	64.32

From these results is seems like a reasonable explanation that the bimetallic strip action adding time to the trailing edge of the cycle could exacerbate the thermo-mechanical damage mechanism.

To take the ramping rate variation to its lower limit, tests were performed with ramping and separation rates of 2.2 nm/s. These tests were done to record the electrical and contact force behavior in great detail to shed light on the contact damage mechanisms. These tests were performed manually in the sense that the operator controlled the ramping. Because of the exceptionally slow ramping rates, only about 50 cycles were performed per test.

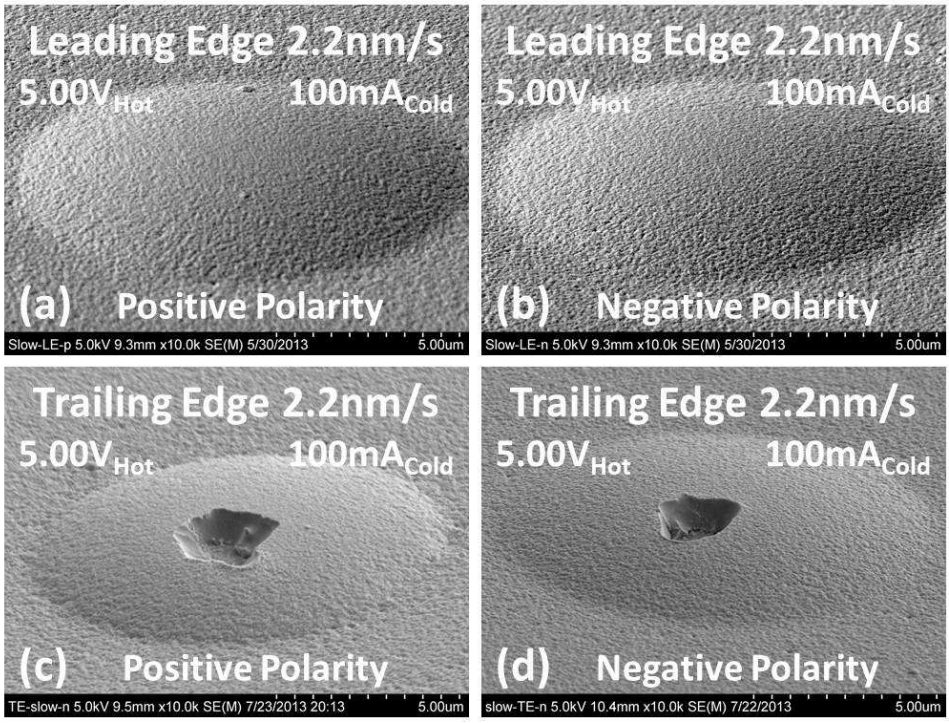

Figure 5.26 2.2 nm/s ramping rate leading and trailing edge hot switching.

Figure 5.26 shows the results from two leading edge hot switching tests and two trailing hot switching tests. All of these tests were done with 5 V_{Hot} and 100mA_{Cold} for about 50 cycles. The trend of rate-dependent trailing edge material transfer seems to extend to this extreme rate, and dramatically so. The amount of material transferred for only 50 cycles of testing at this rate is comparable to the amount of damage done for some the most damaging conditions run for 10^6 cycles. Furthermore, the material transfer for both polarities is away from the contact bump in roughly the same amount. At the leading edge, there is not distinguishable contact damage for the same number of cycles. Additionally, electrostatic snap in was observed for all cycles on the leading edge hot switching tests. Both of these results seem to agree well with the faster-cycled contacts.

5.6 Long Term Bipolar Testing

The term bipolar testing is used to describe a test done with the applied potential alternating polarity with every cycle, as illustrated in Figure 5.27. The premise that bipolar tests are based on is that the net amount of material transferred one cycle will be nearly the same as the amount of material transferred in the opposite direction on the very next cycle. Thus, bipolar hot switching tests are capable of achieving extremely high numbers of cycles because the net amount of material transferred, and thus the total damage done to the contact, is much less as compared to a uni-polar hot switching tests.

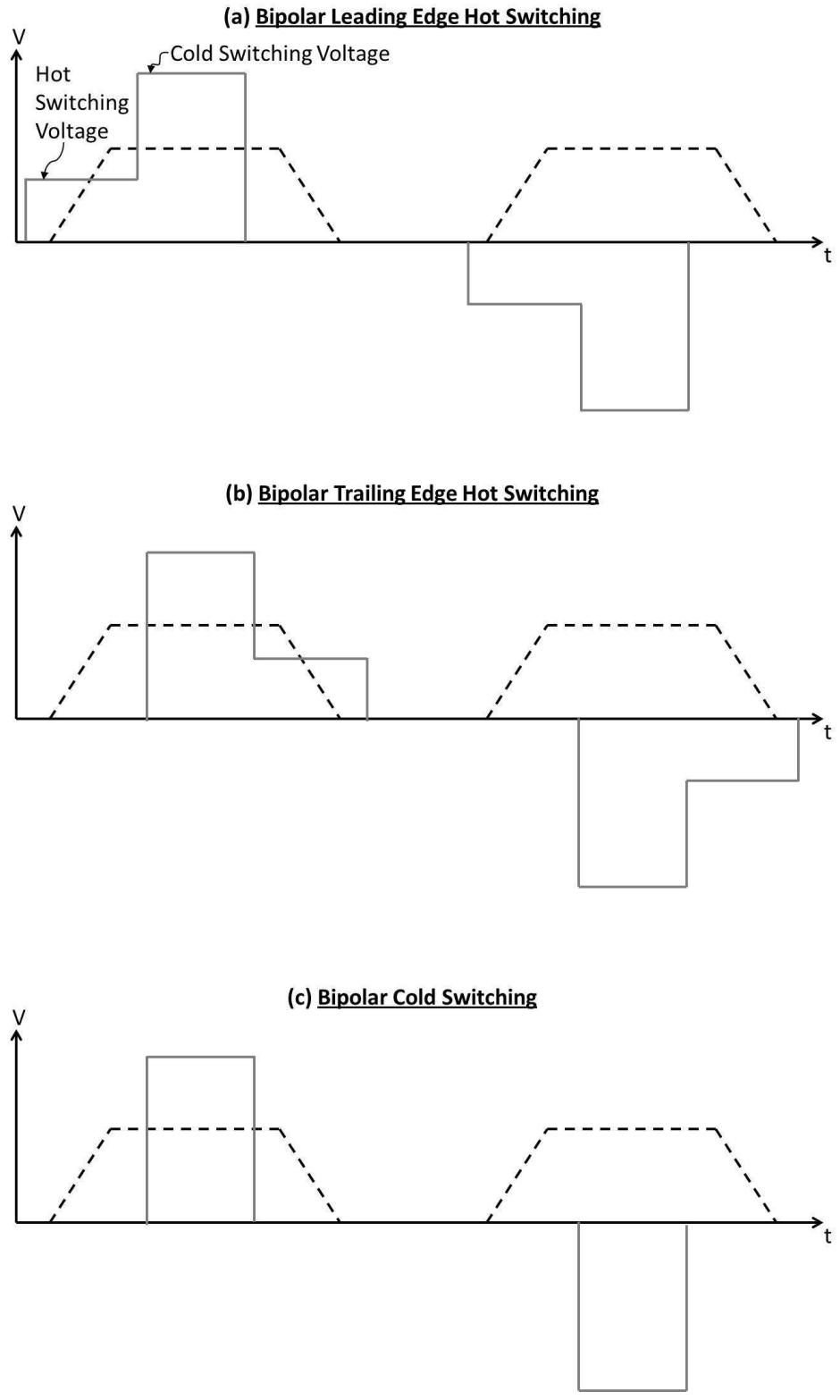

Figure 5.27 Bipolar testing schematic where the dashed lines represent the actuation voltage waveform and the solid grey lines represent the applied voltage waveform.

After a very large number of cycles, any net material transfer in one direction is a result of (a) a slight bias in the directional material transfer mechanisms for one polarity versus the other, or (b) the result of only the unidirectional material transfer mechanisms. Of the two possibilities, (a) seems less likely. In [1] it was shown that positive polarity (contact bump as the anode) and negative polarity (contact bump as the cathode) tests result is about the same amount of directional material transfer. This result suggests that the directional material transfer mechanisms are equally active for both polarities for at least 10^6 cycles.

A third explanation for net material transfer in one direction exhibited over a large number of cycles of bipolar testing is a bias in the testing equipment to one polarity, specifically the op-amp used to generate the applied voltage signal. Indeed, the smallest difference in the magnitude of the applied voltage of one polarity as compared to the opposite polarity could result in an appreciable difference over a large number of cycles. Thus two tests were conducted: one test with the leads from the op-amp connected as they would normally be connected, and one test with the leads switched. Otherwise, all conditions were identical: a 500 Hz bipolar leading edge hot switching test with 3.5 V_{Hot} and 77.5 mA_{Cold} for 10^8 cycles (a very large number of cycles). The resulting contact damage is illustrated in Figure 5.28. The direction of material transfer is the same for both tests, thereby proving that the op-amp is not the cause of the material transfer bias away from the contact bump.

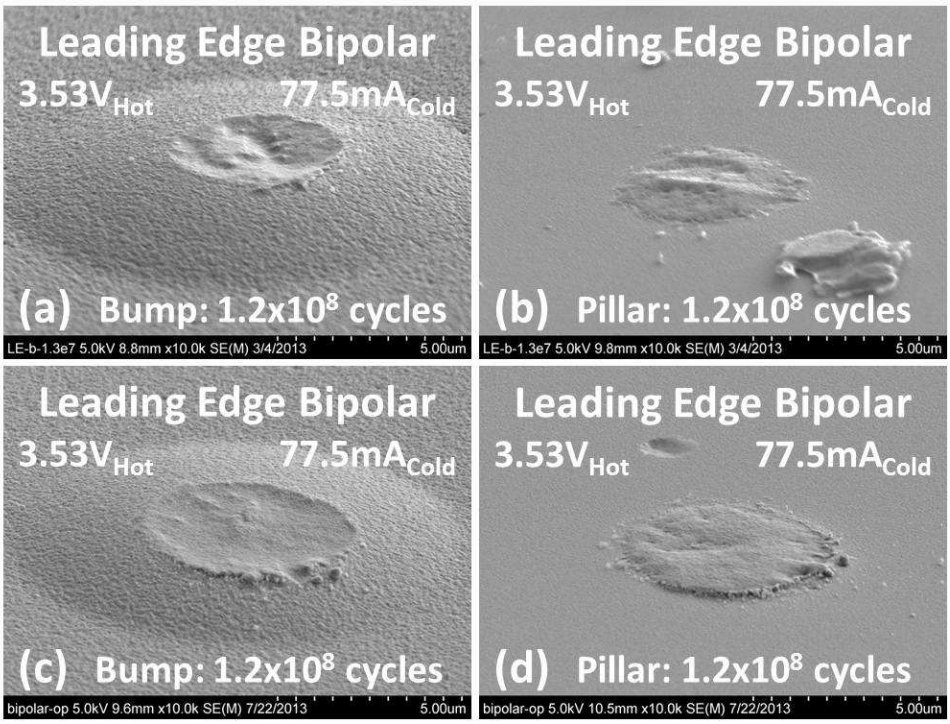

Figure 5.28 Two leading edge long term bipolar tests with the leads reversed.

To explore the long term bipolar behavior of hot switching, leading edge hot switching, trailing edge hot switching, and cold switching experiments were run at 500 Hz with 3.5 V_{Hot} and 77.5 mA_{Cold} for $4x10^7$ cycles. The results are presented in Figure 5.29.

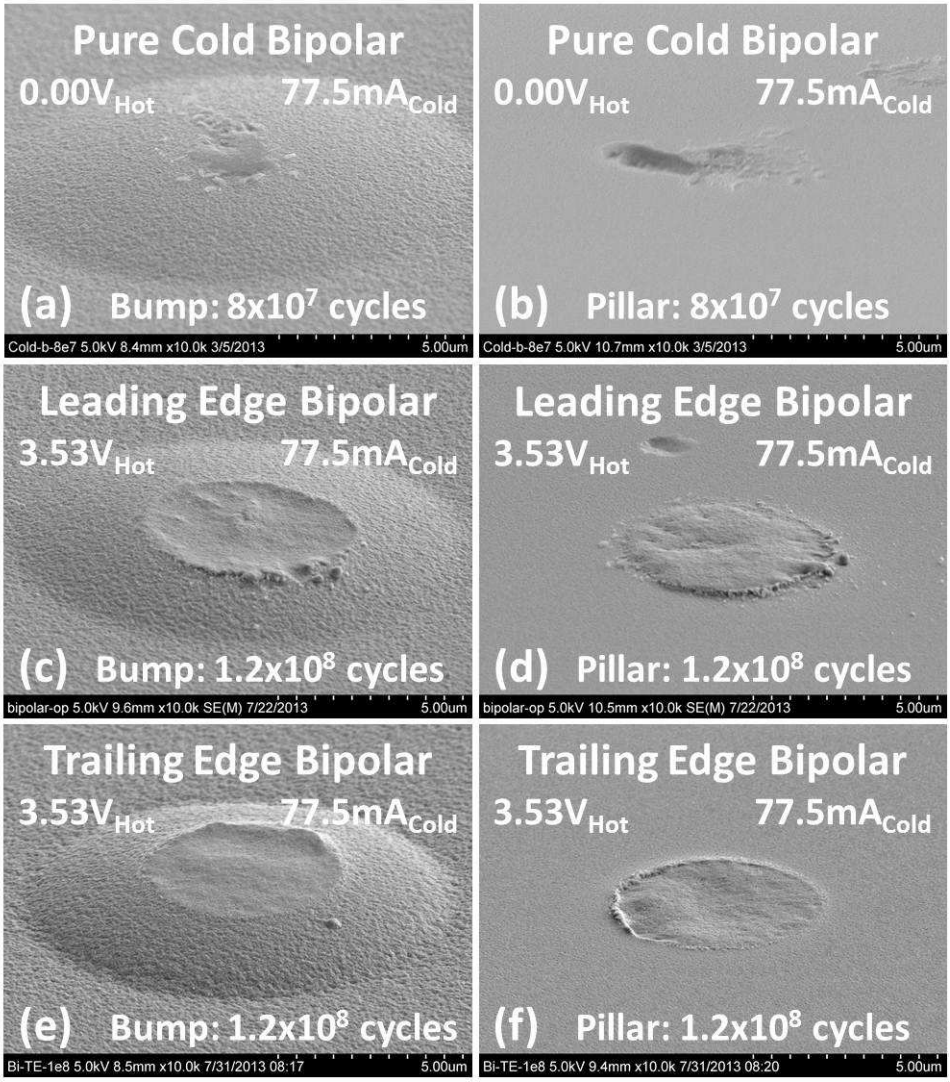

Figure 5.29 Long term bipolar test for leading edge hot switching, trailing edge hot switching, and pure cold switching.

Cold switching long term bipolar testing results in little to no bias in one direction; there is material deposited in both directions. A repeat of this test for 2.5×10^7 cycles yielded similar qualitative results. Based on the shape, consistency, and cloudy look (how quasi- and non-conductive materials appear in the SEM) this is probably a build-up of contaminants such as carbon, or so-called frictional polymers [14]. Such build-ups usually lead to high resistance failure in cold switching tests. This result suggests that the appreciable material transfer observed in the leading edge and trailing edge bipolar tests is indeed a hot switching effect and not a cold switching effect.

The leading edge long term bipolar test results in a significant amount of net material transfer away from the contact bump. This behavior was exhibited in both of the tests presented in Figure 5.28. The direction of net material transfer away from the bump suggests that it is the result of the geometry-biased leading edge thermo-mechanical effect. In other

words, the heating upon contact induces high temperatures that extend far enough into the electrode bodies that the more massive (better heat sink) pillar is the cooler body.

Trailing edge long term bipolar tests seem to result in about the same amount of contact damage as the equivalent leading edge test. If this net material transfer on the trailing edge is also assumed to be the result of the geometry-biased thermo-mechanical mechanism, then this result suggests that leading and trailing edge hot switching result in roughly the same amount of heating. Additionally, this result argues against the bi-metallic strip action cycle-elongation effect at 3.5 V_{Hot} and 500 Hz cycling rate.

5.7 Conclusions

This chapter focused on developing a fundamental understanding of hot switching damage mechanisms by combining specifically-aimed experiments with models to help justify the behavior observed.

On the trailing edge, it was shown that there is a bi-metallic strip action unique to the testing specimen used. This effect is not a damage mechanism itself, but does elongate the amount of time the electrodes are in contact per cycle for trailing edge hot switching, specifically in the low force and high resistance portion of the contact cycle, where the heating is the greatest. This heating combined with the thermal characteristic of the pillar being a much better heat sink than the structure is believed to be the source of material transfer damage away from the contact bump. Recall from Chapter 4 [1], the 600 nm of ruthenium on the pillar side has 300 nm of gold beneath it, making the pillar a much better heat sink. It was believed to be the reason that trailing edge hot switching results in more damage with slowing separation rates. Indeed, in the extreme of separation rate of 2.2 nm/s (very slow), there was a dramatic increase in material transfer damage per cycle.

On the leading edge, an electrostatic pull-in behavior was shown to exist in the test specimens, but is expected to exist in some form in real switches. The electrostatic pull-in model predicts closing-rate independent behavior for separations less than 10 nm, depending on beam stiffness and contact bump size. Material transfer contact damage rate-independence was confirmed experimentally by varying the approach rates. At 2.2 nm/s approach rates, snap-in was observed and no distinguishable contact damage was found after approximately 50 cycles. This was interpreted as consistent with the amount of material expected from this many cycles assuming rate independence (500 nm^3 of transfer per cycle). Note that the snap-in behavior observed may also be an effect of the bi-metallic strip action after initial contact.

The results from experiments and models alike suggest that field dependent material transfer mechanisms are active at less than 10 nm of separation and in time periods on the order of 100 nanoseconds on both the leading and trailing edges; these numbers were attained via modeling combined with observed experimental behavior. The most likely electric field dependent material transfer contact damage mechanism seems to be the direct tunneling induced melting of evaporation. However a metal vapor arc could also account for electric field dependent material transfer. For thermo-mechanical mechanisms, a strong dependence was shown on the amount of time the contact was in the low force and high resistance portion of the contact cycle. Net material transfer resulting from this mechanism is always observed to be away from the contact bump, strongly suggest thermal geometry dependence.

5.8 Chapter 5 References

[1] Hennessy R, Basu A, Adams G and McGruer N 2013 Hot-switched lifetime and damage characteristics of MEMS switch contacts *Journal of Micromechanics and Microengineering* **23** 055003

[2] Holm R and Holm E 1967 *Electric contacts: theory and application* vol 9: Springer-Verlag New York)

[3] Hultgren R, Desai P D, Hawkins D T, Gleiser M and Kelley K K 1973 Selected values of the thermodynamic properties of binary alloys. DTIC Document)

[4] Toda M, Ono T, Liu F and Voiculescu I 2010 Evaluation of bimaterial cantilever beam for heat sensing at atmospheric pressure *Review of Scientific Instruments* **81** 055104--6

[5] Carslaw H and Jaeger J 1959 Conduction of Heat in Solids (paperback,)

[6] Hennessy R P, McGruer N E and Adams G G 2012 Modeling of a Thermal-Electrical-Mechanical Coupled Field Contact *Journal of Tribology* **134** 041402

[7] Marinkovic N, Vukmirovic M and Adzic R 2008 *Some Recent Studies in Ruthenium Electrochemistry and Electrocatalysis*: Springer)

[8] Müller E W 1941 Abreißen adsorbierter Ionen durch hohe elektrische Feldstärken *Naturwissenschaften* **29** 533-4

[9] Zurlev D N and Forbes R G 2003 Field ion emission: the effect of electrostatic field energy on the prediction of evaporation field and charge state *Journal of Physics D: Applied Physics* **36** L74

[10] Tsong T T 1991 Effects of an electric field in atomic manipulations *Physical Review B* **44** 13703

[11] Bouwers A and Cath P 1941 The maximum electric field strength for several simple electrode configurations *Philips Technical Review* **6** 270-8

[12] Simmons J G 1963 Generalized formula for the electric tunnel effect between similar electrodes separated by a thin insulating film *Journal of Applied Physics* **34** 1793

[13] Slade P G 1999 *Electrical contacts: principles and applications* vol 105: CRC)

[14] Chen L, Lee H, Guo Z, McGruer N E, Gilbert K, Mall S, Leedy K and Adams G 2007 Contact resistance study of noble metals and alloy films using a scanning probe microscope test station *Journal of Applied Physics* **102** 074910—7

[15] Pinsker V 2006 Unsteady-state temperature field in a semi-infinite body heated by a disk surface heat source *High temperature* **44** 129-38

[16] Ho C Y, Powell R W and Liley P 1972 Thermal conductivity of the elements *Journal of Physical and Chemical Reference Data* **1** 279

Chapter 6

Conclusions

6.1 Concluding Statements

The work presented in this thesis has focused on hot switching damage in MEMS switch contacts. The state of understanding of hot switching and the resulting damage was advanced by this body of work through both experimental and theoretical modeling.

Using a finite element model, the effect of coupling between the thermal, electrical, and mechanical domains in a hemisphere contacting a half-space was explored. For a force-controlled contact, such as a hemispherical contact bump in a microswitch, the model found that there was not a significant coupling effect; the contact behavior could be accurately modeled by Hertz contact theory. However, for a contact operating under displacement control, such as an asperity on the surface of a contact bump, coupling had a significant effect. Generalized (non-dimensional) curve-fit equations were presented to describe the behavior of the contact in this situation. This model forms a basis for potential future work in the modeling of rough surfaces in electrical contact.

With a specially built micro-contact testing system and microfabricated contact pairs, hot switching tests were conducted to characterize hot switching damage. It was found that hot switching damage mechanisms are active on both the leading (closing) and trailing (opening) edges. Hot switching in a 50 Ω impedance system under 3.5 V_{Hot} bias was found to result in directional material transfer damage of about 500 nm^3 per cycle for both leading and trailing edge hot switching for 4400 μm/s opening and closing rates. Furthermore, the direction of the material transfer damage was shown to be polarity-dependent, from the anode to the cathode.

Possible damage mechanisms were subsequently explored using simple models and specially designed experiments. From this work, it was concluded that material transfer via direct electron tunneling induced evaporation or vapor arcing were the most likely sources of polarity-dependent material transfer and that field evaporation and field emission material transfer via Fowler-Nordhiem tunneling were not plausible explanations. These field-dependent mechanisms were found to be active for separations of less than 10 nm and in time periods on the order of hundreds of nanoseconds. A thermo-mechanical contact damage mechanism comprised of joule heating and thermal geometry was identified. This mechanism transfers material away from the hotter body (contact bump) with strong approach/separation rate dependence: slower rates result in more material transfer. Therefore, it stands to reason that the higher the approach/separation rate, the lower the effect of this damage mechanism.

Bipolar cycling makes possible higher contact lifetimes. It was shown that tests in excess of 1.2×10^8 cycles of hot switching (leading or trailing edge) were easily achievable. Though the exact mechanism responsible for directional material transfer hot switching damage has not yet been identified, it was shown that bipolar cycling is an effective way to maximize contact lifetime. To our knowledge, 120 million cycles under legitimate hot switching conditions has not been previously achieved in the switching environment or testing environment.

This work makes significant progress toward understanding the specific mechanisms responsible for the additional damage associated with hot switching. Practically, the work presented in this thesis can be used in future exploration of this problem. The ultimate goal is to define the exact nature of micro-scale electrical contacts during hot switching. With this knowledge more robust, longer lasting contacts can be built, thereby solving a problem that has

plagued the microswitch and inhibited it from significant commercial market penetration. With that understood, there is still much work that needs to be done.

6.2 Future Work and Experiments

In this section, potential future experiments and models and the value of these exercises are detailed with the hope that this work is picked up where it has been left off.

1) One of the short-comings of the work presented in this thesis is that it was unable to determine if the polarity-dependent material transfer mechanism requires actual physical contact to be made. On the leading edge, the difference between arc transfer and field emission material transfer is that arc transfer requires a metal vapor formed from the vaporization of initially contacting asperities. On the trailing edge, the same situation applies. The test structures used in the contact testing were too compliant to avoid snap-in, thus the behavior at extremely close separations was impossible to determine with our setup. If the material transfer mechanism does not require contact, it is possible to replicate this behavior either by fabrication of much stiffer structures, or by the use of a different apparatus, such as a micro/nano indenter.
2) Leading and trailing edge hot switching tests have been done for different ramping rates for positive polarity (bump as the anode), but not for negative polarity (bump as the cathode). In the latter case, the field mechanism/s should work in the opposite direction as the thermo-mechanical mechanism. Because the thermo-mechanical mechanism has been shown to increase activity with decreasing rate, less and less net material transfer should occur with decreasing separation rates for negative polarity. Perhaps a critical ramping rate can be defined that results in zero net material transfer. This critical rate, should it exist, is a fairly interesting one because this means that the polarity dependent mechanisms and polarity independent mechanism result in roughly the same amount of material transfer. A positive polarity test could be run at the same separation rate and a volume measurement could be taken. If all of these assumptions hold (which may be a stretch), then the directional mechanisms and non-directional mechanisms would each be responsible for half of the net volume transferred. This assumes that there is not a coupling effect between the mechanisms that result in one or both mechanisms to be relatively more or less active in one polarity as compared to the other (which is entirely possible). Taking this hypothesis one step further, because we have shown that the leading edge material directional transfer mechanisms are not rate dependent and we have also shown that leading edge and trailing edge directional material transfer mechanisms result in roughly the same amount of material transfer at 4400 μm/s approach/separation rate, all of these volumes should be approximately equal. This relationship could be used as evidence to determine if there is a coupling effect on the material transfer mechanisms on one polarity versus the other.
3) For trailing edge hot switching at 2.2 nm/s, a very high impedance test should result in very small amounts of material transfer. The conclusion about the slow trailing edge tests was that the significant amount of material transferred was a result of the thermo-mechanical mechanism. Significantly reducing the current should significantly reduce heating and thus eliminate the material transfer away from the bump from this effect.

4) One artifact of the testing system that was used is that the pull-off force can be artificially inflated by the bi-metallic strip action. A fairly simple fix to this artifact is to develop a post-processing filter to account for bi-metallic strip action in pull-off force calculation.
5) It was reported that for 50 Ω, and a 2.2 nm/s approach rate, leading edge tests reported apparently larger pull-in distances. This behavior was attributed to the bi-metallic strip action, essentially the superposition of the deflection profile upon snap-in and a relatively quickly developing thermally-induced deflection profile. To verify this behavior, a fixed-fixed beam profile can be superposed with the deflection profile predicted by the bi-metallic strip model profile. The results could be confirmed experimentally. For the experiment, the contact force could be ramped up to a known but small contact force without an applied voltage. The jump in contact force can be recorded at the moment that the applied voltage is turned on. Although this experiment has already done, the results have yet to be compiled and the accompanying model has not been built.
6) A dynamic model of the electrostatic snap-in could be built to get more accurate numbers for the pull-in time and impact force and to compare these numbers to the pull-off numbers. This is a fairly simple, but powerful approximation given that the leading edge mechanisms seem to happen within the range of electrostatic snap-in. Additionally, this could potentially be matched with test results. A difficultly is that the jumps in the A-B signal are comparable to the noise in the A-B signal, so even if the sampling rate were increased, the pull-in behavior captured may not be representative of the actual pull-in.
7) Another artifact of our testing system is the parasitic capacitance associated with the testing chip itself. It has been shown that the inherent capacitance of the chip is capable of storing enough energy to result in hot switching currents even with series resistances that would negate such effects. This parasitic / unwanted capacitance, though not unique to our testing structures (it would exist to some degree in an actual switch), is effectively limiting our ability to explore the current dependence of the field effect damage mechanisms. Redesigning the test structure chip to have a thicker or different material isolation layer could reduce this parasitic capacitance to a suitable level.
8) A data survey analysis of contact voltage upon release needs to be done to determine what the average voltage upon release is: is this voltage closer to the melting voltage, the boiling voltage or is it somewhere between? What is the deviation and scatter? Determining the answers to these questions could go a long way toward understanding if there is a metal vapor cloud present at the trailing edge. If the typical contact voltage upon release is close to the boiling voltage, then it is more likely that we have a metal vapor cloud forming and subsequent arcing.
9) Preliminary voltage dependence tests show a threshold of material transfer behavior between 3.0-3.25 V_{Hot}. Below this threshold, the direction of material transfer seems to be random. One explanation could be that in this range, one mechanism is being limited while another is not.

6.3 Acknowledgements

This work could not have been done without the help, guidance, and wisdom of Prof. George Adams and Prof. Nicol McGruer. Together they helped me through this program, which at times seemed hopeless. Without their vast knowledge and decades of experience, this research would not have gotten nearly as far as it did. I am extremely grateful for their tutelage in academics, research, and life in general. They have made this experience one of truly higher education in every sense of the phrase, thank you!

Appendix

Experimental Background and Associated Material

A.1 Introduction

This chapter contains the supplemental work associated with the experimental work published. Unless otherwise stated, the material in this chapter applies to all experimental work published.

A.2 Test Sample Fabrication

In this section, a detailed traveler for the fabrication of test samples is covered. It is important to note that the equipment and materials in the clean room may change slightly with time, so parameters such as (but not limited to) etch time, deposition time, and exposure time may vary slightly from the recipe parameters mentioned in this traveler. An adept understanding of each process and each fabrication device is essential to produce acceptable test samples.

A.3.1 Pillar

Pillar Recipe

1. Start is Si Wafer
    a. 380-500μm thick
    b. (1 0 0) Orientation
    c. Polished on ONE side
    d. P-Type Doping: Boron
    e. 1-10 Ω cm Resistivity
2. Standard Pre-Oxidation Clean
    a. Remove Organics / Metals (Piranha Clean)
        i. H_2SO_4:H_2O_2 2:1
        ii. Temp ~115˚C
        iii. Time 10:00 minutes
    b. Rinse
        i. Auto-rinser: 1 run (4 Cycles)
    c. Dewet (Native Oxide Removal)
        i. HF:H_2O 1:50
        ii. Time 0:15 seconds
    d. Rinse
        i. Auto-rinser: 1 run (4 Cycles)
    e. Remove Metallic Impurities
        i. H_2O:HCl:H_2O_2 6:1:1
        ii. Temp 95˚C
        iii. Time 10:00 minutes
    f. Rinse
        i. Auto-rinser: 1 run (4 Cycles)
    g. Rinser / Dryer
        i. Time 300 seconds
3. Standard Wet Oxidation
    a. Load Wafer into Quartz Boat

   i. Don't touch with hands!
   b. Load boat into Bruce Furnace
      i. Total Wet Oxidation Time ~40 minutes
   c. Oxide Growth = ~ 5000A = ~0.5 µm
4. Photolithography (Pillar Mask)
   a. Resist 1818
   b. Spin 4000 rpm
   c. Spin Time 60 seconds
   d. Pre-Bake 115˚C
   e. Bake Time 60 seconds
   f. Expose Time ~8.5 seconds
   g. Developer 319
   h. Develop Time ~50 seconds
   i. Rinse Time 1:00 minute (water running in beaker)

   Notes: The expose and develop times vary – be sure the corners of the pillars come out nicely. When developing, be sure to NOT be too vigorous; a gentile 'swish' is sufficient.
5. Wet Etch: Oxide exposed to create an Oxide Mask
   a. Type BOE
   b. Time 8-12 minutes
   c. Rinse Time 5 minutes (with water running into beaker)

   Notes: The etch time varies depending on the oxide thickness. It is important not to over-etch because the features under the PR could be compromised. Another common way to damage the underlying oxide mask is to create turbulence while etching; this will allow the BOE to get under the PR, so be sure to keep sample still while it is etching in the BOE bath.
6. Strip Resist
   a. Stripper Acetone & Isopropyl
   b. Spin 4000 rpm
   c. Time 60 seconds (20 sec acetone / 20 sec isopropyl / 20 sec dry)
   d. Bake 115˚C
   e. Time 60 seconds
7. Plasma Etch (ICP Plasma Therm)
   a. Lei_pllr.prc
      i. RF_1 60
      ii. RF_2 315
      iii. O2:SF6 30:55
      iv. Pressure 80 mTorr
      v. Backside Cool OFF
      vi. Etch Time 28-30 minutes
      vii. Height 25-28 um

   Note 1: If the etch time is too long, the SiO_2 will be etched off - - this is NOT acceptable for the final samples because it results in rough pillar tops. We want the top of the pillar to be as smooth as possible.

Note 2: This etch is really all about SHAPE, not so much about height. We should sacrifice height for a good shape. The sloped sides shallow enough such that sputtering will produce a good cover, but not too shallow such that there is a potential for the structure to crash into the sides when testing.

8. Wet Etch: Strip Oxide Mask
    a. $HF:H_2O$ 1:2
    b. Time 10-15 minutes

Notes: Steps 7 & 8 should be done immediately before putting the wafers into the MRC chamber so as to ensure that the surface is nice and clean for CrAu deposition. This will ensure good adhesion between the Si surface and the Cr adhesion layer.

9. Piranha Clean
    a. $H_2SO_4:H_2O_2$ 2:1
    b. Temp ~115˚C
    c. Time 10:00 minutes
10. Chrome-Gold Deposition
    a. Lei_CrAu_300nm.prc
        i. 3:00 Chrome Presputter
        ii. 0:30 Chrome Seed Layer
        iii. Opp. Power 165 W
        iv. 7:30 Gold Sputter 300nm
        v. Opp. Power 500 W

        vi. Spin 4 rpm
        vii. Starting Pressure ~1.8e-6 Torr
        viii. Argon Flow 71.7
        ix. Opp. Pressure 13.65 mT
        x. Opp. Power 500 W
11. Dicing
    a. Protective PR
        i. Resist 1818
        ii. Speed 4000 rpm
        iii. Spin Time 60 seconds
        iv. Pre-Bake 115°C
        v. Bake Time 60 seconds
    b. Mount on dicing wafer using PR
        i. Resist 1818
        ii. Speed 4000 rpm
        iii. Spin Time 30 seconds
        iv. (Place Pillar wafer on Dicing wafer)
        v. Pre-Bake 115°C
        vi. Bake Time 4 minutes
    c. Apply Blue Backside tape

d. Dice
    i. Index 1 2.05mm
    ii. Index 2 6.05mm
    iii. Height (0.475mm)* (These vary from wafer to wafer)
    iv. Thickness (0.980mm)* (These vary from wafer to wafer)
    v. Angle 90
    vi. Speed 5
    vii. Diameter 75 mm
e. Strip & Sort
    i. Dirty Bath of Acetone (remove most of PR and Blue Tape)
        1. Soak overnight (roughly 12-15 hours)
    ii. Clean Bath of Acetone
    iii. Second clean bath of Acetone
    iv. Dirty bath of Isopropyl
    v. Clean bath of Isopropyl
    vi. Dry by laying (face up) on tech-wipe
    vii. Try to keep track of which quarter the pillars came from

12. Store according to quarter
    a. Ruthenium deposition with structures

Process Notes: As stated above, we want a pillar with a nicely sloped side that is neither too shallow, nor too steep. Most importantly, we want a clean, near-mirror finished top such that the contact bump makes contact with as flat of a surface as possible. This also makes it easier to find the contact spot when analyzing the samples after testing.

End of Pillar Fabrication

A.3.2 Force Sensor Structure

A. Backside Window Process: Handle Side

1. Start with an SOI Wafer
    a. Device Side
        i. Silicon
        ii. 5.25 +/- 0.1 µm
        iii. (1 0 0) Orientation
        iv. P-type Doping: Boron
        v. 1-10 Ω cm Resistivity
        vi. Polished
    b. Isolation Layer
        i. SiO_2
        ii. 1.0 µm
    c. Handle Side
        i. Silicon

ii. 450 +/- 25 µm
iii. (1 0 0) Orientation
iv. P-type Doping: Boron
v. 1-10 Ω cm Resistivity
vi. Polished

2. Standard Pre-Oxidation Clean
    a. Remove Organics / Metals (Piranha Clean)
        i. H_2SO_4:H_2O_2 2:1
        ii. Temp ~115˚C
        iii. Time 10:00 minutes
    b. Rinse
        i. Auto-rinser: 1 run (4 Cycles)
    c. Dewet (Native Oxide Removal)
        i. HF:H_2O 1:50
        ii. Time 0:15 seconds
    d. Rinse
        i. Auto-rinser: 1 run (4 Cycles)
    e. Remove Metallic Impurities
        i. H_2O:HCl:H_2O_2 6:1:1
        ii. Temp 95˚C
        iii. Time 10:00 minutes
    f. Rinse
        i. Auto-rinser: 1 run (4 Cycles)
    g. Rinser / Dryer
        i. Time 300 seconds
3. Standard Wet Oxidation
    a. Load Wafer into Quartz Boat
        i. Don't touch with hands!
    b. Load boat into Bruce Furnace
        i. Total Wet Oxidation Time ~40 minutes
    c. Oxide Growth = ~ 5000A
4. Protective Coating
    a. Wafer DEVICE SIDE
    b. Resist 1827
    c. Spin 4000 rpm
    d. Spin Time 60 seconds
    e. Pre-Bake 115˚C
    f. Bake Time 2 minutes

Note 1: Be sure to SCRUB spinner surface before using (Acetone & Isopropyl)
This prevents dirtying of the handle side when spinning the device side
Note 2: Be sure to SCRUB hot plate surface before using (Acetone & Isopropyl)
This will prevent scratching of handle side while pre-baking

5. Photolithography (Mask 1: Backside windows)
    a. Wafer HANDLE SIDE

b. Resist 1818
c. Spin 4000 rpm
d. Spin Time 60 seconds
e. Pre-Bake 115˚C
f. Bake Time 60 seconds
g. Expose Time ~8.5 seconds
h. Developer 319
i. Develop Time ~50 seconds
j. Rinse Time 1:00 minute (water running in beaker)

Notes: The expose and develop times vary – be sure the corners of the windows come out sharp.

6. Touch-up & Edge Seal
    a. Handle Side: Use 1827 to fill in the outer-most set of backside windows
        i. This will help ensure fortify the structural integrity of the wafer after the backside windows have been etched
        ii. Use a lab q-tip to do the 'painting'
        iii. Place the wafers on 6-prong spacers to ensure that the device side is not touching any surfaces while touching up and drying
    b. Let dry for 24 hours
    c. Device Side Re-coating
        i. Flip wafer over and fill in any flaws in the device side coating
        ii. Apply PR liberally - usually takes about 0.25 worth of a pipette of 1827 to do this
        iii. Again, use a lab q-tip to do the spreading / 'painting'
    d. Let dry to 48 hours
    e. Edge Sealing
        i. Use a lab q-tip to apply a liberal amount of PR to the edges

    Notes: This process will protect the wafer during the oxide etch. We are using the oxide as a mask. This protective step allows us to keep the integrity of the SiO_2 in areas that we want to protect. The better the oxide mask, the better the product.
7. Wet Etch: Oxide exposed to create an Oxide Mask
    a. Type BOE
    b. Time 8-12 minutes
    c. Rinse Time 5 minutes (with water running into beaker)

    Notes: The etch time varies depending on the oxide thickness. It is important not to over-etch because the features under the PR could be compromised. It is also important not to under-etch, because the TMAH will not be able to etch the underlying Si if the oxide is not removed.
8. Strip Resist
    a. Stripper 1165
    b. Temp 90-95˚C
    c. Agitation 300 rpm
    d. Time 15 minutes
    e. Rinse 5 minutes (water running in beaker)

9. Piranha Clean
    a. H_2SO_4:H_2O_2 2:1
    b. Temp ~115˚C
    c. Time 10 minutes
    d. Rinse 5 minutes
10. Anisotropic Si Etch
    a. Etchant TMHA
    b. Temp 75-80˚C
    c. Agitation 300 rpm
    d. Time ~24 Hours
    e. Rinse 5 minutes (water running in beaker)

Note 1: This etch should take place over 3-4 days. While the hot plate is on, use a glass cover because the TMAH will etch plastic and aluminum foil. Take the wafers out of the TMAH at night.

Note 2: You will know when you have reached the insulating layer of oxide because the windows will have an obvious color change.

Note 3: Be sure that the windows are fully opened. Remember that it is hard to over-etch this step because the etch will terminate in the vertical direction when it reaches the insulating layer.

Note 4: The thickness at the opened up windows is extremely thin. For here on, be very careful when handling these wafers because they are delicate. Sometimes you may get 'wrinkling' in these areas – this is not a problem, it is normal.

11. Remove Oxide Mask
    a. Etchant BOE
    b. Time 10-12 minutes
    c. Rinse 5 minutes (water running in beaker)

B. Contact Bump Process: Device Side

1. Piranha Clean
    a. H_2SO_4:H_2O_2 2:1
    b. Temp ~115˚C
    c. Time 10 minutes
    d. Rinse 5 minutes
2. Photolithography (Pillar Mask)
    a. Resist 1818
    b. Spin 4000 rpm
    c. Spin Time 60 seconds
    d. Pre-Bake 115˚C
    e. Bake Time 60 seconds
    f. Expose Time ~8.5 seconds
    g. Developer 319
    h. Develop Time ~50 seconds
    i. Rinse Time 1:00 minute (water running in beaker)

Note 1: The expose and develop times vary – be sure not to over-expose. You can tell if the bumps are over exposed if the smallest row of bumps is gone. Another good way to tell if you're over exposed is if there are 'dots' in the centers of the circles. This is a very tough round of lithography, it takes a lot of time to perfect the recipe for that given day – the balance between exposure time and develop time must be perfect to get good results.
Note 2: Sometimes HMDS must be used to promote adhesion between the substrate and the PR. To use this, spin the wafer with HMDS at 4000 rpm and bake at 155 for 90 seconds then let the wafer sit for a couple of hours. When you come back to them (after two hours or so), they will be ready to spin with PR as per the instructions above. Be sure that you don't use too much PR in this round of PR, this can cause problems with the exposure and develop times.

3. Reflow PR
    a. Temp 165˚C
    b. Time 3 minutes
4. Plasma Etch Bumps
    a. Lei_rbmp.prc
        i. RF_1 83
        ii. RF_2 400
        iii. O_2:SF_6:Ar 30:8:25
        iv. Pressure 150 mTorr
        v. Backside Cool ON
        vi. Etch Time 9 minutes

Note 1: USE A SECOND WAFER for this etch. Put a dummy wafer UNDER the sample wafer in order to prevent the windows from being blown out by the pressurized backside cooling He. Scott claims that the ICP chuck cannot take two stacked wafers, BUT IT CAN BECAUSE THIS IS THE WAY I HAVE ALWAYS DONE THIS ETCH! You just have to be careful when placing the ceramic cover over the sample and when screwing it down. The result is a nice constant backside cooling pressure of about 2.9-3.0 He Torr.
Note 2: This etch should remove ALL of the PR. If the PR is not all gone upon inspection under the microscope, then it has been under etched. In this case, put the wafer back in the ICP for an appropriate amount of time such that all of the remaining PR is removed.

C. Force Structure Process: Device Side

1. Photolithography (Force Structure Mask)
    a. Resist 1827
    b. Spin 4000 rpm
    c. Spin Time 60 seconds
    d. Pre-Bake 115˚C
    e. Bake Time 60 seconds
    f. Expose Time ~8.5 seconds
    g. Developer 319
    h. Develop Time ~60 seconds
    i. Rinse Time 1:00 minute (water running in beaker)

2. Plasma Etch Structures
    a. Lei_can.prc
        i. RF_1 50
        ii. RF_2 100
        iii. O_2:SF_6:Ar 6:8:3
        iv. Pressure 5 mTorr
        v. Backside Cool ON
        vi. Etch Time 20 minutes

    Note 1: Again, use a dummy wafer to retain backside cooling He pressure.
    Note 2: It will be obvious when the samples are done, the oxide under between the structures (in the window openings) will be completely expose in all parts of the wafer.
3. Dicing
    a. Apply Blue Backside tape
    b. Protective PR
        i. Resist 1818
        ii. Speed 4000 rpm
        iii. Spin Time 60 seconds
        iv. Pre-Bake 115
        v. Bake Time 60 seconds
    c. Dice
        i. Index 1 4.15mm
        ii. Index 2 2.50mm
        iii. Height (0.425mm)* (These vary from wafer to wafer)
        iv. Thickness (0.450mm)* (These vary from wafer to wafer)
        v. Angle 90
        vi. Speed 5
        vii. Diameter 75 mm
    d. Strip & Sort
        i. Break into quarters
            1. Along dicing paths
            2. Cut Blue Tape with razor resulting in 4 quarters of diced samples
        ii. Dirty Bath of Acetone (remove most of PR and Blue Tape)
            1. Soak over night
        iii. Clean Bath of Acetone
        iv. Second clean bath of Acetone
        v. Dirty bath of Isopropyl
        vi. Clean bath of Isopropyl
        vii. Dry by laying (face up) on tech-wipe

    Note: Sometimes an acetone bath is not enough to remove the protective dicing PR. In this case, you must use 1165. If you put the wafer in 1165 at 100C for 24-48 hours (in a petri dish WITH A COVER), this will usually do the trick. You can tell by a simple inspection under a microscope. If this still isn't enough, you could try a piranha clean for 20-30 minutes.
4. Store according to quarter

End of Force Sensor Fabrication

A.3.3 Clean and Deposition Process

Test Sample Clean and Deposition Process

1. Sample Selection
    a. Select 18 good samples

    Note 1: Make sure that the contacts are in good condition as well as the structures

    Note 2: We only deposit 18 at a time because there are only 18 slots for cleaning / releasing
2. Release
    a. $HF:H_2O$ 1:2
    b. Time 10 minutes
    c. Rinse 5 minutes (water running in beaker)
3. Piranha Clean
    a. $H_2SO_4:H_2O_2$ 2:1
    b. Temp ~115˚C
    c. Time 10 minutes
    d. Rinse 5 minutes (water running in beaker)
4. Dry
    a. Place face-up on a tech-wipe
5. Chrome-Ruthenium Deposition
    a. Place sample in deposition holder (centered)
    b. Load sample holder directly under Ru target
    c. Ryan_12mT_2nmCr_300nmRu.prc
        i. 3:00 Etch
        ii. 3:00 Pre-sputter
        iii. 0:20 Cr Sputter (@ 4 rpm)
        iv. 3:00 Pre-sputter
        v. 3:30 Ru Sputter (@ 0 rpm)
            1. Pump Time ~6 hours
            2. Base Pressure < 1.6×10^{-7}
            3. Ar Flow 61.7
            4. Operating Power 300 W
            5. Operating Pressure 12 mTorr
            6. DC Bias ~410-440
6. Inspect and Sort

End of Test Sample Clean and Deposition Process

A.3.4 Sample Naming Convention

Each sample has a unique name that is composed of the oxidation date, the wafer number that batch, the quarter of the wafer that the sample is from, and the material deposition date. Refer to Figure A.1 below.

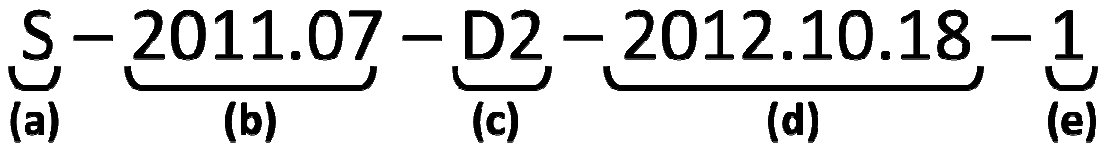

Figure A.1 Sample Naming Convention with each field described below

(a) *Pillar / Structure:* [P / S] This field is used to identify the type of sample. Use 'P' for pillar or 'S' for structure
(b) *Oxidation Date:* [Year.Month] This field contains the year and month of the oxidation.
(c) *Wafer and Location:* [Wafer Location] The first charater is a letter that identifies the specific wafer in the oxidation run, the second charater is a number indicating the section of the wafer that the sample was harvested from.
(d) *Deposition Date:* [Year.Month.Date] This is the date of contact material deposition.
(e) *Test Sample:* [Test Number] This is the test number of that specific sample. For example if the sample was tested third, this field would read '3'.

In addition to supplying every sample with a unique name, the entire fabrication process for that sample can be tracked via its name. Note that this information can be used in conjunction with the lab notebook to identify each fabrication step. Thus, if there is a particular problem, the issue can be tracked back to the source using the sample number and the cleanroom lab notebook.

A.3.5 Force Sensor Wafer Layout

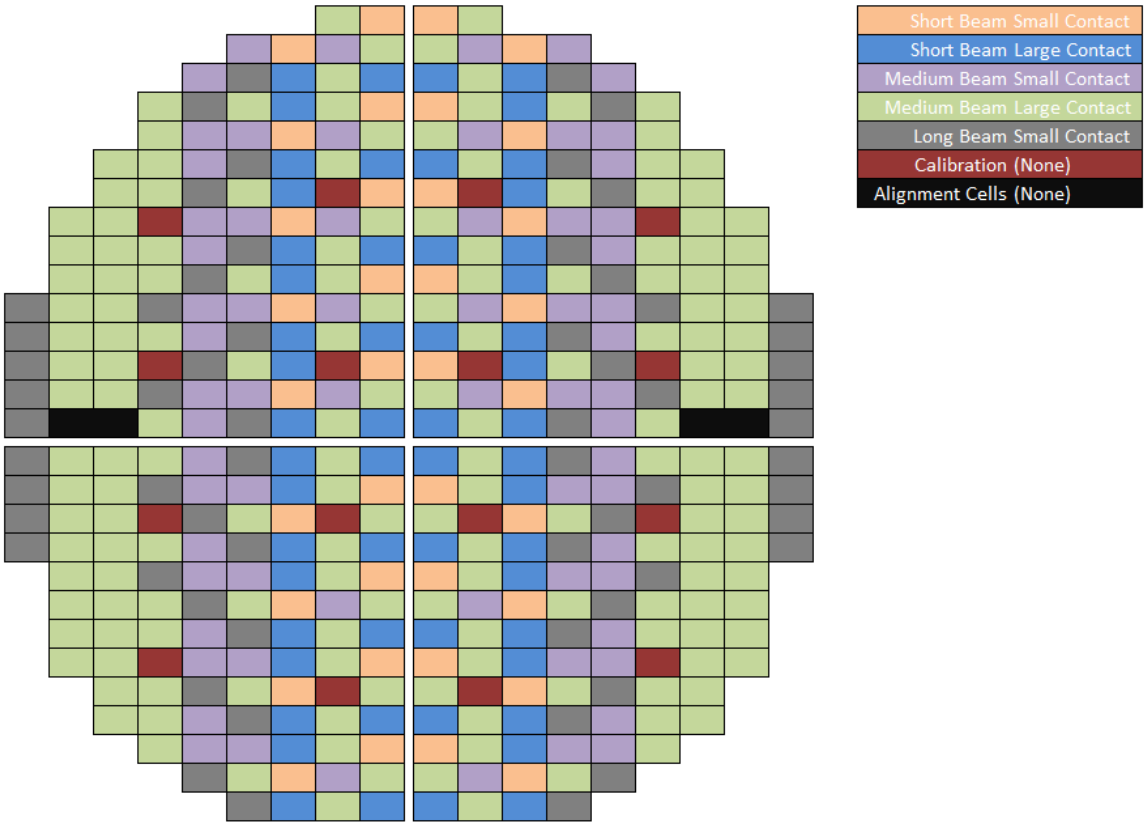

Figure A.2 Schematic of sample layout on a wafer.

Figure A.2 provides the layout of samples on a wafer after fabrication. General information about each of the sample types is contained in Table A.1.

Table A.1 General information about each of the sample types. The colors are consistent with the figure above.

Beam Type	Contact Type	Length (µm)	Bump Radius (µm)	Wafer Count
Short	Small	90	3	54
Short	Large	90	6	34
Medium	Small	120	3	162
Medium	Large	120	6	60
Long	Small	200	3	44

**Ideal thickness for all: 4.5µm*

A.3 Test Sample Analysis

Using ANSYS, models for each beam type were built for static and dynamic analysis. Figure A.3 is a schematic of the test structure shape. Each of the dimensions represented in the figure are defined in Table A.2 for short, medium, and long beams, respectively.

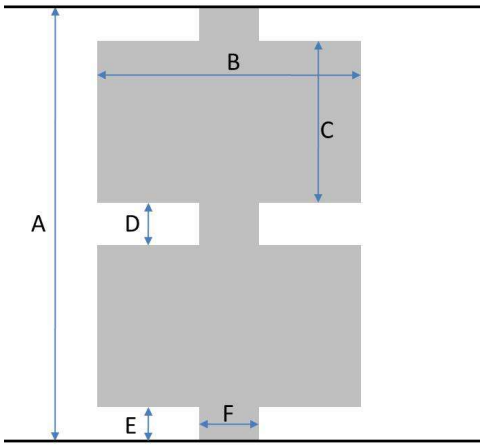

Figure A.3 Test structure shape schematic.

Table A.2 Test structure dimensions.

		Short Structure	**Medium Structure**	**Long Structure**
	Feature	Dimension (µm)	Dimension (µm)	Dimension (µm)
A	Length*	90	120	200
B	Paddle Width	40	40	50
C	Paddle Length	35	40	50
D	Middle Spacing	10	20	50
E	End Spacing	5	10	25
F	Beam Width	20	20	15

These dimensions are ideal dimensions for the test structures. The ideal thickness for all of the beam types is 4.5 µm. However, it is important to note that all of these dimensions vary slightly from sample to sample due to inherent and unavoidable imperfections in the fabrication process and the variance in the device layer thickness of the wafer. For both the static and dynamic analyses, the material was taken to be silicon with a modulus of E = 1.8×10^5 MPa, poisson's ratio of ν = 0.28, and a mass density of 2.33×10^{-15} kg/µm^3 [1].

A.3.1 Static Analysis

The static analysis of the test structures fills two purposes: first, to determine the stiffness for each type of structure, and second, to determine the relationship between the deflection of the center of the beam and the angular rotation of the beam at the middle of the paddle (the δ-θ relation). Both of these properties are necessary for accurate calculation of contact force. The δ-θ relation is used to convert the A-B signal acquired from the AFM into a vertical displacement of the center of the force structure; this is discussed in greater detail in the Test Program section. This vertical displacement can then be equated into a contact force via the structure stiffness.

Five models of each of the beam type were simulated using the dimensions and material properties specified in the previous section and with thicknesses that varied from 2.5-4.5 µm by steps of 0.5 µm. For each of these thicknesses, the stiffness and the δ-θ relations were calculated by applying a concentrated 200 µN force at the center point of structure while applying clamped boundary conditions (zero displacement and zero slope) at both ends of the structure. Note that imperfect end conditions (such as the bending of the membrane) were not considered. Such an effect would result in lower stiffnesses as compared to the calculated values presented here. The three-dimensional solid element Solid186 was used to finely mesh the geometry, and the system was solved in one load step (more load steps were not necessary for this simple system). Linear elastic behavior was assumed, plasticity was not considered.

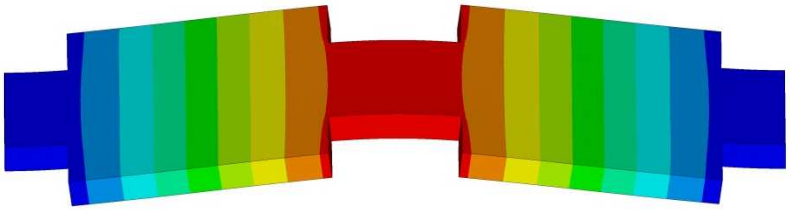

Figure A.4 A medium structure bending under 200 µN force represents the typical deformed shape.

Figure A.4 shows a typical result. As stated above, the deflection of the structure was measured at the center point of the beam while the angular rotation of the structure was measured at the center of one of the paddles; note that the symmetry of the structure results in the absolute value of rotation of the paddles to be identical to each other.

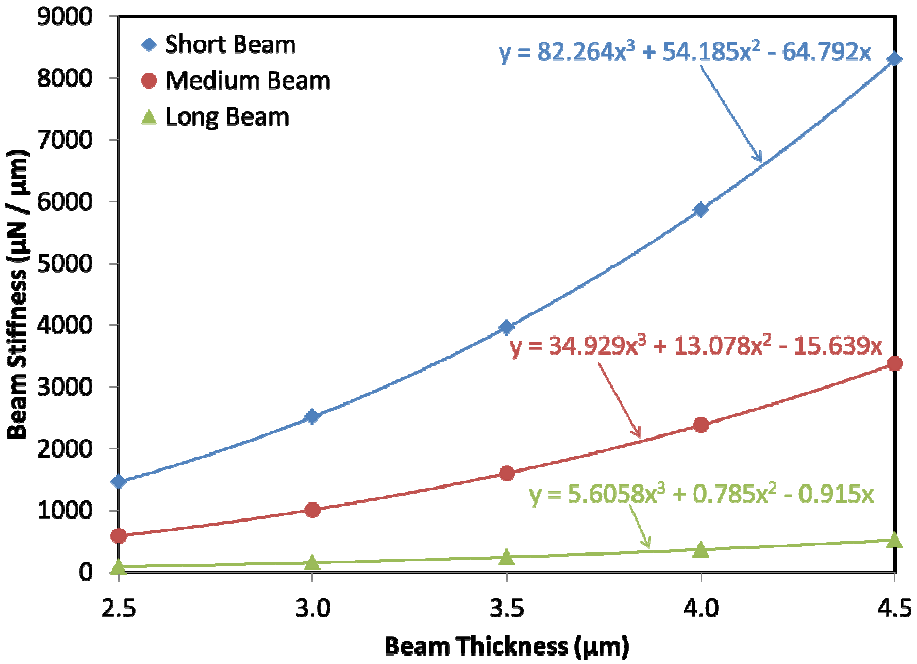

Figure A.5 Beam stiffness vs beam thickness for each beam type.

Figure A.5 presents the model results for beam stiffness for all three beam types. Each set of points was fitted with a cubic polynomial based on theory. Note that the parabolic and linear terms are expected because of the non-uniform shape of the force structures; in essence, the presence of the paddles causes the stiffness to not be directly proportional to the cube of the thickness. These relationships are programmed into the testing and post-processing programs.

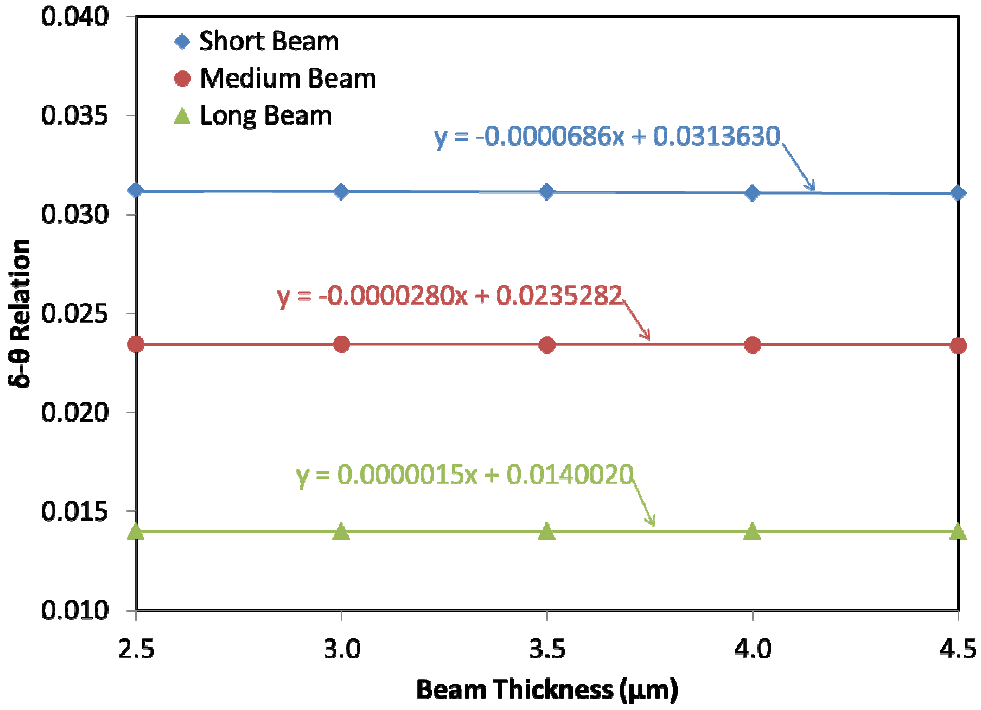

Figure A.6 δ-θ relation vs beam thickness for each beam type.

Figure A.6 presents the model results for the δ-θ relation for all three beam types. Each set of points has a linear curve-fit. However, because the slopes are so small that the δ-θ relation should be considered constant for each beam type. These relationships are also programmed into the testing and post-processing programs.

Based on the data contained in the plots above, a very good estimate of contact force can be calculated from the AFM A-B signal, if the thickness is known. To determine the thickness, dynamic excitation of the calibration structures can be used. Alternatively, any randomly picked sample could be broken in a cross-sectional manner such that the thickness could be measured using the 'measure' functionality of an SEM.

A.3.2 Dynamic Analysis

The purpose of the dynamic analysis is to find the theoretical natural frequencies of the test structures. These natural frequencies are important characteristics to know when conducting high speed testing. Though the testing frequency is not on the same order as the natural frequency of the force structures, phenomena such as contact bounce and vibration upon

release could be present. It is important to be able to distinguish characteristics of the damage mechanisms and the characteristics of the testing structures.

Six models of each of the beam type were simulated using the dimensions and material properties specified in the previous sections. Thicknesses were varied from 2.5-5.0 µm by steps of 0.5 µm. For each of these thicknesses, the Block Lanczos eigenvalue extraction method was used to calculate the first three natural frequencies for each beam type with clamped boundary conditions at both ends. The three mode shapes are illustrated in Figure A.7. The three-dimensional solid element Solid186 was used to finely mesh the geometry, and the system was solved in one load step. Linear elastic behavior was assumed and structural damping was not considered.

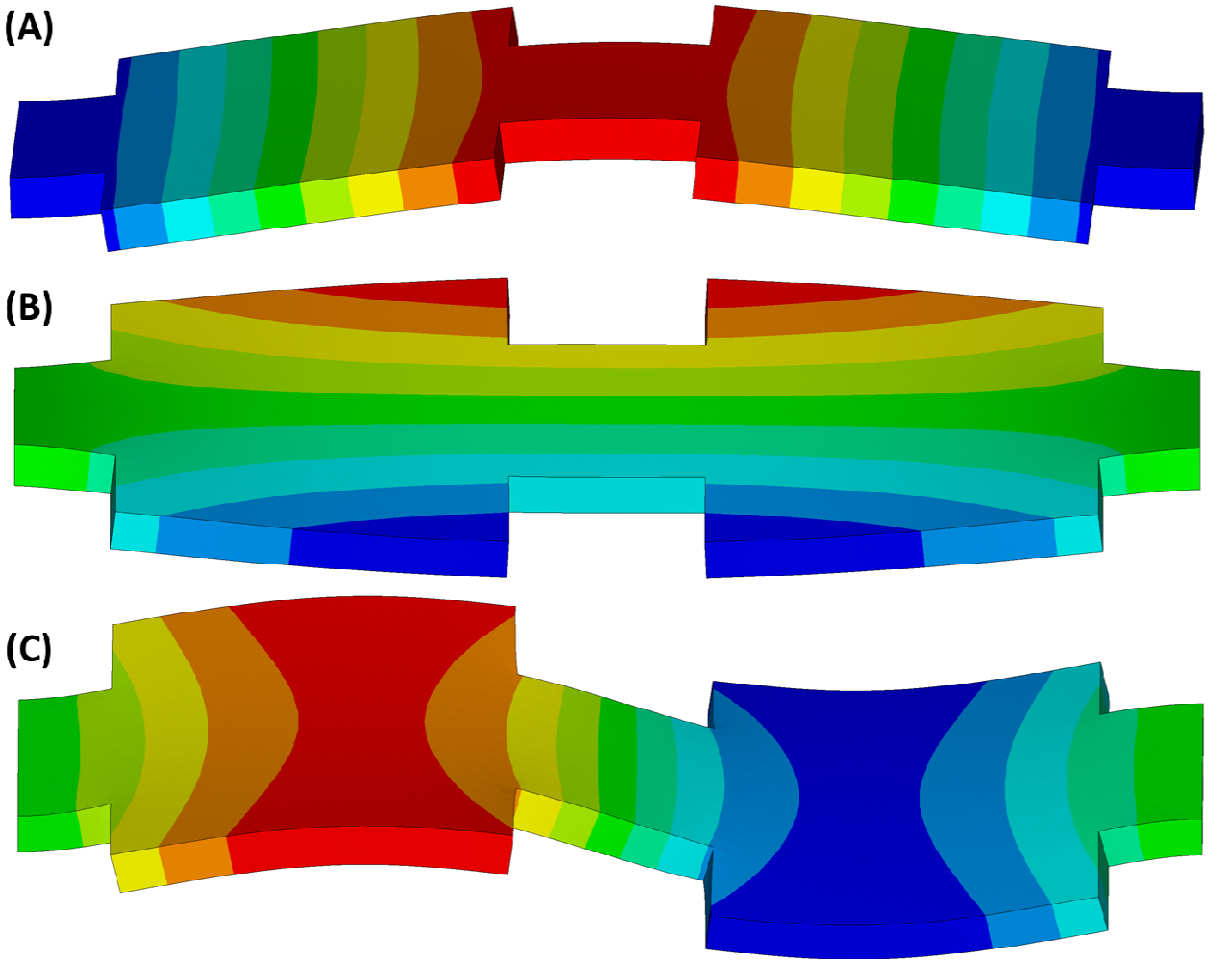

Figure A.7 The first three mode shapes.

Figure A.8 presents the first three natural frequencies for each of the beam types. Note that the natural frequency varies roughly linearly with thickness, which is expected based on theory.

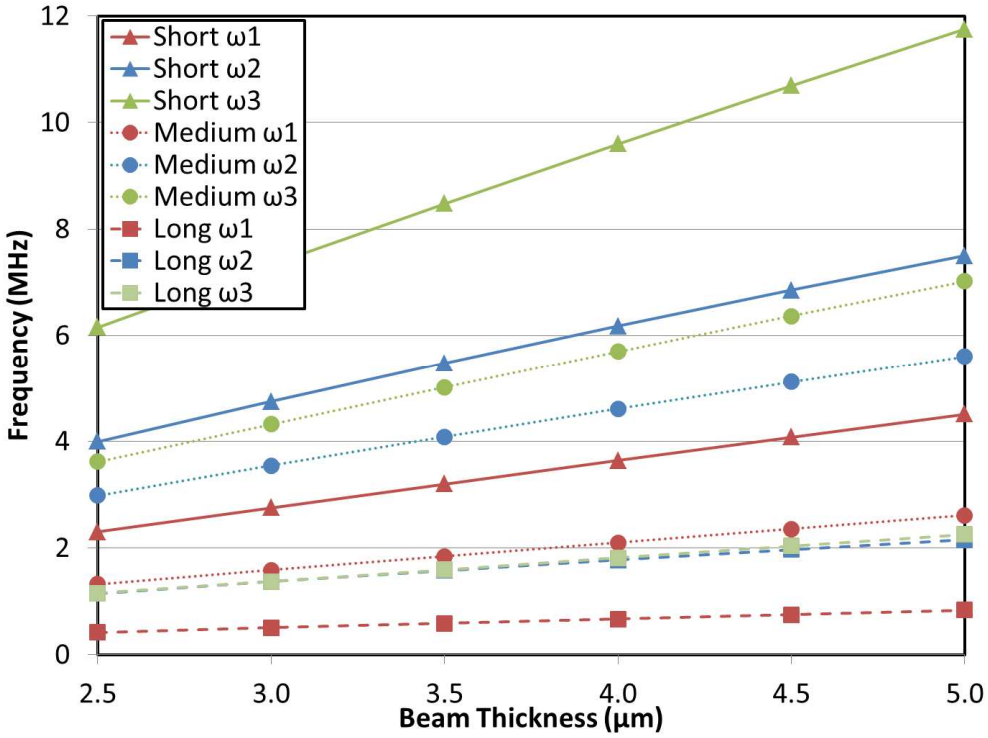

Figure A.8 Dynamic analysis results for the first three natural frequencies of each beam type.

These results can be used in the interpretation of the A-B signal to determine is there is contact bounce or oscillation upon release. In the real system, it seems reasonable that there might be some damping. In this case, the results presented above provide a ballpark estimate of the frequencies of vibration.

A.4 Testing Program

The contact experiments are performed on a modified JEOL SPM5200. Once loaded into the SPM and properly aligned, the experiments are controlled by a custom-built testing program designed in LabVIEW®. This section will introduce the basic functionality of the test program. It is important to note that there is entirely too much programming associated with the test program to cover every sub-program and the theory behind each. Thus, an adept knowledge of LabVIEW® and general programming flow is highly recommended for those altering the program.

A.4.1 Overview

There are essentially three main tasks that the testing program simultaneously performs: output, input, and data storage. Post processing of the raw data is necessary, thus a post processing program has also been constructed to do this task. In the test program, output, input, and data storage all have dedicated loops that are continuously and simultaneously

running while the test program is running. It should be noted that the infrastructure for test automation (in the form of a fourth loop with inputs and outputs) has been built into the test program, but to date, the automation algorithm has not been completed. Output and input are both done via the NI PCI-6259 DAQ.

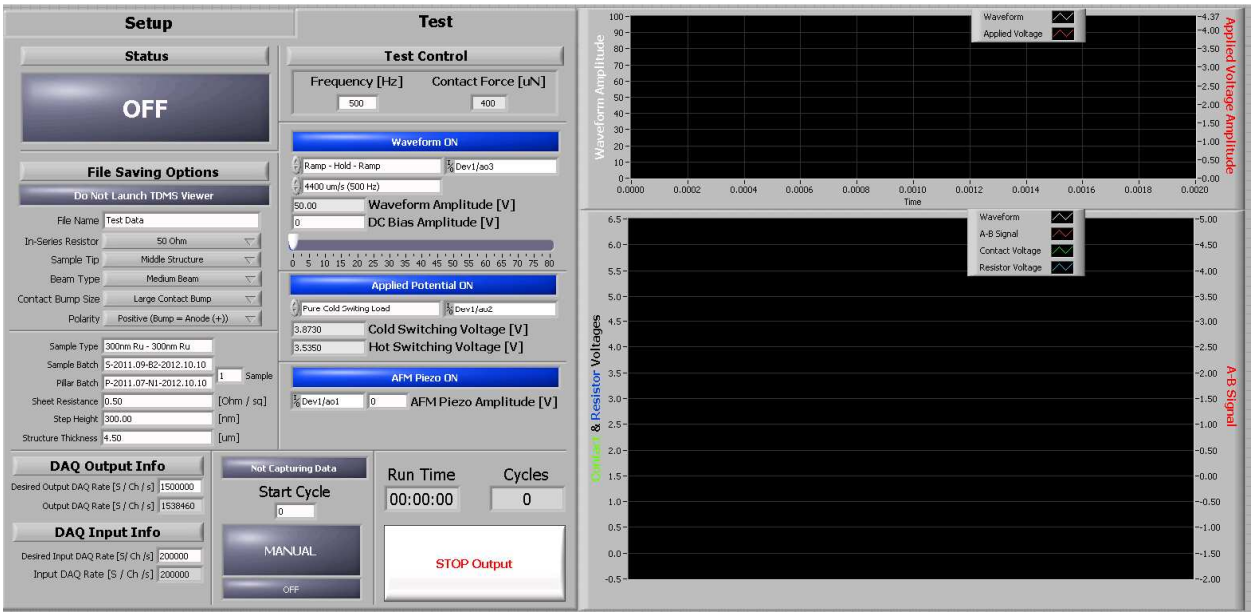

Figure A.9 The test program front panel.

Figure A.9 shows the front panel of the test program. The right half of the front panel is composed of two waveform charts. The top chart is used to display select output data: actuation voltage and applied voltage waveforms. The bottom chart is used to display select input data: read-in actuation waveform, A-B signal, contact voltage, and resister voltage. The generation and reading of each of these signals will be covered in the sections below. The left half of the front panel has two tabs, one for each one of the two operating modes: Setup Mode and Test Mode.

A.4.2 Setup Mode

The Setup Mode is used by the operator after the sample is loaded into the tester, before the test is conducted. The purpose of this mode is to help the operator align the sample and ensure proper contact is being made while also providing an opportunity to establish values such as DC bias, AFM Piezo voltage, and actuation voltage waveform amplitude for the up-coming test.

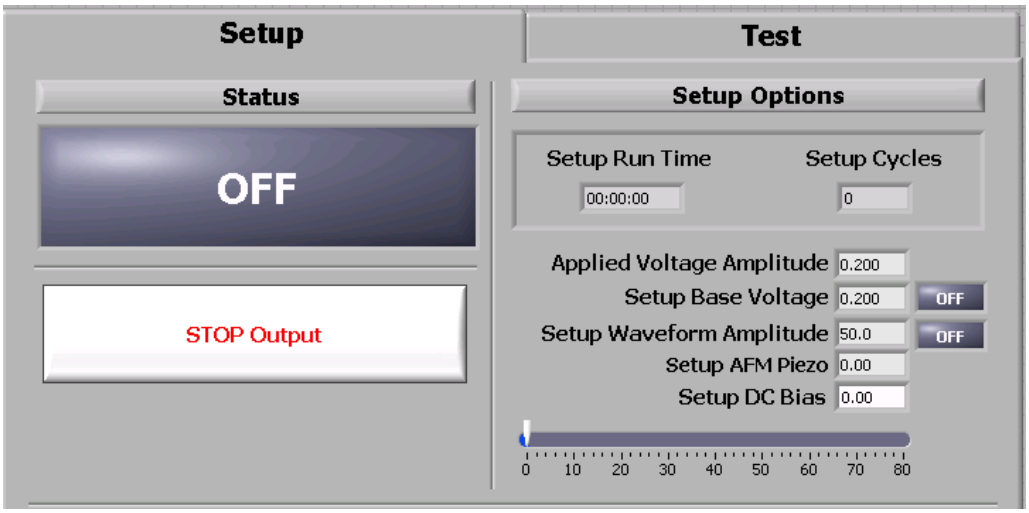

Figure A.10 Setup Mode panel.

Figure A.10 presents the options panel for the Setup mode. Testing in Setup Mode is done at 1 Hz, this mode was designed to ensure that the operator could monitor every cycle while setting up the test, this property cannot be changed. Furthermore, by default, an applied voltage is always applied, unless the value is changed to zero. The following will describe the function and range (if applicable in [brackets]) for each of the features on this panel.

- *On / Off Indicator*: [OFF / SETUP RUNNING] This is the large grey indicator in the top-left of the Setup Mode options panel. When the program is running, the indicator reads 'SETUP RUNNING' and is green, indicating that the program is running properly. This indicator reads 'OFF' and is grey when the program is not running. Any time that the program is running and the indicator reads 'OFF', the program is not running correctly. In this case, the program should be stopped and re-started. If the problem persists, restart LabVIEW® and do not save changes made to the program while running.
- *STOP Output Button*: [STOP] This button is used to stop the program. This button should be used instead of the built-in 'stop execution' button built into LabVIEW®. The reason is that this button not only stops the loops running in the test program, but it also starts the termination sequence that ensures proper functionality of the hardware and software upon the next run. These termination tasks include clearing of all the buffers and a re-initiation of all hardware channels (in and out). For this reason, the program will take a few moments to stop running after this button has been pushed. The only situation in which the built-in LabVIEW® 'stop execution' button should be used is if the program is hanging. In all other cases, this white STOP Output Button should be used to stop the program.
- *Setup Runtime Indicator*: [HH:MM:SS] This indicator is for the operator's convenience; its function and purpose is straight-forward.

- *Setup Cycles Indicator*: [Cycles] This indicator counts the total number of cycles performed in the Setup Mode. As stated above, the purpose of this setup mode is to establish all of these values for the succeeding test. This process is straight forward, but should be done with some urgency because these setup cycles are not counted toward the testing total number of cycles. Thus the fewer cycles it takes to set these parameters, the better.
- *Applied Voltage Amplitude*: [$-10 \leq V \leq 10$] This control sets the amplitude of the voltage applied over the contact. As stated above, this feature cannot be turned off (it can, however, be set to zero if desired). While this value if greater than zero, a constant voltage of that magnitude is applied over the contact. This feature comes in handy when approaching the pillar – this will allow the operator to see if proper electrical contact is made between the pillar and contact during and after approach. By default, the value of this voltage is set to 0.200V because this is a high enough voltage to evaluate the condition of the electrical conduction while setting up, but not high enough to cause significant contact damage.
- *Setup Base Voltage*: [$-10 \leq V \leq 10$] This control sets the hot switching voltage applied to the contact. This feature can be turned on or off via the on / off button to the right of the input field. While this feature is off, the voltage applied over the contact is a 'pure hot switching' waveform; this is to say that the applied voltage is contestant. While this feature is engaged, the value of the Setup Base Voltage becomes the hot switching voltage, while the Applied Voltage Amplitude becomes the cold switching voltage.
- *Setup Waveform Amplitude*: [$0 \leq V \leq 80$] This control sets the amplitude of the setup ramp-hold-ramp waveform. This feature can be turned on or off using the on / off button to the right of the input field. It is important to note that the Amplitude + DC Bias should not exceed 80V because this is beyond the operating limits of the test piezo.
- *Setup DC Bias*: [$0 \leq V \leq 80$] This control sets the magnitude of the constant DC voltage applied to the test piezo. This feature cannot be turned off, but is by default set to zero. Again, it is that the Amplitude + DC Bias does not exceed 80V because this is beyond the operating limits of the test piezo. Note that this feature can be controlled two ways: by entering a value in the input field, or by sliding the slider directly below it.
- *Setup AFM Piezo*: [$-10 \leq V \leq 10$] This control sets the magnitude of the DC voltage sent to the AFM piezo. This piezo controls the elevation of the stage with respect to the testing structure. Positive voltages bring the pillar toward the structure; negative voltages move the stage away from the structure.

A.4.3 Test Mode

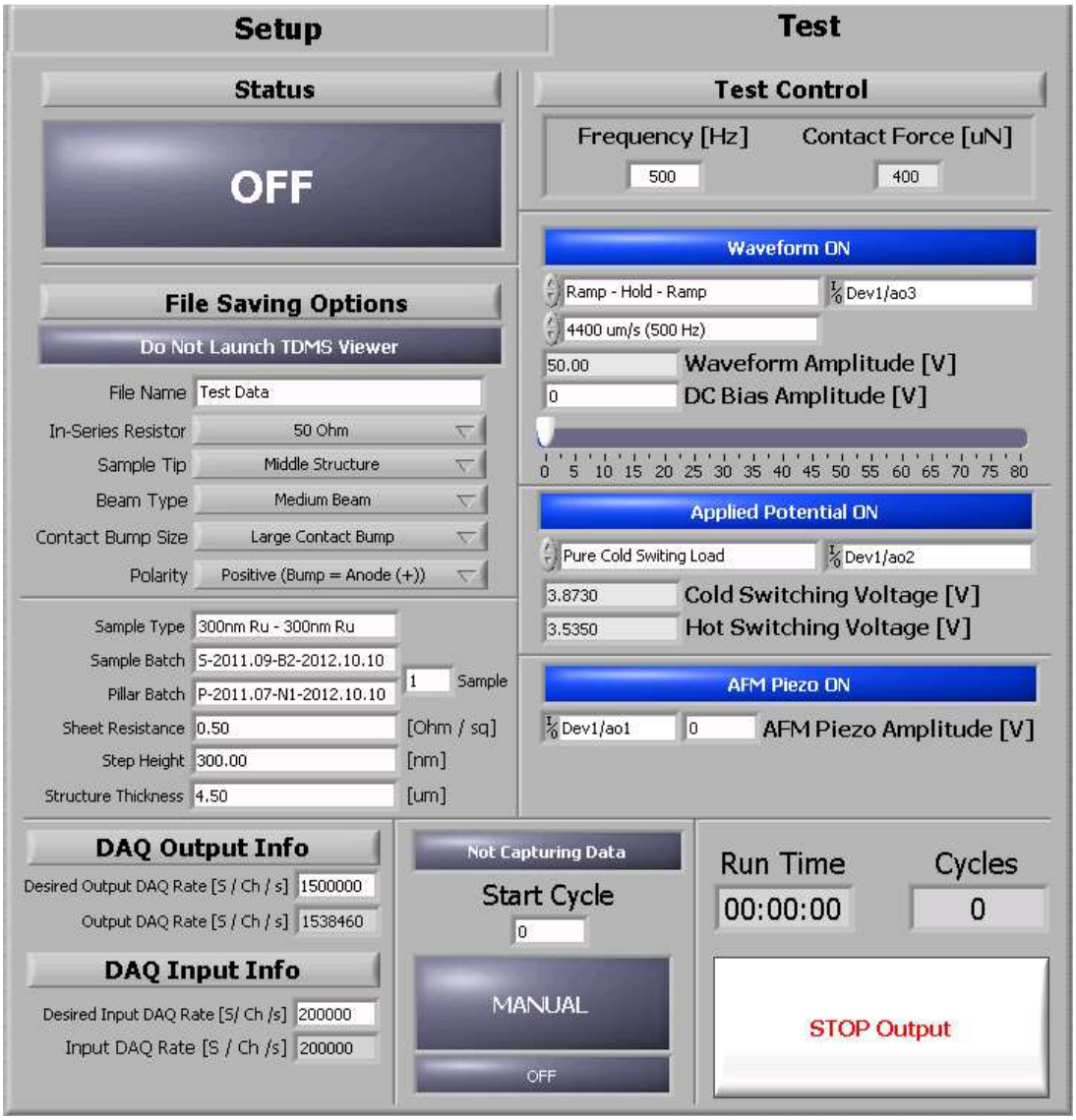

Figure A.11 Test mode panel.

The Test Mode is the mode in which contact testing is actually conducted. Figure A.11 presents the Test Mode Panel. As stated above, the cycles from the Setup Mode are not carried over into the testing mode. As explained below, most of the features of the testing program and adjustable on-the-fly. That being said, it is extremely important to make sure that the test information (all of the fields under the 'File Saving Options' heading as well as the Contact Force input) is properly filled in BEFORE the test is run. This will ensure that the data is properly logged and the program runs properly (with respect to the sample length, thickness, polarity, and resistance calculation).

- *On / Off Indicator*: [OFF / SETUP RUNNING] (see above description – this feature works the same as it works in the Setup Mode)
- *File Name*: This field controls the name of the output TDMS file that contains the raw data from the test. There is no specific naming convention for the tests because the tests are currently identified by the unique sample names, but a descriptive file name is highly recommended such that opening the file is not necessary to identify the test.
- *In-Series Resistor*: [5 Ohm/10 Ohm/20 Ohm/50 Ohm/100 Ohm/200 Ohm/500 Ohm/5k Ohm/95k Ohm] This drop-box is used to identify the in-series resistor used for the test. This value is not used in the testing program, but is saved in the TDMS file and used for post processing.
- *Sample Tip*: [Top Structure / Middle Structure / Bottom Structure] This drop-box is used the identify the structure tested. This identification is done with respect to the AFM optical microscope while the sample is loaded.
- *Beam Type*: [Short Beam / Medium Beam / Long Beam] This drop-box is used to identify the type of structure tested. It is important to input this field correctly before the test begins because the A-B signal guidelines on the input chart are based on this information.
- *Contact Type*: [Small Contact Bump / Large Contact Bump] This drop-box is used to identify the contact type. This information is not used in the testing program, but is saved in the TDMS file and used for post processing.
- *Polarity*: [Positive (Bump = Anode (+)) / Negative (Bump = Cathode (-))] This drop-box is used to identify the polarity of the test. Note that this feature DOES NOT change the direction of the current in the test system, that is done by wiring the test system in a reverse manner. This field is just used to identify the test.
- *Sample Type*: This field is used to identify the contact material and thickness. For example, 300nm Ru – 300nm Ru indicated that this is a Ru-Ru contact pair and each has a thickness of 300 nm. The convention is that the force structure identification goes first.
- *Sample Batch*: This field is used to identify the unique sample batch name as per the naming convention above.
- *Pillar Batch*: This field is used to identify the unique pillar batch name as per the naming convention above.
- *Sample*: This is the test number associated with the sample / pillar batch. For instance, if this were the fifth test done in a given batch of samples and pillars, ‘5’ would be entered in this field.
- *Sheet Resistance*: This measurement is taken after each deposition and should be reported with each test.
- *Step Height*: This field corresponds to the contact material thickness. This measurement is taken after each deposition and should be reported with each test.

- *Structure Thickness*: This field represents the measured thickness of the un-deposited sample. This measurement is taken up to four time in each quarter of the wafer, though thicknesses do not vary significantly. This thickness measurement is used to calculate the displayed guide lines in the input chart as well as the contact force in the post processing program. Thus it is important that this field is correctly filled out before the test begins.
- *Frequency*: [0 ≤ Hz ≤ 500] This field is used to control the test frequency in Hz. This property is adjustable on-the-fly. Currently <1 Hz testing is not supported, though this should be available in the coming weeks.
- *Contact Force*: [µN] This field is used to input the nominal contact force to run the test. When full automation is up and running, this force will be used for controlling the contact force. Until then, this field is just used to calculate the guidelines displayed on the input chart. Again, it is very important to input this value before the test begins.
- *Actuation Waveform Type*: [Ramp-Hold-Ramp / Ramp Up-Ramp Down] This choice-field is used to control the actuation waveform type. This is self-explanitory.
- *Ramping Velocity*: [4400 um/s (500 Hz) / 440 um/s (125 Hz) / 115 um/s (50 Hz)] This choice-field essentially controls the anatomy of the actuation waveform and is primarily designed for the ramp-hold-ramp actuation waveform (the other actuation waveforms were not considered when designing these options, though these options will apply to them). The '4400 um/s' option sets the total duty cycle of the entire actuation waveform to 50. The ramp up and ramp down each have a duty cycle of 25, and the hold has a duty cycle of 50 (both of these duty cycles are taken with respect to the 'on' portion of the pulse). Thus, if the testing frequency is set to 500 Hz and the sample spacing is properly set up to be 600 nm, the closing velocity and opening velocity would be equal to 4400 um/s (hence the option name). The '440 um/s' option sets the total duty cycle of the entire actuation waveform to 68.75. The ramp up and ramp down each have a duty cycle of 45.45, and the hold has a duty cycle of 9.10 (both of these duty cycles are taken with respect to the 'on' portion of the pulse). Thus, if the testing frequency is set to 125 Hz and the sample spacing is properly set up to be 600 nm, the closing velocity and opening velocity would be equal to 440 um/s. The '115 um/s' option sets the total duty cycle of the entire actuation waveform to 97.5. The ramp up and ramp down each have a duty cycle of 48.78, and the hold has a duty cycle of 2.56 (both of these duty cycles are taken with respect to the 'on' portion of the pulse). Thus, if the testing frequency is set to 50 Hz and the sample spacing is properly set up to be 600 nm, the closing velocity and opening velocity would be equal to 115 um/s.
- *Waveform Amplitude*: [0 ≤ V ≤ 80] (see above description – this feature works the same as it works in the Setup Mode)
- *DC Bias*: [0 ≤ V ≤ 80] (see above description – this feature works the same as it works in the Setup Mode) Again, it is that the Amplitude + DC Bias does not exceed 80V because this is beyond the operating limits of the test piezo.

- *Applied Potential Waveform*: [Pure Cold Switching / Hot Switching / Leading Edge Hot Switching / Trailing Edge Hot Switching] This choice-field is used to control the applied potential waverform type. Pure cold switching is a waveform in which the applied potential is only applied while the contact is in the steady-state closed position. Note that there are two features built into this waveform: a pinch-in effect and a mechanical delay shift. Both of these features ensure that the switch is fully closed while the applied voltage is being applied. The Hot Switching applied potential waveform can be used for 'Pure' hot switching, which is the application of a constant voltage throughout the entire switching cycle, or it can be used for hot switching cycle in which the hot switching voltage (on the leading and trailing edges) is lower than the cold switching portion of the waveform. Leading Edge Hot Switching applied potential waveform initiates at the start of the actuation waveform and terminates at the end of the cold switching portion of the waveform. Trailing Edge Hot Switching applied potential waveform initiates at the start of the cold switching portion of the waveform and terminates slightly after the end of the actuation waveform. The reason for the late termination is to ensure that there is an applied potential over the contact even if the adhesion causes the contact to stay closed after the termination of the actuation waveform.
- *Cold Switching Voltage*: [-10 ≤ V ≤ 10] This control sets the amplitude of the cold switching portion of the applied voltage waveform.
- *Hot Switching Voltage*: [-10 ≤ V ≤ 10] This control sets the amplitude of the hot switching portion of the applied voltage waveform.
- *AFM Piezo Amplitude*: [-10 ≤ V ≤ 10] This control sets the magnitude of the DC voltage sent to the AFM piezo. This piezo controls the elevation of the stage with respect to the testing structure. Positive voltages bring the pillar toward the structure; negative voltages move the stage away from the structure.
- *STOP Output Button*: [STOP] (see above description – this feature works the same as it works in the Setup Mode)
- *Runtime Indicator*: [HH:MM:SS] (see above description – this feature works the same as it works in the Setup Mode)
- *Cycles Indicator*: [Cycles] (see above description – this feature works the same as it works in the Setup Mode)
- *Data Capture Indicator*: [Not Capturing Data / Capturing Data] This indicator is grey and reads 'Not Capturing Data' when the program is not recording or writing data to the output field. The indicator turns green and reads 'Capturing Data' when the program is recording data and writing that data to the output file. Note that data is not captured for every single cycle of the test, thus this indicator will flash on and off throughout the test if the capturing mode is set to Auto (see below). If the capture mode is set to Manual (see below), then this indicator will only turn on when the operator pushes the Capture Data button (see below).

- *Data Capture Mode Button*: [Auto / Manual] This button is used to choose the data capturing mode. When the Data Capturing Mode is set to Auto, the program automatically acquires data based on the following criteria: the cycles 1 to 125, then 30 cycles surrounding the values of 10 to the powers of 2.15-2.95 by increments of 0.1, and then 30 cycles surrounding the values of 10 to the powers of 3.00 to infinity by increments of 0.05 (until the program is stopped). This allows for plotting in against a log scale with evenly spaces markers. When the Data Capturing Mode is set to Manual, the program only captures data when the operator presses the Capture Data button (see below), otherwise, the program does not record any data. When the Data Capture Mode Button is changed from Manual to Auto while the program is running, the program will re-initiate the cycle count to the number specified in the *Start Cycle* field and pick up the Auto mode of data capture (as explained above) starting at that cycle.
- *Capture Data Button*: [Off / Capture] This button is used by the operator to manually capture data. Note that this button only works when the Data Capture Mode is in Manual Mode.
- *Desired Output DAQ Rate*: [S/Ch/s] This field specifies the output DAQ rate in samples per channel per second. This rate is limited by the hardware. Furthermore, the *Actual Output DAQ* rate is set automatically by the hardware – the operator has no control over this number. Rather, the desired rate is more of a guideline rate that the operator provides to the hardware, and the hardware picks the actual value based on this input. For the current number of signals being output, the fastest that the hardware can handle is ~1.5 MS/Ch/s. The actual rate is chosen by the DAQ to be 1538460 S/Ch/s. Do not change this rate unless the number of output channels is changed for some reason.
- *Desired Input DAQ Rate*: [S/Ch/s] This field specifies the input DAQ rate in samples per channel per second. This rate is limited by the hardware. Furthermore, the *Actual Input DAQ* rate is set automatically by the hardware – the operator has no control over this number. Rather, the desired rate is more of a guideline rate that the operator provides to the hardware, and the hardware picks the actual value based on this input. For the current number of signals being input, the value should not exceed 200 kS/Ch/s to avoid significant ghosting. Much work and effort was done to optimize this rate.

Using these features, the operator can conduct tests with very good control. The most important part of experimental research is repeatability. The features in this program greatly increase repeatability. With time, the number of features will increase and the robustness of the program will continue to improve.

A.4.4 Output

The output loop of the test program generates voltage waveforms that are supplied to the actuation amplifier, the applied voltage op-amp, and to the SPM stage z-piezo. All three signals are thrown at the same rate of 1538460 S/Ch/s (the DAQ Output Rate). Generally, with each

iteration of the loop, a specific number of samples is supplied to a soft buffer for each of the three channels. The number of samples (and the number of cycles) fed into the buffer is dependent on the test frequency. While the test program is running at less than 20 Hz, the program only generates one cycle's worth of samples per channel. For all frequencies 20 Hz and greater, the program generates (|test frequency / 10|) worth of samples. The buffer is set up in such a way that if the DAQ reaches the end of the buffer without a new set of samples to throw, the DAQ will re-read the current buffer, starting from the beginning. This feature ensures that the program will never shut down because it cannot keep up with the DAQ. The other primary function of this loop is to update the output chart such that it is clearly and accurately displaying the data that it is outputting. When the program is stopped, the output loop is terminated, and all channels are supplied with two loop iterations worth of samples at zero voltage. This ensures that there is zero output after the program is terminated.

A.4.5 Input

The input loop has several jobs. The primary task of the input loop is to read in 5 channels worth of samples from the DAQ at a rate of 200 kS/Ch/s. As stated above, a lot of work was done to optimize this DAQ rate between under-sampling and ghosting, thus this number should not be changed except for very good reason. The five channels the input loop reads with each iteration are:

1) Applied Voltage (reading in / monitoring the applied voltage that is being output from that channel)
2) Voltage over the built-in in-series resistor
3) Voltage over the contact
4) Actuation voltage waveform (reading in / monitoring the applied voltage that is being output from that channel)
5) The A-B voltage signal from the SPM unit

These channels are sampled in this order. The order of sampling has to do with the optimization of the input DAQ rate. This order reduces ghosting on any given channel. With each iteration, the samples read in by the DAQ are stored in a buffer being read and interpreted by the computer. If the computer cannot keep up with the DAQ, the program will terminate prematurely. This can happen if there are a lot of processor-intense tasks being done simultaneously. For this reason, the number of programs running in parallel with the testing program should be minimized, especially while testing.

The second task that the input loop performs is the counting of in-coming cycles while also assigning an exact time to each sample read in. This makes the third input-loop task possible: recording of data. Based on the data capture mode (as described above), the input data loop will either queue the samples into a buffer to be written into the output file, or it will do nothing with them. The fourth and final task the input loop performs is update the input chart such that it is clearly and accurately displaying the data that it is outputting. Not every cycle read in by the DAQ is displayed; the computer monitor does not refresh fast enough to do that. Instead, the refresh rate of the chart is determined by the test frequency. Generally, the slower the test frequency, the slower the refresh rate. The operator, on average, sees one of

every 5 cycles input. The input loop has already been programmed to send data to the automation loop. However, as stated above, the automation algorithm is not complete, so nothing is done with this data.

A.4.6 Data Storage

Of the four loops simultaneously running in the test program, the data storage loop is by far the simplest. The only task this loop performs is the writing of the captured data points into the output TDMS file. This loop never times out, so it is always running in the background, regardless of if it is writing data to the output file or not. This loop writes the samples that are put into the write buffer from the input loop, but when the buffer is empty, the loop does not write anything.

A.4.7 Post Processing

As mentioned above, the test program saves raw test data into a TDMS file. For all captured cycles, the test program records Time (s), Cycle, Normalized Waveform (V), Applied Potential (V), A-B Signal (V), Contact Voltage (V), and Resistor Voltage (V) for every sampled point. The default sampling rate is 200 kS/Ch/s is order to get proper resolution of all of the signals. Thus, these TDMS test data files can become quite cumbersome. The purpose of the Post Processing Program is to condense the data into a more manageable form as well as perform some additional calculations for analysis purposes.

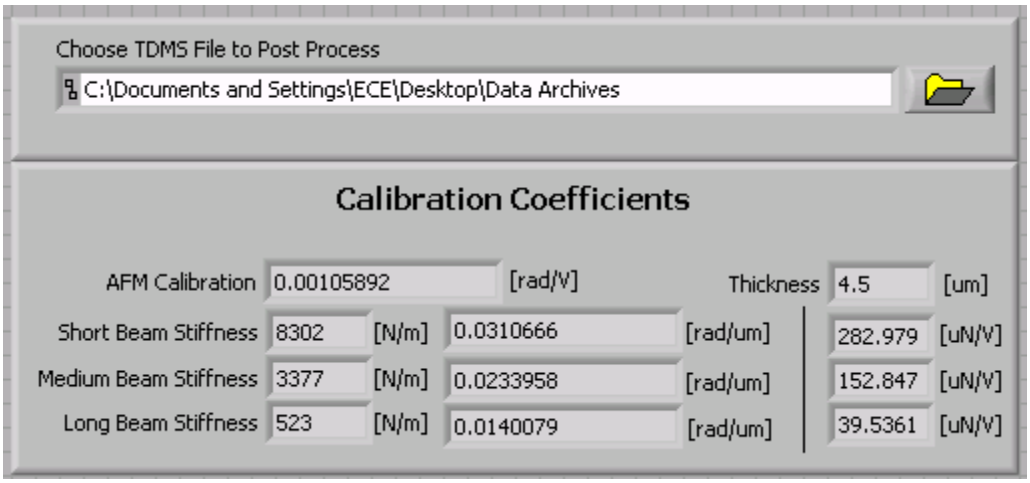

Figure A.12 Post processing program front panel.

Figure A.12 represents the front panel of the Post Processing Program. The only input to the Post Processing Program is the TDMS file name. This can be input manually, but the operator can also browse for the file by pressing the 'browse file' button to the right of the input field. Below the file name input field are a set of indicators that show the mechanical calibration constants used by the program to calculate contact force from the A-B signal.

- *AFM Calibration:* [rad/V] This value represents the rotation of the cross section of the sensor to the change in A-B voltage. This value is a built-in calibration constant that is controlled by the AFM. Every time the AFM is re-calibrated, this value needs to be updated in the post processing program sub-VI called 'Beam Stiffness.vi'.
- *Thickness:* [μm] This is the thickness of the beam as input by the user when the sample was tested. This value is stored in the TDMS file automatically and does not need to be input in the Post Processing Program.
- *Short, Medium, and Long Beam Stiffness:* [N/m] This value is calculated based on the thickness of the beam and the stiffness relationship established from the static analysis outlined above.
- *Rotation-Deflection Relationship:* [rad/μm] This value is calculated based on the thickness of the beam and the θ-δ relationship established from the static analysis outlined above.
- *Force-Voltage Relationship:* [μN/V] This is essentially the calibration constant used to calculate the contact force from the A-B voltage.

Running the Post Processing Program will condense the TDMS file into a tab-delineated text file (.TSV). This word file is broken up into 3 different sections:

1) Test Information: The next section contains two columns with all of the test information.

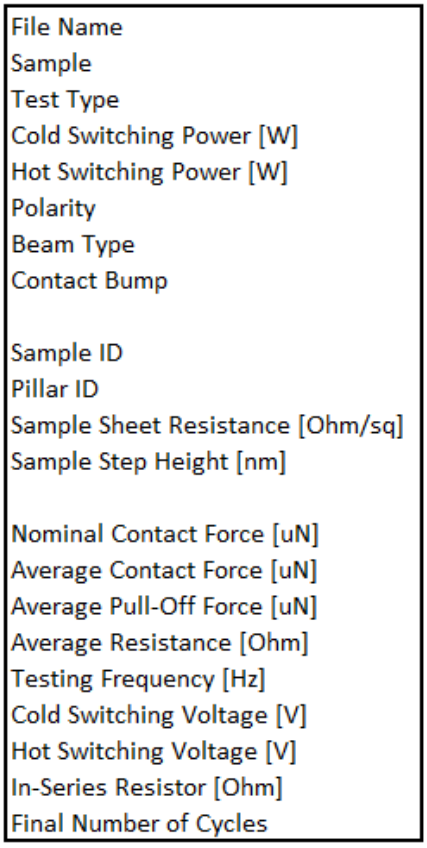

Figure A.13 Test Information Data Categories.

Figure A.13 shows all of the categories contained in the Test Information section of the .TSV file. This section makes it easy for the operator to identify the exact test conditions without tedious searching. Further, the data contained in this section allows the user to copy / paste into the Test Log file (a file that lists all tests done).

2) Single Cycle Data: Directly beneith the Test Information section is a set of columns that contain the individual cycle data. Below is a list of each category and a brief explanation:
   a. Time [s]: The time at which the cycle is initiated. For pure cold switching, trailing edge hot switching, and hot switching, the cycle is initiated the moment that the applied voltage reaches 92% of the cold switching voltage. For leading edge hot switching, the cycle is considered initiated the moment that the applied voltage reaches 92% of the hot switching voltage. For pure hot switching, the cycle is considered initiated at the start of the actuation waveform ramp up.
   b. Cycle: This is the cycle being considered for which all of the calculations in a given row are done for. The cycle number is taken to be the cycle at the initiation of the cycle as determined above.
   c. Waveform Holding Voltage [V]: This is the normalized waveform voltage during the 'holding' portion of the actuation cycle. The 'holding' portion is specifically defined as

the period of time while the cold switching voltage is being applied and considered to be in the steady state closed position.

d. A-B Baseline Voltage [V]: When the switch is in the steady state open position, there should be zero force applied to the structure. However, this neutral position has shown a tendency to drift slightly as the test goes on, especially with long tests. The exact reason is unknown, but it is suspected that there are a combination of reasons including, but not limited to plastic deformation, movement of the force structure in the holder, movement of the laser dot, etc. To compensate for drift, the A-B Baseline measurement is essentially measured between every cycle. The contact force is measured with respect to the A-B baseline. This value is the average of all of the points after the adhesion period and before the ramp-up portion of the actuation waveform.
e. A-B Holding Voltage [V]: This is the average of all of the A-B signal points while the cold switching voltage is being applied and the switch is in the steady-state closed position.
f. Contact Force [μN]: This value is calculated using the A-B Holding Voltage and the A-B Baseline Voltage in conjunction with the Force-Voltage Relationship above. This is an average of all of the points while the cold switching voltage is being applied and the switch is in the steady-state closed position.
g. A-B Pull-Off Voltage [V]: This is the minimum A-B signal reading in the adhesion region of the actuation waveform. This region is defined as the period directly following the ramp-down portion of the actuation waveform. This is not an averaged value – this is a single point value.
h. Pull-Off Force [μN]: This value is calculated using the A-B Pull-Off Voltage and the A-B Baseline Voltage in conjunction with the Force-Voltage Relationship above. This represents the adhesion force experienced by the contact.
i. Cold Switching Applied Voltage [V]: This is the average of all of the Applied Potential signal points while the cold switching voltage is being applied and the switch is in the steady-state closed position.
j. Contact Voltage [V]: This is the average of all of the Contact Voltage signal points while the cold switching voltage is being applied and the switch is in the steady-state closed position.
k. Resistor Voltage [V]: This is the average of all of the Resistor Voltage signal points while the cold switching voltage is being applied and the switch is in the steady-state closed position.
l. Contact Resistance [Ω]: Using the average Contact Voltage measurement and the average Resistor Voltage measurement, the Contact Resistance is measuring the four-wire equation presented above.
m. Corrected Contact Resistance [Ω]: To compensate for alternate current paths through the testing system in parallel to the actual contact between the bump and pillar, a

formula was developed to calculate an adjusted contact resistance value. This equation is integrated into the post-processing program.

n. Intercept [%]: This is the percentile that the A-B signal started rising with respect to the actuation waveform. This value essentially represents the spacing between the pillar and structure. This value is extremely important for the automation algorithm.

3) Plotting Data: Directly to the right of the single cycle data section is the plotting data section. As stated above the Test Program captures groups of 30 points centered at cycle values of specific log based interval values. The plotting data section averages the data from these 30 cycles to obtain one plotting point for each of the categories: Cycle, Contact Force, Pull-Off Force, and Contact Resistance.

Using the Post Processing Program, the operator can quickly condense an entire test worth of raw data into a manageable set of representative data. The best part of having a separate program for this purpose is that re-processing of data is not only possible, but easy to do should a problem ever arise. For example, if it is discovered that the A-B signal was not appropriately calibrated, the raw data can be re post-processed with a new calibration value to get the actual contact force values associated with the test. This saves a lot of time and effort.

Finally, a template excel spreadsheet has been created with a custom macro to automatically plot and format the .TSV file generated from the Post Processing file. This is an un-essential program, though, so the details of that spreadsheet and macro will not be covered in this document.

A.5 Volume transfer calculation

When characterizing the damage to the micro contacts tested, it becomes exceedingly important to have a quantifiable method of doing so, as opposed to just qualitative description of the damage (such as that provided by an SEM micrograph). For this reason, I developed a volume calculation method to quantify the material transferred from one electrode to the other in a contact pair that was tested. The following section will provide an outline of the volume calculation program as well as the theory it is based on.

After a test is conducted on a contact pair, an SEM micrograph is taken of the contact to verify that the test was a success. Contact contamination, alignment drift, contact not on contact bump, and contact defects are all examples of reasons to declare a test as unsuccessful. An example of an SEM micrograph of a successful test is presented in Figure A.14(a). This was a trailing edge hot switching test with a hot switching voltage of 3.53 V_{Hot} and a cold switching voltage of 3.83 V_{Cold} with a 50 Ω series resister at 500 Hz for 10^4 cycles. This test will serve as an example of the volume calculation method; the following process outline steps will all refer to this test.

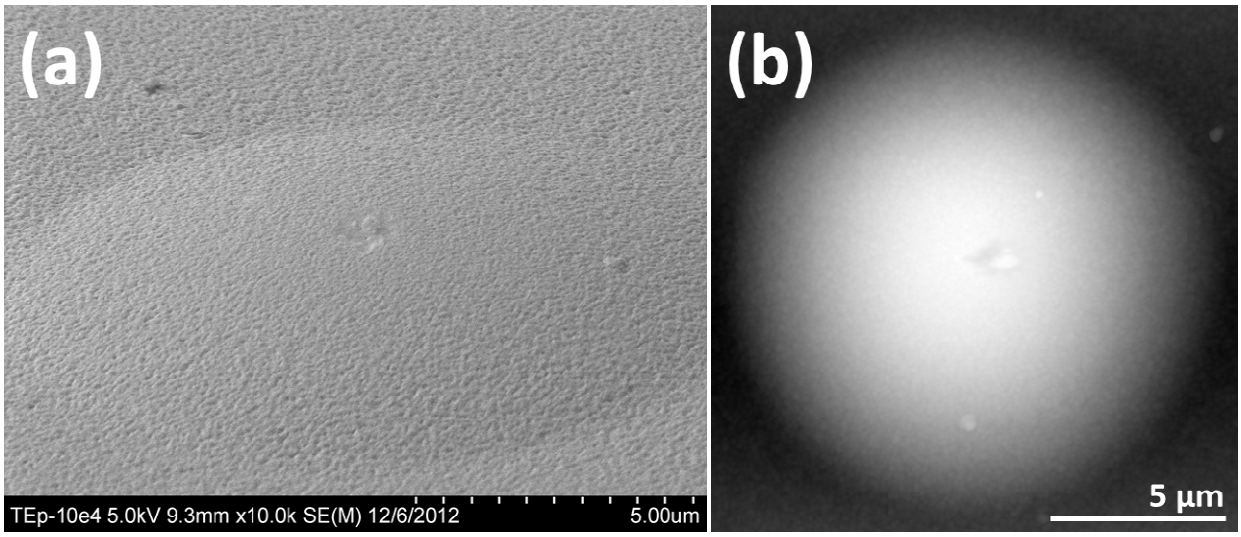

Figure A.14 (a) SEM of a Contact Bump (b) AFM of the same contact bump.

Once the test is verified, an AFM image of the sample is taken using a well calibrated AFM as shown in Figure A.14(b). Both the sharpness of the tip and the calibration of the AFM are critical for this process, the accuracy of the volume calculation depends heavily on both. The size of the AFM image is 15µm x 15µm so as to capture the entire contact bump. Because the JEOL 5200 SPM does not export point-cloud files, Gwyddion® software pack must be used to produce a point cloud from the exported image. To do this, the AFM image exported from the JEOL 5200 must be opened with Gwyddion®. Using the save-as functionality, the image can be saved to a tab-deliniated text file (.txt). Note that with this text file should not be exported with a header column.

Using the MATLAB program 'Full_Bump_Calculation.m', the first thing the user will be prompted to do is to choose a file to open. The user should open the text file from Gwyddion®.

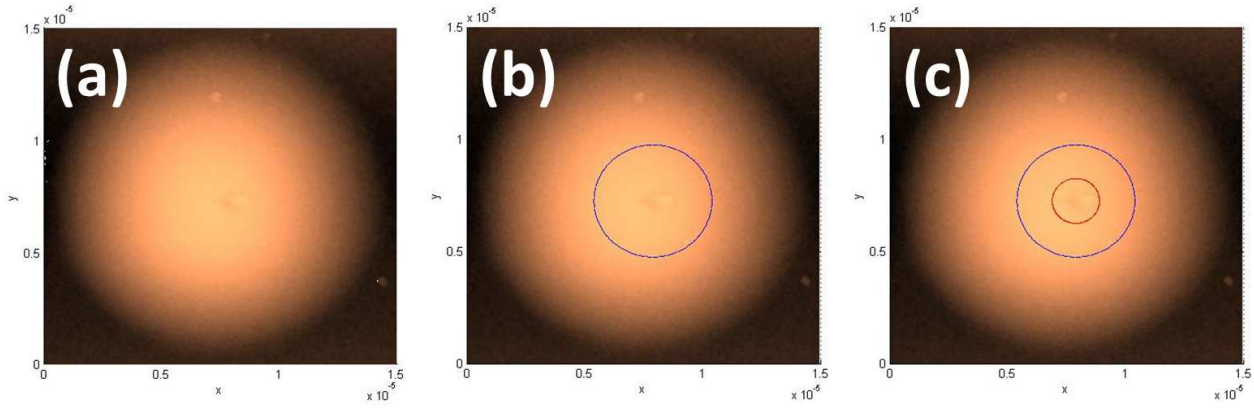

Figure A.15 Volume calculation program rendering of AFM image.

The program will then render a representation of the AFM as shown in Figure A.15(a). Next, the program prompts the user to define the 'outer circle'; this is the region over which the program will produce a curve fit. This region must include the damage area. Generally, it is desirable to keep this area small enough such that there is enough area for the surface fitting algorithm to estimate the curvature of the surface, but also small enough to keep the run-time of the surface fitting algorithm manageable. In this case, because the damage area is not large, an outer radius of 2.50 µm will suffice. The location of the center of the circle is done iteratively by the user. Once the user is satisfied with the size and location of the outer region, the program prompts the user to define the 'inner region'. The inner region is the damage region. These points will be excluded when surface fitting. This is done so that the damage region points do not influence surface fit. In this case, the radius of the inner circle is defined as 1.00 µm.

The volume calculation program then surface fits the so-called 'non-damage' points with an equation of the form of Equation (A. 1). The 'non-damage' points are all of the points contained within the boundaries of the blue circle, excluding those points contained within the red circle.

$$z(x,y) = A\cos\big(B(x-x_0)\big)\cos\big(C(y-y_0)\big) + D\cos\big(E(x-x_0)\big)\cos\big(F(y-y_0)\big) + G(x-x_0) + H(y-y_0) + I \quad \text{(A. 1)}$$

The form of this surface equation was chosen based on the superposition of two wavy surfaces and an elevated and slanted surface. It was found empirically that this form generally fit the surface contour of the contact bumps the best as compared to spherical and paraboloid forms.

To generate a surface, the curve-fitting tool in MATLAB optimizes the surface using the non-linear least squares method to solve for the coefficients A-I. To ensure convergence, the limit of optimization iterations is set high (50,000 iterations) and LAR robust solving method is used. The result is a three dimensional rendering of the surface, as pictured in Figure A.16.

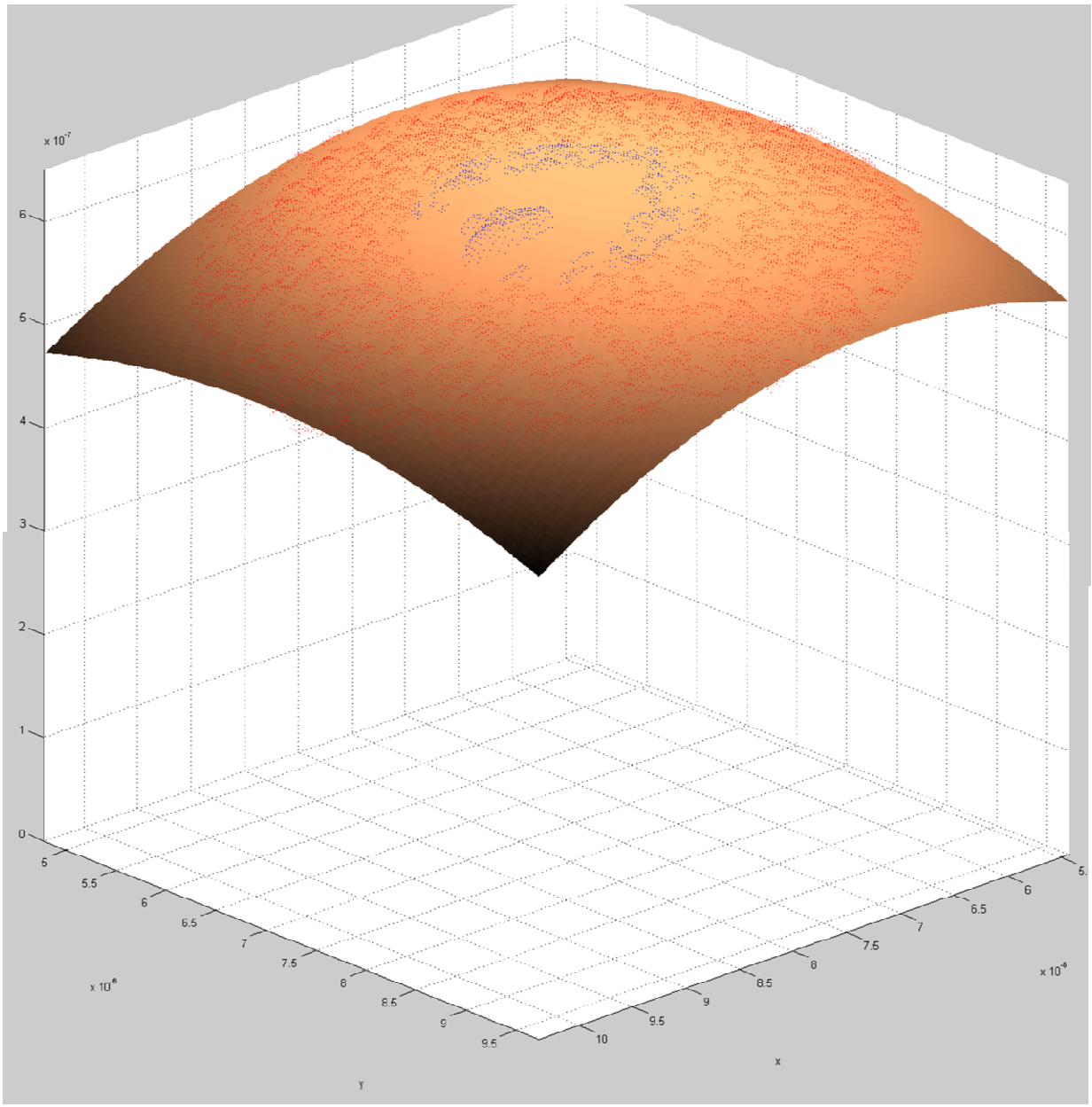

Figure A.16 Generated surface fit with non-damaged area points (red) and damaged area points (blue).

The red points represent the non-damaged area that was surface-fit while the blue points represent the damaged area. The material transfer volume is determined by subtracting the curve fit surface from the actual surface point-by-point and multiplying by the distance between points; this is simple numerical integration. Thus, a pit in the contact will result in a negative volume and a mound on top of the contact bmp will result in a positive volume. Note that the 'bald' spots in the damaged area represent regions where all of the points lie below the surface – these are the pits in the contact bump. As expected, for this particular sample, the

net volume transfer is negative. The total volume transferred away from this contact bump was roughly $-2.63 \times 10^{-2}\ \mu m^3$.

This program had to be verified in some manner. To do this, conservation of mass was demonstrated. This exercise yield the expected result: the amount of material missing from one electrode was roughly equal to that gained by the opposing electrode. Note that this was done for several different samples.

A.6 Appendix References

[1] Senturia, S. D., 2001, Microsystem design, Kluwer academic publishers Boston, MA.